A

DNS and transient growth analysis of aircraft wakes.

The effect of aircraft tail configuration

by

Christopher Luke Ellis

A Thesis submitted to Monash University

for the degree of

Doctor of Philosophy

August 2012

Department of Mechanical and Aerospace Engineering

Monash University

To my parents, who have supported me and put up with me living at home for a few more years.

Statement of Originality

This thesis contains no material that has been accepted for the award of a degree or diploma in this or any other university. To the best of the candidate's knowledge and belief, this thesis contains no material previously published or written by another person except where due reference is made in the text of this thesis.

Candidate: Chris Ellis

<Submission Date>

"And it worked?"

"In point of fact it didn't,

but I'm convinced the theory is sound."

Colonel John Patterson,

The Ghost and the Darkness, 1996.

Abstract

This thesis describes an analysis of the transient growth characteristics of arrangements of parallel vortices including vortex pairs and four-vortex systems. These flows are a useful model for the far-wake created by the combination of a wing and tail of an aircraft. These wakes can be extremely hazardous to aircraft moving through the same airspace, and increase in strength as the lift of the generating aircraft increases. Given that aircraft have undergone a significant jump in size with the Airbus A380 and the C-17 Globemaster aircraft, the investigation of these types of vortex flows has experienced renewed interest. Specifically, this study investigates an equal strength two-vortex system, a symmetric four-vortex system (with the vortex strength equal, but opposing in vorticity sign across the mid-plane for each vortex pair) with varying vertical displacement of the vortex pair that represents the tail vortex pair, and an asymmetric strength four-vortex system (with the vortex strength differing across the mid-plane) with a similar varying vertical displacement of the tail vortex pair. The 'flat tail' and 'high tail' cases referred to later in the thesis refer to the cases without and with vertical displacement of the tail vortex pair respectively (for example, the Airbus A380 is a 'flat tail' aircraft and the C-17 Globemaster is a 'high tail' aircraft).

It was found in all the cases studied that by seeding various vortex flows with the perturbations that lead to optimal energy growth (created from a transient growth analysis in the linear regime) it is possible to obtain very large reductions in the time required to cause transition into the non-linear regime and subsequent destruction of the coherence of the vortex flow.

The transient growth analysis performed on the symmetric four-vortex system demonstrated that both the 'high tail' and 'flat tail' configurations were most unstable to the transient growth of perturbations at the same axial wavenumber, $k\,a_1 = 5.3$. This gave the perturbation that leads to optimal energy growth, centered in the tail vortex pair of the system in the form of a mode [-1,1,1] elliptic instability.

The three-dimensional direct numerical simulation (DNS) of the four-vortex study demonstrated that there are two main vortex interactions present in the growth and subsequent destruction of four-vortex flows. If the instability has reached a sufficient magnitude in the tail vortex pair before entering the highly strained region between the wing vortex pair, the tail vortices are forced to interact with each other, causing a rapid breakdown into small scale flow structures. Conversely, if the instability in

the tail vortex pair has not reached the critical magnitude before entering this highly strained region, the tail vortex pair will not interact with each other, leading to a slower growth due to the interaction between the wing and tail vortices alone.

The asymmetric four-vortex study found an immediate growth of the instability, by seeding the flow with the perturbation that leads to optimal energy growth. One finding of interest is that the perturbation that leads to optimal energy growth is predominantly contained within the weaker tail vortex. The three-dimensional DNS demonstrates that the instability grows in the weaker tail vortex first, causing its destruction, then continuing through the other vortices in order of strength.

The implication of this study is that by seeding the wake with specific perturbations, the time that is required to eliminate the hazard of the wake can be decreased significantly, reducing the hazard to trailing aircraft. This would allow a reduction in the spacing of aircraft through airports, increasing throughput. This increase in throughput would allow for airports to reduce the fuel usage of aircraft having to wait to land due to the wakes of other aircraft, while maintaining safety. Another implication of the study for real aircraft is that the seeding of instabilities in the wake is most effective if seeded within the tail vortex pair, which would mean that a control system only needs to be present on the tail, reducing the cost of such a system.

An important discovery by this study is the importance of the transition into the non-linear growth for systems comprising of more than two vortices and how the interactions can change due to the magnitude of the instability as the vortices enter favourable regions.

A major implication of this study is to elucidate the limitations of vortex filament methods used in previous studies (Crow 1970; Crouch 1997; Fabre & Jacquin 2000; Bristol *et al.* 2004) compared to methods such as the transient growth method. These limitations are due to the vortex filament ignoring any viscous interaction (such as two-dimensional vortex stripping) between the vortices and the assumption of a specific mode shape of the instability.

Acknowledgments

Ainslie Ellis
Peter Ellis
Greg Sheard - Supervisor
Kris Ryan - Supervisor

Monash E-Research centre

Publications arising from this thesis

Ellis, C.L., Ryan, K. & Sheard G.J. 2009 Two-dimensional computational analysis of 'high tail' configuration aircraft wake vortex pairs. *In proceedings of the Seventh International Conference on CFD in the Minerals and Process Industries*, Melbourne, Australia, December, 2009.

Ellis, C.L., Ryan, K. & Sheard G.J. 2010 A Three-Dimensional Transient Growth and DNS Analysis of 'High Tail' and 'Flat Tail' Aircraft Configurations. *In proceedings of the 17th Australasian Fluid Mechanics Conference*, Auckland, New Zealand, December 2010.

Ellis, C.L., Ryan, K. & Sheard G.J. Non-linear growth of transient and optimal three-dimensional disturbances in a counter-rotating vortex pair. *Physics of Fluids*, to appear.

Nomenclature

List nomenclature here.

Symbol	Description
$\S$	Thesis section
$\int$	Integration
∇	Vector gradient operator (grad)
∇^2	Del squared (or div grad) operator
Re	Reynolds Number
q	Swirl
k	Axial wavenumber
a_1	Initial strong vortex core radius
a_2	Initial weak vortex core radius
a_{tv}	Time varying vortex core radius
b	Vortex separation
Γ	Vortex circulation
h	Vertical displacement of tail vortex pair
$\mathbf{u}$	Velocity vector field
t	Time
p	Pressure
ν	Kinematic viscosity
v_{az}	Azimuthal vortex velocity
τ_{xx}	x-component of rate of strain in the x-direction
τ_{yy}	y-component of rate of strain in the y-direction
τ_{xy}	x-component of rate of strain in the y-direction
T_0	Initial orbital period of a tail vortex around its corresponding wing vortex

Continued on the next page.

Continued from previous page.

Symbol	Description
T_{2V}	Two-vortex normalisation time
T_{st}	Time the flow is seeded with the optimal perturbation
T_{VST}	Time from flow seeding
b_0	Aircraft wingspan
z_{ds}	Downstream distance
AR	Wing aspect ratio
C_L	Wing lift coefficient
σ_{GR}	Instability growth rate
$\bar{t}$	Non-dimensional time coefficient
m	Number of mesh elements
x, y, z	Spatial coordinates
u, v, w	Velocity components in the x,y and z direction respectively
E	Kinetic energy in the flow
$\mathscr{A}$	Evolution operator for the linearised Navier–Stokes equation
$\bar{\tau}$	Physical time horizon for the transient growth analysis
τ	Normalised time horizon for the transient growth analysis
ϵ_{int}	Change in interpolated values from DNS
n_s	Number of snapshots used in an interpolation
p_n	Polynomial order
p_f	Number of Fourier modes
ϵ	Estimated polynomial order
δ	Tail vortex circulation drop normalised by initial circulation
$G(\tau)$	Growth amplification factor
λ_2	The second largest eigenvalue of the symmetric tensor $\mathbf{S}^2 + \Omega^2$ (as per Jeong & Hussain 1995)
$\mathbf{S}$	Symmetric part of the velocity tensor gradient $\nabla\mathbf{u}$
Ω	Asymmetric part of the velocity tensor gradient $\nabla\mathbf{u}$

Contents

Introduction

Wingtip vortices are a byproduct of lift generated by wings of an aircraft. A vortex sheet comprising small co-rotating vortices are shed from any defect or change in wing profile or when high pressure air from underneath the wing flows around the outer edges of the wing tip. This vortex sheet rolls up into a large wingtip vortex (McCormick 1995). These vortices have the effect of creating a net downward flow behind the aircraft, causing a hazard for any aircraft trailing the lead aircraft, if the trailing aircraft encounters either vortex in the pair. If an aircraft encounters one of the vortices, it may induce a large rolling moment on the trailing aircraft. This can pose a real danger to following aircraft, as evidenced by the crash of the American Airlines Flight 587 Airbus A300 in New York, on 12 November 2001, due to a failure of its rudder when abrupt corrections were applied after passing through another aircraft's wake (NTSB Report Number AAR-04-04).

As aircraft are becoming heavier, the wake vortices they produce also increase in size and strength. The residence time of these vortices limits the frequency at which aircraft can take off or land, which ultimately limits the maximum passenger throughput of airports prompting research into mechanisms for reducing the impact of these vortices in aviation (Gerz *et al.* 2002).

This type of problem also presents a particular challenge at military airfields, as the airfield traffic can be large and the types of aircraft moving through the airspace vary greatly in size. For example, on the smallest scale, air superiority fighters, such as the Lockheed Martin F-22 Raptor, tend to be on the scale of a 14 metre wingspan with a mass of 30 tonne (Gunston 1995); while at the opposite end of the scale, the C-17 Globemaster aircraft has a 52 metre wingspan and a mass of 265 tonne (Gunston 1995). This extreme disparity in size means that the wake of a C-17 could be extremely hazardous to small fighter aircraft passing through its wake. The effect of a large aircraft wake is likely to be a hazard even in open air, as fighters tend to fly in close

formation and a large perturbation to the aircraft can cause it to impact with other aircraft in the formation if traveling at lower speeds.

Recent research into wake vortices has investigated the detailed process by which these vortex systems are created. In addition, the natural degradation of these systems after a period of time has also been investigated. This degradation has been found to be due to viscous properties of the fluid, but is not completely understood. It has also been shown that the tail vortex pair can have a significant effect on the behavior of the larger and stronger wing vortex pair (Rennich & Lele 1999). While some studies have been completed that investigated the interaction between the vortex pairs of the wings and tail, there has been no research into how different aircraft tail configurations, for example high tail aircraft such as the C-17 Globemaster, affect this interaction. Prior investigations have concentrated on global instabilities, giving only an understanding of asymptotic instability behaviour in the wake. With a view to dispersing the wakes behind behind aircraft as rapidly as possible, an analysis of the transient growth of disturbances to these wakes may yield new insight. As yet, the transient growth analysis method (e.g. see Barkley *et al.* 2008) has not been applied to this type of fluid system, and this forms a key component of this study.

This research utilises three-dimensional modeling software to model and analyse the interaction between a number of vortex configurations of varying strength ratio. This provides a greater understanding of these interactions, potentially providing a method of inducing rapid breakdown of the vortex configurations.

Chapter 1

A Review of the Literature

1.1 Early research

The earliest research in this field was conducted by Sir William Thomson (Lord Kelvin) in 1880. He published a study investigating vibrations in an isolated vortex (Thomson 1880). This analytical study consisted of adding perturbations to a columnar vortex in an inviscid flow using a linearised analysis. The perturbations, now known as Kelvin waves, were of the form,

$$v = \Phi(r)e^{i(kz-\omega t+m\theta)} + c.c., \tag{1.1}$$

where k is the axial wavenumber, m is the azimuthal wavenumber or mode, ω is a frequency related to k and m, and *c.c.* designates the complex conjugate. Thomson found that perturbations added to a single solitary vortex would neither grow nor decay, meaning that ω is real or zero. However, the perturbations would rotate as the vortex rotated.

As the hazards of aircraft wakes became clear, interest in these flows prompted detailed investigation into the dynamics of idealized representations of these aircraft wakes, such as pairs of two-dimensional vortices. These investigations began around the 1970s (Crow 1970; Barker & Crow 1975). The primary reason for this renewed interest was the development of the Boeing 747, with its significant increase in size and weight over earlier commercial aircraft. The high-pressure air generated under the wing of an aircraft skips around the wingtip, causing a number of trailing vortex pairs to form in the air and trail behind the aircraft with a strength proportional to the lift provided by the wing. Early work in this field discovered a long wavelength instability that can potentially lead to the destruction of these vortex pairs (Crow 1970). For equal strength vortices, this long wavelength instability is characterised by a sinusoidal, long

FIGURE 1.1: An example of the Crow instability in an aircraft contrail. Photo by H. Raab (2011)

wavelength instability that is symmetrical about the plane dividing the two vortices and inclined at approximately 45° to a line from the vortex centres (Bristol *et al.* 2004). The Crow instability, as it has since become known, is observed in the contrails of modern aircraft and an example is shown in figure 1.1.

As an aircraft encounters the trailing vortices of a preceding aircraft, one of two effects can occur. If the trailing aircraft enters only one vortex, then it can create a large rolling moment on the aircraft. The rapid corrections required to level the aircraft can cause structural damage to the tail and control surfaces. This kind of accident occurred in 2001 with American Airlines Flight 587 where rapid and aggressive corrections made by the pilot caused the separation of the vertical stabiliser (National Transportation Safety Board (NTSB) Aircraft Accident Report NTSB/AAR-04/04). If the trailing aircraft enters between the two trailing vortices, which is most common in the case of a landing strip, then the flow causes a large downforce on the aircraft. This downforce counters the lift on the aircraft and can cause a rapid loss in altitude. In the case of a landing aircraft, when the altitude is already small, this reduction in lift can be catastrophic.

Work by Mason & Marchman (1972) used wind tunnels to simulate aircraft wakes while Miller & Brown (1971) and Lezius (1973) used water towing tanks to simulate these simple vortex pairs. While experimental work can provide a Reynolds number that is similar to an actual aircraft in flight, it also presents a significant problem due to turbulent noise. This turbulent noise could have the effect of masking short wavelength instabilities in the flow being analysed. This turbulent noise can also cause 'vortex wandering' which has the effect of making the vortices appear larger than they actually are (Barker & Crow 1975).

The other challenge with wind tunnel and towing tank experiments is interference with the vortex pairs due to the probe used to measure the vortex pair. The physical

presence of the probe has the effect of causing the vortex to move away from the probe, disturbing the behaviour of the vortex pair (Barker & Crow 1975). Earlier work by Baker *et al.* (1974) used a laser anemometer to measure the vortex within a water towing tank. The advantage with a laser anemometer is that it eliminates the probe interference. However, the turbulent noise inherent within experimental results still remains and this noise provides a likely explanation for the observation of only long wavelength instabilities in early studies.

More recently, Constant *et al.* (1994) demonstrated that Doppler LiDAR can be used to measure the actual wake of a landing aircraft in open air. This method is useful for detecting the vortices produced by an aircraft, and tends to be simple and robust (Gerz *et al.* 2002). Unfortunately, this method is prone to error when measuring close to the vortex core, and also has difficulties distinguishing between the fluid flow due to the vortex and the ambient background turbulence (Gerz *et al.* 2002).

As computing technology has advanced, the computing speed and memory resources have increased exponentially, allowing for the direct simulation of these wake vortex configurations. In the early 1980s, new methods of directly simulating a fluid flow were developed that provided high-order results, an example of which is the spectral element method developed by Karniadakis *et al.* (1991). Computational simulations have the advantage of eliminating probe interference and turbulent noise. For a direct numerical simulation of a wake vortex system, the Re must be reduced to $O(10^5)$ to allow for reasonable computational times. This decrease in Re causes the turbulence on the smallest scale to be damped out by viscous forces (Leweke & Williamson (1998) and Meunier & Leweke (2005)). This is not a significant limitation to the present study, as the instabilities that lead to the destruction of aircraft wakes are far above the scale of the turbulence being damped out. The other advantage of computational simulations is that, due to the lack of turbulent noise, they can demonstrate growth of shorter wavelength instabilities that are distinct from other noise sources in high Re experimental setups.

1.2 Single vortex immersed in a strain-rate field

1.2.1 Vortex profiles

There are a number of vortex velocity profiles frequently used to model the vortices in the wake of an aircraft. These radial profiles of tangential velocity are covered below

and are summarized in Gerz *et al.* (2002).

1.2.1.1 Rankine vortex

$$v_\theta(r) = \frac{\Gamma_0}{2\pi r_c}\frac{r}{r_c} \text{ for } r \leq r_c,\ v_\theta(r) = \frac{\Gamma_0}{2\pi r} \text{ for } r > r_c$$

1.2.1.2 Lamb–Oseen vortex (Gaussian profile without axial flow) (Lamb 1923)

$$v_\theta(r) = \frac{\Gamma_0}{2\pi r}\left\{1 - \mathrm{e}^{\left(-1.2526\left(\frac{r}{r_c}\right)^2\right)}\right\}$$

1.2.1.3 Hallock–Burnham vortex (Burnham & Hallock 1982)

$$v_\theta(r) = \frac{\Gamma_0}{2\pi r}\frac{r^2}{r^2 + {r_c}^2}$$

1.2.1.4 Adapted vortex (Proctor 1998)

$$v_\theta(r) = 1.4\frac{\Gamma_0}{2\pi r}\left\{1 - \mathrm{e}^{\left(-10\left(\frac{r_c}{b}\right)^{0.75}\right)}\right\} \times \left\{1 - e^{\left(-1.2526\left(\frac{r}{r_c}\right)^2\right)}\right\} \text{ for } r \leq r_c\ v_\theta(r) = \frac{\Gamma_0}{2\pi r}\left\{1 - \mathrm{e}^{\left(-10\left(\frac{r_c}{b}\right)^{0.75}\right)}\right\} \text{ for } r > r_c$$

1.2.1.5 Smooth blending vortex profile (Winkelmans *et al.* 2000)

$$v_\theta(r) = \frac{\Gamma_0}{2\pi r}\left\{1 - \mathrm{e}^{\left(-\frac{\beta_i\,(r/b)^2}{\left\{1 + \left[(\beta_i/\beta_o)\,(r/b)^{5/4}\right]^p\right\}^{1/p}}\right)}\right\} \text{ with } \beta_0,\ \beta_i \text{ and } p = 10,\ 500$$

and 3 respectively.

1.2.1.6 Multiple scale vortex (Jacquin *et al.* 2001)

$$v_\theta(r) = \frac{\Gamma_0}{2\pi r_i}\frac{r}{(r_i r_o)^{1/2}} \text{ for } r \leq r_i.\ v_\theta(r) = \frac{\Gamma_0}{2\pi\,(r_o r)^{1/2}} \text{ for } r_i \leq r \leq r_o.\ v_\theta(r) = \frac{\Gamma_0}{2\pi r} \text{ for } r \geq r_o.$$

One of the most commonly used vortex profiles in this field of study is the Lamb–Oseen vortex, a vortex with a Gaussian profile without axial flow.

1.2.2 Strain rate definition

In fluid mechanics, the strain rates are a measure of the rate of change of the three directions of velocity (u, v, w) in each of the Cartesian directions (x, y, z). This leads to 9 different strain rates as there are three directions of velocity and three Cartesian directions. The most common way of presenting these strain rates are as a 2^{nd} order tensor,

$$\dot{\boldsymbol{e}} = \begin{vmatrix} \dot{\varepsilon}_{11} & \dot{\varepsilon}_{12} & \dot{\varepsilon}_{13} \\ \dot{\varepsilon}_{21} & \dot{\varepsilon}_{22} & \dot{\varepsilon}_{23} \\ \dot{\varepsilon}_{31} & \dot{\varepsilon}_{32} & \dot{\varepsilon}_{33} \end{vmatrix} = \begin{vmatrix} \dot{\varepsilon}_{xx} & \dot{\varepsilon}_{xy} & \dot{\varepsilon}_{xz} \\ \dot{\varepsilon}_{yx} & \dot{\varepsilon}_{yy} & \dot{\varepsilon}_{yz} \\ \dot{\varepsilon}_{zx} & \dot{\varepsilon}_{zy} & \dot{\varepsilon}_{zz} \end{vmatrix}. \tag{1.2}$$

Within this matrix, each component is defined as,

$$\dot{\varepsilon}_{ij} = \frac{1}{2}\left(\frac{\partial u_i}{\partial x_j} + \frac{\partial u_j}{\partial x_i}\right), \tag{1.3}$$

where $\dfrac{\partial u_i}{\partial x_j}$ is the derivative of u_i with respect to x_j, adopting tensor notation.

Within the context of vortex studies, the two-dimensional x-y strain-rate,

$$\dot{\varepsilon}_{xy} = \frac{1}{2}\left(\frac{\partial u}{\partial y} + \frac{\partial v}{\partial x}\right), \tag{1.4}$$

is the most important as it usually dominates the strain rate that causes the elliptic instability. However, it is possible to have a non-zero strain rate when $\dot{\varepsilon}_{xy} = 0$.

1.2.3 Vorticity definition

Vorticity is a measure of the rotation of a fluid flow. In a similar manner to the strain rate, the vorticity forms a 2^{nd} order tensor,

$$\dot{\boldsymbol{e}} = \begin{vmatrix} \dot{\omega}_{11} & \dot{\omega}_{12} & \dot{\omega}_{13} \\ \dot{\omega}_{21} & \dot{\omega}_{22} & \dot{\omega}_{23} \\ \dot{\omega}_{31} & \dot{\omega}_{32} & \dot{\omega}_{33} \end{vmatrix} = \begin{vmatrix} \dot{\omega}_{xx} & \dot{\omega}_{xy} & \dot{\omega}_{xz} \\ \dot{\omega}_{yx} & \dot{\omega}_{yy} & \dot{\omega}_{yz} \\ \dot{\omega}_{zx} & \dot{\omega}_{zy} & \dot{\omega}_{zz} \end{vmatrix}. \tag{1.5}$$

Within this matrix, each component is defined as,

$$\dot{\omega}_{ij} = \frac{1}{2}\left(\frac{\partial u_i}{\partial x_j} - \frac{\partial u_j}{\partial x_i}\right) \tag{1.6}$$

where $\dfrac{\partial u_i}{\partial x_j}$ is the derivative of u_i with respect to x_j, adopting tensor notation.

In the context of vortex studies, the x-y component of vorticity (representing rotation about the z-axis) is the most commonly used as the majority of the rotation of the flow is in the x-y plane.

1.2.4 Reynolds number definition

Reynolds number is a dimensionless variable used in fluid mechanics to characterise properties of a flow. It is a measure of the ratio of inertial to viscous forces in a given flow. The Reynolds number allows dimensional similitude between different experiments. For vortex studies Reynolds number, Re, is defined based on the circulation of the wing vortex, Γ_1, and the kinematic viscosity, ν, as

$$Re = \frac{\Gamma_1}{\nu}. \tag{1.7}$$

1.2.5 Swirl strength definition

Swirl strength, q, is a variable used when a vortex is subjected to an axial flow. Swirl strength is defined as the ratio between the peak angular velocity component to the peak axial velocity component.

1.2.6 Three-dimensional vortex studies

Early research into vortex flows began with Batchelor (1964) investigating a single vortex with axial flow using an analytical approach. As this was the first time that vortices with axial flow had been investigated, any vortex with a Gaussian profile with axial flow is now known as a "Batchelor vortex". One of the main findings of Batchelor was that, after an asymptotic timeframe in the presence of viscosity, a vortex will eventually evolve into a Gaussian vortex profile.

By examining a single vortex in an externally imposed strain rate field, a basic model of a two-vortex system can be constructed. Tsai & Widnall (1976) took this approach, investigating a single Rankine vortex filament in an externally imposed strain field by use of an analytical stability analysis. Parallel to the study by Tsai & Widnall (1976), Moore & Saffman (1975) also investigated a single vortex filament in an externally imposed strain field. The difference between the two studies is that, while Tsai & Widnall (1976) considered a Rankine vortex, Moore & Saffman (1975) considered a generic vortex profile. This analytical stability analysis was performed on a vortex in weak strain with an axial wavenumber $k\,a = \mathcal{O}(1)$. Tsai & Widnall found that the vortex had a peak instability growth rate for a range of axial wavenumbers, $k \approx 2.5, 4.5$ and 6.5, for a stationary Kelvin wave with an azimuthal wave number equal to -1 and +1. They found that these unstable regions of short axial wavelength occurred because of the circular cross section of the vortex filament becoming elliptical due to the externally

imposed strain field. This short axial wavelength instability is now known as the elliptic instability and is a Kelvin pair which resonates with the very small externally imposed strain field. Kerswell (2002) published a review of the discovery and development of the understanding of the elliptic instability.

Pierrehumbert (1986) investigated the stability of a two-dimensional vortex within inviscid, incompressible flow to three-dimensional perturbations. Pierrehumbert utilised the linearised Navier–Stokes equations and reduces the instability to an eigenvalue problem. He computed the eigenvalues for a number of instabilities, finding that at short wavelengths along the vortex axis, the eigenmode is concentrated near the centre of the vortex. This leads to the conclusion that, at short wavelengths, the growth rate becomes independent of the wavelength.

At the same time, Bayly (1986) was investigating the three-dimensional instability of elliptical flows and follows directly on from Pierrehumbert (1986). Bayly presented a theory to clarify the physical and mathematical nature of the elliptic instability. The study extended Pierrehumbert (1986), finding that the structure of the instability is independent of length scale in the limit of large wavenumber. The results of Bayly correspond extremely well with that of Pierrehumbert (1986).

Using both analytical and experimental methods Landman & Saffman (1987) investigated three-dimensional viscous instabilities that occur on a single Rankine vortex with an infinite core size immersed within an externally imposed strain field at a Reynolds number of $Re = 40\,000$. They demonstrated that the inviscid instability mechanisms that lead to vortex destruction persist even when the viscosity is non-zero. In addition, they found that a typical vortex structure is large enough to support these three-dimensional instabilities, even when viscosity is present. Landman & Saffman suggested that the Reynolds number could be as low as $Re = 1000$ and still support the three-dimensional instabilities that lead to vortex destruction. This is an extremely beneficial discovery, as it allows the analysis of the instabilities present in aircraft wakes that lead to the destruction of the wake, without having to simulate the extremely high Reynolds number, $Re \approx \mathcal{O}(10^8)$, present for commercial aircraft.

Waleffe (1990) presented a physical interpretation for the mechanism with an analytical treatment of three-dimensional instabilities of a two-dimensional elliptical flow. Waleffe demonstrates an analytical representation for a localised solution which is directly consistent with previous studies. The solution presented by Waleffe demonstrates

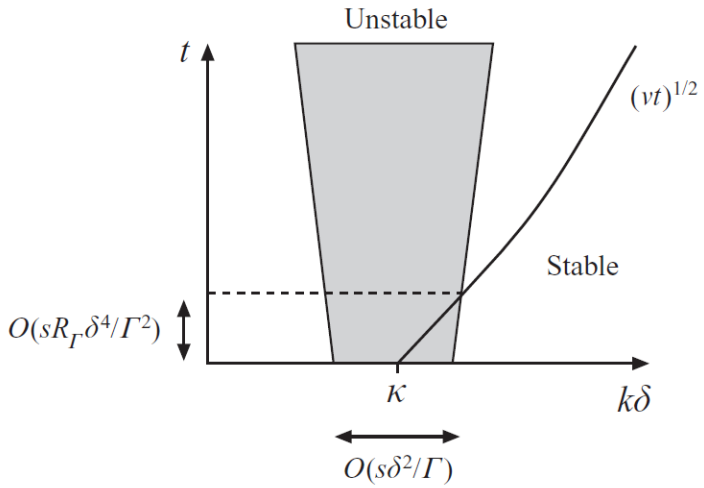

FIGURE 1.2: A reproduction of figure 2(a) from Eloy & Le Dizès (1999) displaying the temporal evolution of the product $k\delta$ for a Lamb–Oseen vortex. Note that the symbol, δ represents the vortex core size, a, used elsewhere. Reproduced with permission from Cambridge University Press, who retain the copyright.

that for a structured solution, only the average vorticity has the possibility to stay in the stretching direction, leading to the growth rate becoming reduced to 9/16 times the basic strain rate with a decay term of $-\nu k v^2$, where ν is the viscosity, k is the axial wavenumber and v is the velocity.

Studies into single vortices were continued by Jiménez *et al.* (1996) who investigated the case of a single Lamb–Oseen vortex immersed in a weak plane strain at a Reynolds number of $Re = 3500$. They began their investigation by using an analytical approach, then compared the results against a computational simulation. They found that the results were approximately Gaussian in profile in distorted co-ordinates. They also found that the asymptotic expansion they used is only valid within the vortex core. Their results indicated that vortices of two-dimensional turbulence are sufficiently long lived to be controlled by viscous diffusion, even for a relatively large Reynolds number.

Eloy & Le Dizès (1999) conducted an analytical study of two types of vortices, Lamb–Oseen and Burgers vortices, in a non-axisymmetric strain field. Eloy & Le Dizès employed a function that describes the boundary of a vortex core, such that the pressure inside the core is equal to outside the core which is derived in Moore & Saffman (1975). This function is also a measure of the interaction of the vortex with the strain field. One of the primary investigations of Eloy & Le Dizès revolves around the Kelvin mode instability. They investigate the effect of viscosity and stretching in changing the non-

dimensional axial wavenumber, $k\,a$, from the most unstable situation. Their analysis showed that for every value of vortex core size, a, there is an axial wavenumber, k, which will maximise the growth rate of the instability. This led to the conclusion that the vortex core size, a, is a suitable length scale to normalise the axial wavenumber, k. Hence, as the vortex core size increased over the temporal evolution, $a \approx \sqrt{{a_0}^2 + 4\omega t}$, Eloy & Le Dizès investigated how a vortex detunes itself during the evolution due to this change. This detuning has the effect of causing the growth rate to decrease with time, resulting in a subcritical instability in the vortex. Figure 1.2 demonstrates this detuning by showing that, as the vortex evolves in time, the vortex core will only remain in the unstable region for a finite length of time. One of the other findings of Eloy & Le Dizès was that the internal strain rate of a vortex can be influenced by both the external strain rate and the vortex profile. This led to the conclusion that the profile of the vortex can change the stability of the vortex, leading to a change in the maximum possible growth rate of an instability in the vortex. For Gaussian and Rankine vortex profiles, the maximum growth rate for the mode [-1,1] instability approximates well to $\sigma \approx \dfrac{9}{16} s_0$, where s_0 is the perpendicular strain rate in the vortex centre.

Olendraru & Sellier (2002) investigated a single Batchelor vortex using a linear stability analysis at a range of Reynolds numbers, $500 \leq Re \leq 10\,000$. They found, that for moderate levels of swirl, $q < 1$, inviscid spatial modes quickly reached an asymptotic limit as long as $Re \geq 2000$. They found for large values of swirl, $q > 1$, the growth rates of inviscid spatial modes are weak and highly sensitive to the magnitude of the Reynolds number. Their study revealed that, for intermediate values of Reynolds number, 'viscous' bending modes begin to dominate the instability mechanism. They find that the 'viscous' bending modes are spatial counterparts to the temporal asymmetric modes discovered by Khorrami (1991) and then confirmed by Mayer & Powell (1992).

Antkowiak & Brancher (2004) investigated, using a transient perturbation energy growth analysis method, a single Lamb–Oseen vortex at a Reynolds number range of $500 \leq Re \leq 5000$. They found that the growth amplification factor had a primary peak at an axial wavenumber of $k\,a = 1.4$ with a secondary peak at $k\,a = 2.4$. Their results displayed that the axial wavenumber of the peak transient energy growth is independent of Reynolds number and that the perturbation that leads to optimal energy growth on a single Lamb–Oseen vortex comprises of a three-dimensional spiral structure with stretching and tilting. The key finding of Antkowiak & Brancher is that $m = 1$

disturbances are subject to transient amplification. This amplification is a combination of a local Orr mechanism and the effect of global vortex induction.

As an understanding of the dynamics of a single vortex progressed, methods for controlling and enhancing the destruction of vortices were studied. For example, Matalanis & Eaton (2007) suggested that miniature trailing edge effectors could be used to introduce spatial disturbances into the vortex, causing rapid destruction though the Crow instability. They tested this hypothesis by using a single vortex generator in a wind tunnel, and found for all of the static deflections of the trailing edge effectors, there was no change in how diffuse or concentrated the vortex was. They did find that deflection of the vortices caused by the trailing edge effectors caused the deflection predominantly in the lift direction, with a small deflection in the spanwise direction. These deflections were static and did not cause an increase in the growth of instabilities.

Around this time, methods for analysing the transient response of flows to two- and three-dimensional perturbations were being developed, leading Heaton & Peake (2007) to investigate a single Batchelor vortex at a Reynolds number of $Re = 5000$ with a swirl regime of $q \gtrsim 2$. Heaton & Peake hypothesized that stronger transient growth was possible in a single Batchelor vortex than in a Lamb–Oseen vortex, due to the nature of the three-dimensional inviscid instabilities that occur in Batchelor vortices. They showed that large transient growth of the energy within the perturbations is possible through bending instability modes. Heaton & Peake concluded that the transient growth of perturbations was a possible route to vortex destruction.

Investigations into single vortices continued with an analytical and computational study by Lacaze *et al.* (2007). Their investigation studied a single Batchelor vortex at a finite Reynolds number, in an externally imposed strain field in an inviscid flow with a correction term to account for a reduced growth rate. This effectively allowed the study of all Reynolds numbers. They found that axial flow modified the characteristics of the elliptic instability. They found that the presence of a small axial velocity breaks the symmetry between principal Kelvin modes [-1,1], such that the elliptic instability is no longer a sinuous stationary deformation. Lacaze *et al.* found that for moderate axial velocity, the principal Kelvin mode [-1,1], disappears because one of the modes becomes highly damped. The conditions that cause the damping of the [-1,1] mode cause the increased amplification of another mode [0,-2]. As the axial velocity was increased further, the [0,-2] mode became damped out and led to the formation of a

[-1,-3] mode. They came to the conclusion that as the axial velocity can reach up to 10% of the maximum azimuthal velocity in the wake of a real aircraft, the principal mode of [0,-2] could form in a real wake flow. In addition, they did not expect the long wavelength Crow instability to be affected by weak axial flow.

Following the work by Lacaze *et al.* (2007), Abid (2008) investigated the dynamics of a single Batchelor line vortex using both a linear stability analysis and DNS at a Reynolds number of $Re = 1000$. Abid found that the non-linear effects of the instability are confined to the region near the vortex axis and become more significant as the swirl, q, increases. For a low value of swirl, Abid selected a four helix DNS mode in agreement with the most unstable mode obtained from the linear stability analysis. He found that, as the swirl was increased, the non-linear effects manifested themselves by a long wavelength mode generated near the vortex axis, leading to the conclusion that the difference between the non-linear evolution and the linear eigenmode theory was related to the transient growth of optimum perturbations resulting from the non-normality of the linearised Navier–Stokes equations about shear flows.

At the same time that Lacaze *et al.* (2007) and Abid (2008) were conducting their studies into a single Batchelor vortex, Fontane *et al.* (2008) was looking at the forcing of instabilities in a Lamb–Oseen vortex. Using a linear stability analysis at a range of Reynolds numbers, $500 \leq Re \leq 10\,000$, to investigate the response of a single Lamb–Oseen vortex to continuous white noise forcing, Fontane *et al.* found that the energy gain of the perturbations was a maximum for an axial wavenumber of $k = 0$ (a two-dimensional perturbation) and decreased as the axial wavenumber increased. They concluded that the input structures that are favoured in the $k \to 0$ limit only correspond to disturbances that grow infinitely slowly. This effect means that these favoured disturbances may not have sufficient time to grow in finite-time experiments, implying that, for short to medium timescale experiments and simulations, the selection of finite-time optimal perturbations will be significantly different.

1.3 Simple vortex pairs

1.3.1 Two-dimensional vortex pair studies

After the work by Crow (1970) many others began to look into this field. Given the lack of computing power available, most of this work was accomplished by analytical or experimental methods. Pierrehumbert (1980) performed an analytical study of a

two-vortex system, developing an efficient relaxation method. This method was able to compute the properties of a family of vortex pairs with distributed velocity, propagating without shape through a homogeneous, inviscid fluid. While this method was better than those previously employed, in terms of number of operations needed to achieve convergence, it did have some drawbacks. One of these drawbacks was that any information on secondary bifurcation points was lost during the process. The other drawback was that it was assumed that the fluid was inviscid and was purely two-dimensional. Pierrehumbert found the existence of a limiting vortex, and, as such, an upper bound for r/x_c, where r is the vortex core radius and x_c is the centroid of the right hand vortex to the $x = 0$ line. This was in contrast to the previous work by Saffman (1979), who indicated that a steady state could be found for arbitrarily large r/x_c.

A short time later, Sarpkaya (1983) investigated systems of counter-rotating vortex pairs produced within a towing tank. These experiments were carried out at a Reynolds number of $4 \times 10^4 \leq Re_{chord} \leq 5 \times 10^5$. He found that the vortex pairs formed into horseshoe vortices and ultimately into vortex rings and that these vortex rings are one of the primary mechanisms of vortex destruction (figure 1.3). He also observed that the formation of the horseshoe vortices was a result of the instability discovered by Crow (1970). These experiments carried out by Sarpkaya also had the effect of demonstrating that the linear theory created by Crow (1970) is sound right up until the time when the vortices link. He also demonstrated that core bulging and bursting caused the destruction of the vortices (figure 1.4). Sarpkaya (1983) also carried out experiments observing the behaviour of counter-rotating vortex pairs in stratified fluids. As the density of the atmosphere changes depending on the height from the ground, this adds another effect present in real aircraft wakes to the experiment. Sarpkaya found that when weak stratification was present in the fluid, the linking of the vortices into the horseshoe vortex and vortex core bursting were still the primary mechanisms that lead to the destruction of the vortices. However, when strong stratification was present, the amplitude of the Crow instability remained relatively small and did not lead to linking of the vortices, which suppressed the creation of the horseshoe vortices and subsequent ring vortices. In the case of strong stratification, Sarpkaya found that the lifespan of the vortices was determined by the initial turbulence generated by the vortex pair; turbulence generated by core bursting; and countersign vorticity generated at the

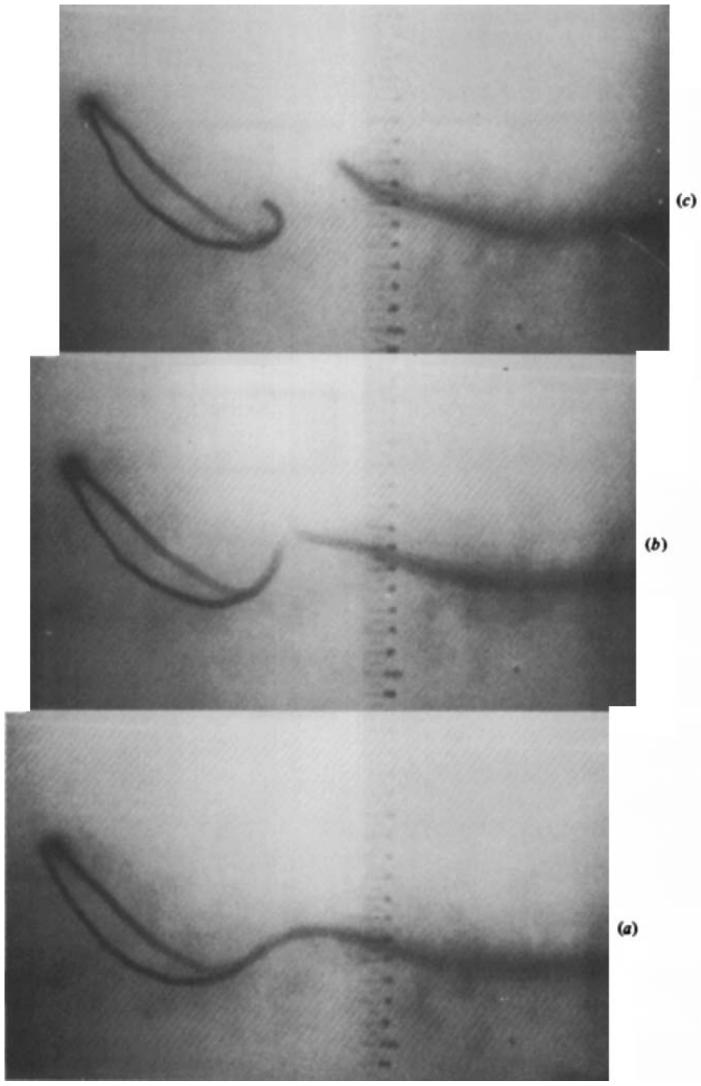

FIGURE 1.3: A reproduction of figure 7 from Sarpkaya (1983) displaying the temporal evolution of the long wavelength instability. (a) displays the development of the horseshoe vortex, (b) displays the linking of the vortices and (c) the formation of the first vortex ring. Reproduced with permission from Cambridge University Press, who retain the copyright.

boundaries of the recirculation cell.

In the late 90s, computing power had reached the stage where two-dimensional direct numerical simulations (DNS) could be carried out on these types of vortex flows. Garten *et al.* (1998) considered a two-dimensional two-vortex system with varying degrees of stratification. They used two Lamb–Oseen vortices at a Reynolds number based on the vortex circulation of $Re = 6283$ and found that stratification in the base fluid had the effect of generating counter-sign vorticity around each of the primary vortices through baroclinic effects (figure 1.5). When weak stratification was present, they observed that the primary effect of the stratification was to advect the primary vortices together,

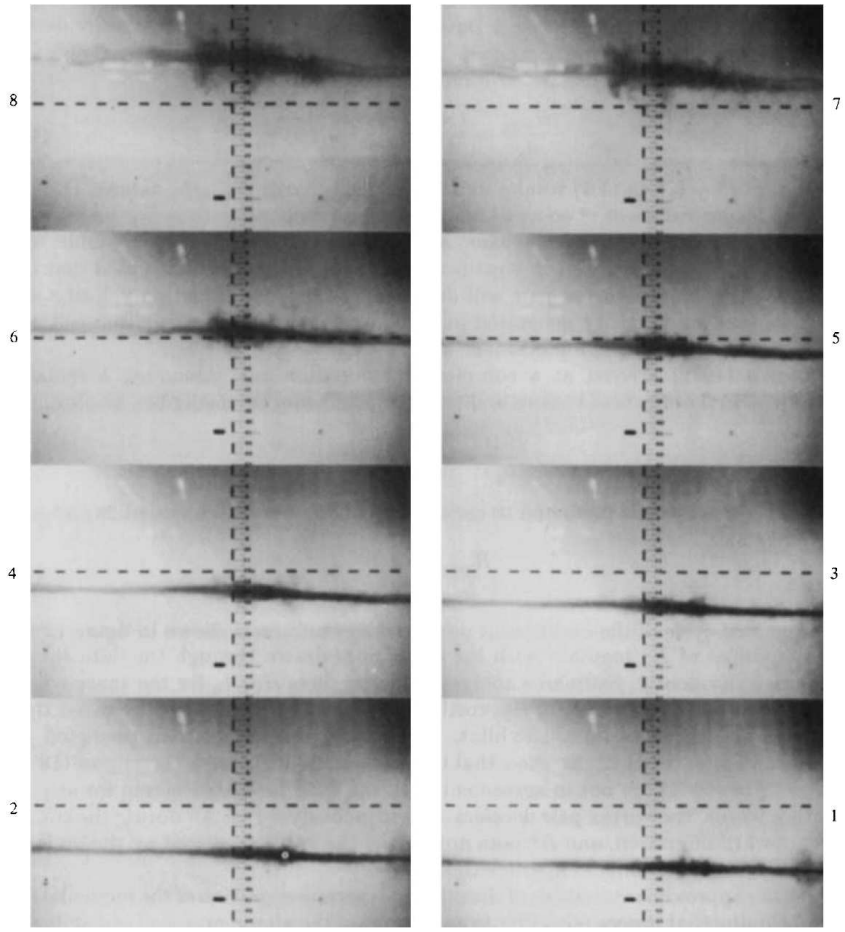

FIGURE 1.4: A reproduction of figure 11 from Sarpkaya (1983) displaying the last stages of the temporal evolution of the long wavelength instability. (1)-(8) shows the evolution of core bulging and bursting in the wake of a NACA-0012 wing. Reproduced with permission from Cambridge University Press, who retain the copyright.

decreasing their separation distance and causing an increase in vertical propagation speed. This advection also had the effect of increasing the strain imposed on each of the vortices by the other. They also found that when strong stratification was present, internal gravity wave radiation was dominant, causing a rapid reduction in the intensity and spatial coherence of each vortex. Garten *et al.* (1998) also investigated the two-dimensional case where a counter-rotating vortex pair encountered a layer of constant shear in stratified and unstratified fluids. This case is analogous to what would occur when the wake of an aircraft encountered a patch of atmospheric turbulence. They found that when a vortex pair encountered a field of constant shear, when no stratification was present in the fluid, it caused the vortex pair to begin to rotate. However, the rotating vortex pair did not lose any coherence. Contrary to the previous case, in the case where stratification was present, they observed that when a counter-

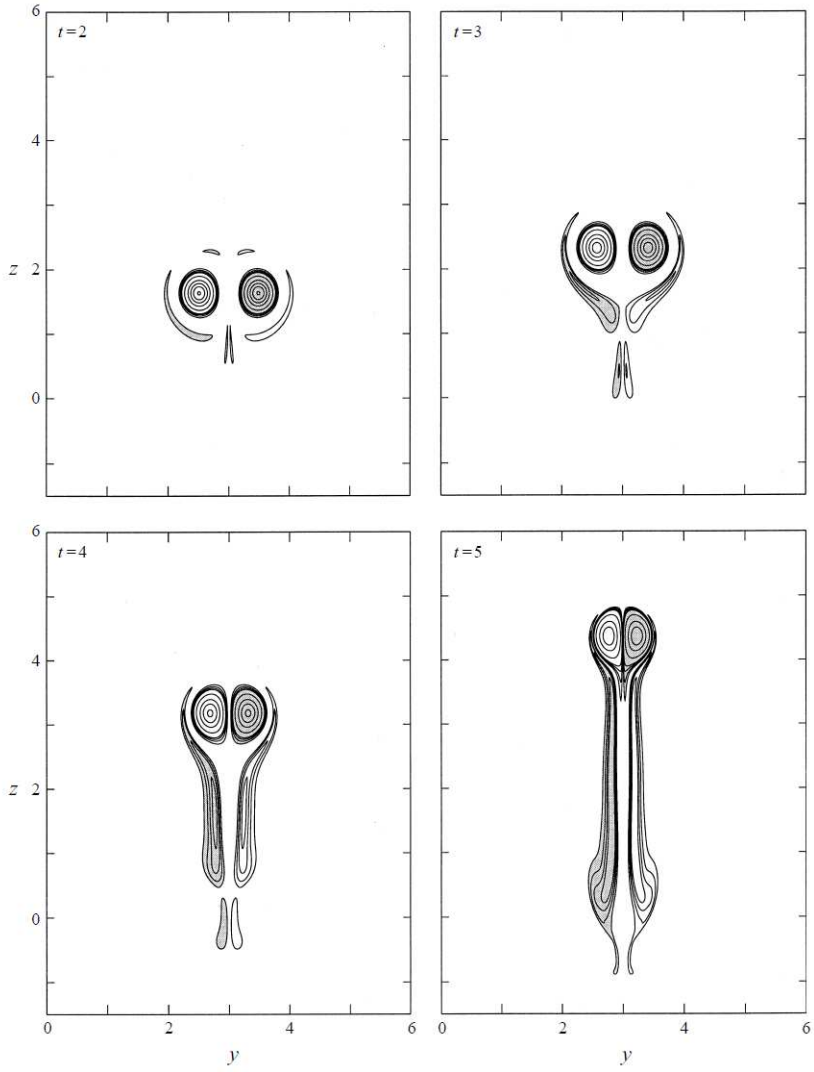

FIGURE 1.5: A reproduction of figure 1 from Garten *et al.* (1998) displaying contours of vorticity for an upward propagating vortex pair in stratification. The baroclinically generated wake is demonstrated to evolve around the vortex pair. Reproduced with permission from Cambridge University Press, who retain the copyright.

rotating vortex pair encountered a constant shear, it could lead to the emergence of a single vortex with the same sign as the background shear. This effect was more likely with higher Reynolds numbers and stronger stratification.

The research carried out by Meunier & Leweke (2001) (described in section 1.3.2) was quickly followed up by more detailed examination of the merger of co-rotating vortex pairs by Meunier *et al.* (2002) to search for a merging criterion for two dimensional vortices. Meunier *et al.* (2002) combined the previous work by Meunier & Leweke (2001) with further experiments and two-dimensional DNS to identify the stages in the merging process. Meunier *et al.* found that there were three stages to the merging pro-

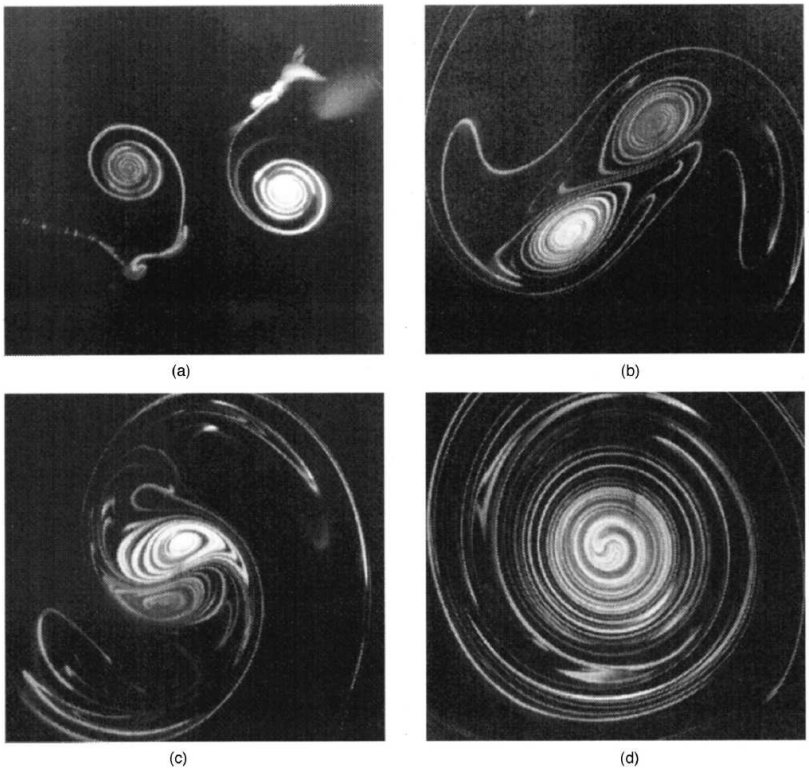

FIGURE 1.6: A reproduction of figure 1 from Meunier *et al.* (2002) displaying the stages of merging of two co-rotating vortices at a $Re \approx 2000$ at (a) $t^* = 1.1$, (b) $t^* = 1.7$, (c) $t^* = 2$ and (d) $t^* = 3.1$. Reproduced with permission from the American Institute of Physics, who retain the copyright.

cess, beginning with a viscous stage where the square of the vortex core size increased linearly with time without merging (figure 1.6(b)). The second stage was for the two vortices to merge on a convective timescale (figure 1.6(c)), followed by the diffusion of filaments of vorticity into a final axisymmetric distribution of vorticity (figure 1.6(d)). Meunier *et al.* found that the transition between the first two stages of the vortex merger was directly related to the critical core size of the vortices.

At the same time, Le Dizès & Verga (2002) were performing similar computational studies on a pair of co-rotating Lamb–Oseen vortices at a range of Reynolds numbers, $500 \leq Re \leq 16\,000$. They found that, for a Gaussian vortex profile, time evolutions of the elliptic deformations on a non-viscous timeframe are identical for all of the investigated Reynolds numbers. As a part of their investigation, Le Dizès & Verga found that all axisymmetric vortex profiles relax towards a Gaussian vortex profile, and that a two-vortex system will also relax to a unique state that corresponds to a vortex system with Gaussian profiles. Le Dizès & Verga found that this unique state can be parameterized by a pair of parameters, the ratio of vortex core size to vortex

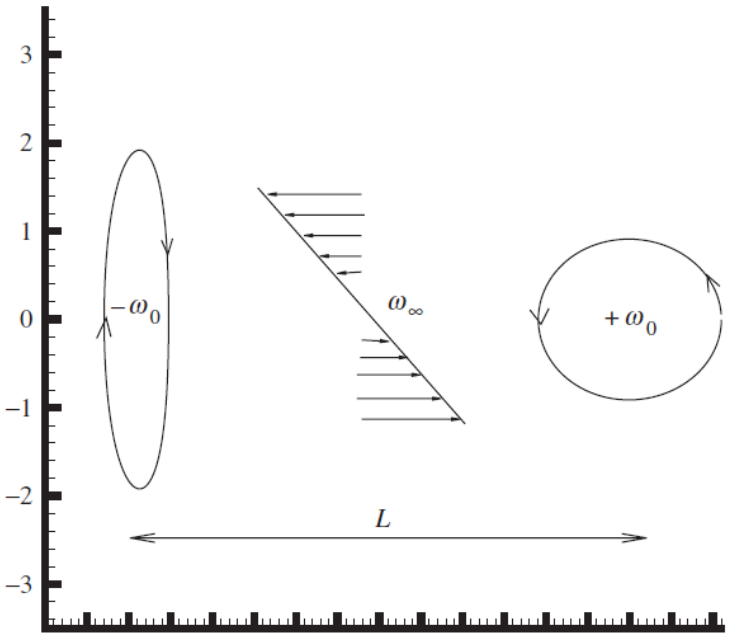

FIGURE 1.7: A reproduction of figure 3 from Hill & Saffman (2002) displaying the deformation of vortices due to a cross-shear perpendicular to the vortex axis. Reproduced with permission from Proc. A R. Soc. Lond, who retain the copyright.

separation, a/b, and the vortex circulation, Γ. These parameters lead to the strain rate, ε. This conclusion for co-rotating vortex pairs is very similar to the earlier findings by Sipp *et al.* (2000) for counter-rotating vortex pairs. Le Dizès & Verga observed in the simulations that the system had a weak dependence on Reynolds number. This led them to the conclusion that viscous relaxation of a co-rotating, two-vortex system cannot be perfectly identical to the relaxation of a single axisymmetric vortex (which has no Reynolds number dependence). Their findings also confirmed the experimental findings of Meunier & Leweke (2001), that because the viscosity causes a/b to grow with time, the two vortices will always merge without the presence of an external strain field or a third vortex.

While experimental and computational investigations were being undertaken on the merging of co-rotating vortex pairs, Hill & Saffman (2002) were studying the effects of wind shear on counter-rotating vortex pairs as this is a common occurrence in real aircraft wakes. They used an analytical approach to study the two-dimensional interactions of point vortices and finite core size vortices, with a cross-shear perpendicular to the vortex axis. They found that, when using analytical methods with point vortices, wind shear has little effect on the vortex motion, aside from horizontal displacement

and an asymmetry of the streamlines. As point vortices are a very simple model, Hill & Saffman continued the analysis using vortices of finite core size. This led to the finding that the vortex cores can be deformed significantly, or to a very minor degree, depending on the sign of the vorticity of the vortex compared to the vorticity of the shear (figure 1.7). When the vortex is co-rotating relative to the shear, the vortex retains its circular shape to a good degree. Conversely, they found that when the vortex is counter-rotating relative to the shear, the vortex tends to be significantly deformed into a long, thin shape, perpendicular to the line joining the centroids of the vortex and the shear. Hill & Saffman suggested that observed asymmetric properties are due to wind shear, but conceded that other explanations could be more significant.

So *et al.* (2007) studied the interactions between unequal, counter-rotating vortex pairs, similar to the interaction between a wing and tail vortex. They studied the effect of various ratios of weak to strong vortex strength, $\Gamma_2/\Gamma_1 = -0.1, -0.37$ and -0.73, and Reynolds numbers $Re = 6660, 13\,340$ and $20\,000$, and compared these to the case of an equal strength counter-rotating vortex pair, $\Gamma_2/\Gamma_1 = -1$, finding that the interaction between the vortex pairs is dependent on the ratio of weak to strong vortex strength. They observed that differences between the induced strain on the vortices caused them to evolve with different magnitudes of evolution. This led to the discovery that the weaker vortex required more time to settle than the stronger vortex. So *et al.* came to the conclusion that the final states of the vortices were independent of the Reynolds number and only dependent on the the ratio of the vortex strength and the initial spacing of the vortices. It is important to note that the general equations of Le Dizès & Laporte (2002) also predict this behaviour.

1.3.2 Three-dimensional vortex pair studies

Thomas & Auerbach (1994) experimentally investigated a counter-rotating vortex pair at a Reynolds number of $2000 \leq Re \leq 12\,000$, using a water tank with dye visualisations. Having carried out experiments with one vortex and demonstrating that it was stable, they found that both the long- and short-wave instability mechanisms they observed in the vortex pair depended crucially on the interaction between the two vortices. They observed that the wavelengths of the instabilities were approximately constant through the evolution in time. Thomas & Auerbach also found that the wavelength of the long wavelength instability was affected by the length of the container and

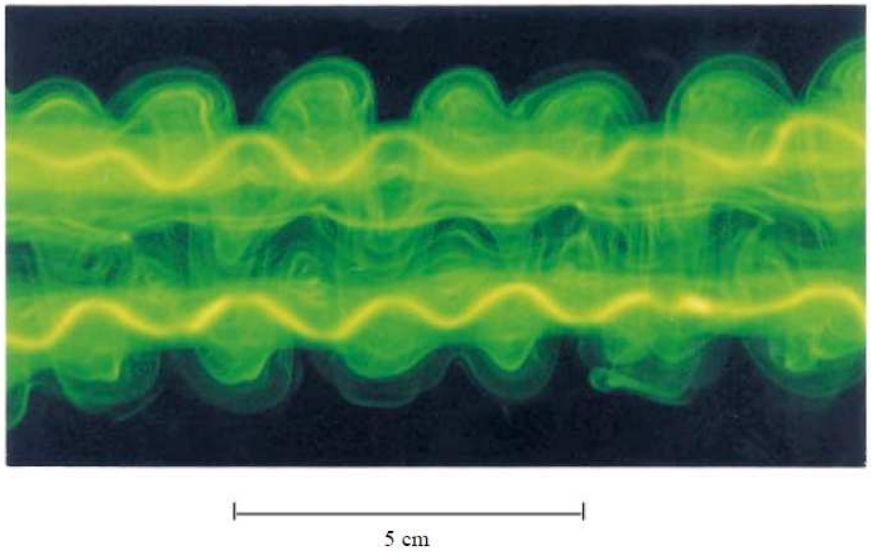

FIGURE 1.8: A reproduction of figure 5(a) from Leweke & Williamson (1998) displaying the vortex cores of a vortex pair distorted by the elliptic instability. Reproduced with permission from Cambridge University Press, who retain the copyright.

the experimental method used. Despite the experimental error, the long wavelength instability was within 20% of the theoretical calculations by Crow (1970).

At the same time Garten *et al.* (1998) were performing two-dimensional investigations, Leweke & Williamson (1998) were performing experiments utilising dye visualisation in water at a Reynolds number of $Re = 2\,750$ to observe the cooperative elliptic instability for the first time in an open flow. The non-dimensional axial wavenumber that Leweke & Williamson found for the elliptic instability agreed well with the previous study conducted by Thomas & Auerbach (1994). Leweke & Williamson observed, in agreement with previous analytical studies, that the wavelength of the elliptic instability scaled with the core size of the vortices and that as the vortices came closer to each other, the mutually induced strain increased, causing an increase in the growth rate of the elliptic instability. They observed that the elliptic instability caused a loss in symmetry around the plane separating the vortices early in the evolution, and evolve in a cooperative manner, as shown in Figure 1.8. As the instability evolved, they found that it caused the creation of smaller, perpendicular, secondary vortices around the stagnation points of the primary vortices. They observed that the interaction between the primary and secondary vortices led to rapid decay of the primary vortices. Leweke & Williamson found that for a Lamb–Oseen-type Gaussian vortex profile, the non-dimensional axial wavenumber of the elliptic instability should be approximately

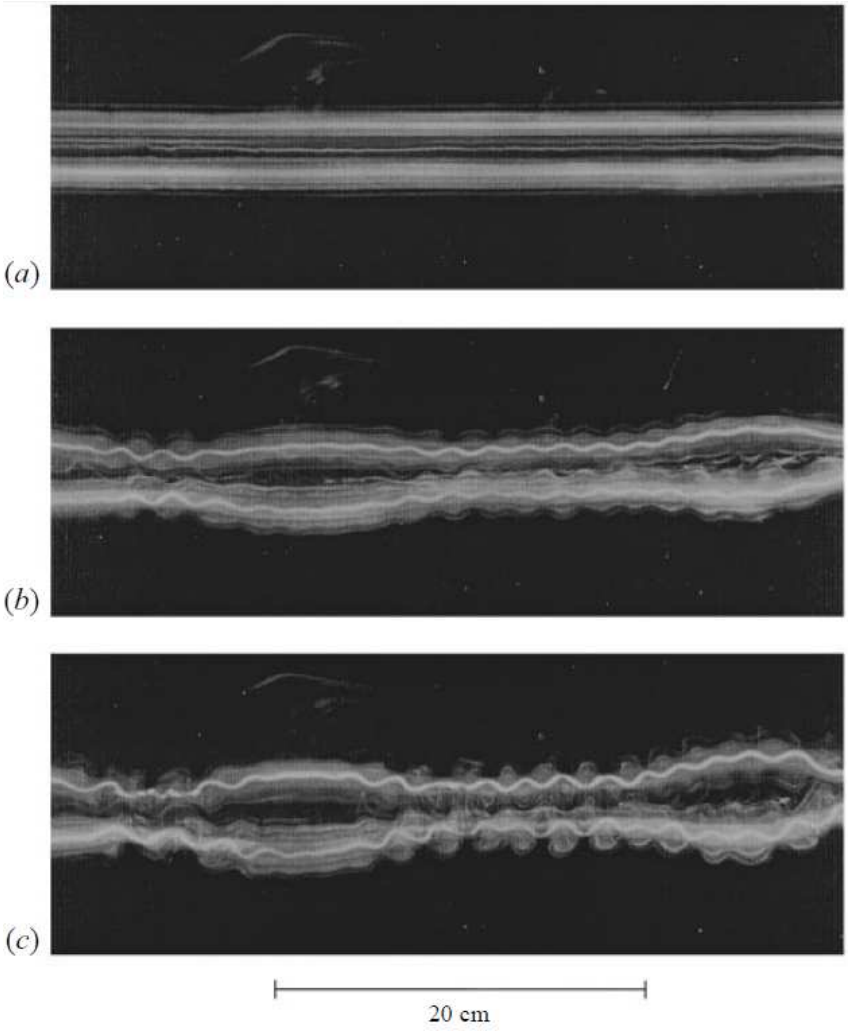

FIGURE 1.9: A reproduction of figure 4 from Leweke & Williamson (1998) displaying a temporal evolution of a combined long- and short-wave instability. Reproduced with permission from Cambridge University Press, who retain the copyright.

$k\,a = 2.3$. They suggest that the simultaneous interaction between the long-wave Crow and the short-wave elliptic instability distribute the initial large scale energy to smaller scales much more effectively than either instability alone. This simultaneous interaction can be seen in Figure 1.9.

Research into the effect of stratification continued with Holzapfel & Gerz (1999) using Large Eddy Simulations (LES) to investigate vortex pairs in stratified fluids. They found that the prominent effects – the deceleration, detrainment and acceleration – are caused by the interaction between the vortex vorticity and baroclinic vorticity present in stratified fluids. While LES does provide advantages in computing time and resources, it also fails to resolve the smallest scale turbulence that can be present in these types of flows because it implements a model for the smaller scale flows, rather

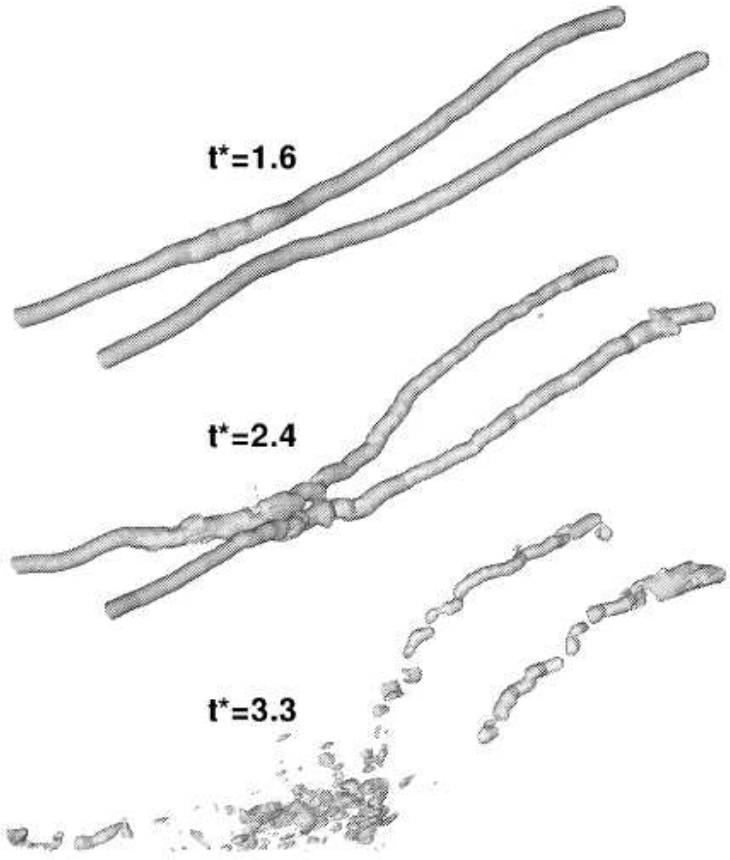

FIGURE 1.10: A reproduction of figure 13 from Holzapfel *et al.* (2001) displaying a temporal evolution of a combined long- and short-wave instability in a stratified fluid.

than DNS, which resolves the flow field down to the smallest scales.

Holzapfel *et al.* (2001) continued to study the effects of stably stratified environments on vortex pairs at a Reynolds number of $Re = 7400$. They found that atmospheric turbulence, coupled with baroclinic vorticity, had the effect of causing the long wavelength Crow instability to be dominantly promoted. They found that when stratification and atmospheric turbulence were present, they caused the sequence of dominant instability processes to be reversed. This meant that the Crow instability formed first, followed by the short wavelength elliptic instability, leading to accelerated decay when the vortices link. This had the overall effect of suppressing the formation of descending vortex rings. This can be seen in figure 1.10 as the first image displays the Crow instability forming, $t^* = 1.6$; the middle image showing the short wavelength instability, $t^* = 2.4$; with the third image showing the destruction of the vortices in the third image, $t^* = 3.3$. Holzapfel *et al.* also found that the presence of very strong stratification can cause the vortex pair to rebound back to flight level due to baroclinic vorticity, but that the

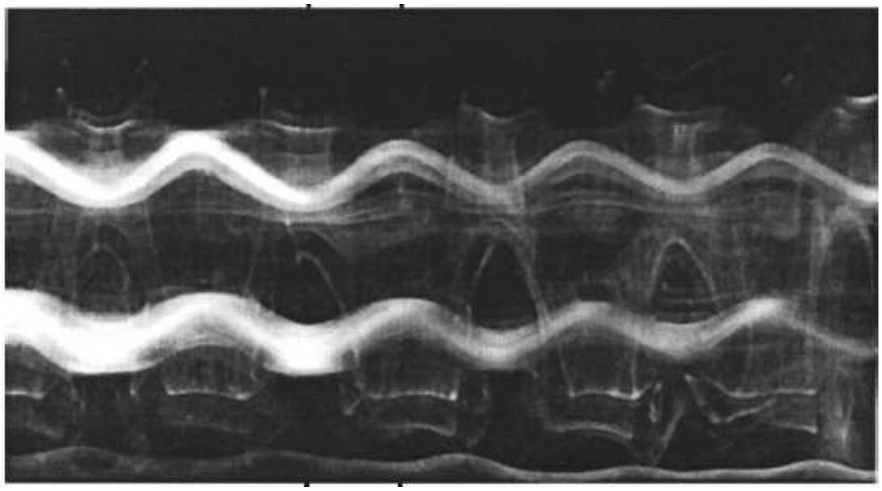

FIGURE 1.11: A reproduction of figure 4 from Meunier & Leweke (2001) showing the vortex cores of a co-rotating vortex pair undergoing anti-symmetric elliptic instability. Reproduced with permission from the American Institute of Physics, who retain the copyright.

primary vortices can lose much of their vorticity in the process.

By using a Direct Numerical Simulation (DNS) approach, all scales of flow may be resolved, but at the cost of higher computational resources. Laporte & Corjon (2000) performed DNS on a counter-rotating vortex pair in an unstratified fluid at a Reynolds number of $Re = 2400$ to investigate the elliptic instability. Laporte & Corjon found that, during the linear growth phase of the elliptic instability, the vortex core size increased significantly due to viscous diffusion. They found that the most unstable non-dimensional axial wavenumber was $k\,a = 2.35$. At this wavenumber, due to the elliptic instability, the decay in circulation from its initial level is approximately 40%. This result was in excellent agreement with the previous experimental work by Leweke & Williamson (1998). This shows that DNS techniques can be an effective compliment to experimental work, as DNS eliminates extraneous sources of noise that are unavoidably present in laboratory experiments.

As the vortex sheet is shed off the back of an aircraft wing, multiple smaller vortices are shed off discontinuities on the wing structure, such as flap edges, engines and other structural pieces. This has led to research into the merging of co-rotating vortices to model how the vortex sheet eventually forms into the large vortices found in the far wake. One of the first experiments that investigated the three dimensional properties of the merging process was carried out by Meunier & Leweke (2001). Their investigation was carried out on a co-rotating vortex pair at Reynolds number of $700 \leq Re \leq 4000$ in a water tank. They found that there was a ratio between critical vortex core size, a_c,

and vortex separation, b_0, of $a_c/b_0 = 0.29$, above which vortex merger was initiated. In addition to this, they found that increasing the Reynolds number and/or reducing the ratio of initial core size to initial separation, a_0/b_0, caused the viscous phase before the vortices merge to last longer, allowing for three-dimensional instabilities to form while the two vortices are still separated. This three dimensional instability causes the vortex cores to deform sinusoidally in an anti-symmetric manner as shown in Figure 1.11. This instability is similar to the elliptic instability in counter-rotating vortex pairs, with a long wavelength instability suppressed by the rotation of the vortex pair. Meunier & Leweke came to the conclusion that that the three-dimensional instability is an elliptic instability of the strained vortical flow in the cores, leading to fluid becoming wrapped around the other vortex. This wrapping of fluid evolves into an "almost explosive" breakdown of the vortices into small scale structures before they relaminarise into a single viscous vortex. One of the significant discoveries Meunier & Leweke made was that merging will always occur for viscous flows. While theoretical two-dimensional studies had been conducted (Brandt & Iverson 1977; Saffman & Szeto 1980), Meunier & Leweke (2001) did find very specific data on the three dimensional merging of co-rotating vortices.

As a counterpoint to the work by Meunier & Leweke (2001); Meunier *et al.* (2002); Le Dizès & Verga (2002), Laporte & Leweke (2002) investigated the dynamics of the elliptic instability in counter-rotating vortex pairs using both experimental and computational methods at a Reynolds number of approximately $Re = 2400$. Using both experimental and computational methods, Laporte & Leweke sought to test the analytical theory that the elliptic instability is due to a resonance between the neutral three-dimensional perturbation waves and the local strain experienced by the vortex. This led to the observation of an in-phase axial variation of the elliptic mode for large ratios of vortex core size to vortex separation, a/b, as shown in Figure 1.12. Leweke & Williamson (1998) demonstrated that this in-phase relationship is due to a condition where the components of the velocity are linked on both sides and normal to the median plane separating the vortices. Laporte & Leweke noted that, as the vortices are brought closer together, relative to the vortex core size, the linking of velocity becomes stronger. From these observations, Laporte & Leweke theorised that, for smaller ratios of vortex core size to vortex separation, the phase relationship between the two vortices is more likely to be random, due to the nature of the noise exciting the unstable modes being stronger

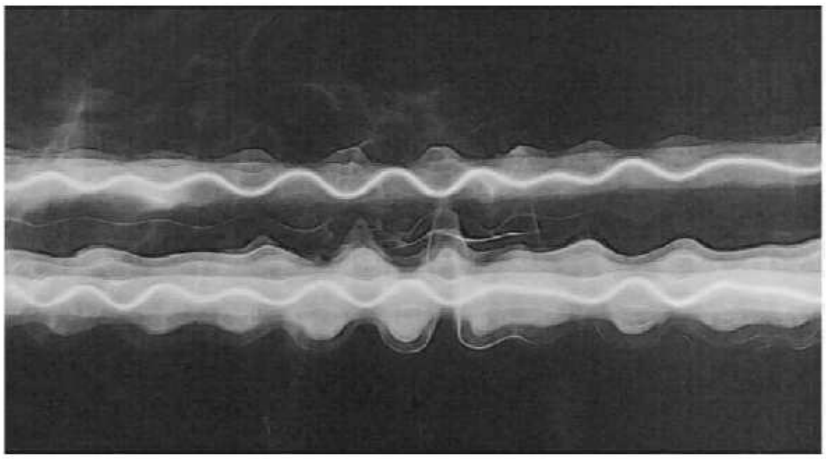

a) Experiment ($Re = 2.75 \times 10^3$, $a/b = 0.2$, and $t^* = 6.8$)

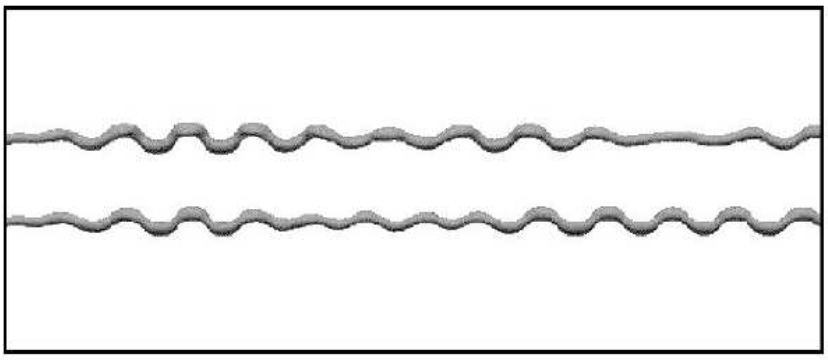

b) DNS ($Re = 2.4 \times 10^3$, $a/b = 0.25$, and $t^* = 8.8$)

FIGURE 1.12: A reproduction of figure 2 from Laporte & Leweke (2002) displaying the evolution of a short-wave instability on a vortex pair during the linear phase. Reprinted with the permission of the American Institute of Aeronautics and Astronautics.

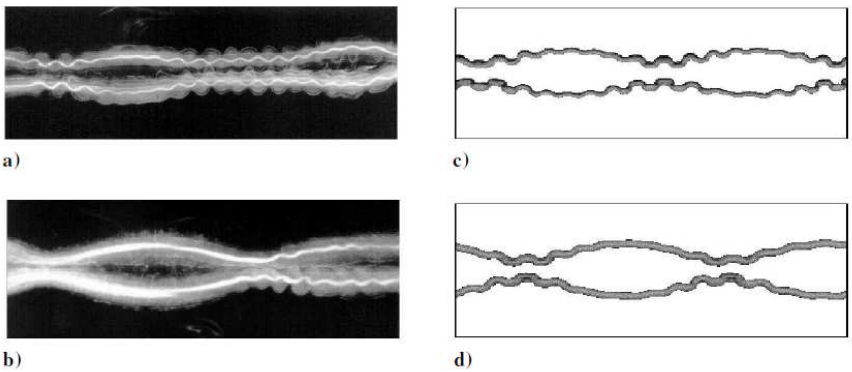

FIGURE 1.13: A reproduction of figure 13 from Laporte & Leweke (2002) displaying the evolution of the of the combination of long- and short-wave instabilities on a vortex pair with (a-b) Experimental and (c-d) DNS methods. Reprinted with the permission of the American Institute of Aeronautics and Astronautics.

than the linking of the velocity across the median plane. Laporte & Leweke found that the non-dimensional axial wavenumber, $k\,a$, favoured by the DNS and experimental methods, were reasonably close to each other. Laporte & Leweke also observed, in later stages of the evolution, that bridges of vorticity crossed between the primary vortices, forming perpendicular secondary vortices. They observed that the inviscid growth rate of the elliptic instability is almost 40% greater than the inviscid growth rate of the Crow instability alone. This led to the discovery that, for a pure elliptic instability, the circulation drop was approximately 40%. However, when the elliptic instability and Crow instability develop simultaneously, both the experimental and DNS results show a drop in circulation of approximately 80%. Figure 1.13 shows the effect of the combination of the elliptic and Crow instabilities on the vortex pair.

A short time later Bristol *et al.* (2004) extended the analytical work by Crow (1970), looking at unequal vortex pairs in an unstratified fluid by accounting for the orbital motion of the system. Bristol *et al.* found that the rotation of planar perturbations needed to be overcome to enable instabilities to grow within the flow. Long term simulations conducted by Bristol *et al.* of a co-rotating case suggested that a three dimensional mechanism was present that allowed for vortex merger. This mechanism began with an elliptic instability on one vortex. They found that as vorticity crossed local streamlines, it led to the formation of vorticity bridges, which eventually leads to the merging of the vortices. For the case of a counter-rotating vortex pair, the weaker vortex became wrapped around the stronger, leading to the creation of loops of vorticity. These loops eventually formed rings that self-induced away from the system.

Continuing the investigations into stratified flows, Liu (2006) performed experiments in a towing tank of a two-vortex, counter-rotating system. Liu defined the atmospheric boundary layer near ground level as low stratification, and was able to demonstrate, for the first time, visualisations of detrainment phenomena in vortex wakes in very low stratification. However, this level of very low stratification does not occur in the atmosphere showing a discrepancy between the observations made by Liu and the theoretical work by Crow (1974). Liu (2006) also demonstrated that for three-dimensional wake trajectories, symptoms of a relatively weak detrainment are present for relatively low stratification.

At the same time that Liu (2006) was conducting their investigation, Nomura *et al.* (2006) were also studying the effects of a counter-rotating vortex pair in stratification,

by using DNS at a Reynolds number of $Re = 2400$. Nomura *et al.* found that weak stratification had an overall weak effect on the vortex pair. They did find that weak stratification caused the vortex pair to be drawn together. As previous studies into the elliptic instability (Laporte & Leweke 2002) have shown, as the separation of the vortex pair decreases, the mutually induced strain becomes greater, increasing the growth of the elliptic instability. Nomura *et al.* also found that when strong stratification was present, there was a significant effect on the interactions with the instability mode observed. Given the stratification is stronger in that case, Nomura *et al.* observed a significantly greater effect of the baroclinic torque, forcing the vortices even closer. This resulted in a higher axial wavenumber and a more complex radial structure of the instability.

Given advances in computing power, Orlandi (2007) was able to study, using DNS at a Reynolds number of $3000 \leq Re \leq 30\,000$, a pair of co-rotating vortices. The results Orlandi (2007) found for the two-dimensional DNS were very similar to Meunier & Leweke (2001); Meunier *et al.* (2002), in that the merging of the vortices was directly related to the separation and Reynolds number; lower Re and reduced separation both caused a shortening of the merger time. The work by Orlandi (2007) extended the previous two-dimensional work by looking at a three-dimensional DNS, and found that it did not differ greatly from the two-dimensional case.

Given the connection between vortex wake destruction and the Crow instability, Brion *et al.* (2007) conducted a global linear stability analysis on a simple counter-rotating vortex pair at a Reynolds number of $Re = 3600$. They found that by stretching the vorticity at the leading hyperbolic point of the vortex dipole, a periodic array of vortex rings were generated along the length of the vortices. This caused a reduction in the characteristic time of the Crow instability by a factor of two.

In recent years, as the understanding of the instabilities that cause the destruction of vortex wakes improved, some researchers, such as Bearman *et al.* (2007), began to look for ways to excite these instabilities to speed up their destruction. Bearman *et al.* (2007) investigated the forcing of instabilities on an equal strength counter-rotating vortex pair through pulsing of air jets blowing in the spanwise direction from the wingtips. Bearman *et al.* found that forcing at the frequency of the Crow instability enhances the growth rate of the instability, leading to faster vortex destruction. As a counter to this, they found that forcing frequencies outside of the Crow instability actually caused

the retardation of the growth until the forcing frequency died out, only then allowing the preferred frequency to grow. This led to the conclusion by Bearman *et al.* that the frequencies used to force instabilities would have to be carefully selected, otherwise the wake hazard would linger for longer than normal.

Roy *et al.* (2008) performed linear stability analysis on a pair of co-rotating Batchelor vortices, allowing for a rotating strain field, significantly altering the modes that grow. Roy *et al.* also used a higher Reynolds number than many previous studies at around $Re = 14\,000$ and $31\,400$. Their studies were similar to the investigations carried out by Lacaze *et al.* (2007) and found similar results. They found that, when axial velocity was present, it caused new elliptic instability modes to appear. The investigation carried out by Roy *et al.* found that for small core size to vortex separation ratio, a/b, the principal modes of azimuthal wavenumber found by previous studies (Laporte & Leweke 2002) became more stable, while other principal modes became unstable and replaced the previous modes. Roy *et al.* examined larger core size to separation ratios, and found that other modes appeared, but were not the most unstable modes.

More recently, a method for investigating the transient response of a generic system was developed by Barkley *et al.* (2008), which is discussed later in § 1.5. Donnadieu *et al.* (2009) used this method of transient growth analysis to investigate the transient response of a pair of counter-rotating Lamb–Oseen vortices at Reynolds numbers of $Re = 2000$ and $10\,000$. They found that, for short times, the transient response can be up to 50 times greater than the growth rate for a global linear stability analysis. Donnadieu *et al.* found that, over longer times, the transient response approached the growth rate for a linear stability analysis. They found that the unstable axial wavenumbers corresponded well with the inviscid theory of Crow (1970); Le Dizès & Verga (2002).

de Sousa & Pereira (2009), continuing the work by Meunier & Leweke (2001); Meunier *et al.* (2002); Roy *et al.* (2008), investigated the merging of a co-rotating pair of Batchelor vortices. They used DNS with Reynolds numbers of $Re = 1500, 2000$ and 2700. They found that initial azimuthal disturbances grow and result in the appearance of large scale sheets of helical vorticity. They observed the development of helical instability waves, causing the axial velocity deficit to be weakened faster than the tangential velocity. This effect led to the prevention of the formation of large scale flow structures. They surmised that these effects cause the vortices to form into a more stable state with

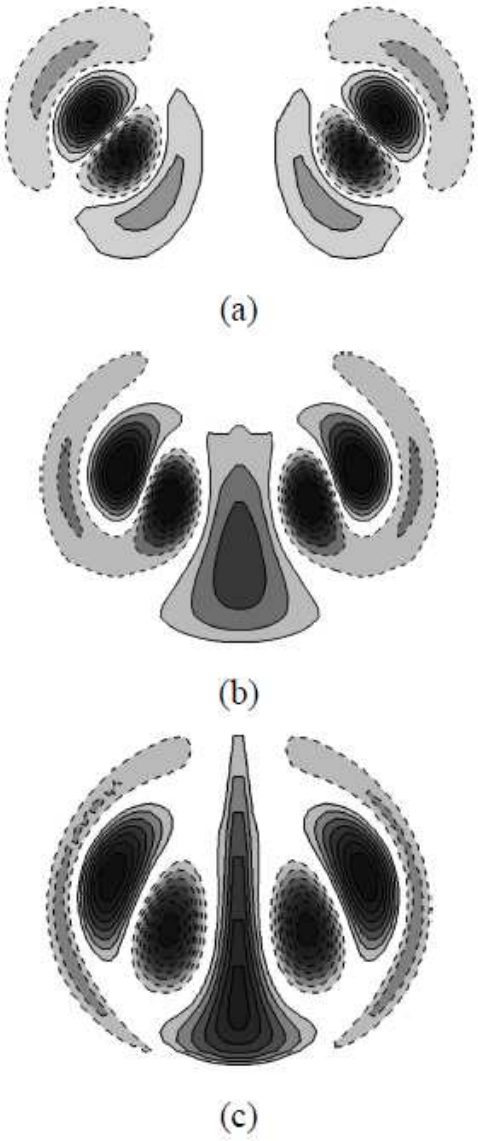

FIGURE 1.14: A reproduction of figure 9 from Boustead *et al.* (2010) displaying the contours of the vorticity field mode shapes of the perturbations taken at the peak growth rates. Separation is (a) $a/b = 0.251$, (b) $a/b = 0.3625$ and (c) $a/b = 0.4385$. Used with permission from Inderscience, who retain copyright.

a higher swirl value, q. de Sousa & Pereira mentioned that, after the previous observed flow effects, the evolution is somewhat similar to the evolution of a pair of co-rotating Lamb–Oseen vortices. This evolution consisted of a three-dimensional instability, causing a deformation of the vortex cores, which is amplified by reduced vortex separation. This deformation leads to vorticity exchange between the vortices and their eventual merger.

As the vortex separation is such an important factor in the elliptic instability (Le Dizès & Verga 2002), Boustead *et al.* (2010) investigated, using linear stability analysis

and DNS, the effect of the ratio of vortex core size to vortex separation, a/b, on the growth of instabilities on a pair of counter-rotating Lamb–Oseen vortices at a Reynolds number of $Re = 20\,000$. They found that, as the vortex spacing was reduced, the growth rate of non-principal axial wavenumbers is enhanced relative to the principal axial wavenumbers. Boustead *et al.* found that the perturbation fields for the principal unstable modes comprised a pair of counter-rotating vortex pairs within each stream tube. They observed that, at close vortex spacing, these pairs of counter-rotating vortex pairs in the perturbation field could merge to cause coupling of the vortex stream tubes in the vortex cross-over region (figure 1.14). The results demonstrated that the fluid cross-over region could exist at any separation, but was greatly enhanced as the initial separation of the vortex pair, b, was reduced.

Continuing the initial work of So *et al.* (2007), these researchers (So *et al.* 2011) continued the study of a pair of unequal Lamb–Oseen vortices at a Reynolds number of $Re = 2400$ and $14\,000$, using linear stability analysis. They identified three instability modes across the range of circulation ratio, $-1.0 \leq \Gamma_2/\Gamma_1 \leq -0.1$. Two of these modes are Kelvin modes and one is a Crow instability mode. They found that, as Γ_2/Γ_1 tends to zero, the global growth rate of the Kelvin mode [-1,1] decreases and the growth rate of the Crow and [-2,0,-1] mode increases. They also found that the Crow instability exhibits strong growth on both vortices down to a circulation ratio of $\Gamma_2/\Gamma_1 \approx -0.15$, below which the growth of the Crow instability begins to reduce in strength.

While Donnadieu *et al.* (2009) investigated the transient growth properties of a counter-rotating Lamb–Oseen vortex pair, it was based only on the linearised Navier–Stokes equations. All of the previous computational research using DNS has investigated the linear growth, and resulting non-linear growth, of the flow by seeding with perturbations that consist of white noise. So far, no research has investigated the response of two-vortex flows to perturbations from the transient growth method that lead to optimal energy growth. By seeding with the optimal perturbations, linear growth in the vortices can be immediately created, potentially leading to a significantly shorter lifespan of the vortices before they are destroyed.

1.4 Multiple vortex pair systems

It has been shown that the strength of the vortex pair produced from the tail of an aircraft can be anywhere up to 50% of the strength of the vortex pair produced by the

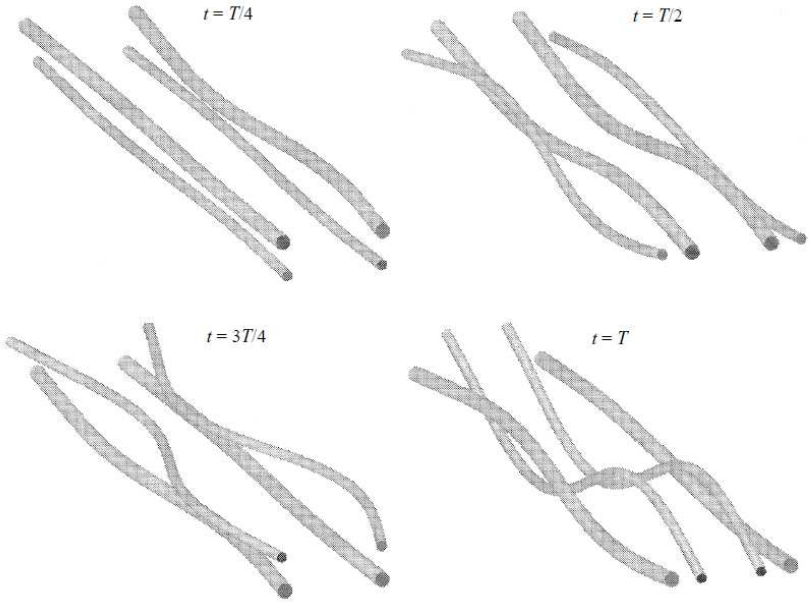

FIGURE 1.15: A reproduction of figure 13 from Crouch (1997) showing a long-wave instability occurring on the outer vortices and moving to the inner vortices over one period, T. Reproduced with permission from Cambridge University Press, who retain the copyright.

wings (Rennich & Lele 1999). The presence of the vortex pair shed by the tail can have a significant effect on the two dimensional kinematic properties of the stronger vortex pair shed by the wings. While four-vortex systems have been investigated by Crouch (1997), and Fabre & Jacquin (2000), the focus has been on the generation of three-dimensional instabilities in the main wing vortex pair. To date, no research has investigated how a change in the aircraft tail configuration affects the overall vortex system. For heavy lift aircraft such as the C-17 Globemaster, the tail can be offset vertically by up to 20% of the span of the wings. This research is particularly pertinent to military airfields, where the majority of the aircraft are either very large, high tail, heavy lift aircraft, such as the C-17, or much smaller fighter type aircraft.

An understanding of the stability of these flows is of interest, as it can provide insight into how to disrupt these types of flows to reduce the hazard for trailing aircraft. Crouch (1997) investigated, using vortex filaments, the instability and transient growth of a system comprising two pairs of co-rotating vortices. This type of four-vortex system is representative of the vortex system generated by an aircraft from the wingtips or any discontinuity along the wing surface, such as flaps. Crouch found that the system is dominated by a shorter wavelength instability than the Crow instability, exhibiting a growth rate of 60-100% greater than the Crow instability. Crouch used a vortex filament

model to model the wake of the aircraft. This vortex model does not capture what is occurring within the vortex core and is limited to sinuous instability modes, excluding the study of Kelvin modes. This is in contrast to this thesis, which uses a more realistic vortex profile that allows for the analysis of all of the Kelvin mode instabilities. Crouch used a Floquet-type analysis to look at the stability of the vortex system. A limitation of this analysis is that it assumes a periodic flow. However, wake vortices are subject to diffusion from the moment they form and thus strictly lack the time periodicity required for a Floquet-type linear stability analysis. Crouch also ignored any lateral movement of the vortices, which occurs as the tail vortex pair travels around the wing vortex pair. He found that the spacing and relative circulation between the flap and wing vortices had relatively little effect on the long wavelength Crow instability. This was in direct contrast to short wavelength instabilities, which Crouch found were significantly affected by the spacing and relative circulation. He found that instabilities grow faster on the weaker vortex pair as shown in Figure 1.15. He found that transient growth of perturbations could amplify the perturbation by approximately 10-15 times over one period of rotation for the long wavelength Crow instability. He also found that when both vortex pairs were excited, little transient growth of perturbations was present, while exciting only one pair of the vortices caused significant transient growth.

Fabre & Jacquin (2000) used a similar method to Crouch to investigate a system comprising two pairs of counter-rotating vortices. This type of four-vortex system is indicative of the kind of wake shed from aircraft wings and the aircraft tail. Fabre & Jacquin found that without a long wavelength instability being forced onto the system, the primary method of destruction was a short wavelength instability that only affected the weaker tail vortex pair. Fabre & Jacquin used a wing-to-tail vortex separation ratio of $0.1 \leq b_2/b_1 \leq 0.15$. This is not indicative of real aircraft geometry, which instead is closer to $b_2/b_1 \approx 0.4$ (Gunston 1995). This a possible reason why the instability in the tail vortex pair did not have any noticeable effect on the wing vortex pair. Fabre & Jacquin also used a stationary vortex system, which is limited, as it does not take into account that the weaker tail vortex pair will transit around the stronger wing vortex pair. This rotation of the base flow field will cause a rotation of the strain field on the stronger wing vortex pair, allowing for instabilities to form, which may have the potential to accelerate destruction.

At the same time as Fabre & Jacquin (2000) were conducting their research, Ortega

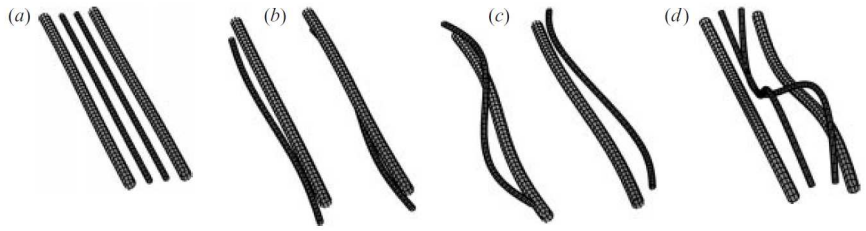

FIGURE 1.16: A reproduction of figure 5 from Fabre *et al.* (2002) showing a long-wave instability occurring on the outer vortices and moving to the inner vortices. Reproduced with permission from Cambridge University Press, who retain the copyright.

& Savaş (2000) were performing experimental work on two- and four-vortex systems in a towing tank at a Reynolds number of $Re = 107\,000$. The four-vortex system Ortega & Savaş studied was a counter-rotating system similar to Fabre & Jacquin (2000). Ortega & Savaş found that the weaker inner vortices develop a sinusoidal instability at approximately 20 spans downstream, and that the inner vortices begin to curl around the stronger wingtip vortices at between 20 and 27 spans downstream. This curling of the weaker inner vortices is the mechanism that leads to non-linear evolution, and occurs from 27 spans downstream.

A little later, Crouch *et al.* (2001) began to look at active methods for inducing instabilities in a multiple-vortex wake. By using both a towing tank and a numerical analysis, they found that active control could be used to excite instabilities in the far wake of an aircraft in the 'flaps down' configuration. The results that Crouch *et al.* found are promising for the enhancing of instability growth in the far wake of an aircraft, however, they did identify a number of issues that would need to be resolved for actual aircraft. These issues related to the performance of the aircraft in flight, the viability for an aircraft with the active method, and the effectiveness of the enhanced instability on the hazard to trailing aircraft.

Following the earlier work of Fabre & Jacquin (2000), Fabre *et al.* (2002) continued to study instabilities in a four-vortex counter-rotating model of the far wake of an aircraft. Fabre *et al.* used a vortex filament method with a linear stability analysis to investigate the instabilities in the four-vortex model. They found that large optimal growth rates are possible, but require large tail to wing circulation ratios, Γ_2/Γ_1. This large circulation ratio would lead to large loading on the wings, which would be structurally unsound on a real aircraft. Fabre *et al.* found that, for a periodic four-vortex system, optimal perturbations that correspond to a short to medium axial wavelength

instability, which mainly affects the weaker, inboard vortices, grow faster than the Crow instability. They speculated that forcing a long wavelength Crow instability in a four-vortex system may lead to a better guarantee of final dissipation. Figure 1.16 shows how a long wavelength instability excited in the tail vortex pair can cause a long wavelength instability to form in the wing vortex pair.

Haverkamp *et al.* (2005) continued the previous study by Crouch *et al.* (2001) into active and passive methods for inducing instabilities in the wake of an aircraft. Haverkamp *et al.* investigated, using a towing tank, a four-vortex counter-rotating configuration. They found that high tail loads resulted in highly unstable vortex systems, leaving little recognisable vortex structure in the far wake. They also found that for a wing to tail circulation ratio of $\Gamma_2/\Gamma_1 \leq -0.29$, there was no significant alleviation of the wake hazard. This was because the instability for a small circulation ratio led to the destruction of the weaker vortices with little effect on the stronger vortices. For a low angle of attack with oscillating ailerons, Haverkamp *et al.* found that higher wavenumbers produced a significantly faster breakup of wake vortices in the far field. For a high angle of attack with oscillating ailerons they found that the oscillation caused a rearrangement of the vortex structure, but did not cause enhancement of instabilities, and therefore an alleviation of the wake hazard. The frequency they found for optimal forcing of the instabilities in the four-vortex system they studied are close to the first bending mode of an aircraft wing, potentially leading to structural problems.

Continuing the research into four-vortex counter-rotating systems, Stumpf (2005) used DNS to look at a counter-rotating system with a outer to inner vortex circulation ratio of $\Gamma_2/\Gamma_1 = -0.35$. Stumpf found that, in the far wake, a shortwave instability grows in the tail vortex pair as they are pulled around the stronger wing vortex pair. This instability in the tail vortex pair leads to an instability in the wing vortex pair (shown in figure 1.17). Stumpf also showed that white noise as a model of atmospheric turbulence did not trigger the Crow instability, but did trigger shortwave instabilities. Stumpf came to the conclusion that four-vortex wakes have the potential to alleviate wake hazards.

At the same time, Hubbard & Marquis (2005) looked at both counter- and co-rotating four-vortex systems with a range of outer to inner vortex circulation ratios, by using a two-dimensional point vortex model. Their primary investigation was to study the vortex trajectory, rather than the vortex interactions. They found that the

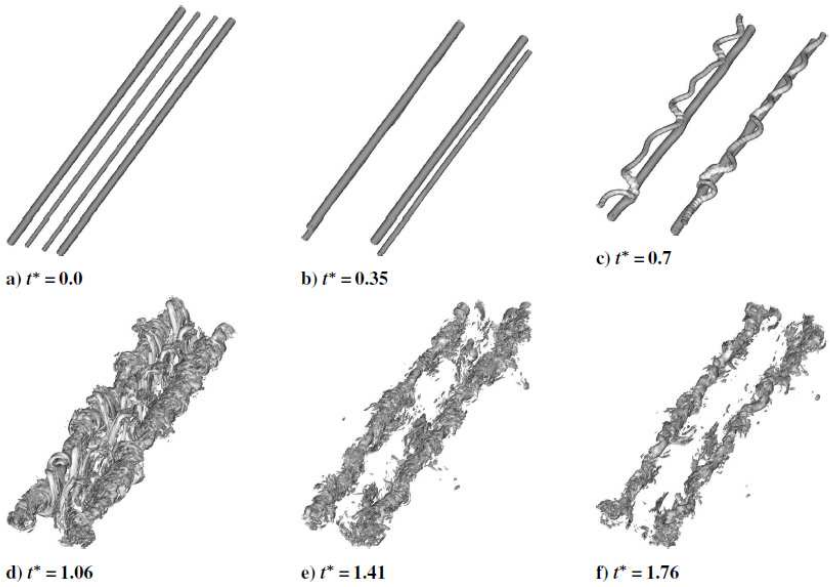

FIGURE 1.17: A reproduction of figure 9 from Stumpf (2005) showing a short-wave instability occurring on the outer vortices and moving to the inner vortices. Reprinted with permission of the American Institute of Aeronautics and Astronautics.

trajectory of rigidly translating systems are easily perturbed by weak and strong shear layers, and concluded that instability mechanisms that utilise cooperative instability between vortex pairs on either side of the wake are more likely to survive shear-layer interactions.

Kauertz & Neuwerth (2007) took a four-vortex counter-rotating system and investigated, using a water towing tank, possible methods of exciting instabilities that would lead to earlier alleviation of the wake hazard. One of the methods they investigated was the use of winglets on a wing, but found that oscillation of the winglet rudder did not accelerate the decay of the wake hazard. However, they did find that optimal configuration of passive static rudders could destabilise the vortex systems more rapidly. They also found that the vortex wake was sensitive to a small sideslip, but such a configuration would be unfavourable in a real aircraft.

The analysis of multiple vortex wakes has been extended to include other possible sources of turbulence, such as the the work by Allen & Breitsamter (2008a) that investigated the effect on an aircraft wake of the landing gear. Allen & Breitsamter used a 1:19.25 scale half-model in a wind tunnel with hot wire anemometry to conduct the study. They found that the main wing vortices moved slightly further outboard, retarding the roll up process in the near wake. Allen & Breitsamter discovered that landing gear did cause an increase in turbulence in the near wake, but did not enhance

inherent wake instabilities, or have an effect on the overall wake dynamics.

Allen & Breitsamter (2008b) also conducted a study into large winglets and winglet flaps attempting to induce instabilities in the wake of large transport aircraft. They conducted this study using a 1:32 scale half model of a four engine aircraft within a wind tunnel and testing with hot-wire anemometry. Allen & Breitsamter discovered that seven main vortices are shed off discontinuities along the wing surface. Their results showed that deflection of the winglet flaps cause a concentration of turbulent kinetic energy in the frequency range associated with the long wavelength Crow instability. The deflection of the winglet flaps also produced additional vortical structures in the wing tip area, causing enhanced roll up that leads to the rolled up vortex forming closer to the aircraft.

Continuing the previous research by Allen & Breitsamter (2008a,b), Allen & Breitsamter (2009a) investigated a set of four counter-rotating vortices using a wind tunnel, and measured with hot wire anemometry. They found that large instabilities grow in the tail vortex pair significantly faster than in the wing vortex pair. This instability in the tail vortex pair causes a long wavelength instability to form in the wing vortex pair. Allen & Breitsamter did not actually observe any coiling of the tail vortex around the wing vortex, which is in contrast to what was observed by Ortega & Savaş (2000), but this could be explained by the locations where the hot-wire measurements were taken.

Using the same setup at Allen & Breitsamter (2008b), Allen & Breitsamter (2009b) also investigated the possibility of using oscillating winglet flaps, both symmetric and asymmetric deflections, to enhance vortex merger. They found that oscillations in the winglet flaps could cause vortices to merge in a shorter timeframe. This leads to larger perturbations in the remaining rolled up vortex. Allen & Breitsamter found that the asymmetric deflection of the flaps was favourable from a aircraft flight perspective, as it reduced the oscillation in lift, side forces and pitching moment. However, they also found that the asymmetric oscillations displayed lower amplification of instabilities than the symmetrical case. Similar to Haverkamp *et al.* (2005), Allen & Breitsamter found that the frequencies that cause an amplification of instabilities is limited to a fairly narrow band, with amplifications within this band occurring up to a factor of 20 times the initial forcing amplitude.

One of the most recent works published was by Babie & Nelson (2010) and investigated both co- and counter-rotating four-vortex systems using experimental methods.

The study was conducted at a Reynolds number of $Re = 15\,800$ and simulated the kind of wake generated by a wing/flap configuration. Babie & Nelson found that a range of strong to weak vortex circulation ratio and span are consistent with the growth of a long-wavelength instability. They also found that the wavelength of the instability scales with the effective vortex span between the counter-rotating wingtip/flap vortex vortex pair on each side of the wake. This leads to the finding that the instability growth rate is consistent with the predicted growth rate as scaled by the applied strain within the wingtip/flap vortex pair on each side of the wake. They found that the first short axial wavelength bending mode was identified within the vortex core boundary for each of the unstable wake configurations. The streamwise evolution of the short wavelength mode that Babie & Nelson found is consistent with the elliptic instability mode.

At the same time, Schaeffer & Le Dizès (2010) were using three-dimensional DNS to investigate two- and four-vortex counter-rotating Lamb–Oseen vortices at a Reynolds number of $Re = 6300$. One interesting point about the study conducted by Schaeffer & Le Dizès is that they used a circulation ratio $\Gamma_2/\Gamma_1 = 1$. They found that the main effect of non-linear evolution of the elliptic instability was to increase the effective core size. The increase in effective core size was shown to be able to occur multiple times, and that small deformations caused by the elliptic instability could cause large increases in the effective core size. The study into four-vortex systems conducted by Schaeffer & Le Dizès found that the vortex circulation was conserved, even given that the vortex core size can increase by approximately 40%, while only taking 1/5th of the time that a two-vortex system would take. As with the two-vortex investigation, they found that the elliptic instability could rapidly increase the effective core size, even for high Reynolds numbers. They found that the nonlinear dynamics primarily occurred in four steps. First, concentrations of vorticity formed in thin layers at the periphery of the vortex. Then, vortex loops formed from the thin layers of vorticity were expelled and this leads to the entire structure breaking down. Lastly, a relaminarisation process leads to the vortex reforming into a larger and weaker vortex.

So far both counter- and co-rotating four-vortex systems have been investigated by previous researchers. However, no research has been conducted into the effect of having an aircraft tail significantly displaced vertically, as is the case in heavy lift aircraft. In addition to this, no-one has investigated

if there is an optimum seeding position in the orbit of the tail vortex pair to ensure the most rapid vortex destruction. These areas are investigated by this thesis.

1.5 Global stability analysis and transient growth analysis

The stability of these flows is a field of interest as it can provide information about potential methods to disrupt these types of flows to reduce the hazard for trailing aircraft. Crouch (1997) investigated, using vortex filaments, the instability and transient growth of instabilities for co-rotating vortex pairs. Crouch used Floquet analysis to look at the stability of the vortex system. This type of stability analysis has the limitation that it requires a base system that is periodic, where the condition after a period of time τ is the same as the initial condition. Similar studies have looked at the stability of a pair of counter-rotating vortex pairs. Both Crouch (1997) and Fabre *et al.* (2002) considered a simplified Kelvin mode of instability that has no azimuthal mode shape. Both studies used a vortex filament as a further simplification. This simplification limits the size of the instability that can be investigated to scale larger than order of the vortex core radius. However, Lacaze *et al.* (2007) investigated a full range of Kelvin mode shaped instabilities with a Batchelor vortex. They discovered that these mode shapes are significantly damped even with small axial flow. Lacaze *et al.* (2007) also found that non-sinusoidal mode shapes are more excited as the axial flow increases. Axial flow is not uncommon in aircraft wakes due to ambient turbulence in the air and the air moved due to the engine exhaust (Batchelor 1964).

Several studies used a frozen base flow to conduct the stability analysis (So *et al.* (2008), Lacaze *et al.* (2007) and Leweke *et al.* (2004)). Wakes consisting of parallel vortex tubes, however, are subject to diffusion from the moment they form and, as such, are not completely described by a frozen base flow or the perfectly time-periodic flow required for conventional linear stability analysis. For a more complex system, such as multiple vortex pairs, the extremely transient nature of this flow means that only a transient growth analysis is capable of analysing this type of base flow.

Transient growth of perturbations in these types of flow can be very important as they have the potential to alter the base flow severely and cause destruction of the wake vortices. Barkley *et al.* (2008) developed a method of transient growth analysis based on examining the energy of a perturbation after a length of time τ, compared with

its initial energy. The authors used this method on known flows to verify the method (Blackburn *et al.* 2008a,b).

Blackburn *et al.* (2008a) investigated the case of transient growth over a backward facing step. This type of geometry is a fundamental case in fluid mechanics, as it shows separation resulting from severe changes in geometry in an open flow (Blackburn *et al.* 2008a). They found, for a two dimensional optimal growth computation, that the growth amplification factor is $O(6 \times 10^4)$. Blackburn *et al.* (2008a) noted that, in comparison to previous work looking at similar geometry with a slightly higher Re (Marquet *et al.* 2006), the predicted optimal growth amplification factor was $O(10^2)$ less than the values found by Blackburn *et al.* (2008a). This indicates that transient growth may be far stronger than the global instability modes and contribute to their excitation.

1.6 Summary

So far, significant research has been conducted into single-, double- and multiple-vortex systems. While some research has investigated the transient response of two-vortex flows, there has not been any investigation into the effect of seeding these two-vortex flows with the perturbations that lead to optimal energy growth. The first results chapter of this thesis seeks to demonstrate that, by seeding the two-vortex flow with specific modes at specific axial wavenumbers, the growth of instabilities can be accelerated over systems seeded with simple white noise.

By contrast, the four-vortex flow has had fewer investigations conducted to understand the dynamics underpinning such flows. Investigations into both counter- and co-rotating flows have been conducted by previous researchers, but no research has been conducted to investigate the effect of a vertical displacement of the tail vortex pair as would occur in a heavy lift aircraft. In addition, a transient growth analysis of the type conducted by Blackburn *et al.* (2008a,b) has not been conducted on this type of four-vortex flow. The second chapter of this thesis seeks to understand the change in the dynamics and transient response to perturbations that occurs due to a change in the vertical displacement of the tail vortex pair. The third chapter of this thesis extends the investigation to study the effects

of an asymmetric four-vortex flow (the kind of change in circulation that would occur in a banking aircraft).

By extending the previous work in this field, the investigations studied here could provide insight into the most effective method of perturbing the four-vortex flow to ensure rapid destruction of an aircraft wake.

Chapter 2

Methodology

This chapter describes the methods employed throughout this thesis to study the two-, symmetric four-, and asymmetric four-vortex aircraft wake model. It begins by examining the system under investigation, then defines the key parameters for the studies, presents the mathematical description of the problem, describes how the mathematical model is implemented numerically, then examines the transient growth analysis technique, and demonstrates the implementation of the three-dimensional solver. Finally, an error analysis is conducted and grid independence is verified.

Figure 2.1 shows a schematic representation of the counter-rotating two-vortex system investigated in the first results chapter of this thesis. The variables under investigation for the two-vortex system are the vortex circulation, Γ_1, the initial vortex core size, a_1 and the vortex spacing, b_1. Figure 2.2 shows a schematic representation of the system under investigation in the second and third results chapters of this thesis. As the four-vortex system is more complicated, the wing vortex circulation is defined as Γ_1, the tail vortex circulation as Γ_2, the wing vortex core size as a_1, the tail vortex

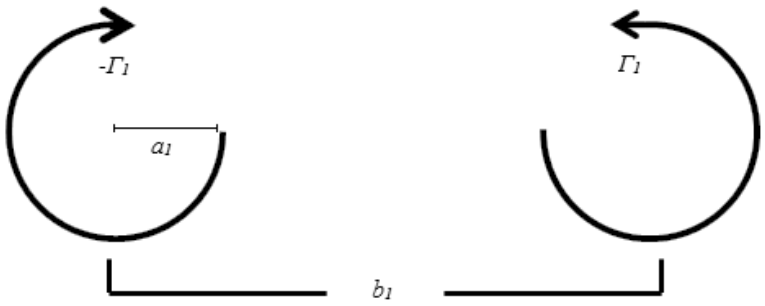

FIGURE 2.1: Diagram displaying the layout of the initial vortex set and defining the span variable, b_1, for the two-vortex system model.

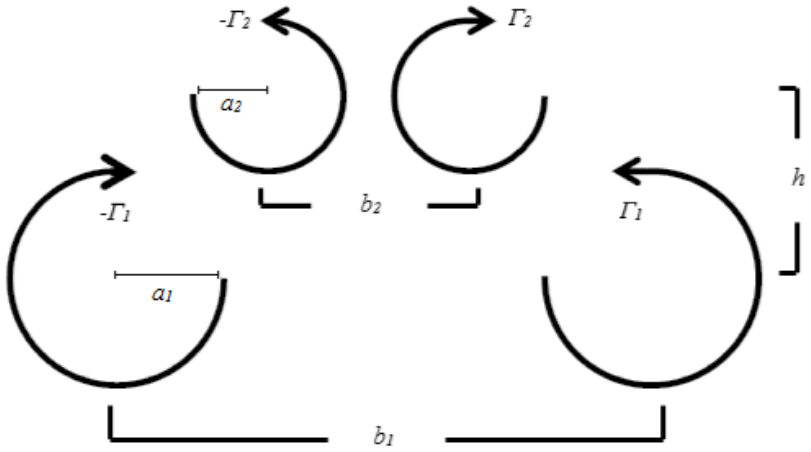

FIGURE 2.2: Diagram displaying the layout of the initial vortex set and defining the wing vortex span, tail vortex span and height variables (b_1,b_2 and h respectively) for the four-vortex system model.

FIGURE 2.3: Contour plot of vorticity for the initial conditions of the 2 vortex system model in two-dimensional space. Contour lines represent unit increments in non-dimensional vorticity. The minimum and maximum vorticity levels were -8 and 8 in the left and right tail vortices respectively. Dashed lines represent negative vorticity levels.

core size as a_2, the horizontal wing vortex separation as b_1, the horizontal tail vortex separation as b_2 and the vertical displacement of the tail vortex pair as h. The setup of the wing/tail vortex system comprises two pairs of counter-rotating vortices with the tail vortex pair having opposite sign to the wing vortex pair.

2.1 Initial conditions

Figure 2.3 displays the initial position of the two-vortex problem with an initial separation of b_1. This vortex separation is used to normalise all length scales. It is important to note that this study is only concerned with parallel vortices: no helical vortex wakes, such as those wakes caused by helicopters, wind turbines or long wavelength unequal strength vortices, have been modeled in this study. Figure 2.4 displays the initial positioning of the four-vortex arrangements for the high and flat tail models. Figure 2.4(a)

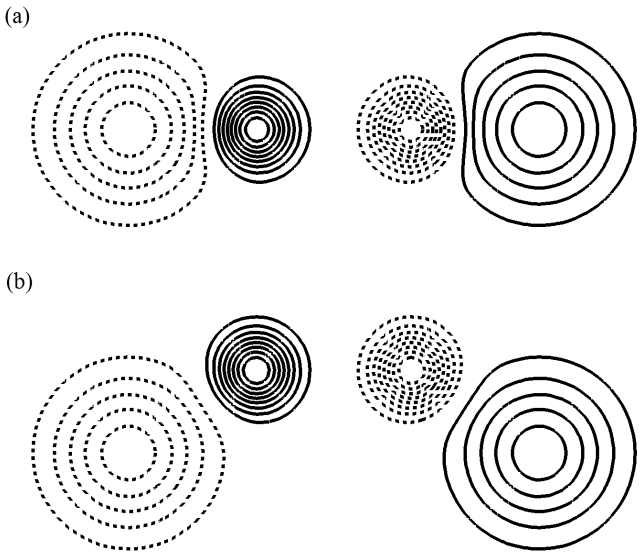

FIGURE 2.4: Contour plot of vorticity for the initial conditions of the (a) flat tail and (b) high tail case in two-dimensional space. Contour lines represent unit increments in non-dimensional vorticity. The minimum and maximum vorticity levels were -8 and 8 in the left and right tail vortices respectively. Dashed lines represent negative vorticity levels.

TABLE 2.1: Table of four-vortex 'high tail' wake model variables used throughout the studies considered in this thesis. Note that the only change for the 'flat tail' case is $h/b_1 = 0$.

Γ_2/Γ_1	h/b_1	b_2/b_1	a_1/b_1	a_2/a_1	Re
-0.4	0.2	0.38	0.176	0.5	20 000

shows the case of the 'flat tail' configuration with $h/b_1 = 0$. Figure 2.4(b) shows the 'high tail' case with the tail vortex pair displaced vertically ($h/b_1 = 0.2$). This was chosen to correspond to the vertical displacement of the tail of the C-17 Globemaster aircraft from its wings. A value of $\Gamma_2/\Gamma_1 = -0.4$ was chosen for the ratio between the wing and tail circulation in Chapter 4 and this corresponds to the values found in the literature for a heavy lift aircraft in landing configuration (Rennich & Lele 1999). For Chapter 5, an inequality in the circulation of 15% is introduced to both the wing and tail vortex pairs to provide the system with asymmetry. This corresponds to the left wing vortex having 15% more circulation and the right tail vortex having 15% more circulation than their paired vortex. The horizontal displacement of the tail to wing vortex separation was chosen to be $b_2/b_1 = 0.38$ corresponding to the ratio of wing to tail span of the C-17 Globemaster aircraft.

2.2 Mathematical model

The vortex profile used is that of a Gaussian vortex and was chosen to be consistent with previous work in the area (Crouch 1997; Fabre *et al.* 2002; So *et al.* 2008, 2011). In addition, Le Dizès & Verga (2002) demonstrated that other vortex profiles evolve into a Gaussian vortex profile after a short transient relaxation period. The azimuthal velocity field of a single Gaussian vortex is given by

$$v_{rz} = \frac{\Gamma}{2\pi r}\left(1 - e^{-\left(\frac{r}{a_i}\right)^2}\right), \tag{2.1}$$

where r is the radial distance from the centre of the vortex and a_i is the vortex core radius, where $i = 1$ and 2 is used to denote the wing and tail vortex respectively. For these studies, $a_1/b_1 = 0.176$ and the ratio of tail vortex core size, a_2, to wing vortex core size is $a_2/a_1 = 0.5$. This was chosen to make the tail vortices self-similar to the wing vortices. The vortices are Lamb–Oseen vortices, which are defined by the Gaussian azimuthal velocity given in equation 2.1, which contain no axial flow component.

The global rotation rate of the vortices, Ω, can be normalised by the vortex initial turnover time (ITT), $t_{ITT} = 2\pi a_1^2/\Gamma$, such that non-dimensional vorticity, ω^*, is related to the dimensional global rotation rate by

$$\Omega^* = \frac{\Omega 2\pi a_1^2}{\Gamma}. \tag{2.2}$$

The system is evolved in time by solving the incompressible Navier–Stokes equations

$$\frac{\partial \mathbf{u}}{\partial t} = -(\mathbf{u}\cdot\nabla)\mathbf{u} - \nabla p + \nu\nabla^2\mathbf{u}, \tag{2.3}$$

$$\nabla\cdot\ \mathbf{u}\ = 0, \tag{2.4}$$

where 2.3 and 2.4 are the momentum and continuity equations respectively and $\mathbf{u}$ is the velocity field, t is the time, p is the kinematic pressure, and ν is the kinematic viscosity of the fluid.

In this case a Reynolds number, Re, is defined based on the circulation of the wing vortex, Γ_1, and the kinematic viscosity, as

$$Re = \frac{\Gamma_1}{\nu}. \tag{2.5}$$

In this study a Reynolds number $Re = 20\,000$ was considered, consistent with the ranges considered in similar vortex studies (Lele 2001; Haverkamp *et al.* 2005; Roy *et al.*

2008). It is assumed that the instabilities being investigated are consistent across the range of Re observed between an aircraft and these simulations. This assumption is reasonable as the primary method of destruction of this type of vortex system is caused by perturbations with wavelengths that are far above the scale of turbulence damped out by the higher viscosity inherent in these simulations (Landman & Saffman 1987).

All two-vortex studies are normalised by the reference time, $T_{2V} = 2\pi b_1^2/\Gamma$. $T_{2V} = 1$ corresponds to the time it takes for the centres of the vortex cores to propagate a distance equal to their spacing, b_1 (Crouch 1997). All four-vortex studies are normalised by the orbit of the tail vortex pair around the stronger wing vortex pair, T_0. Crouch (1997) defines an equation for the orbital angular frequency of a weaker vortex pair around a stronger vortex pair as $\Omega_C = 1/\delta^2$, where δ is defined as $0.5(b_1 - b_2)/b_1$. However, this model for the orbit of the tail vortices is limited as it assumes that δ is small and the vortices remain undistorted. If δ is not small, or the vortices become distorted, then the frequency can drop lower than $\omega = 1/\delta^2$ (Crouch 1997). Because of the limitations of this formula, T_0 was computed from a simple two-dimensional DNS of the 'high tail' case; the same value is used throughout as the orbit period is the same for the 'high tail' and 'flat tail' cases.

2.2.1 Dominant strain

The dominant strain referred to in later chapters is defined as

$$\varepsilon_{dom}^2 = \tau_{xy}^2 - \tau_{xx}\tau_{yy}, \tag{2.6}$$

where

$$\tau_{xy} = \frac{1}{2}\left(\frac{\mathrm{d}u}{\mathrm{d}y} + \frac{\mathrm{d}v}{\mathrm{d}x}\right), \tag{2.7}$$

$$\tau_{xx} = \frac{\mathrm{d}u}{\mathrm{d}x}, \tag{2.8}$$

$$\tau_{yy} = \frac{\mathrm{d}v}{\mathrm{d}y}, \tag{2.9}$$

that was first used by Ryan *et al.* (2011). This is considered the 'dominant' strain as it is the component of strain in the x-y plane that, when coupled with ω_{xy}, acts to dominate the definition of the λ_2 field (defined as the criterion for identification of a vortex proposed by Jeong & Hussain (1995)) when the strain in any plane other than the x-y plane is minimal (e.g. $\tau_{zz} \approx 0$). Given the configurations of the vortices examined in this thesis, it is reasonable to assume that $\tau_{zz} \approx 0$.

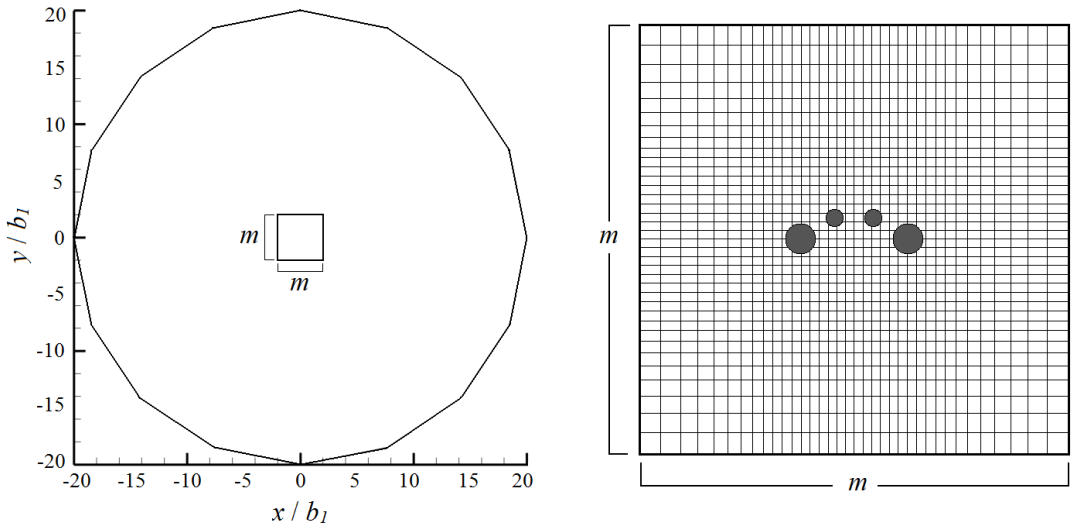

FIGURE 2.5: Left: The full computational domain, identifying the refined region at the centre. Right: A detailed view of the refined region of the mesh. The dark shaded circles identify the vortex cores of the 'high tail' four-vortex system for reference. The refined region extends over $-2 \leq x/b_1 \leq 2$ and $-2 \leq y/b_1 \leq 2$, and comprises $m \times m$ elements with $m = 36$.

2.3 Numerical simulation method

The system described in § 2.2 is simulated with a computational fluid dynamics solver employing a spectral-element discretization in space and a third-order operator splitting technique for time integration based on backwards differentiation. The solver employs a nodal formulation, in which Lagrangian tensor-product polynomials are employed in each element. The polynomial degree, p_n, can be changed for a given simulation to control special resolution. More detail may be found in Karniadakis *et al.* (1991). This algorithm has been used extensively to study a number of wake and vortex flows (Sheard *et al.* 2007, 2009; So *et al.* 2011).

A single mesh was constructed for use throughout this project, which is shown in figure 2.5. Care was taken to ensure that the mesh is sufficiently large to render negligible dependance of the results on the domain size. On the mesh boundaries, a Dirichlet condition is imposed on the velocity field to specify a uniform cross flow to counteract the propagation of the vortices, thus maintaining their position in the refined region of the mesh. The mesh contains 1794 elements with the majority located in the central refined region. The boundaries of the domain are $20b_1$ from the vortex system, ensuring that any effect from the domain boundary is negligible. As the outer region contains no important flow structures, significantly lower resolution is used to

reduce the computational expense of the simulations. Despite the initial configuration possessing a reflective symmetry about the vertical centerline, the full system of vortices was always resolved to permit reflective symmetry-breaking behavior in the evolving vortices to be captured.

2.4 Transient growth analysis

Transient growth analysis is a method for determining the optimal initial linearised disturbances leading to maximum energy growth over a specified time interval. While global stability analysis predicts the asymptotic stability of a flow, where the evolution is contributed to only by a single leading eigenmode of the system, transient growth analysis is able to capture large short-timescale amplifications which can emerge due to the interaction between the non-orthogonal eigenmodes of the linearised evolution operator of the Navier–Stokes equations. The implementation of the transient growth analysis suitable for time-stepping solvers was initially proposed by Barkley *et al.* (2008); Blackburn *et al.* (2008b,a), and this implementation method was used throughout this study to conduct the transient growth analysis. A description of the implementation of this method is described in this section. The transient growth analysis method is particularly attractive for analysing this kind of flow system due to the highly transient nature of the base flow field, which lacks the time periodicity required for a global linear stability analysis. This method begins by defining an operator $\mathscr{A}(t)$ describing the evolution of a perturbation field over a time interval t,

$$\mathbf{u}'(t) = \mathscr{A}(t)\mathbf{u}'(0). \tag{2.10}$$

The norm used by Barkley *et al.* (2008) to quantify the size of a perturbation is the total kinetic energy of the perturbation field. By normalizing the energy growth of the perturbation with its initial energy and using the evolution operator such that

$$\frac{E(\bar{\tau})}{E(0)} = \left(\mathscr{A}(\bar{\tau})\mathbf{u}'(0), \mathscr{A}(\bar{\tau})\mathbf{u}'(0)\right) = \left(\mathbf{u}'(0), \mathscr{A}^*(\bar{\tau})\mathscr{A}(\bar{\tau})\mathbf{u}'(0)\right), \tag{2.11}$$

where $\mathscr{A}^*(\bar{\tau})$ is the adjoint evolution operator to $\mathscr{A}(\bar{\tau})$ in the L^2 norm, it becomes possible to find the dominant eigenvalues of $\mathscr{A}^*(\bar{\tau})\mathscr{A}(\bar{\tau})$ which dictate the largest possible energy growth for a linear disturbance over a given time interval $\bar{\tau}$. This property arises from the close association between the eigenvalues of $\mathscr{A}^*(\bar{\tau})\mathscr{A}(\bar{\tau})$ and the singular value decomposition of $\mathscr{A}(t)$ (Barkley *et al.* 2008). The action of the evolution

(a) $\tau = 0.446$ (b) $\tau = 5.35$

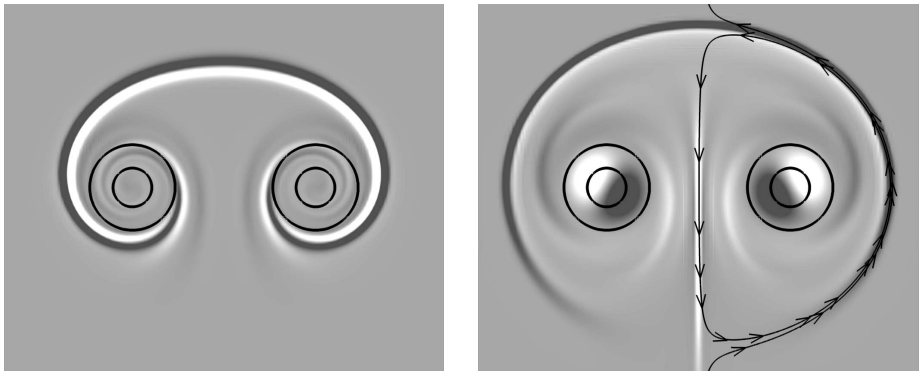

FIGURE 2.6: An example of the optimal initial condition for a two-vortex equal strength system computed at $Re = 20\,000$ and $k\,a_1 = 2.12$, with (a) $\tau = 0.446$ and (b) 5.35. Streamlines relative to the vortex pair are plotted on the right half-plane in (b) to elucidate the location of hyperbolic points above and below the vortex pair. Axial vorticity contours are plotted on the base flow (lines) and the linearised perturbation field (flooded contours).

operator, $\mathscr{A}(\bar{\tau})$, on the perturbation vector is equivalent to integrating the linearised Navier–Stokes equations,

$$\delta_t \mathbf{u}' = -(\mathbf{U}\cdot\nabla)\mathbf{u}' - (\mathbf{u}'\cdot\nabla)\mathbf{U} - \nabla p' + Re^{-1}\nabla^2\mathbf{u}' \tag{2.12}$$

and

$$\nabla\cdot\mathbf{u}' = 0, \tag{2.13}$$

(where $\mathbf{u}'$ and p' denote the perturbation velocity and pressure fields respectively) forward in time, and the effect of the adjoint operator, $\mathscr{A}^*(\bar{\tau})$, on the perturbation vector is the equivalent of integrating the adjoint Navier–Stokes equation,

$$-\delta_t \mathbf{u}^* = -(\mathbf{U}\cdot\nabla)\mathbf{u}^* + (\nabla\mathbf{U})^T\cdot\mathbf{u}^* - \nabla p^* + Re^{-1}\nabla^2\mathbf{u}^* \tag{2.14}$$

and

$$\nabla\cdot\mathbf{u}^* = 0, \tag{2.15}$$

(where $\mathbf{u}^*$ and p^* denote the adjoint perturbation velocity and pressure fields respectively) backwards in time over $\bar{\tau}$. More detailed information and implementation of this method is provided in Barkley *et al.* (2008). The eigenvalue solver used in this study has been validated and employed in the past in linear stability analysis of other flows (Sheard *et al.* 2009; Sheard 2011) and produced results consistent with an independent formulation of the algorithm (Blackburn & Sheard 2010).

The advantages of this method is that the perturbation evolution and adjoint operators do not need to be explicitly constructed, which is not viable for problems as large

as the one investigated in this study. When using the Arnoldi package eigenvalue solver employed by the code, only the effect on the perturbation field through time integration using the forward or adjoint linearised Navier–Stokes equations is required. The eigenvalue solver outputs both the leading eigenvalue and the corresponding eigenvector of $\mathscr{A}^*(\bar{\tau})\mathscr{A}(\bar{\tau})$, which corresponds to the leading singular value and right singular vector of $\mathscr{A}^*(\bar{\tau})$; the right singular vector specifies the optimal initial condition leading to the largest possible energy growth for a linear disturbance evolving over time $\bar{\tau}$.

An example of how the initial perturbation field that leads to maximum energy growth can change with change in $\bar{\tau}$ is shown in figure 2.6. This figure shows the optimal initial condition for a a two-vortex equal strength system computed at $Re = 20\,000$ and $k\,a_1 = 2.12$, with (a) $\tau = 0.446$ and (b) 5.35. As τ increases (figure 2.6(b)), the initial optimal perturbation field begins to resemble the global instability mode for the mode [-1,1,1] elliptic instability. In contrast, the vortex cores in the short-τ optimal initial disturbance field are devoid of a perturbation vorticity dipole, but retain a different pattern of strong vorticity (figure 2.6(a)), and the umbrella band of perturbation above the vortices lies inside the hyperbolic streamlines. Hereafter, this perturbation field will be referred to as the 'initial optimal perturbation field'.

Due to the requirement to integrate the adjoint equations backwards in time, an interpolation method is used to reconstruct the base flow during the adjoint operation. To determine the accuracy of the interpolation method, a two-dimensional DNS of the four-vortex 'high tail' configuration was compared to the interpolated base flow. The four-vortex 'high tail' model was considered as it was likely to demonstrate a higher error than the 'flat tail' or two-vortex case. The Reynolds number was set at $Re = 20\,000$ as it is the highest used in this study and therefore imposes the greatest strain on the resolution of the system. The comparison was made using the average percentage of the differences in the L_2 norm between the DNS and interpolated flow across $t/T_0 = 0.5$ intervals in the range $0 \leq t/T_0 \leq 3$. The average percentage of the differences is defined as ϵ_{int}.

Two interpolation approaches for the velocity field were considered: polynomial interpolation and Akima spline interpolation. Tests determined that polynomial interpolation produced undesirable wiggles in the reconstructed base flow, which is responsible for the massive errors seen in figure 2.7 as $\epsilon_{int} > 10^{12}$ for the largest number of interpolation points used.

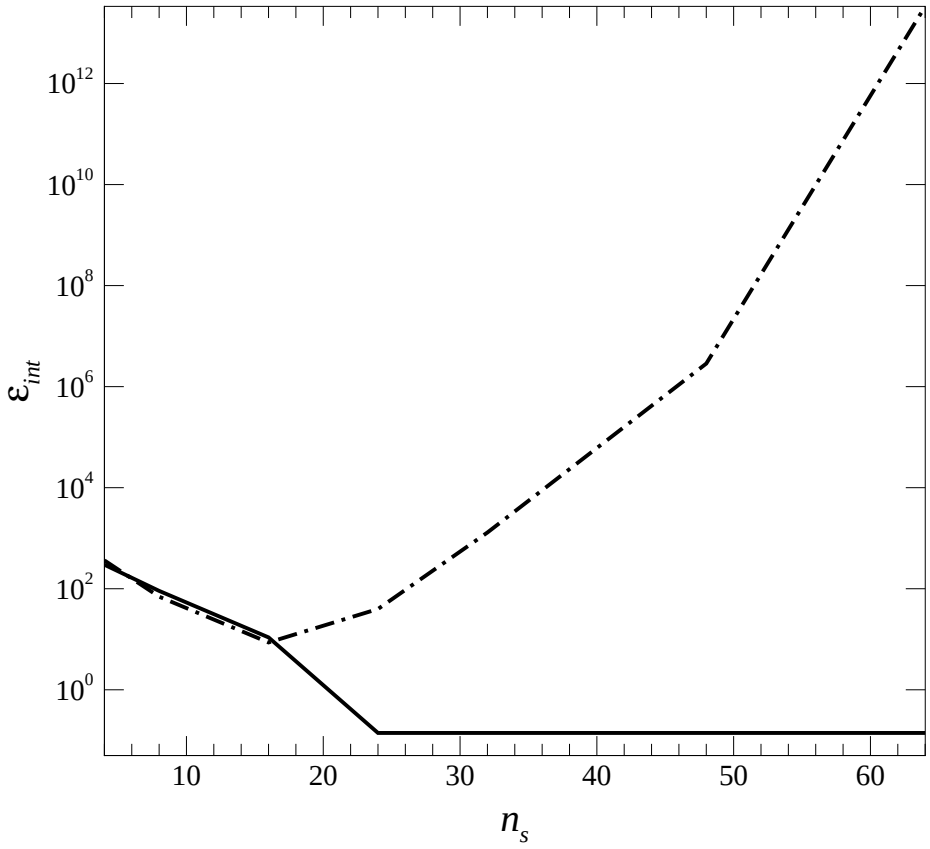

FIGURE 2.7: Plot of difference between interpolation values and DNS values (ϵ_{int}) against number of snapshots used to create the interpolation, n_s. Dotted line represents interpolation using a polynomial method and solid line represents Akima interpolation method.

However, Akima interpolation (Akima 1970), which are known to be effective in suppressing wiggle artifacts, was found to provide a very close reproduction of the time evolution of the flow, as shown by $\epsilon_{int} < 0.14\%$ in figure 2.7, and is therefore employed throughout this study. Pleasingly, the Akima interpolation method demonstrates rapid convergence with increasing number of velocity field snapshots: the plateau in Akima interpolation error corresponds to the limit of machine precision.

As with linear stability analysis, this transient growth analysis method assumes that the perturbations are small. Thus if the predicted amplification energies are large, the disturbance can become non-linear, leading to bulk changes in the flow. This thesis will investigate the possibility that optimal disturbances can accelerate the destruction of the vortex system by invoking nonlinear growth in the flow.

2.5 Three-dimensional DNS method

The three-dimensional direct numerical simulations reported in this thesis are conducted using a spectral element-Fourier method (Karniadakis 1990; Karniadakis & Sherwin 1999; Henderson 1999), in which the same spectral-element discretization in the x–y plane as used by the two-dimensional solver is used, with the addition of a Fourier expansion of the velocity field in the z (out-of-plane) direction. The extent of the axial domain for the three-dimensional simulations was chosen to correspond to the peak axial wavenumber found from the transient growth analysis for the two-vortex and symmetrical four-vortex system. The axial extent for the asymmetrical four-vortex system was chosen to correspond to the axial extent of the symmetrical four-vortex system to allow for better comparison between the two cases.

In this study three-dimensional simulations are used to validate the transient growth analysis by seeding the three-dimensional flow with the optimal disturbance fields predicted by the transient growth analysis. In addition, the three-dimensional simulations will importantly be used to study the non-linear evolution characteristics of the disturbance fields.

2.6 Grid independence

A grid resolution study was undertaken to quantify the error in the simulations. This grid resolution study was conducted by examining the solution dependance on polynomial order, p_n, and the number of Fourier planes, p_f, independently. The symmetric four-vortex 'high tail' case was selected for the grid independence study as it was the most complex case investigated and likely to have the largest errors. $Re = 20\,000$ was selected as it is the highest Reynolds number used during the study. The specific definition of the variables in the symmetric four-vortex 'high tail' case are defined in table 2.1.

2.6.1 Element size

While it is tempting to suppose that a small number of very high-order elements could be employed to discretize the flow in the refined region of the mesh, in practice it is found that elements need to be modestly sized in relation to the larger-scale flow structures. Within the vicinity of the vortices, the elements have an maximum aspect ratio of approximately 1.675, with a reduction in size towards the centre of the refined

TABLE 2.2: Table of polynomial order p_n against ϵ_{L2} at $t/T_0 = 3$ to approximate the error in the simulations.

p_n	ϵ_{L2}
5	0.00040143
6	0.000144981
7	6.69167E-05
8	3.61214E-05
9	2.24026E-05
10	1.44944E-05
11	9.58284E-06
12	6.28801E-06
13	3.9665E-06
14	2.3571E-06
15	1.25617E-06
16	5.40948E-07
17	1.20547E-07
18	7.48872E-08
19	1.01157E-07

region where the vortices are located. The largest of the mesh elements are the extreme corners of the refined region with the elements in the central area of the refined region being 40% of the size of the largest elements. The width of the smallest elements, w, is defined by $w/b_1 = 0.08$.

In the refined region of the mesh, the elements within the vicinity of the vortices are of a width such that $w/a_1 = 0.4539$ for the wing vortices and $w/a_2 = 0.9091$ for the tail vortices. The ratio of element size to vortex core radius is also consistent with previous computational work by So *et al.* (2007); Boustead *et al.* (2010); So *et al.* (2011).

2.6.2 Polynomial order

In order to quantify the uncertainty due to finite resolution in the x-y plane of the simulations, errors were approximated by taking the energy in the fundamental mode (L_2) with a polynomial order $p_n = 20$ as a reference value for estimating the error in the lower resolution cases. The percentage change of the lower polynomial cases compared to the reference case is defined as $\epsilon_{L2} = 100 \times |E(p_n) - E(p_n = 20)|/E(p_n = 20)$. From table 2.2 and figure 2.8, a polynomial order $p_n = 13$ was selected as it was deemed to provide a suitable balance between error ($\epsilon_{L2} = 3.9665 \times 10^{-4}\%$) and compute time, and was therefore selected for the computations reported hereafter.

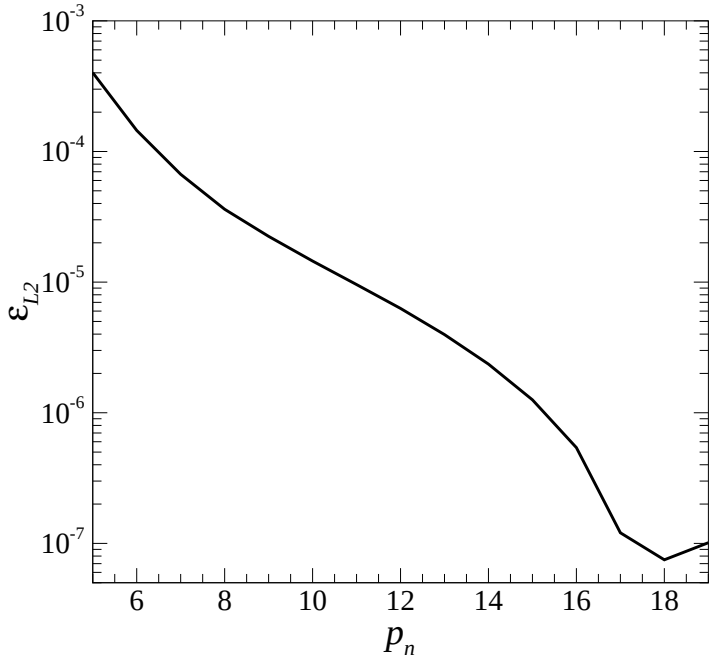

FIGURE 2.8: Plot of polynomial order p_n against ϵ_{L2} at $t/T_0 = 3$ for the symmetric 'high tail' case to approximate the error in the simulations.

TABLE 2.3: Table of polynomial order p_n against ϵ_σ at $t/T_0 = 3$ to approximate the error in the simulations.

p_n	ϵ_σ
5	0.149313368
6	0.323827901
7	0.074653213
8	0.035087382
9	0.005345918
10	0.011019582
11	0.000635867
12	0.002074199
13	0.000438485
14	0.000629367
15	5.00581E-05
16	5.46354E-05
17	3.57246E-05
18	6.93442E-06
19	8.00044E-06

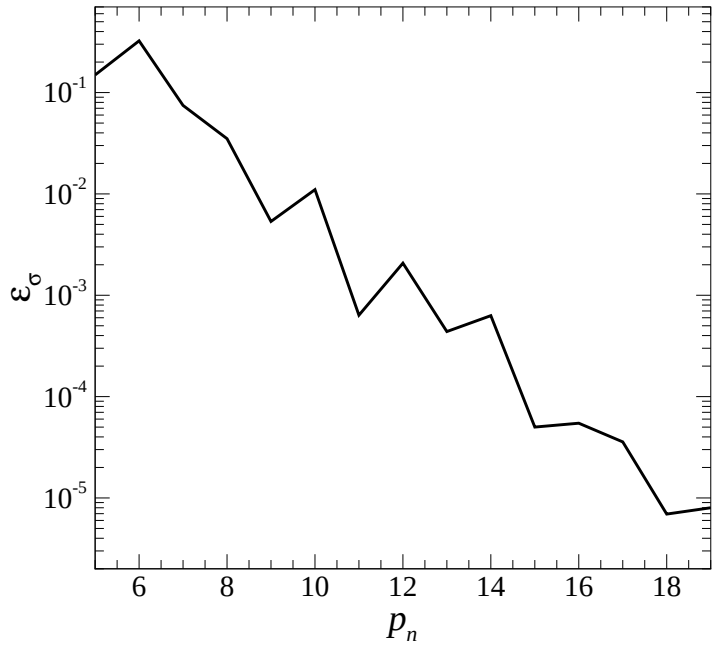

FIGURE 2.9: Plot of polynomial order p_n against ϵ_σ at $t/T_0 = 3$ for the symmetric 'high tail' case to approximate the error in the simulations.

To ensure that the error is within acceptable levels, the strain at the centre of the wing vortex was examined at $t/T_0 = 3$. As with the energy in the fundamental mode, the strain was computed for an increasing polynomial order, p_n. The highest polynomial order case, $p_n = 20$, was used as a reference for the error of the lower polynomial cases as a percentage, $\epsilon_\sigma = 100 \times |\sigma(p_n) - \sigma(p_n = 20)|/\sigma(p_n = 20)$. As the strain rate is the addition of two derivatives, this variable should produce the largest error and therefore be a good indicator as to the error in the simulation. As table 2.3 and figure 2.9 displays polynomial order $p_n = 13$ was deemed to give a good balance between computation time and error ($\epsilon_\sigma = 0.0438485\%$).

Since the vorticity is defined as the subtraction of two derivatives, it should also provide a good estimate of error in the simulation and was computed (by using $\epsilon_\omega = 100 \times |\omega(p_n) - \omega(p_n = 20)|/\omega(p_n = 20)$, similar to ϵ_σ above) to estimate the error as shown in table 2.4. The flow was evolved to $t/T_0 = 3$ to ensure sufficient time to allow the error to grow. As table 2.4 shows, the error for $p_n = 13$ is particularly small ($\epsilon_\omega = 2.172 \times 10^{-4}\%$) and so this polynomial order was deemed to provide a good balance between error and computation time.

TABLE 2.4: Table of polynomial order p_n against ϵ_ω at $t/T_0 = 3$ to approximate the error in the simulations.

p_n	ϵ_ω
5	0.000745492
6	0.000545423
7	5.32267E-05
8	3.18138E-05
9	2.1304E-05
10	3.18136E-06
11	5.59518E-06
12	4.46277E-06
13	2.17182E-06
14	1.55277E-06
15	1.21961E-06
16	1.27877E-06
17	1.50574E-08
18	7.37179E-09
19	1.39574E-09

TABLE 2.5: Table of number of fourier modes, p_f against the sum of the perturbation energy across all of the Fourier modes normalised by the highest resolution case, $E(p_f)/E(p_f = 20)$.

p_f	$E(p_f)/E(p_f = 20)$
4	0.065667992
8	0.098349501
12	0.001405918
16	4.89256E-05

2.6.3 Fourier modes

In order to quantify the uncertainty due to finite resolution in the Fourier expansion (z plane), errors were approximated by examining the sum of the energy in the Fourier modes after the flow has begun to evolve and normalising by a case with 20 Fourier modes, $p_f = 20$. The symmetric four-vortex 'high tail' case (defined in § 2.1) seeded with the optimal perturbation was used at $Re = 20\,000$ as it was deemed to be the most complex case and the highest Reynolds number used throughout this study. The axial domain was chosen to correspond to one wavelength of the [-1,1,1] mode present and the perturbation was seeded in only the leading Fourier mode. This allows for smaller, higher frequency perturbations to be captured with a minimum of computational memory resources. The energy in the optimal perturbation used was 0.01522%

TABLE 2.6: Table of number of fourier modes, p_f against the perturbation energy in the second Fourier mode normalised by the highest resolution case, $E(p_f)/E(p_f = 20)$.

p_f	$E(p_f)/E(p_f = 20)$
4	0.281088271
8	0.087784609
12	0.01596279
16	0.006604896

of the initial energy in the base flow. Throughout these studies, both the optimal and white noise perturbations used had similar (within half and order of magnitude) energy. The seeding with the optimal perturbation was used as it allowed immediate growth of the perturbation in the linear regime. The time selected was $t/T_0 = 0.2$ as this time is well into the linear regime where the instability has had time to grow to a significant magnitude. The maximum number of Fourier modes, $p_f = 20$ was used as the reference as it is the largest number of Fourier modes possible with the computational resources available.

Sixteen Fourier modes was selected as it was deemed to provide a suitable balance between error (0.00489% for the case of the sum of the Fourier modes and 0.66% for the second Fourier mode) and finite available computational resources and computation time (table 2.5 and 2.6).

2.6.4 Timestepping

Given the third-order time accuracy of the scheme, the timestep required for stable evolution of the flow ($\delta t = 0.00005T_0$) provided negligible time integration errors. A study was conducted and found that a decrease in the timestep by a factor of 10 only produced a difference in the strain rate of 0.0612%. It is of importance to note that as the flow structures become smaller, the required timestep also needs to decrease due to a stability restriction inherent in the spectral element method (along with other discretization methods). This is known as the Courant–Friedrichs-Lewy condition and is a necessary condition for the convergence of the solution of partial differential equations (Courant *et al.* 1928). The general form of the Courant–Friedrichs-Lewy condition in n-dimensional space for a first order partial differential equation is,

$$\Delta t \sum_{i=1}^{n} \frac{u_{x_i}}{\Delta x_i} \leq C \tag{2.16}$$

where x_i is a spatial variable of dimension, i, where i is an integer from $i = 1$ to n. For a general case, C is a constant that is dependant on the partial differential equation that is being solved. It is important to note that the Courant–Friedrichs-Lewy condition is a necessary condition, but may not be sufficient for convergence of a particular set of partial differential equations.

If the timestep is held constant for many of the three-dimensional computations reported in this thesis, the simulation will eventually diverge and terminate as the flow structures become smaller. This does not invalidate the evolution prior to the divergence. If the timestep is progressively decreased, the smallest flow structures could be evolved, but this leads to prohibitively long simulations and is only required if long term non-linear growth is to be considered. As most of this thesis is only concerned with the linear and early non-linear growth of instabilities in the flows, an eventual divergence of the flow is considered acceptable as the data before the divergence is valid.

2.7 Vortex filament analysis method

By using a vortex filament method, a theoretical, inviscid value of peak axial wavenumber can be found to compare to the peak value of axial wavenumber found with the transient growth method described later in this chapter. This section describes the development of the governing equations for the vortex filament method and equations for the motion of the unperturbed vortex cores used to determine the theoretical peak axial wavenumber. This method is solved by utilising a MATLAB code separately to the spectral-element solver described earlier in this chapter.

2.7.1 Governing equations

Consider several vortex filaments, each of different circulation strength. The velocity at any point in the flow field may be determined from the Biot–Savart formula (Moore & Saffman 1972). The Biot–Savart formula can be used to determine the velocity components at the vortex filament locations by writing

$$\mathbf{U}_n = \sum_{m=1}^{M} \frac{\Gamma_m}{4\pi} \oint \frac{\mathbf{R}_{mn} \times \mathbf{dL}_m}{|\mathbf{R}_{mn}|^3}, \tag{2.17}$$

where $\mathbf{U}_n$ is the velocity at some position along the n^{th} vortex filament, Γ_m is the circulation of the m^{th} vortex filament, $\mathbf{R}_{mn}$ is a vector describing the distance from

the vortex filament n to the vortex filament m, and $\mathbf{dL}_m$ is an incremental distance along the vortex filament m. Note that equation 2.17 allows for M vortex filaments to interact and as such, is a generalisation of previous models (for example Crow 1970; Crouch 1997; Fabre & Jacquin 2000).

The distance between two vortex filaments is defined as,

$$\mathbf{R}_{mn} = x_{mn}\mathbf{i} + y_{mn}\,\mathbf{j} + z_{mn}\mathbf{k} + (\mathbf{P}'_m - \mathbf{P}_n)., \tag{2.18}$$

where

$$x_{mn} = x_m - x_n, \tag{2.19a}$$

$$y_{mn} = y_m - y_n, \tag{2.19b}$$

$$z_{mn} = z'_m - z_n. \tag{2.19c}$$

Here, x_n, y_n and z_n describe the unperturbed x, y and z position of the n^{th} vortex filament, and $\mathbf{P}_n$ describes the perturbation vector acting on the n^{th} vortex filament. Where $m = n$, the primes are used to distinguish different locations along the vortex filament. The perturbation vector has components in the x–y plane and denotes the filament position relative to its unperturbed position, it may be written as,

$$\mathbf{P} = P_x(z,t)\mathbf{i} + P_y(z,t)\mathbf{j}, \tag{2.20}$$

where P_x and P_y are the x and y components of the perturbation respectively.

An infinitesimally long segment of the vortex filament m may be defined as

$$\mathbf{dL}_m = \left(\frac{\partial \mathbf{P}_m}{\partial z_m} + \mathbf{k}\right) \mathrm{d}z_m. \tag{2.21}$$

In order to close the governing mathematical model, the vortex transport theorem can be used, which states that an element of vorticity will move with the local velocity. This implies that both the unperturbed vortex and the perturbation will move as a result of the local velocity.

For a position vector, $\mathbf{R}_n$, describing the position of the n^{th} vortex filament with respect to the origin, the time evolution of this vector is described by,

$$\frac{\partial \mathbf{R}_n}{\partial t} = (U_n + u_n)\,\mathbf{i} + (V_n + v_n)\,\mathbf{j} - w_n \left(\frac{\partial \mathbf{P}_n}{\partial z_n}\right), \tag{2.22}$$

where U_n and V_n are the x and y components of the velocity due to the unperturbed vortex filaments surrounding the n^{th} vortex; and u_n, v_n and w_n are the components of the perturbation velocity. The position vector $\mathbf{R}_n$ may be written as

$$\mathbf{R}_n = \mathbf{R}_{n0} + \mathbf{P}_n, \tag{2.23}$$

where $\mathbf{R}_{n0}$ is the position of the unperturbed vortex filament n from the origin. From this definition it may be written as,

$$\frac{\partial \mathbf{R}_n}{\partial t} = \frac{\partial \mathbf{R}_{n0}}{\partial t} + \frac{\partial \mathbf{P}_n}{\partial t}, \tag{2.24a}$$

$$\frac{\partial \mathbf{R}_{n0}}{\partial t} = U_n \mathbf{i} + V_n \mathbf{j}, \tag{2.24b}$$

$$\frac{\partial \mathbf{P}_n}{\partial t} = u_n \mathbf{i} + v_n \mathbf{j} - w_n \left(\frac{\partial \mathbf{P}_n}{\partial z_n} \right). \tag{2.24c}$$

Equation 2.24c governs the growth of the vortex perturbations on the n^{th} vortex. The velocity components for the n^{th} vortex are obtained by substituting equations 2.18 and 2.20 into equation 2.17. Following Crow (1970), Crouch (1997) and Bristol *et al.* (2004), equation 2.17 can be linearised by taking a Taylor series expansion of equation 2.18 about the unperturbed vortex filament position. Note that the term $\partial \mathbf{P}_n / \partial z_n$ in equation 2.24c is typically much smaller than the other terms in the equation, and may be ignored to a first-order approximation.

Therefore, there are two linearised equations describing the motion of the unperturbed vortex filaments in the x–y plane

$$U_n = \sum_{m=1}^{M} \frac{\Gamma_m}{4\pi} \int_{-\infty}^{\infty} \frac{y_{mn}}{\left[x_{mn}^2 + y_{mn}^2 + z_{mn}^2\right]^{3/2}} \, \mathrm{d}z_{mn}, \tag{2.25a}$$

$$V_n = \sum_{m=1}^{M} \frac{\Gamma_m}{4\pi} \int_{-\infty}^{\infty} \frac{-x_{mn}}{\left[x_{mn}^2 + y_{mn}^2 + z_{mn}^2\right]^{3/2}} \, \mathrm{d}z_{mn}. \tag{2.25b}$$

Following Crouch (1997), the solution of these equations allows the stability of the system to be determined through the use of a Floquet stability analysis. Details of this analysis technique are presented in chapters 4 and 5.

There is also two linear equations describing the perturbation velocity acting on the n^{th} vortex filament,

$$u_n = \sum_{m=1}^{M} \frac{\Gamma_m}{4\pi} \left[\int_{-\infty}^{\infty} \frac{(P'_{ym} - P_{yn}) - z_{mn}\dfrac{\partial P'_{ym}}{\partial z'_m}}{[x_{mn}^2 + y_{mn}^2 + z_{mn}^2]^{3/2}} \,\mathrm{d}z_{mn} - \int_{-\infty}^{\infty} \frac{3y_{mn}x_{mn}(P'_{xm} - P_{xn})}{[x_{mn}^2 + y_{mn}^2 + z_{mn}^2]^{5/2}} \,\mathrm{d}z_{mn} - \int_{-\infty}^{\infty} \frac{3y_{mn}^2(P'_{ym} - P_{yn})}{[x_{mn}^2 + y_{mn}^2 + z_{mn}^2]^{5/2}} \,\mathrm{d}z_{mn} \right], \tag{2.26a}$$

$$v_n = \sum_{m=1}^{M} \frac{\Gamma_m}{4\pi} \left[\int_{-\infty}^{\infty} \frac{z_{mn}\dfrac{\partial P'_{xm}}{\partial z'_m} - (P'_{xm} - P_{xn})}{[x_{mn}^2 + y_{mn}^2 + z_{mn}^2]^{3/2}} \,\mathrm{d}z_{mn} + \int_{-\infty}^{\infty} \frac{3x_{mn}^2(P'_{xm} - P_{xn})}{[x_{mn}^2 + y_{mn}^2 + z_{mn}^2]^{5/2}} \,\mathrm{d}z_{mn} + \int_{-\infty}^{\infty} \frac{3y_{mn}x_{mn}(P'_{ym} - P_{yn})}{[x_{mn}^2 + y_{mn}^2 + z_{mn}^2]^{5/2}} \,\mathrm{d}z_{mn} \right]. \tag{2.26b}$$

The definitions for u_n and v_n can be substituted into equation 2.24c to develop a linear differential equation governing the growth of the perturbation,

$$\begin{aligned} \frac{\partial \mathbf{P}_n}{\partial t} = {} & \sum_{m=1}^{M} \frac{\Gamma_m}{4\pi} \left[\int_{-\infty}^{\infty} \frac{(P'_{ym} - P_{yn}) - z_{mn}\dfrac{\partial P'_{ym}}{\partial z'_m}}{[x_{mn}^2 + y_{mn}^2 + z_{mn}^2]^{3/2}} \,\mathrm{d}z_{mn} - \int_{-\infty}^{\infty} \frac{3y_{mn}x_{mn}(P'_{xm} - P_{xn})}{[x_{mn}^2 + y_{mn}^2 + z_{mn}^2]^{5/2}} \,\mathrm{d}z_{mn} - \int_{-\infty}^{\infty} \frac{3y_{mn}^2(P'_{ym} - P_{yn})}{[x_{mn}^2 + y_{mn}^2 + z_{mn}^2]^{5/2}} \,\mathrm{d}z_{mn} \right] \mathbf{i} \\ & + \sum_{m=1}^{M} \frac{\Gamma_m}{4\pi} \left[\int_{-\infty}^{\infty} \frac{z_{mn}\dfrac{\partial P'_{xm}}{\partial z'_m} - (P'_{xm} - P_{xn})}{[x_{mn}^2 + y_{mn}^2 + z_{mn}^2]^{3/2}} \,\mathrm{d}z_{mn} + \int_{-\infty}^{\infty} \frac{3x_{mn}^2(P'_{xm} - P_{xn})}{[x_{mn}^2 + y_{mn}^2 + z_{mn}^2]^{5/2}} \,\mathrm{d}z_{mn} + \int_{-\infty}^{\infty} \frac{3y_{mn}x_{mn}(P'_{ym} - P_{yn})}{[x_{mn}^2 + y_{mn}^2 + z_{mn}^2]^{5/2}} \,\mathrm{d}z_{mn} \right] \mathbf{j}. \end{aligned} \tag{2.27}$$

Inspection of equation 2.27 indicates that where $m = n$, a pole exists in each of the integrands as $z_{mn} \to 0$. Crow (1970) overcame this problem of the existence of the pole by using the cutoff method. Widnall *et al.* (1974) showed that this led to spurious results at high wavenumbers. Instead this problem can be avoided by following Saffman (1992) by replacing this term with a numerically calculated estimate of the self induction term for a Rankine filament. This technique is exactly the same as that used by Bristol

et al. (2004). The self induction of each vortex core was calculated through solution of the dispersion equations provided by Saffman (1992).

2.7.2 Linear analysis

General solutions to the linearised governing equation (equation 2.27) are assumed to have the form

$$\mathbf{P}_n = \widehat{P_x} e^{ikz_n}\mathbf{i} + \widehat{P_y} e^{ikz_n}\mathbf{j}, \tag{2.28}$$

where $\widehat{P}_x$ and $\widehat{P}_y$ represent the component perturbation amplitudes, acting on the n^{th} vortex filament, in the x and y directions respectively (note that the analysis in § 2.7.1 allows us to preclude perturbation growth in the z direction). Equation 2.28 can be substituted into equation 2.27 and the integral terms can be analytically solved. Details of this technique may be found in Crow (1970).

In order to non-dimensionalize the governing equations, several definitions are required. First, every filament has an associated circulation, which may be normalised by the maximum filament circulation in the system,

$$\Gamma_m = \Lambda_m \Gamma_{max}. \tag{2.29}$$

Here, Λ_m is the ratio of the circulation of the m^{th} filament with the maximum filament circulation in the system.

The distance between the two furthest vortex cores in the cluster is defined as b. The distance between any two vortices within the cluster may be written as b_{mn} (here, m represents the m^{th} filament and n represents the n^{th} filament). Therefore

$$b_{mn}^2 = (x_{mn})^2 + (y_{mn})^2, \tag{2.30a}$$

$$\gamma_{mn}^2 = b_{mn}^2 / b^2. \tag{2.30b}$$

Additional normalisations are introduced,

$$\chi_{mn} = \frac{x_{mn}}{b}, \quad \mu_{mn} = \frac{y_{mn}}{b}, \quad \xi_{mn} = \frac{z_{mn}}{b}, \tag{2.31}$$

$$\beta = kb. \tag{2.32}$$

All terms can be temporally non-dimensionalised to form

$$t = t^* \tau, \tag{2.33}$$

where τ is dimensionless and t^* is defined as

$$t^* = \frac{2\pi b^2}{\Gamma_{max}}. \tag{2.34}$$

$$\begin{aligned}\frac{d}{d\tau}\left(\widehat{P_{xn}}\right) &= \Lambda_n \varpi_n \widehat{P_{yn}} \\ &+ \textstyle\sum_{m=1,m\neq n}^{M} \frac{\Lambda_m}{\rho_{mn}^2}\Big[\sin(2\theta_{mn})\widehat{P_{xn}} \\ &- \cos(2\theta_{mn})\widehat{P_{yn}} - \varrho_{mn}\widehat{P_{xm}} + \psi_{mn}\widehat{P_{ym}}\Big],\end{aligned} \tag{2.35a}$$

$$\begin{aligned}\frac{d}{d\tau}\left(\widehat{P_{yn}}\right) &= -\Lambda_n \varpi_n \widehat{P_{xn}} \\ &+ \textstyle\sum_{m=1,m\neq n}^{M} \frac{\Lambda_m}{\rho_{mn}^2}\Big[-\cos(2\theta_{mn})\widehat{P_{xn}} \\ &- \sin(2\theta_{mn})\widehat{P_{yn}} + \chi_{mn}\widehat{P_{xm}} + \varrho_{mn}\widehat{P_{ym}}\Big],\end{aligned} \tag{2.35b}$$

where ρ_{mn} is the non-dimensional distance between the vortices n and m, θ_{mn} is the angle of the vortex n relative to m, and

$$\begin{aligned}&\psi_{mn} = \beta^2\rho_{mn}^2 K[0,\beta\rho_{mn}] + \beta K[1,\beta\rho_{mn}] - \sin^2(\theta_{mn})\cdot\beta^2 K[2,\beta\rho_{mn}],\\ &\chi_{mn} = \cos^2(\theta_{mn})\beta^2 K[2,\beta\rho_{mn}] - \beta^2\rho_{mn}^2 K[0,\beta\rho_{mn}] - \beta K[1,\beta\rho_{mn}],\\ &\varrho_{mn} = \cos(\theta_{mn})\sin(\theta_{mn})\beta^2 K[2,\beta\rho_{mn}],\\ &\varpi_n(k) = \frac{b^2}{a_i^2}\left(\frac{2k}{\sqrt{k^2+\kappa_n^2}} - 1\right),\end{aligned} \tag{2.36}$$

where κ_n is the **n**th root from the dispersion relation defined as:

$$\frac{1}{\beta a}\frac{J_m'(\beta a)}{J_m(\beta a)} = -\frac{K_m'(ka)}{kaK_m(ka)} - \frac{sm\sqrt{\beta^2+k^2}}{ka^2\beta^2} \tag{2.37}$$

where $s = \pm 1$ (Saffman 1992, page 232, equation 6). It is important to note that the dispersion relation in Saffman (1992) is for a Rankine vortex. As the profile used throughout this thesis elsewhere is that of a Gaussian profile, it will introduce error into the peak axial wavenumber found through this method. As this method is a first approximation, it is considered an acceptable simplification.

2.7.3 Vortex filament transient growth analysis

The filament method described above may be written in the general form,

$$d/d\tau P = [A][P]. \tag{2.38}$$

This equation, coupled with a time marching technique, may be used to evolve the perturbation forward in time. This thesis employs a fourth order Runge–Kutta technique to evaluate the time evolution matrix **A** from equation 2.7.3 such that we may write

$$P_{\tau_n} = [A]P_{t_0} \tag{2.39}$$

Following the transient growth analysis theory, the transient growth amplification factor may then be assessed through the definition that $G(\tau)$ is the maximum eigenvalue of $[A][A]*$, where $[A]*$ is the adjoint evolution operator.

The Runge–Kutta technique employed a timestep of $0.01 \times T_{2V}$, and the evaluation of the transient growth amplification factor occurred at an integer number of base vortex revolution, i.e. $n \times T_{2V}$.

2.7.4 Motion of unperturbed vortex cores

Calculating the motion of the unperturbed vortex cores requires the solution of equations 2.25a and 2.25b. The integral terms in each of these equations may be determined analytically, and these equations may be written in non-dimensional form as,

$$U_n^* = \frac{\mathrm{d}\chi_n}{\mathrm{d}\tau} = \sum_{m=1}^{M} \Lambda_m \frac{\mu_{mn}}{\chi_{mn}^2 + \mu_{mn}^2}, \tag{2.40a}$$

and

$$V_n^* = \frac{\mathrm{d}\mu_n}{\mathrm{d}\tau} = \sum_{m=1}^{M} \Lambda_m \frac{-\chi_{mn}}{\chi_{mn}^2 + \mu_{mn}^2}, \tag{2.40b}$$

where

$$U_n^* = U_n \frac{2\pi b}{\Gamma_{max}}, \tag{2.41}$$

$$V_n^* = V_n \frac{2\pi b}{\Gamma_{max}}. \tag{2.42}$$

$$\tag{2.43}$$

Chapter 3

Results: Kinematics and stability of an equal strength counter-rotating two-vortex system model

This chapter reports on the study of a two-vortex counter-rotating aircraft wake model with symmetrical strength about the $x = 0$ plane. This model is indicative of the vortices shed from the wings of a large commercial aircraft in the far wake. This type of aircraft wake model has been commonly used in the past to study the dynamics of the far wake. For this chapter, the time interval that a perturbation is allowed to grow in the transient growth analysis, $\bar{\tau}$, is normalised by the time scale $T_{2V} = 2\pi b^2/\Gamma$, giving the normalised time $\tau = \bar{\tau}/T_{2V}$ (as defined in chapter 2, § 2.2). As a first order approximation, the vortex cores will expand throughout the evolution in the fluid according to the relationship, $a_{tv}(t) = \sqrt{a_1^2 + 4\upsilon t}$ (Schaeffer & Le Dizès 2010).

3.1 Context for transient growth analysis

Previous studies have investigated the linear response of global instability mechanisms in counter-rotating two-vortex systems (Le Dizès & Laporte 2002; Donnadieu *et al.* 2009). They found that for the elliptic instability, the first two branches of the instability (as denoted by the last number in the mode label) correspond to a non-dimensional axial wavenumber of $k\,a_1 = 2.26$ for the Kelvin mode [-1,1,1] and $k\,a_1 = 3.96$ for the mode [-1,1,2]. For reference, the shapes of these first two modes are shown in figure 3.1. The first branch, mode [-1,1,1], is defined as having a single pair of opposite-sign vorticity lobes within the vortex core and a pair of lobes of opposing sign vorticity outside

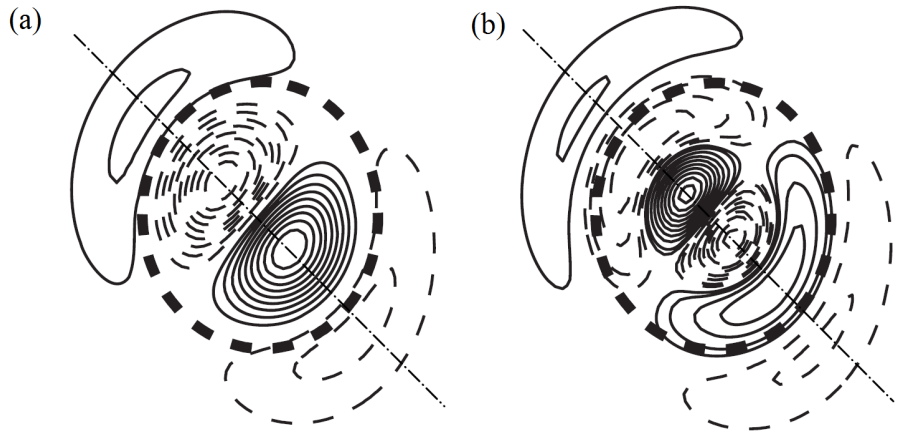

FIGURE 3.1: A reproduction of figure 4 from Donnadieu *et al.* (2009) displaying the elliptic instability mode shapes of (a) the [-1,1,1] mode and (b) the [-1,1,2] mode. Each image is the perturbation within the left vortex. These perturbation fields display reflective symmetry about the $x = 0$ plane. The dash-dot line has been added to illustrate the line that the cores of the vorticity lobes lie on. Reproduced with the permission from the American Institute of Physics, who retain the copyright.

the vortex core such that the central points of the vorticity lobes all lie on a straight line (dashed-dot line in figure 3.1(a)). The second branch, mode [-1,1,2], is defined as having two pairs of opposite-sign vorticity lobes within the vortex core and a third pair of opposing sign vorticity lobes outside of the vortex core, where the central point of all of the lobes lie on a straight line (dashed-dot line in figure 3.1(b)). Inviscid theory predicts that the growth of both modes will be the same (Le Dizès & Laporte 2002), but as the second mode is structurally more complex, it is affected by viscosity to a larger degree and therefore has a lower growth amplification factor as shown in the next section.

3.2 Transient growth analysis

In this section, the response of the counter-rotating vortex pair to a number of transient perturbations, and the linearised transient growth of the perturbations, is studied at a range of axial wavenumbers. Figure 3.2 displays the results of a transient growth analysis of the two-vortex system for $\tau = 5.35, 3.56, 2.67$ and 1.78. The dashed and dash-dot lines correspond to the peak axial wavenumbers, $k\,a_1 = 2.26$ and 3.96, for the [-1,1,1] and [-1,1,2] global instability modes respectively, from inviscid theory (Le Dizès & Laporte 2002). The transient growth analysis reveals that peak energy amplification occurs at $k\,a_1 = 2.12$ with a secondary peak at $k\,a_1 = 3.7$. These peaks occur at an

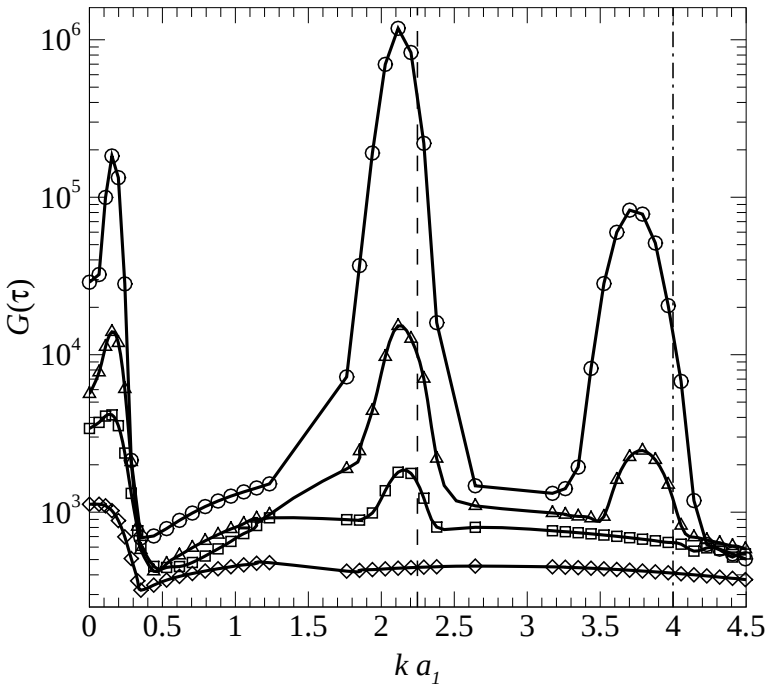

FIGURE 3.2: Transient growth amplification factor $G(\tau)$ plotted against axial wavenumber $k\,a_1$ computed for $Re = 20\,000$. $\diamond, \square, \Delta$ and $\circ$ represent $\tau = 1.78, 2.67, 3.56$ and 5.35 respectively. The dashed and dash-dot lines show respectively, the peak wavenumbers for the [-1,1,1] and [-1,1,2] global instability modes from inviscid theory (Le Dizès & Laporte 2002).

axial wavenumber which is consistent with the instability modes [-1,1,1] and [-1,1,2] found in previous studies (Donnadieu *et al.* 2009). It is interesting to note that for $\tau = 1.78$, no obvious mode peaks are present, leading to an approximately constant growth amplification factor. The instability mode [-1,1,1] becomes apparent at $\tau = 2.67$ with an axial wavenumber of $k\,a_1 = 2.12$, but the secondary mode [-1,1,2] is not present at this value of τ. The secondary mode [-1,1,2] is first observed at $\tau = 3.56$ with an axial wavenumber of $k\,a_1 = 3.7$. Both peaks grow significantly as τ is increased. These results strongly imply that the modes [-1,1,1] and [-1,1,2] both have characteristic timeframes that are required before the modes can form.

The peaks in energy amplification in the vicinity of the [-1,1,1] and [-1,1,2] modes shift to slightly lower $k\,a_1$ values as τ increases. The most likely reason for this occurring is as a result of the enlargement of the vortices over time due to the viscous diffusion via $a_{tv}(t) = \sqrt{a_1^2 + 4\nu t}$.

It is of interest that the peak found for the transient growth analysis that corresponds to the Crow instability, $k\,a_1 = 0.154$, corresponds relatively well to previous

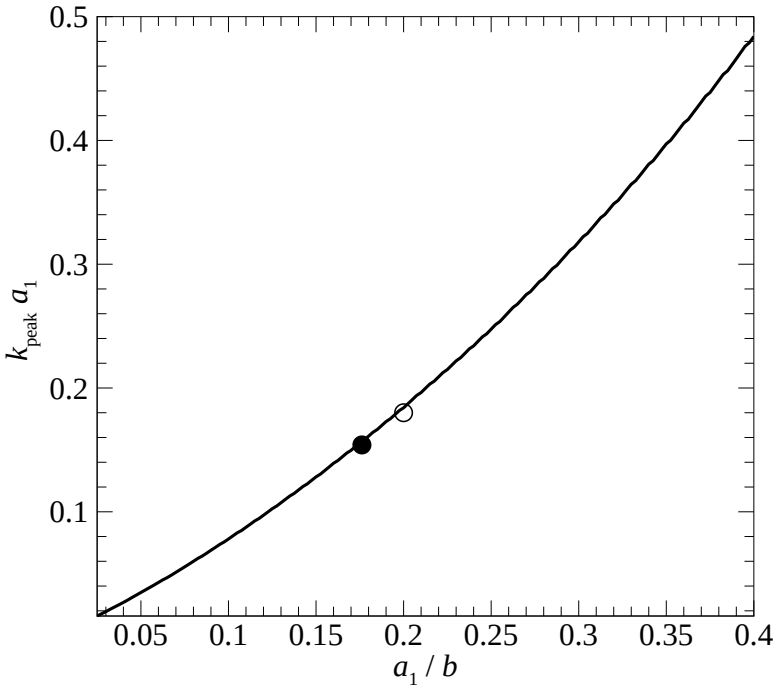

FIGURE 3.3: Theoretical asymptotic peak axial wavenumber, $k_{peak}\, a_1$, plotted against vortex core to separation ratio, a_1/b (solid line). The solid dot represents the separation ratio and peak axial wavenumber found from the transient growth analysis in this study ($a_1/b = 0.176$ and $k\, a_1 = 0.154$) and the open dot represents the separation ratio and peak axial wavenumber found by Brion *et al.* (2007) ($a/b = 0.2$ and $k\, a_1 = 0.18$).

studies that have investigated this. Brion *et al.* (2007) found a peak in growth rate for the Crow instability at around $k\, a = 0.18$, which, given that they used a slightly different ratio of core size to separation ($a/b = 0.2$ for Brion *et al.* (2007) compared to $a_1/b = 0.1762$ in this study), this small difference is not surprising. Furthermore, the growth amplification factor predicted in the waveband of the Crow instability is extremely large ($G(\tau) \approx 1.82 \times 10^5$ for $\tau = 5.35$), and is within an order of magnitude of the growth amplification factor for the mode [-1,1,1] elliptic instability. What is of interest is that axial wavenumber, where the peak in the growth amplification factor occurs for the Crow instability, does not change significantly for the values of τ investigated here.

An asymptotic vortex filament method was employed to investigate the predicted theoretical maximum for the peak axial wavenumber of the Crow instability. This technique is the same as that described by Crow (1970). The self-induction of each vortex was calculated through the solution of the dispersion equations described by

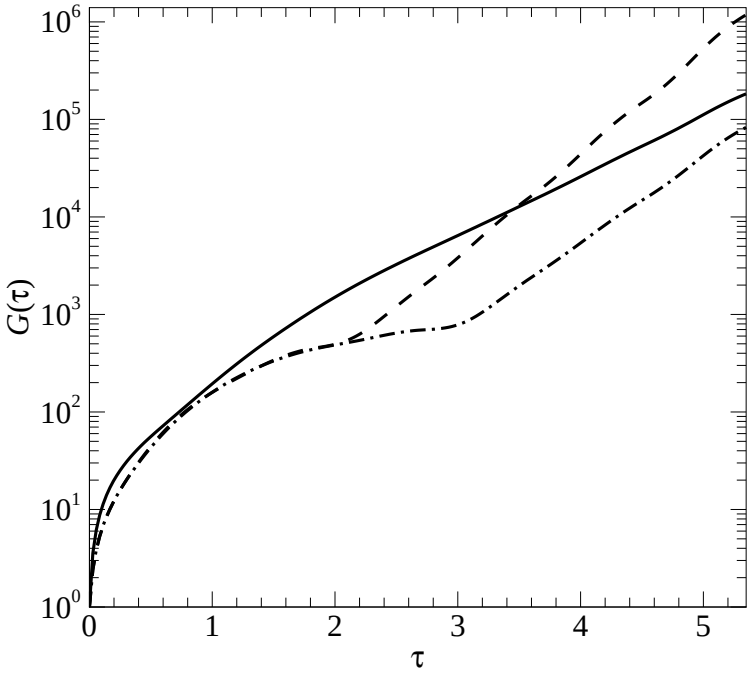

FIGURE 3.4: Transient growth amplification factor $G(\tau)$ plotted against τ computed for $Re = 20\,000$. The dashed, dash-dot and solid lines represent axial wavenumbers $k\,a_1 = 2.12, 3.7$ and 0.176 respectively. These axial wavenumbers correspond to the mode [-1,1,1] and [-1,1,2] of the elliptic instability and the Crow instability respectively.

Saffman (1992). The asymptotic vortex filament method assumes that perturbations take the form of sinuous oscillations along the axis of each vortex. The model can be reduced to an eigenvalue problem, where the eigenvalues represent the global growth rate, and the eigenvectors represent the mode shape components. Figure 3.3 shows the results of an asymptotic filament study conducted to examine the change in peak axial wavenumber, $k\,a_1$, for the Crow instability against change in vortex separation ratio, a_1/b. It shows that the peak axial wavenumber found in the transient growth analysis (shown in figure 3.2) for the Crow instability ($k\,a_1 = 0.154$) and the previous work done by Brion *et al.* (2007) both correspond well to the theoretical predictions for the peak axial wavenumber from the vortex filament study for the separation ratios used.

The functional variation of $G(\tau)$ with τ at specific axial wavenumbers will now be considered. Figure 3.4 displays a plot of growth amplification factor, $G(\tau)$, against τ. For smaller values of τ, both elliptic instability modes investigated here follow the same trend until $\tau = 2.10$, where the mode [-1,1,1] becomes asymptotic from this point and gains a constant growth rate. By contrast, the mode [-1,1,2] continues for longer on the

original trend until $\tau = 3$, at which time it also becomes asymptotic with a constant growth rate. This reinforces the observation that both the elliptic modes [-1,1,1] and [-1,1,2] have characteristic timeframes that are required before the instability modes form and the instability reaches asymptotic growth. In addition to this, the energy required for the [-1,1,2] mode to enter the linear growth regime requires a larger energy than the mode [-1,1,1]. This demonstrates that the mode [-1,1,1] instability will form in preference to the mode [-1,1,2], as it requires less energy to reach the linear growth regime. This is also supported by the asymptotic analyses that also show that the [-1,1,1] mode has a larger asymptotic linear growth rate compared to the mode [-1,1,2].

It is of interest to note that the trend for the Crow instability follows a similar pattern to the mode [-1,1,1] and [-1,1,2] elliptic instability, except that it enters a broadly linear regime at a significantly smaller value of τ. The Crow instability does appear to have three separate regions of linear increase in growth amplification factor. The first region begins from $\tau = 0$ and finishes at $\tau < 0.25$ and has a growth rate of $\sigma_{GR} = 5.20$. The second region begins at $\tau = 0.25$ and ends at $\tau = 1.91$ and has a growth rate of $\sigma_{GR} = 1.01$. For $\tau > 1.91$, the Crow instability appears to enter a third region of linear increase of growth amplification factor with a growth rate of $\sigma_{GR} = 0.625$. Another item of interest is that, for $\tau \leq 3.47$, the Crow instability exhibits larger growth amplification factor than both the mode [-1,1,1] and [-1,1,2] elliptic instabilities. This demonstrates that the growth of the Crow instability is more susceptible to the effects of transient growth of perturbations than both of the elliptic instabilities studied here, strongly implying that over short periods of time, the Crow instability will exhibit larger instability growth.

Figure 3.5 displays the optimal perturbation vorticity mode shape found from the transient growth analysis computed at $Re = 20\,000$ for an axial wavenumber of $k\,a_1 = 2.12$, corresponding to the mode [-1,1,1] elliptic instability for (a) $\tau = 1.78$ and (b) $\tau = 2.23$. These two values of τ directly bracket the transition of the growth amplification factor into the linear regime shown in figure 3.4 for the mode [-1,1,1] of the elliptic instability. One major difference of interest in the optimal perturbation field is that, before the growth amplification factor reaches the linear regime, there is no perturbation within the vortex core (figure 3.5(a)). After the growth amplification factor becomes linear, a weak dipole of perturbation appears within the vortex core that corresponds to the asymptotic solution of the mode [-1,1,1] elliptic instability.

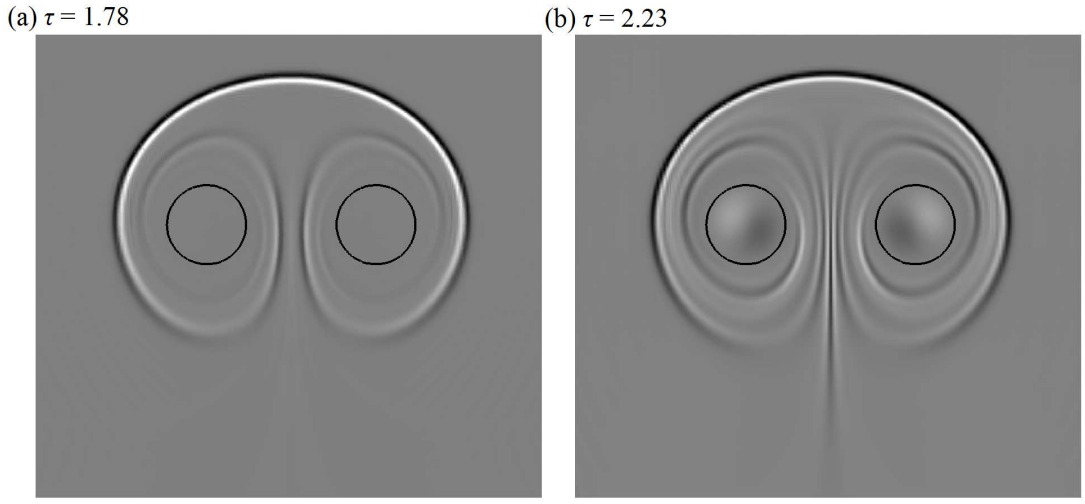

FIGURE 3.5: The optimal initial condition of the [-1,1,1] elliptic instability mode computed at $Re = 20\,000$ and $k\,a_1 = 2.12$, with (a) $\tau = 1.78$ and (b) $\tau = 2.23$. Axial vorticity contours are plotted on the base flow (lines) and the linearised perturbation field (flooded contours).

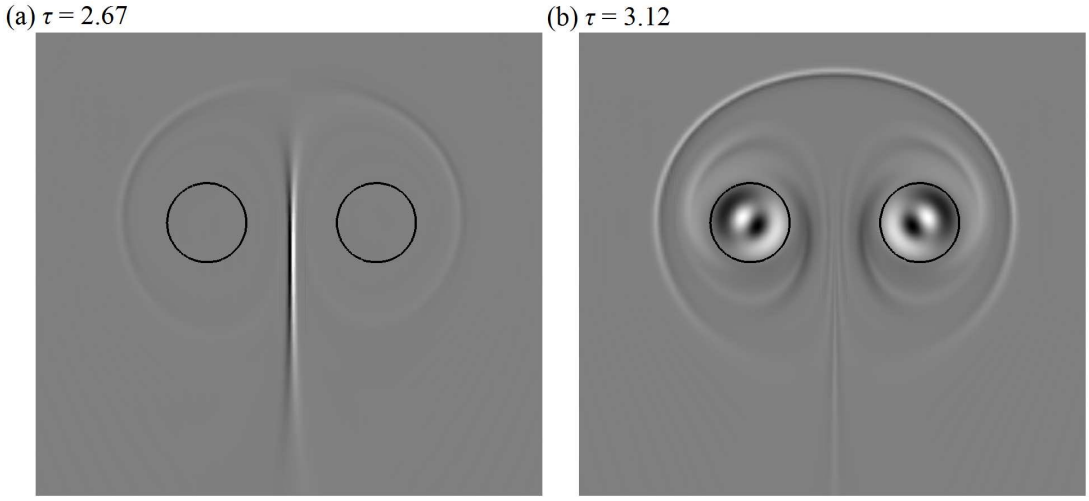

FIGURE 3.6: The optimal initial condition of the [-1,1,2] elliptic instability mode computed at $Re = 20\,000$ and $k\,a_1 = 3.7$, with (a) $\tau = 2.67$ and (b) $\tau = 3.12$. Axial vorticity contours are plotted on the base flow (lines) and the linearised perturbation field (flooded contours).

It is of interest to note that the strongest perturbation in both cases in figure 3.5 is the smear of oppositely signed perturbation above the vortex cores. This strongly implies that the best way to cause an instability to grow is to induce an oscillation above the vortex pair.

Figure 3.6 displays the optimal perturbation vorticity mode shape found from the transient growth analysis computed at $Re = 20\,000$ for an axial wavenumber of $k\,a_1 = 3.7$, corresponding to the mode [-1,1,2] elliptic instability for (a) $\tau = 2.67$ and (b) $\tau = 3.12$. These two perturbation fields directly bracket the transition of the growth

amplification factor into the linear regime shown in figure 3.4, for the mode [-1,1,2] of the elliptic instability. The transition of the mode [-1,1,2] perturbation field into the linear regime shown in figure 3.4, is significantly more severe than for the mode [-1,1,1] elliptic instability shown in figure 3.6. The optimal perturbation field transitions from a single smear of oppositely signed perturbation between the vortices (figure 3.6(a)) to a perturbation field resembling the asymptotic solution of the mode [-1,1,2] elliptic instability (figure 3.6(b)). One item of interest worth noting is that a spiral structure of perturbation has formed around the outside of the vortex cores, as well as a smear of oppositely signed perturbation above the vortices. This is similar to the mode [-1,1,1] elliptic instability shown in figure 3.6. This large change in the optimal perturbation field is likely for the same reason as the mode [-1,1,1] elliptic instability - the larger value of τ allows the perturbation to convect into the cores of the vortices and form into the structures that resemble the asymptotic solution.

3.3 Vortex filament analysis

Using the vortex filament method developed in § 2.7, a theoretical prediction of the peak axial wavenumber can be calculated for the equal-strength, counter-rotating, two-vortex system. This theoretical prediction can be used to compare with the transient growth analysis.

Figure 3.7 shows the growth amplification factor, $G(\tau)$ computed using the vortex filament method developed in § 2.7 to create a theoretical prediction of the three-dimensional response. It demonstrates that the vortex filament method predicts a long wavelength instability at $k, a_1 = 0.08$. The long wavelength instability corresponds relatively well with the predicted peak in the transient growth analysis of $k, a_1 = 0.154$. It is important to note that the growth amplification of the vortex filament study is under-estimated. The under-estimation of the growth amplification is due to the vortex filament method assuming a specific mode shape of the instability (which is controlled at the beginning of the simulation). In contrast, the transient growth analysis finds the optimal initial perturbation, limited only by available spatial resolution. This is demonstrated in the next section where the initial optimal perturbations do not necessarily resemble the final global instability modes.

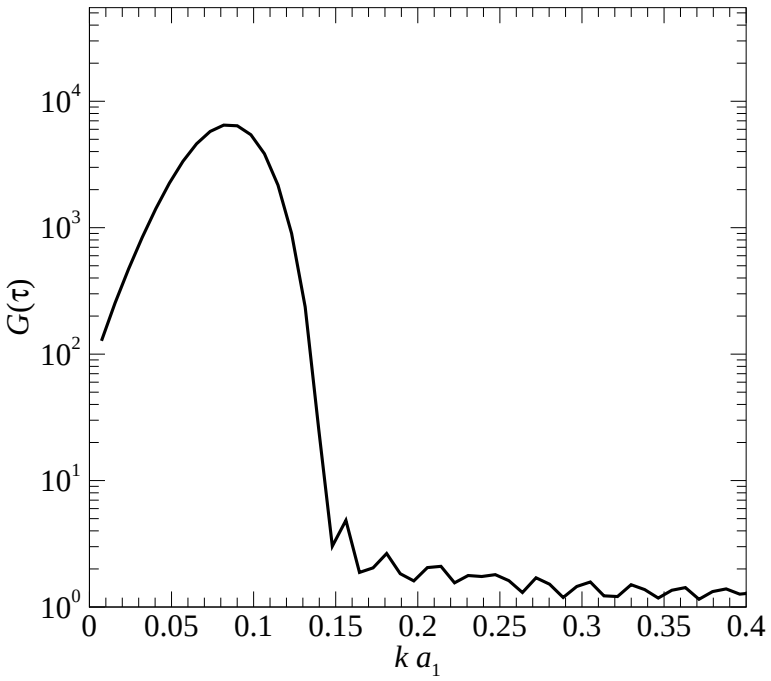

FIGURE 3.7: Vortex filament growth amplification factor $G(\tau)$ plotted against axial wavenumber $k\,a_1$ computed for $Re = 20\,000$. $\tau/t_{2V} = 5.35$ for these simulations. The solid line represents the vortex filament study conducted for the long wavelength Crow instability.

3.4 Evolution of the optimal perturbation fields

In this section, the perturbations that lead to optimal energy growth over the time τ found as an output of the transient growth method (described in chapter 2) are evolved using the linearised Navier–Stokes equations. These simulations are computed by evolving a base flow and perturbation field utilising the linearised Navier–Stokes equations to prevent the perturbations from causing a change in the base flow. The linearised simulations were evolved to $t/T_{2V} = 5.35$, which provided sufficient time for the perturbation to evolve into a steady state.

Figure 3.8 shows the time history of the perturbation energy normalised by the initial energy of the solution of the linearised Navier–Stokes equation for both the Crow and the mode [-1,1,1] elliptic instabilities. Initially, the linear perturbation energy for the mode [-1,1,1] elliptic instability is slightly larger, only being surpassed by the perturbation for the Crow instability at around $t/T_{2V} = 1.5$. This behaviour is a little surprising as the transient growth analysis implies that the Crow instability will have a slightly larger growth amplification factor in this very early regime, $t/T_0 < 1$

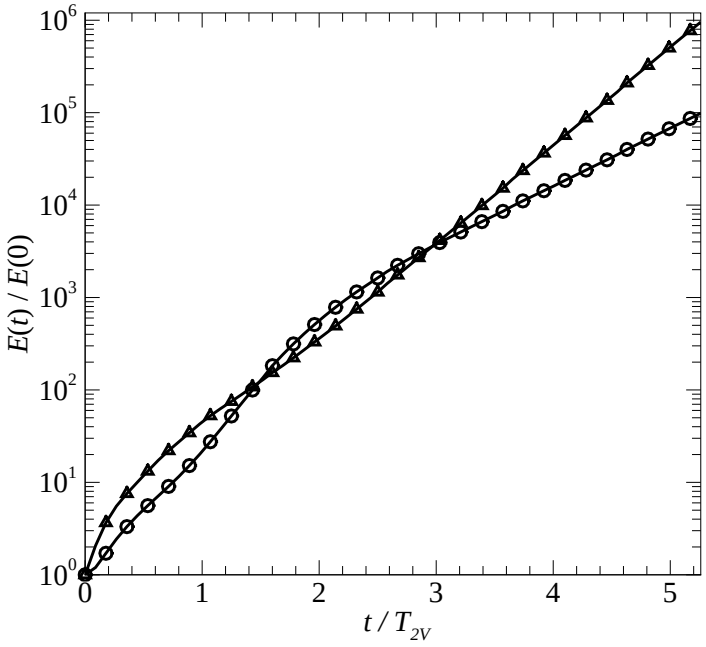

FIGURE 3.8: Time history of perturbation energy normalised by initial energy of the solution of the linearised Navier–Stokes equation. ∘ represents the Crow instability ($k\,a_1 = 0.155$) and △ represents the mode [-1,1,1] elliptic instability ($k\,a_1 = 2.12$) cases. The initial perturbation field was set from $\tau/t_{2V} = 5.35$.

(figure 3.4). After this time, the linear perturbation energy in the Crow instability is greater until $t/T_{2V} = 3$. This behaviour is not surprising as the peak in the growth amplification factor shown in figure 3.2 shows that for values of $\tau = 2.67$, the peak in growth amplification factor for the Crow instability is larger than the mode [-1,1,1] elliptic instability. Following this behaviour, the energy in the perturbation of the mode [-1,1,1] elliptic instability grows larger for longer timeframes, and this is mirrored by the peak growth amplification factor in the transient growth analysis for $\tau = 5.35$ demonstrating a higher value for the mode [-1,1,1] elliptic instability.

3.4.1 Elliptic instability

Donnadieu *et al.* (2009) noted that for optimal disturbances arising from transient growth analysis for an equal stength, counter-rotating two-vortex system without axial flow over short times (i.e. $\tau = 0.025$), the predicted optimal disturbance field differs significantly from the global stability mode at the same axial wavenumber. They found that with increasing τ, the optimal disturbance mode shape approaches that observed for the global mode, and the growth amplification factor, G, varies exponentially with

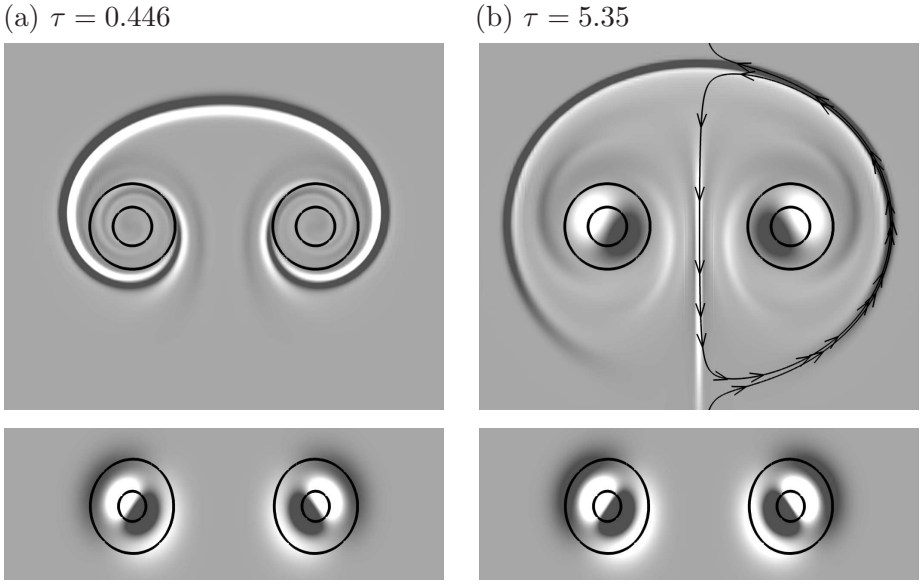

FIGURE 3.9: Top: The optimal initial condition computed at $Re = 20\,000$ and $k\,a_1 = 2.12$, with (a) $\tau = 0.446$ and (b) 5.35. Streamlines relative to the vortex pair are plotted on the right half-plane in (b) to elucidate the location of hyperbolic points above and below the vortex pair. Bottom: These optimal perturbations integrated to $t/T_{2V} = 5.35$ in a simulation utilising the linearised Navier–Stokes equations. Axial vorticity contours are plotted on the base flow (lines) and the linearised perturbation field (flooded contours).

τ. The present study demonstrates identical behaviour; optimal disturbances captured at short and long time intervals are shown in figure 3.9. The optimal initial fields differ markedly. The long-τ optimal initial disturbance (figure 3.9(b), top) exhibits structures resembling the global instability modes within the cores of the vortices, along with a band of perturbation vorticity following the streamline, relative to the right half-plane, passing through the hyperbolic points (this was also seen by Donnadieu *et al.* 2009).

In contrast, the vortex cores in the short-τ optimal initial disturbance field are devoid of perturbation vorticity, and the umbrella band of perturbation above the vortices lies inside the hyperbolic streamlines. In both instances, after long time integration, transients die away and the disturbance resembles a [-1,1,1] instability mode (figure 3.1(a)), differing only by the level of energy amplification produced.

Figure 3.10 displays the optimal perturbation field for the [-1,1,2] mode of the elliptic instability evolved using a linearised Navier–Stokes solver to prevent the perturbation from changing the base flow. It is interesting to note that the initial optimal perturbation is very similar to the optimal perturbation for the [-1,1,1] mode for the longer wavelength (figure 3.9(a)). The difference in axial wavenumber means that the perturbation evolves in a different manner to the [-1,1,1] mode, eventually growing into the

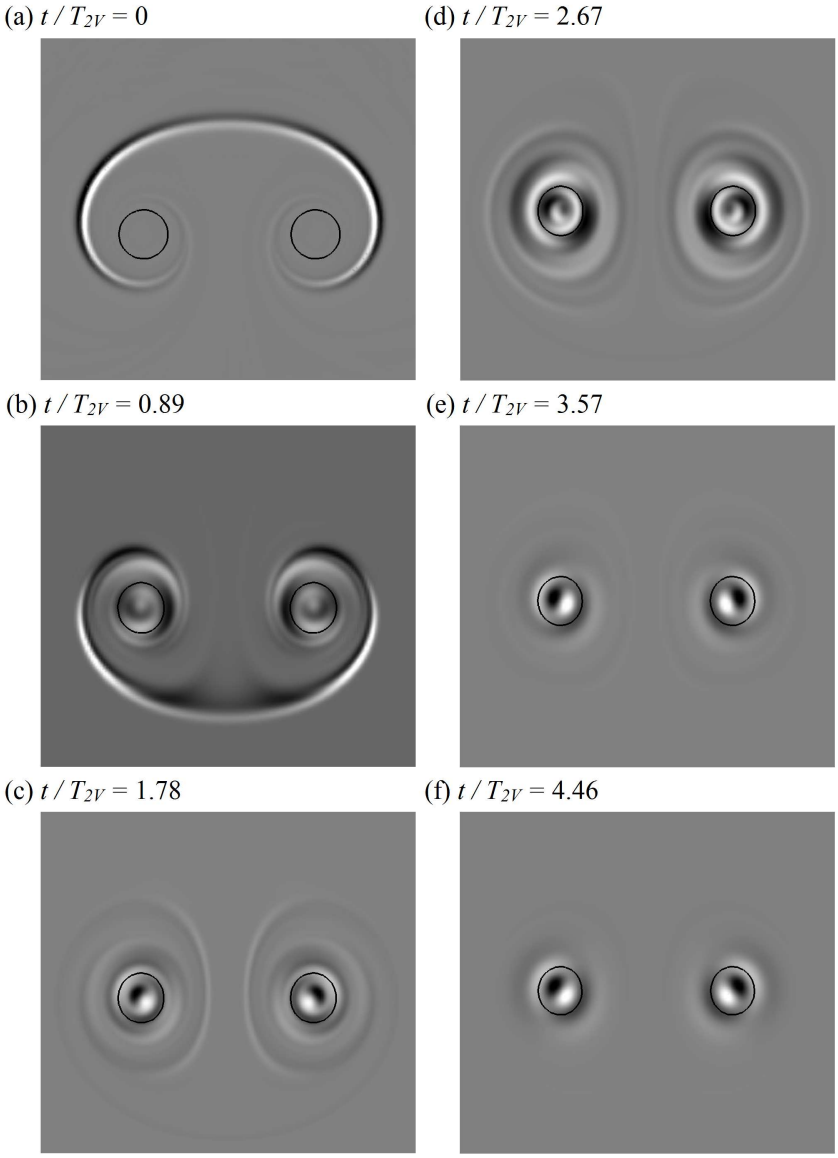

FIGURE 3.10: (a) The optimal initial condition of the [-1,1,2] elliptic instability mode computed at $Re = 20\,000$ and $k\,a_1 = 3.7$, with $\tau = 0.445$. (b)-(f) The optimal perturbations integrated to $t/T_{2V} = 0.89, 1.78, 2.67, 3.56, 4.46$. Axial vorticity contours are plotted on the base flow (lines) and the linearised perturbation field (flooded contours).

asymptotic solution of the [-1,1,2] mode. It is of interest to note that the perturbation goes through an intermediate stage resembling the asymptotic [-1,1,2] mode (as seen in Donnadieu *et al.* 2009) within the the vortex cores (figure 3.10(c)). However, the presence of perturbation in the region surrounding the vortex cores causes the perturbation to become significantly more agitated (figure 3.10(d)) before it settles into a perturbation roughly corresponding to the asymptotic perturbation field, but with the perturbation dipole not quite at 45^o to the horizontal plane (figure 3.10(e)). After fur-

ther time, $t/T_{2V} \approx 4.46$, the perturbation finally settles at 45^o to the horizontal plane (figure 3.10(f)), corresponding to the asymptotic solution.

3.4.2 Crow instability

Figure 3.11 displays the optimal perturbation field for the long-wavelength Crow instability evolved using the linearised Navier–Stokes solver to prevent the perturbation from changing the base flow. Figure 3.11(a) shows the initial optimal perturbation field found through the transient growth analysis method with the base flow vortices overlayed as lines while (b)-(h) shows the temporal evolution of the perturbation field. The initial optimal perturbation field shows a strong streak of vorticity between the vortex pair along $x = 0$ and a significantly weaker halo encircling the vortices, in a similar manner to that seen in figure 3.9(b). This initial perturbation field is very similar to the optimal field found by Brion *et al.* (2007). After a short evolution, a stronger field of positive and negative axial vorticity forms beneath the pair of vortices (figure 3.11(b)). By $t/T_{2V} = 1.34$, a strong dipole has formed within the cores of the vortices, arranged at approximately 50° to the line between the centres of the vortex cores, with a thin, but strong, region of vorticity surrounding the vortex pair (figure 3.11(d)). As the flow is evolved further to $t/T_{2V} = 1.78$, the vorticity far outside the vortex cores begins to damp out, while the dipole within the vortex cores continues to settle to approximately 45° to the line between the centres of the vortex cores (figure 3.11(e)). After a longer period of time, $t/T_{2V} = 3.12$, all of the perturbation vorticity outside the vicinity of the vortex cores have decayed, leaving the strong perturbation dipole (figure 3.11(h)), which is consistent with previous studies of the Crow instability (Brion *et al.* 2007).

3.5 Direct numerical simulation

In this section, a number of three-dimensional simulations were conducted to study the response of the two-vortex flow to seeding by both the optimal perturbations shown in the previous section, and by white noise. Both the short-wavelength elliptic instability and the long-wavelength Crow instability are considered in isolation in different simulations. For these simulations, the polynomial order was set to $p_n = 13$ with 16 Fourier modes ($p_f = 16$) included in the axial discretization. The periodic wavelength of the axial domain was selected to encompass a single axial wavelength of the instability of interest.

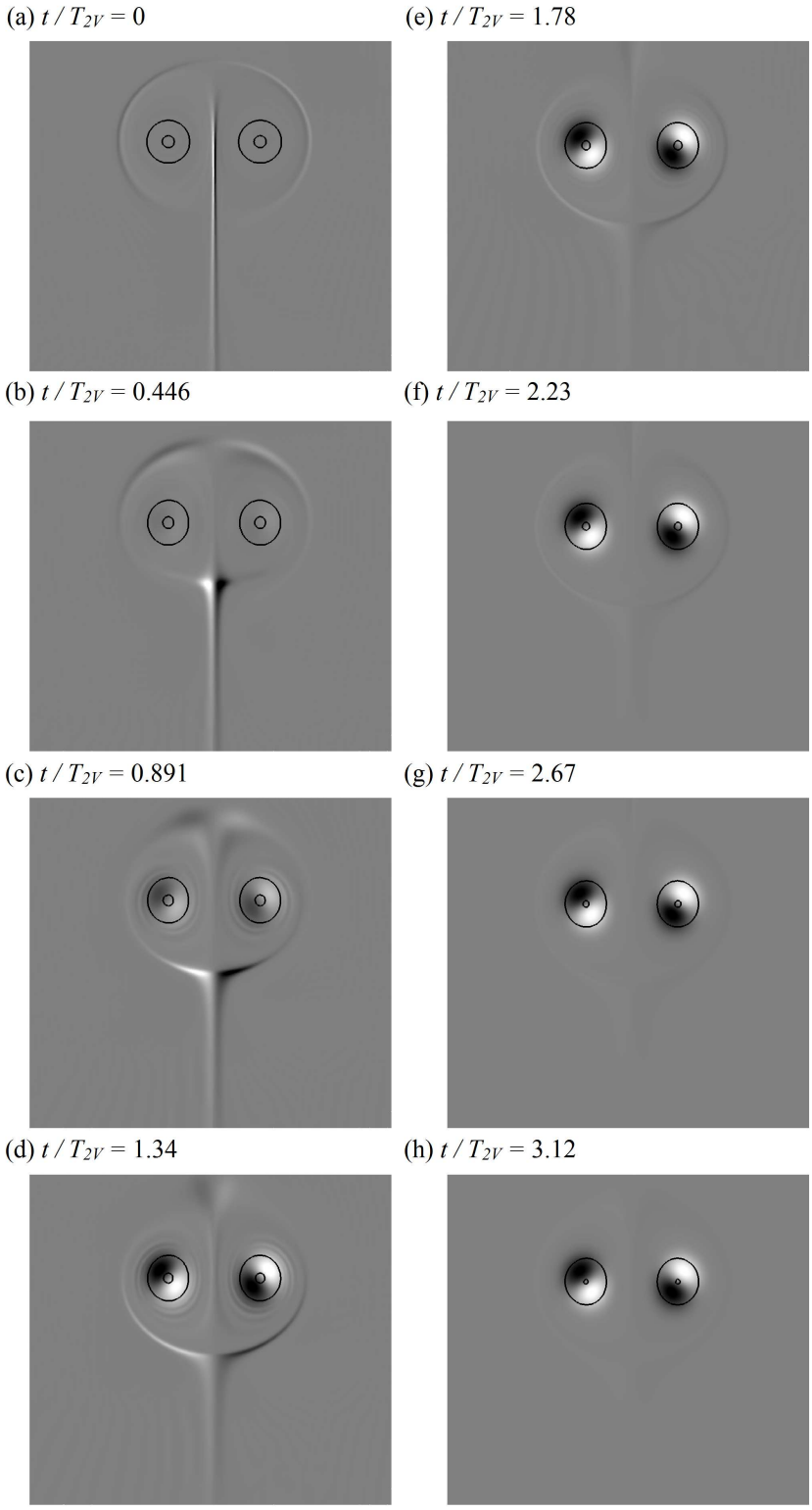

FIGURE 3.11: (a) The optimal initial condition for the Crow instability computed at $Re = 20\,000$ and $k\,a_1 = 0.155$, with $\tau = 5.35$. (b)-(f) The optimal perturbations integrated to $t/T_{2V} = 0.89, 1.78, 2.67, 3.56, 4.46, 5.35, 6.24$. Axial vorticity contours are plotted on the base flow (lines) and the linearised perturbation field (flooded contours).

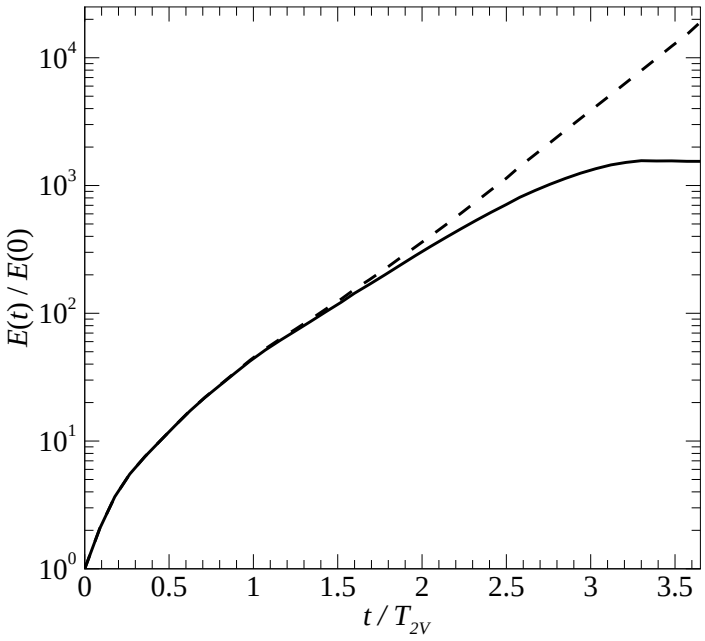

FIGURE 3.12: Time history of perturbation energy normalised by initial energy ($E(0)$). The dashed line represents the solution of the linearised Navier–Stokes equation and the solid line represents the energy in the non-zero Fourier modes of the DNS. Simulations were seeded with the optimal disturbance field predicted for $\tau = 5.35$. The axial wavenumber was set to $k\,a_1 = 2.12$, corresponding to the dominant wavenumber of the mode [-1,1,1] elliptic instability.

Figure 3.12 shows a time history of the energy in the perturbations, normalised by the initial energy in the perturbations. Up to $t/T_{2V} \approx 1.5$, both sets of data follow almost exactly the same trend. After that time, the energy in the perturbation evolved with the linearised Navier–Stokes equations continues to grow at the same rate, reaching $E(t)/E(0) \approx 25\,000$ at $t/T_{2V} = 3.65$. The perturbation energy in the DNS tapers off after $t/T_{2V} \approx 1.5$ as non-linear effects lead to saturation of the three-dimensional flow structures, causing the mode to be less conducive to growth. The perturbation energy in the DNS reaches a peak energy of $E(t)/E(0) = 1550$ at $t/T_{2V} = 3.38$. Thereafter it plateaus, as the flow field is no longer conducive to growth of the instability (also shown by Schaeffer & Le Dizès 2010).

The evolution time history in the Crow instability will now be considered. Figure 3.13 shows a time history of the energy in the perturbation, normalised by the initial energy in the perturbations. Up to $t/T_{2V} \approx 1.75$, both the data sets follow similar trends, with the linearised solution producing slightly higher energy. For

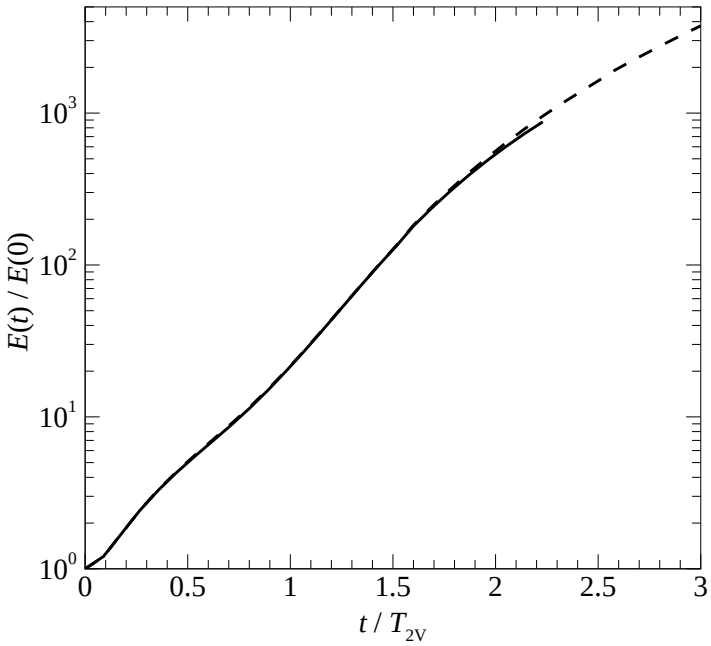

FIGURE 3.13: Time history of perturbation energy normalised by initial energy ($E(0)$). The dashed line represents the solution of the linearised Navier–Stokes equation and the solid line represents the energy in the non-zero Fourier modes of the DNS. The perturbation that leads to optimal energy growth was from $\tau = 5.35$. The axial wavenumber was set at $k\,a_1 = 0.155$ to correspond to the Crow instability.

$t/T_{2V} \geq 1.75$, the DNS starts to become non-linear and the energy growth begins to plateau slightly compared to the energy in the perturbation in the simulation using the linearised Navier–Stokes equation. Even after significant evolution of the DNS, the perturbation energy is still very similar to the simulation evolved using the linearised Navier–Stokes equations. This implies that the predominant mechanism of the Crow instability is the linear evolution of the perturbations.

Figure 3.14 shows the energy in the perturbations for both two-vortex flows seeded with the optimal perturbations (described in § 2.4) for the [-1,1,1] elliptic instability and the Crow instability (shown in figure 3.9(a) and 3.11(a)), and the same flows seeded with white noise, normalised by the initial energy in the perturbations. The axial wavenumber for the elliptic and Crow DNS studies are the same as those examined for the linearised studies. The base flow for all the DNS cases is the same, except for the difference between the axial wavenumber of the elliptic and Crow instability. Perturbation energy from the DNS simulations demonstrates overwhelmingly that optimal disturbances yield energy growths vastly larger than the cases seeded with white

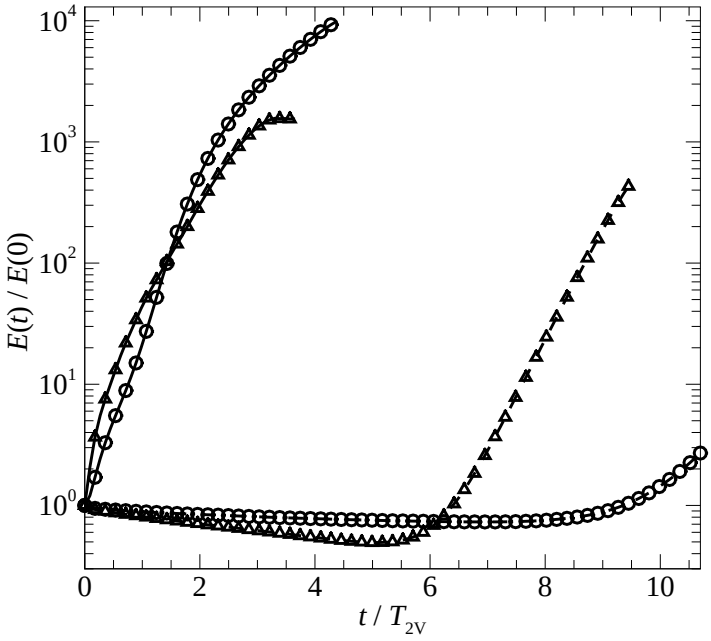

FIGURE 3.14: Time history of perturbation energy, normalised by initial energy. ∘ and △ represents the Crow instability ($k\,a_1 = 0.155$) and elliptic instability ($k\,a_1 = 2.12$) cases respectively. Solid lines represent the cases seeded with the optimal perturbation; dashed lines represent the cases seeded with white noise.

noise over a significantly shorter period of time. The cases seeded with white noise require significantly longer evolution times for the instability modes to emerge from the white noise. For the case of the short-wavelength elliptic instability seeded with white noise here, it is just beginning to grow at $t/T_{2V} \approx 5$. This is because only specific invsicid modes are susceptible to growth in this kind of flow, and so can draw energy from the base flow field into the Fourier modes. Therefore, over the initial phase of the simulation, the energy time history is dominated by the decay of the majority of the modes contained in the white noise perturbation. This decay removes energy in the perturbation through the effect of damping due to viscosity until the growth of the unstable mode dominates the perturbation energy. After a significant period of time, the cases seeded with white noise demonstrate similar growth to the cases seeded with the optimal perturbation. For the elliptic instability, the perturbation only reaches the initial energy after $t/T_{2V} \approx 6.4$: a significant delay in the growth of instabilities that lead to the destruction of the vortices. The Crow instability requires even more time for the perturbation energy to reach a magnitude of the initial seeding energy, occurring after $t/T_{2V} \approx 9.35$. It is important to note that, because the white noise seeding is a

random combination of many modes of varying magnitude, the overall time required for the flow to enter an obvious linear growth regime may shift slightly when repeating these simulations. In the cases seeded with the optimal perturbations, the modes that can draw energy from the base flow field are artificially promoted, overcoming the damping effect of viscosity. This demonstrates that, if an aircraft wake can be seeded with an optimal perturbation, the time it takes to be destroyed can be significantly reduced over the time they would take to dissipate following instability growth from ambient turbulence in the air alone.

The cases seeded with the optimal perturbations, as shown in the previous section, demonstrate significant growth as soon as the flows are seeded, and rapidly become non-linear. It is interesting to note that initially the normalised energy is greater in the short-wavelength elliptic instability (until $t/T_{2V} \approx 1$), but leads to a lower energy ($E(t)/E(0) \approx 10^3$) upon saturation. Given that the vortex core radius a_{tv} has only increased by 2% at $t/T_{2V} = 1$ (according to the first order approximation), it is highly unlikely that the increase in vortex core size is a key factor in this effect. By contrast, the long-wavelength Crow instability demonstrates a lower normalised energy initially, but surpasses the short-wavelength elliptic instability at $t/T_{2V} \approx 1$ and reaches a normalised energy almost an order of magnitude higher ($t/T_{2V} \approx 4.3$). As shown previously, the Crow instability is only just diverging from linear growth, showing that this delay in non-linear growth can lead to a significantly higher perturbation energy. This is an interesting outcome, and demonstrates that the non-linear effects cause a significant change in the perturbation energy of the two cases, as the purely linear case shows the energy in the perturbation of the elliptic instability to always be of greater magnitude then the Crow instability (figure 3.8).

Figure 3.15 shows a time history of the perturbation energy growth rate, σ_{GR}, for the mode [-1,1,1] elliptic instability at an axial wavenumber of $k\,a_1 = 2.12$. It shows that, for both the optimal and white noise cases, they reach a linear stage where the growth rate is constant around $\sigma_{GR} \approx 0.14$. It is interesting to note that the case seeded with the optimal perturbation reaches this linear growth regime in approximately 14% of the time taken by the case seeded with white noise. Another point of interest is that the case seeded with the optimal perturbation begins with a significantly higher growth rate, and actually drops in growth rate to reach the linear regime. This is interesting as it is the opposite to the case seeded with white noise. This higher growth rate before the linear

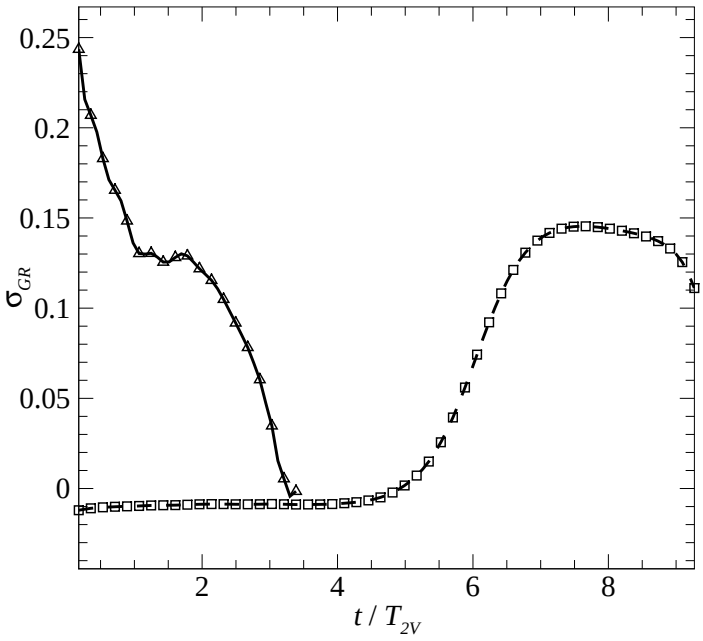

FIGURE 3.15: Time history of perturbation energy growth rate, σ_{GR}, for the mode [-1,1,1] elliptic instability at an axial wavenumber of $k\,a_1 = 2.12$. The dashed line with □ represents the case seeded with white noise and the solid line with △ represents the case seeded with the perturbation that leads to optimal energy growth.

regime indicates that the energy in the perturbation will be greater before entering the linear regime, which explains why the linear region of instability growth for the case seeded with the optimal perturbation is significantly shorter - approximately half the time - than the case seeded with white noise. The drop in growth rate after the linear regime demonstrates the flow becoming non-linear, and occurs once the perturbation energy saturates. Since the perturbation energy is greater in the case seeded with the optimal perturbation, it will reach this saturation criterion earlier in the linear regime.

3.5.0.1 Comparison of strain rate to growth rate

Previous literature has found a theoretical relationship between the growth rate of the elliptic instability and the strain rate imposed on a vortex. For a single, unbounded vortex in a strain field, the growth rate is related to the strain through the relationship

$$\sigma = \frac{9}{16}\epsilon, \tag{3.1}$$

where σ is the growth rate of the instability (calculated from the velocity) and ϵ is the strain imposed on the vortex core (**?**Waleffe 1990; Leweke & Williamson 1998;

Kerswell 2002). Waleffe (1990) also determines that viscosity in the fluid has the effect of reducing the maximum growth rate due to a decay term of $-\nu k^2 v^2$. In the current study, the growth rate is found to be $\sigma_{GR} \approx 0.14$, with a strain rate of $\epsilon = 0.221$. While the ratio of $\sigma_{GR}/\epsilon = 0.636$ it is important to note that σ_{GR} is calculated with respect to the energy, and so is double what the growth rate calculated from velocity would be. Taking this into account, the growth rate, based on velocity, is well within the range expected for a vortex in an externally imposed strain field with viscosity (Waleffe 1990; Leweke & Williamson 1998).

3.5.1 Crow instability

Visualisation of the evolving three-dimensional structures will now be described. Many of the visualisations are plotted with iso-surfaces of λ_2. The λ_2 field is defined as the criterion for identification of a vortex proposed by Jeong & Hussain (1995). The iso-surfaces are overlaid with flooded contours of the dominant strain, which is defined in chapter 2.

Figure 3.16 shows a time sequence of iso-surfaces of λ_2 plotted from a three-dimensional DNS of the two-vortex long-wave instability case investigated in § 3.2.2. The left side shows the case seeded with the optimal perturbations displayed in the previous section, while the right side shows the case seeded with white noise of a similar energy magnitude. The case seeded with the optimal perturbation quickly begins to deform. This sinuous deformation to approximately 45°, symmetrical about the $x = 0$ plane, is consistent with the Crow instability (Crow 1970). The long-wavelength case seeded with white noise displays no discernable instability growth. This is not to say that the instability is not there, but that the instability growth is insufficient to be noticeable over the time interval shown here.

The flooded contours of dominant strain in figure 3.16(a v) demonstrate that the strain on the vortices increases significantly at the apex of the vortices as they are drawn together.

3.5.2 Mode [-1,1,1] elliptic instability

Figure 3.17 shows a time sequence of iso-surfaces of λ_2 plotted from a three-dimensional DNS of the two-vortex short-wavelength instability (mode [-1,1,1] elliptic instability) case investigated in § 3.2.1. The left side shows the case seeded with the optimal perturbations displayed in the previous section, while the right side shows the case

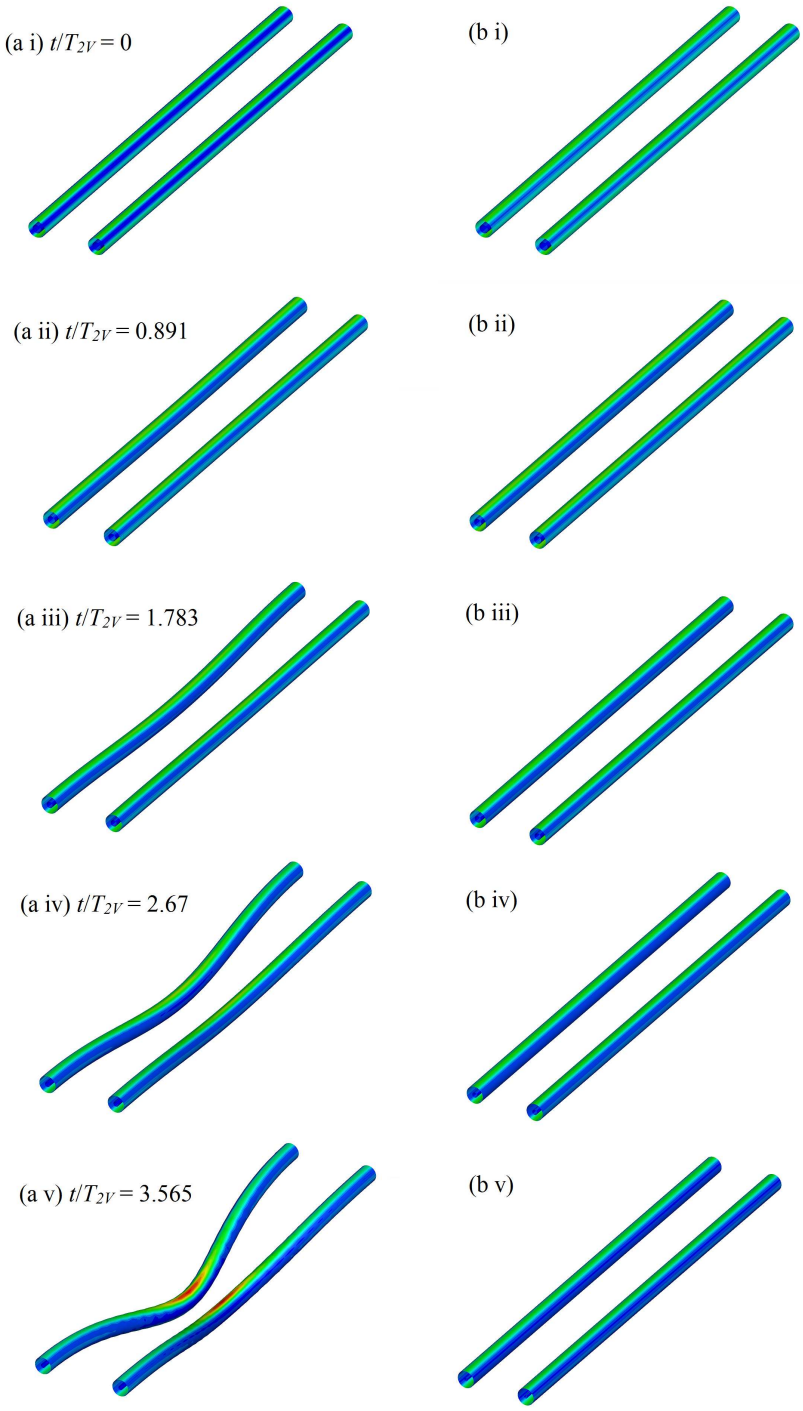

FIGURE 3.16: Time sequences of iso-surfaces of λ_2 plotted from a three-dimensional simulation of the two-vortex case with an axial extension corresponding to the Crow instability at a wavenumber of $k\,a_1 = 0.155$. The iso-surfaces are flooded with the dominant strain. $Re = 20\,000$ for these simulations. (a i)-(a v) displays the flow seeded with the perturbation that leads to optimum energy growth at $t/T_{2V} = 0, 0.891, 1.783, 2.67, 3.565$ respectively. (b i)-(b v) displays the flow seeded with white noise at the same times.

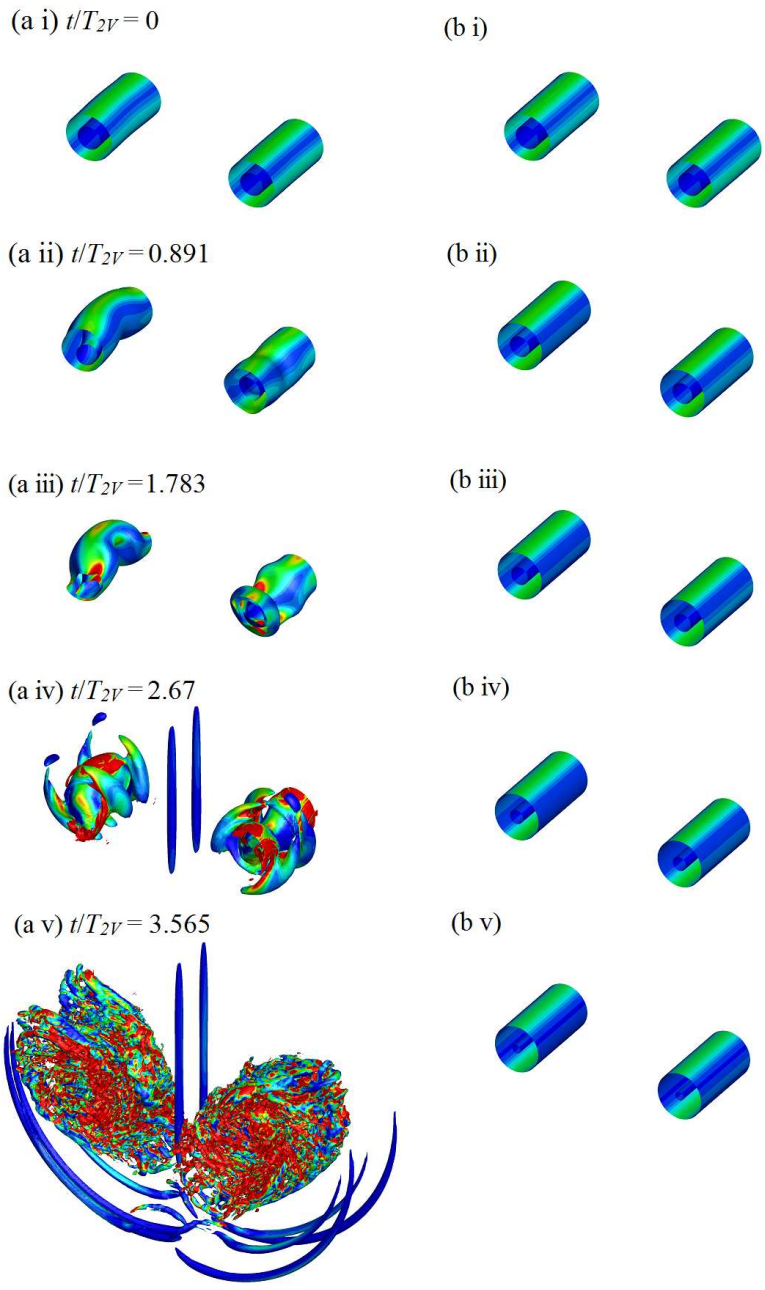

FIGURE 3.17: Time sequences of iso-surfaces of λ_2 plotted from a three-dimensional simulation of the two-vortex case with an axial extention corresponding to the elliptic instability at a wavenumber of $k\,a_1 = 2.12$. The iso-surfaces are flooded with the dominant strain. $Re = 20\,000$ for this simulations. (a i) - (a v) display the flow seeded with the perturbation that leads to optimum energy growth at $t/T_{2V} = 0, 0.891, 1.783, 2.67, 3.565$ respectively. (b i) - (b v) display the flow seeded with white noise at the same times.

seeded with white noise with a similar energy magnitude. It is interesting to note that, in a very short timeframe, the flow seeded with the optimal perturbation quickly causes the vortex pair to deform as a sinuous waviness along the axial direction. As can be seen in figure 3.17(a iii), this deformation of the vortex core occurs at approximately 45° to the horizontal plane. As is typical of the elliptic instability, the left vortex is deformed at approximately +45° while the right vortex is deformed at approximately −45° to the horizontal plane between the vortex cores, with positive angle taken clockwise from the left of the vortex. As the flow evolves, azimuthal vortex filaments form around the cores of the vortices with high levels of dominant strain in the outside of the 'bows' of the deformed vortex cores (figure 3.17(a iv)). Once the flow reaches longer times, the vortex cores rapidly become highly disturbed, as can be seen in figure 3.17(a v). This transformation into small scale flow structures is the final stages of vortex destruction before the flow reaches a scale that can be damped out by the fluid viscosity. Close examination of the small scale flow structures at $t/T_{2V} = 5.565$ showed that the structures are of an order of five times the local grid mesh. Snapshots, which are not shown in this thesis, closer to the simulation divergence, show different flow structures that are of a scale of the local grid mesh and are obviously artifacts of computational aliasing. In addition, the azimuthal vortex filaments have extended to surround the bottom half of the vortices. In contrast there appears to be no discernable instability in the case seeded with white noise, even after a significant period of time (figure 3.17(b v)). As with the previous case investigating the Crow instability, the case seeded with white noise does have an instability present, though the magnitude is not of sufficient size to be observable.

3.6 Transition into non-linear growth

In this section, the transition of the flow into the non-linear growth regime is studied. This transition into the non-linear growth regime is characterised by bulk changes in the base flow field caused by the growth of the instabilities. Fields of λ_2, $[\omega_y^2 + \omega_x^2]^{0.5}$ and $\mid \omega \mid$ are used to interrogate the evolution of the three-dimensional modes. ω_y and ω_x are the components of vorticity about the y and x axes respectively. The λ_2 field is used as it shows the presence of a vortex and can show how coherent the vortex is during the breakdown. The presence of flow in the $[\omega_y^2 + \omega_x^2]^{0.5}$ field demonstrates the transition of flow from two-dimensional flow in the x–y plane to three-dimensional flow.

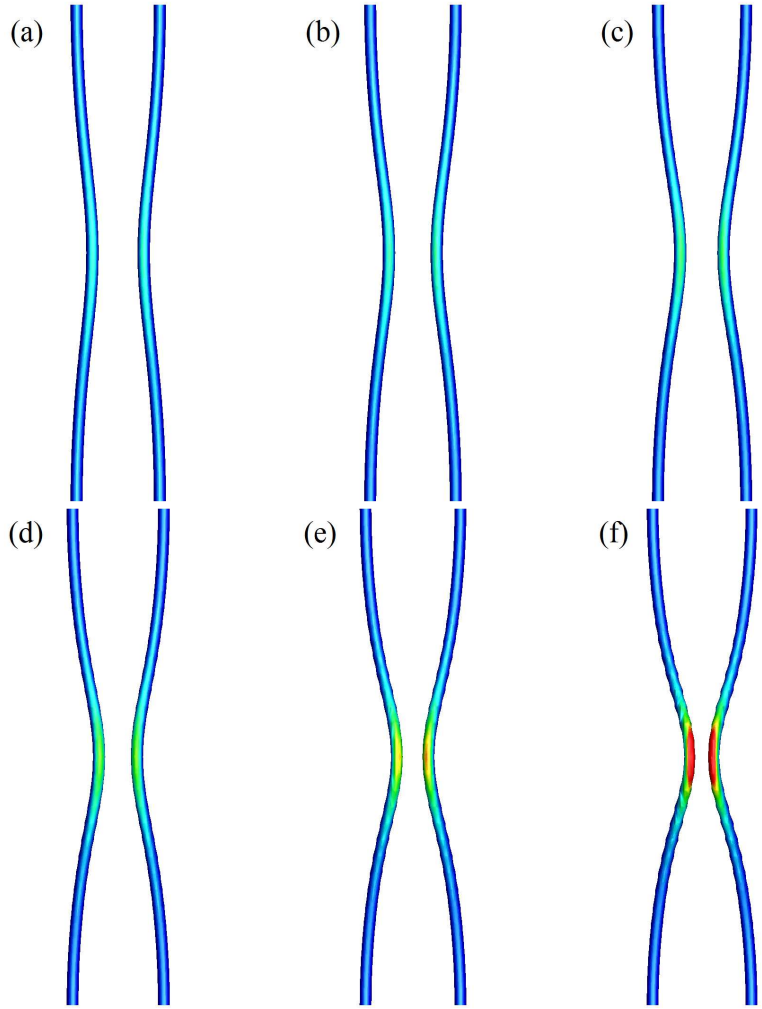

FIGURE 3.18: Time sequences of iso-surfaces of λ_2 with dominant strain flooding plotted from a three-dimensional simulation of the two-vortex case with an axial extension corresponding to the Crow instability at a wavenumber of $k\,a_1 = 0.155$. $Re = 20\,000$ for this simulation. (a)-(f) display the flow seeded with the perturbation that leads to optimum energy growth ($\tau = 5.35$) at $t/T_{2V} = 3.12, 3.30, 3.47, 3.65, 3.83, 4.01$ respectively.

The $\mid \omega \mid$ field shows the overall structure of the flow as it transitions into the non-linear regime.

3.6.1 Crow instability

Figures 3.18 - 3.20 show a top-down view of the iso-surfaces for the long-wavelength Crow instability case seeded with the optimal perturbation. Figure 3.18 shows that the dominant mode for the Crow instability causes a sinusoidal distortion in the vortex pair, symmetrical about the plane separating the vortices. The dominant strain for the Crow instability is confined to the region that is most distorted by the instability - the central 'bow' in the vortices. This strain becomes large when the most deformed section

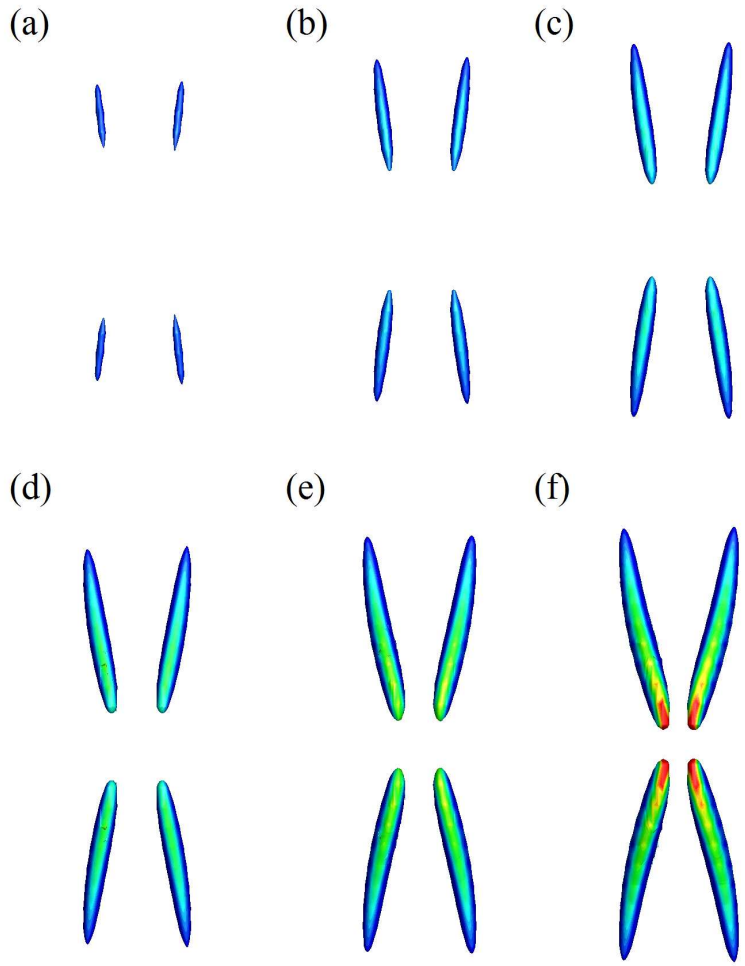

FIGURE 3.19: Time sequences of iso-surfaces of the $[\omega_y^2 + \omega_x^2]^{0.5}$ field with dominant strain flooding plotted from a three-dimensional simulation of the two-vortex case with an axial extension corresponding to the Crow instability at a wavenumber of $k\,a_1 = 0.155$. $Re = 20\,000$ for this simulation. (a)-(f) display the flow seeded with the perturbation that leads to optimum energy growth ($\tau = 5.35$) at $t/T_{2V} = 3.12, 3.30, 3.47, 3.65, 3.83, 4.01$ respectively.

of the vortices approach each other (figure 3.18(f)). This bowing of the vortices is typical of the Crow instability, and has been shown in previous literature to lead eventually to the vortices joining to form vortex rings, with a diameter approximately equal to the instability wavelength (Leweke & Williamson 2010). It is interesting to note that a short wavelength instability is becoming apparent in figure 3.18(f). This short wavelength instability could be the beginning of an elliptic instability as is has been shown previously that the interaction of the Crow and elliptic instability produces greater ability for the large scale energy to be distributed to smaller scales more effectively

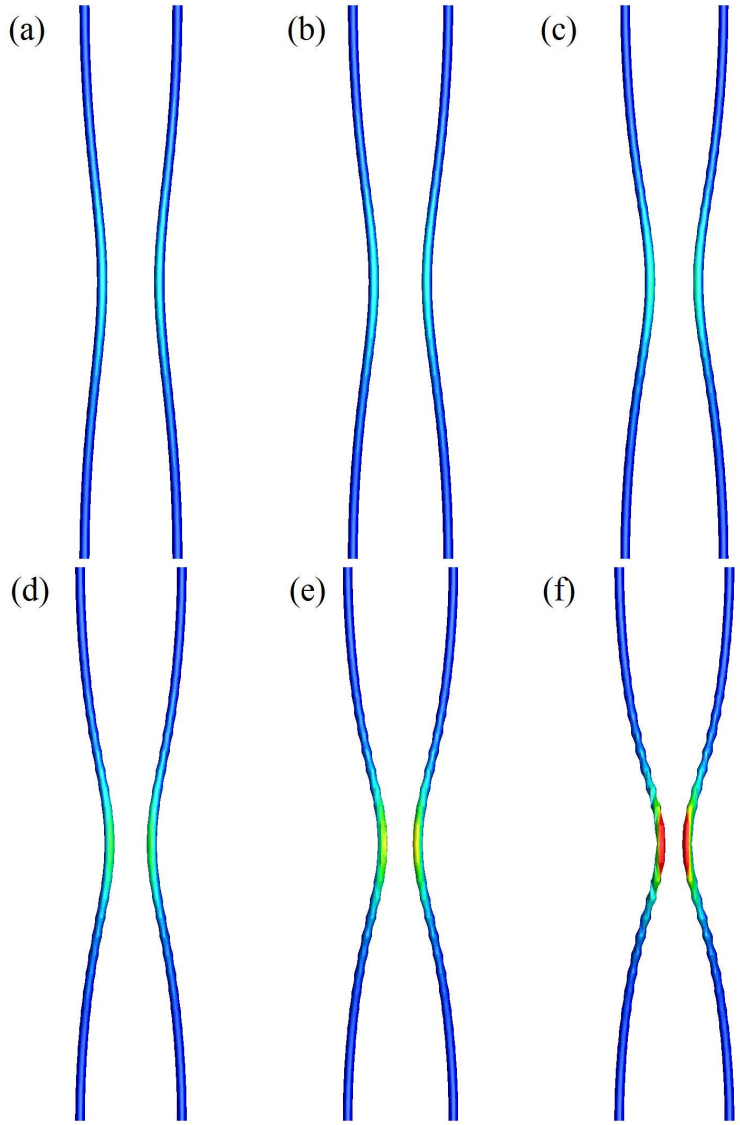

FIGURE 3.20: Time sequences of iso-surfaces of vorticity magnitude with dominant strain flooding plotted from a three-dimensional simulation of the two-vortex case with an axial extension corresponding to the Crow instability at a wavenumber of $k\,a_1 = 0.155$. $Re = 20\,000$ for this simulation. (a)-(f) display the flow seeded with the perturbation that leads to optimum energy growth ($\tau = 5.35$) at $t/T_{2V} = 3.12, 3.30, 3.47, 3.65, 3.83, 4.01$ respectively.

than either instability alone Leweke & Williamson (1998). The increased magnitude of the short wavelength instability where the vortices are closer, and therefore more highly strained, indicates that it is likely an elliptic instability.

Figure 3.19 shows iso-surfaces of the $[\omega_y^2 + \omega_x^2]^{0.5}$ field, again flooded with the dominant strain. It shows that even late in the evolution, the flow is predominantly two-dimensional in the axial direction with very little vorticity in directions other than the axial direction (figure 3.19(a)). As the vortices become highly deformed, the magnitude of the vorticity in directions other than the axial direction grows in the regions other

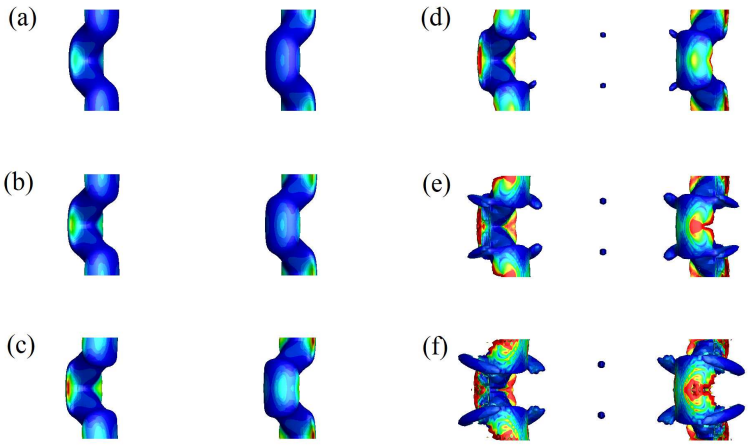

FIGURE 3.21: Time sequences of iso-surfaces of λ_2 with dominant strain flooding plotted from a three-dimensional simulation of the two-vortex case with an axial extension corresponding to the elliptic instability at a wavenumber of $k\,a_1 = 2.12$. $Re = 20\,000$ for this simulation. (a)-(f) display the flow seeded with the perturbation that leads to optimum energy growth ($\tau = 5.35$) at $t/T_{2V} = 1.87, 2.05, 2.23, 2.41, 2.58, 2.76$ respectively.

than the middle or ends of the vortices (figure 3.19(d)). Later in the evolution, the magnitude of vorticity in directions other than the axial begins to grow into the central region where the flow is highly strained (red region in figure 3.19(f)).

It is interesting to note that figures 3.18 and 3.20 are very similar in structure. Due to the nature of the λ_2 field, any locations where the ω_z^2 exceeds that of the dominant strain (defined in chapter 2), the local fluid flow is dominated by the axial vorticity and the λ_2 field will identify a vortex core at this location. Conversely, when the magnitude of the dominant strain is greater than the ω_{xy}^2, the local fluid flow is dominated by the strain field and the λ_2 field will not identify a vortex core at this location (Jeong & Hussain 1995). This similarity between the λ_2 field and vorticity magnitude demonstrates that the the axial component of strain rate is lower than the vorticity magnitude and perpendicular to it throughout the transition into non-linear instability growth. The lack of difference between figure 3.19 and 3.20 implies that the vast majority of the vorticity is confined to the axial plane throughout the transition into non-linear instability growth.

3.6.2 Mode [-1,1,1] elliptic instability

Figures 3.21 - 3.23 show a view from below of the iso-surfaces for the short-wavelength mode [-1,1,1] elliptical instability case seeded with the optimal perturbation. This view

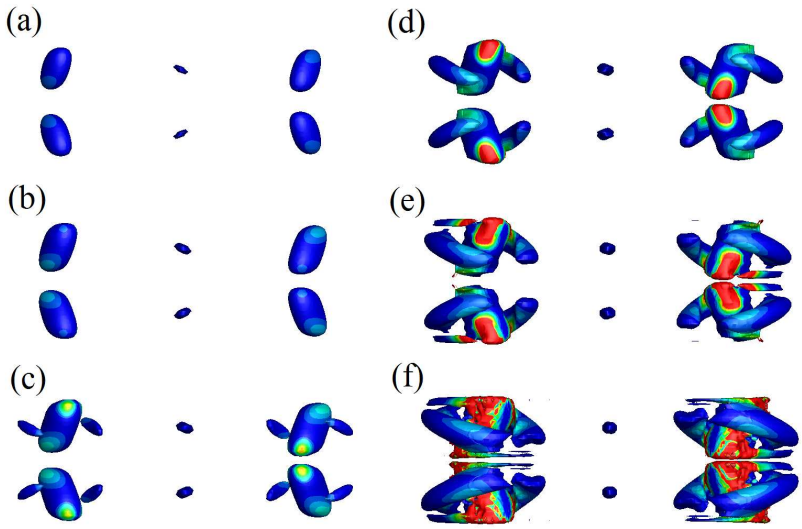

FIGURE 3.22: Time sequences of iso-surfaces of the $[\omega_y^2 + \omega_x^2]^{0.5}$ field with dominant strain flooding plotted from a three-dimensional simulation of the two-vortex case with an axial extension corresponding to the elliptic instability at a wavenumber of $k\,a_1 = 2.12$. $Re = 20\,000$ for this simulation. (a)-(f) display the flow seeded with the perturbation that leads to optimum energy growth ($\tau = 5.35$) at $t/T_{2V} = 1.87, 2.05, 2.23, 2.41, 2.58, 2.76$ respectively.

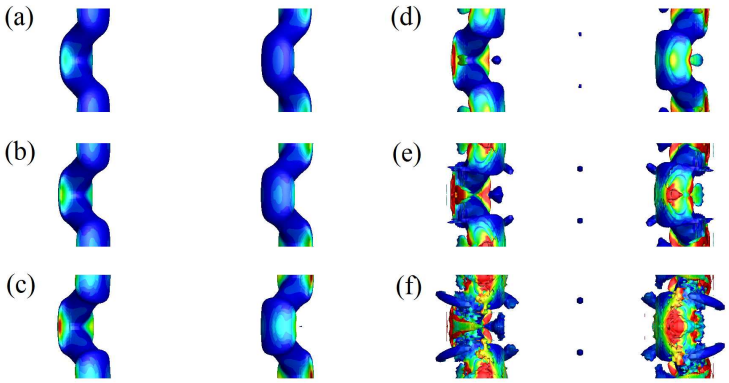

FIGURE 3.23: Time sequences of iso-surfaces of vorticity magnitude with dominant strain flooding plotted from a three-dimensional simulation of the two-vortex case with an axial extension corresponding to the elliptic instability at a wavenumber of $k\,a_1 = 2.12$. $Re = 20\,000$ for this simulation. (a)-(f) display the flow seeded with the perturbation that leads to optimum energy growth ($\tau = 5.35$) at $t/T_{2V} = 1.87, 2.05, 2.23, 2.41, 2.58, 2.76$ respectively.

is chosen to highlight the flow structures that occur as the elliptic instability enters the non-linear regime. Figure 3.21(a) shows that, when the elliptic instability has grown to the stage when it begins to cause a bulk change in the base flow, it begins by deforming the vortex pair at approximately $\pm 45^{\circ}$ with respect to the line between the centres of the vortex cores. The dominant strain on the vortices is maximum on the inside of the bend in the vortex, as is shown on the left hand side of figure 3.21(a). This peak in dominant strain increases and spreads over the outside of the bend, as shown in light blue on the right of figure 3.21(c). Figure 3.21(d) shows that lobes of λ_2 are beginning to form off the primary vortex pair and grow larger during the evolution.

Figure 3.22 shows iso-surfaces of the $[\omega_y^2 + \omega_x^2]^{0.5}$ field flooded with the dominant strain. It shows that early in the transition to the non-linear regime, the flow is predominantly two-dimensional with only a small amount of $[\omega_y^2+\omega_x^2]^{0.5}$ present (figure 3.22(a)) where the vortex cores are becoming distorted in a sinuous manner (figure 3.21(a)). At $t/T_{2V} = 2.05$, regions of $[\omega_y^2 + \omega_x^2]^{0.5}$ occur on the outside of the vortex cores, approximately perpendicular to the vortex cores (figure 3.22(c)). These regions of $[\omega_y^2 + \omega_x^2]^{0.5}$ grow into long lobes that begin to encircle the vortex cores (figure 3.22(d)). As the flow evolves into highly three-dimensional flow, the lobes of $[\omega_y^2 + \omega_x^2]^{0.5}$ almost completely encircle the vortex cores, while the fields within the vortex cores grow to dominate the vortex core (figure 3.22(f)). The regions of highest dominant strain (coloured red in the flooded contours) correspond with the regions of the vortex cores that are most distorted.

Figure 3.23 shows iso-surfaces of vorticity magnitude, flooded with the dominant strain. A comparison of figures 3.23(a) - (c) with figures 3.21(a) - (c) shows that the fields are the same, demonstrating that the ω_z^2 field is higher than the dominant strain. This indicates that the flow is dominated by the axial vorticity, and so the λ_2 field identifies a vortex core where the vorticity magnitude is dominated by the axial vorticity. As the flow evolves, the dominant strain becomes greater than the ω_z^2 field, showing differences between the iso-surfaces of λ_2 and vorticity magnitude (figures 3.21(d) and 3.23(d) respectively). These regions grow, forming lobes of vorticity magnitude (figure 3.23(f)) that are not present in the λ_2 field (figure 3.21(f)).

3.7 Summary

This chapter reported on the results of a study into the dynamics of an equal strength, counter-rotating, two-vortex system as a model of an aircraft wake created by the wings of the aircraft. The study began with a transient growth analysis at a range of axial wavenumbers. This study found that the first two Kelvin modes, [-1,1,1] and [-1,1,2], require a certain amount of time before they become apparent in the transient growth analysis. The [-1,1,1] mode only becomes apparent at $\tau = 2.67$ with an axial wavenumber of $k\,a_1 = 2.12$. The second mode, [-1,1,2], appears at $\tau = 3.56$ with an axial wavenumber of $k\,a_1 = 3.7$. It is interesting that, for the values of τ that were investigated, the Crow instability becomes apparent at $\tau = 1.78$ with an axial wavenumber of $k\,a_1 = 0.155$. This is of interest as the literature had identified the global mode of the Crow instability with an axial wavenumber of $k\,a = 0.18$ (Brion *et al.* 2007).

The transient growth analysis provides the perturbation that will lead to optimal energy growth, and an analysis of these fields for the Crow and elliptic instability was conducted. In addition, the fields were evolved using the linearised Navier–Stokes equations and investigated. It was found that the elliptic instability formed into the asymptotic solution of a pair of dipoles similar to that found in the literature. While the initial optimal perturbation field for the Crow instability at an axial wavenumber of $k\,a_1 = 0.155$ looks very different to the global mode, it does evolve into the global mode after a short period of time.

Next, a DNS study was conducted on both the elliptic and Crow instabilities, investigating the effect of seeding the flow with the optimal perturbations against white noise of similar energy magnitude. To the author's knowledge, this is the first time such a study has been conducted. This study found that the instability in the DNS seeded with the optimal perturbation quickly grew to a stage where it became non-linear and caused the base flow to deform significantly. By contrast, the perturbation that consisted of white noise began to decay almost immediately before growing after a very long period of time. This decaying of the white noise perturbation is because only a small number of instability mode shapes are conducive to growth. Because of this, the overall energy in the perturbation will appear to decay away, while the mode that is conducive to growth will begin at a very small magnitude and take a long period of time to grow to a magnitude where the total perturbation energy is dominated by the

energy of the modes conducive to growth.

Chapter 4

Results: Kinematics and stability of an equal-strength four-vortex system

This chapter covers the study of a four-vortex, counter-rotating aircraft wake model with symmetric vortex strength about the vertical mid-plane. This model is applicable to the far wake of virtually any fixed-wing aircraft, and also considers the effect of vertical displacement of the tail vortex pair. This significant vertical displacement is common on heavy lift aircraft as it allows for a design that facilitates easy loading of large items into the aircraft.

4.1 Equal-strength four-vortex system model

The initial position of the four-vortex system has already been defined in chapter 2. Figure 2.4 displays the initial positioning of the four-vortex systems for the high and flat tail models. Figure 2.4(a) shows the control case of the 'flat tail' configuration with $h/b_1 = 0$. Figure 2.4(b) shows the 'high tail' case with the tail vortex pair displaced vertically with $h/b_1 = 0.2$. This was chosen to correspond to the vertical displacement of the tail of the C-17 Globemaster aircraft relative to its wings. In chapter 4, a value of $\Gamma_2/\Gamma_1 = -0.4$ was chosen for the ratio between the wing and tail circulation and this corresponds to the values found in the literature for a heavy lift aircraft in landing configuration (Rennich & Lele 1999). The horizontal displacement of the tail to wing vortex separation was chosen to be $b_2/b_1 = 0.38$, which corresponds to the ratio of wing to tail span of the C-17 Globemaster aircraft.

For these studies, $a_1/b_1 = 0.176$ and the ratio of tail vortex core size, a_2, to wing vortex core size is $a_2/a_1 = 0.5$. This was chosen to make the tail vortices self-similar

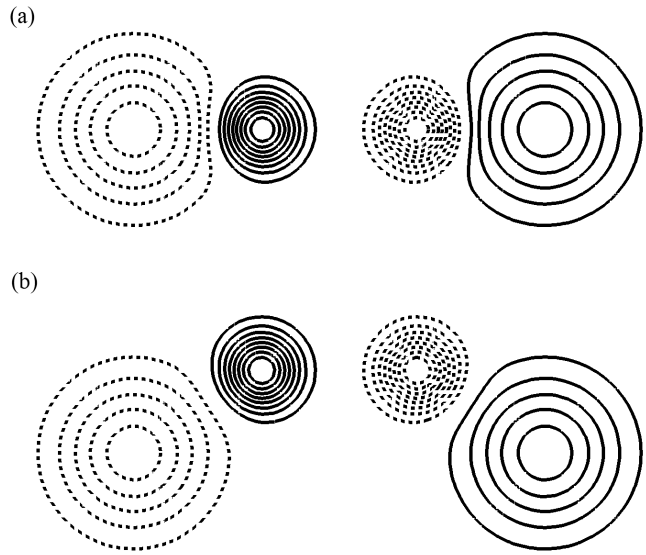

FIGURE 4.1: Contour plots of vorticity for the initial conditions of the (a) flat tail and (b) high tail case in two-dimensional space. Contour lines represent unit increments in non-dimensional vorticity. The minimum and maximum vorticity levels were -8 and 8 in the left and right tail vortices respectively. Dashed lines represent negative vorticity levels.

to the wing vortices.

All times are normalised by the initial orbit period of the tail vortex, T_0, around the wing vortex, consistent with previous four-vortex studies (Crouch 1997; Fabre & Jacquin 2000; Crouch *et al.* 2001). T_0 was calculated from a two-dimensional DNS of the 'high tail' case and the same value is used throughout, as the orbit period is the same for the 'high tail' and 'flat tail' cases.

4.2 Two-dimensional flow

In this section, the two-dimensional kinematics of the counter-rotating four-vortex model are considered first. Following this the circulation history of the vortices are considered, followed by the long-term stability of the system. The linearised transient growth model is considered last to elucidate the observations from the DNS.

4.2.1 Two-dimensional kinematics

To consider the two-dimensional kinematics, two cases were computed: the 'high tail' and 'flat tail' cases described in § 4.1. Figures 4.2 and 4.3 plot the trajectories of the vortices over $0 \leq t/T_0 \leq 0.5$ for the 'flat tail' and 'high tail' configurations respectively. Throughout this initial stage of their evolution, both cases are symmetric about the

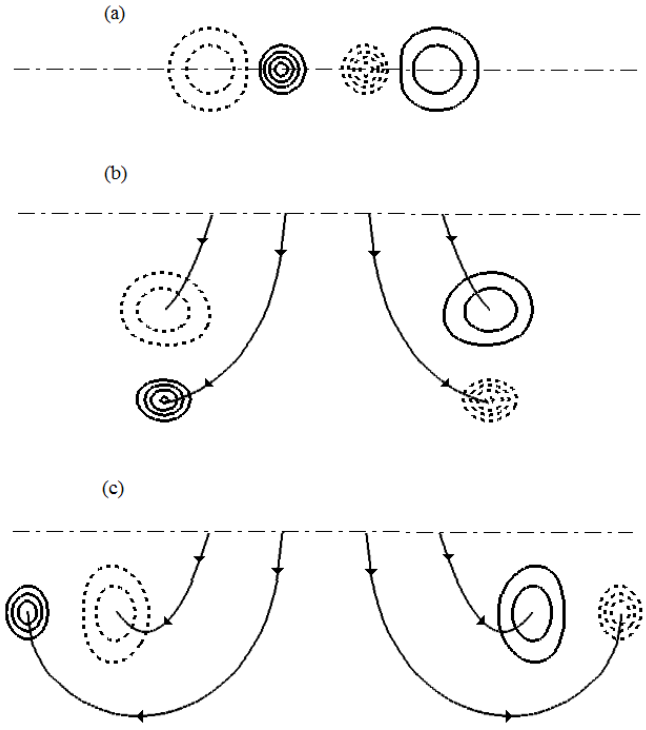

FIGURE 4.2: A time sequence of contour plots of vorticity for the 'flat tail' case at (a) $t/T_0 = 0$, (b) 0.25 and (c) 0.5. Contour lines are at vorticity increments of 2. The minimum vorticity is -8 and the maximum is 8 in the right- and left-tail vortex respectively. Dashed and solid lines represent negative and positive vorticity respectively. The dashed-dot line shows $y = 0$. The thin line with arrows shows the trajectory from the initial configuration of the four vortices.

vertical mid-plane. Figure 4.2 visualises the flow for the 'flat tail' two-dimensional case. This figure shows that the wing vortex pair only descends a small amount through $0 \leq t/T_0 \leq 0.5$. Figure 4.3 shows that the tail vortex pair descends considerably faster in the 'high tail' configuration during the same time period. In both cases the vortices adapt to the strain fields present from the surrounding vortices, with the wing and tail vortices all becoming elongated into elliptical shapes. An investigation into the strain rate is covered later in detail in § 4.2.4. Figures 4.2 and 4.3 show that a small difference in the initial vertical displacement of the tail can have a significant effect on the movement of the vortex pair produced by the main wing over a short timeframe. They also show that (at least initially) the flows are reflectively symmetric about the vertical centreline, and the weaker tail vortices orbit around their respective wing vortices.

The respective vertical travel of the wing vortex pairs for the two cases is considered in figure 4.4. As can be seen, the wing vortex pair in the 'flat tail' case only travels

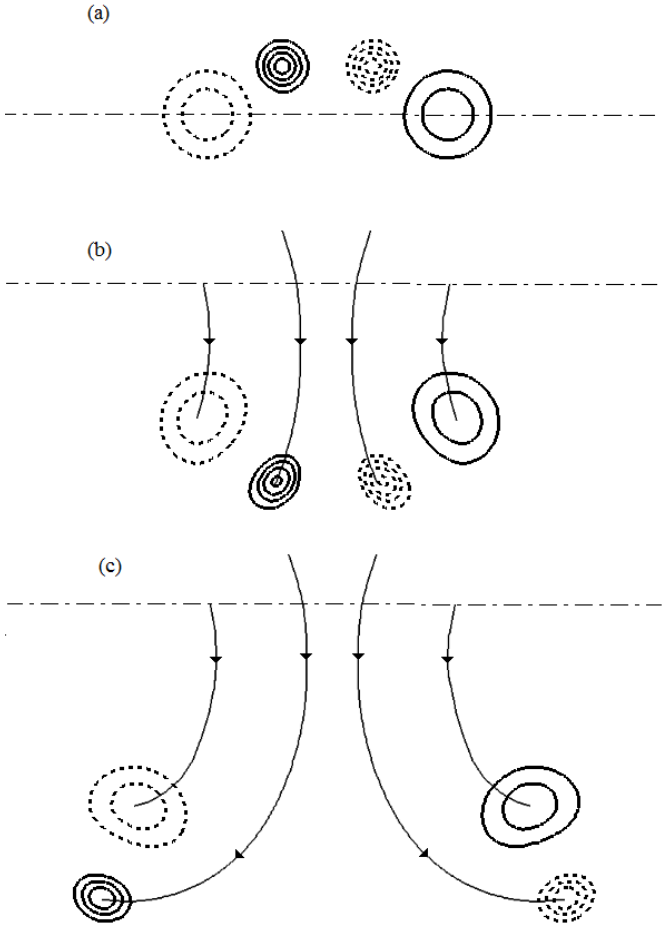

FIGURE 4.3: A time sequence of contour plots of vorticity for the 'high tail' case at (a) $t/T_0 = 0$, (b) 0.25 and (c) 0.5. Contour scale and lines are as per figure 4.2.

to a vertical displacement of approximately $0.36b_1$ from its initial position by time $t/T_0 = 0.5$, where as a change in the initial vertical displacement of the tail vortex pair by as little as $0.2b_1$ causes the wing vortex pair to descend to approximately $0.85b_1$ over the same normalised time period. This large difference in wing vortex drop is due to the tail vortex pair providing a downward induced velocity over a longer part of the cycle in the initial stages before each tail vortex swings beneath the corresponding wing vortex.

The behaviour shown in figure 4.2 and 4.3 can by extension show that as the tail vortices orbit the wing vortices, the downward propagation speed will vary significantly throughout the orbit period. This is due to the induced velocity on the wing vortex pair by the tail vortex pair changing direction as the tail vortex pair orbits the wing vortex pair. For example, when the tail vortices are inside the wing vortices, their induced

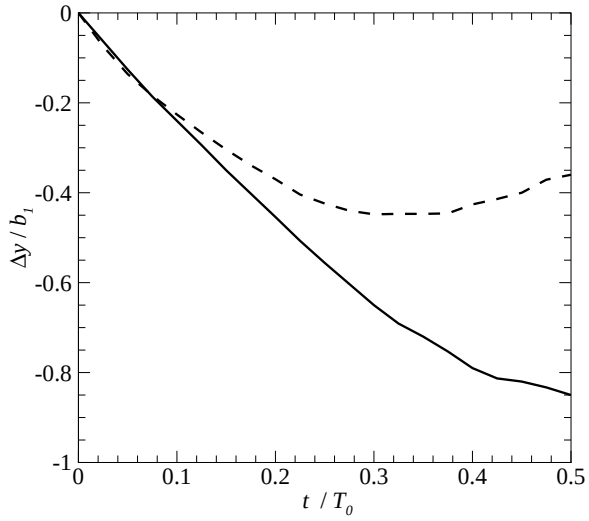

FIGURE 4.4: A plot of drop, against normalised time, t/T_0 of the centre of the wing vortex core, Δy, for the 'high tail' and 'flat tail' cases. The dashed line represents the 'flat tail' case and the solid line represents the 'high tail' case.

velocity acts to push their respective wing vortices downward, whereas when the tail vortices are outside, their induced velocity acts to retard the downward trajectories of the system. This rotation of the tail vortex pair will also induce a vibration in the wing vortex pair over the period of rotation of the tail vortex pair.

4.2.2 Vortex circulation history

This section examines the change in circulation of the wing and tail vortices for the 'high tail' and 'flat tail' cases. Figure 4.5(a) shows that the general trend of the tail circulation for both cases exhibits a decay in a qualitatively similar manner. Given that the Re of both cases is the same, the circulation decay is dependent only on viscosity. The 'high tail' case exhibits a small but sudden drop in circulation around $t/T_0 = 1.5$, which will be discussed shortly. The circulation for the wing vortex in both cases decays at a relatively constant rate, implying that viscous diffusion dominates the circulation reduction process and is unaffected by the initial vertical displacement of the tail vortex pair. It is interesting to note that the decay rate of both the tail and wing vortices is approximately the same, implying that the decay rate is independent of circulation.

The small increase in circulation in the 'high tail' wing vortex at $t/T_0 \approx 4.25$ is due to a postprocessing artifact, as a symmetry breaking instability shown in the next section causes some of the circulation from the tail vortex on the other side of the

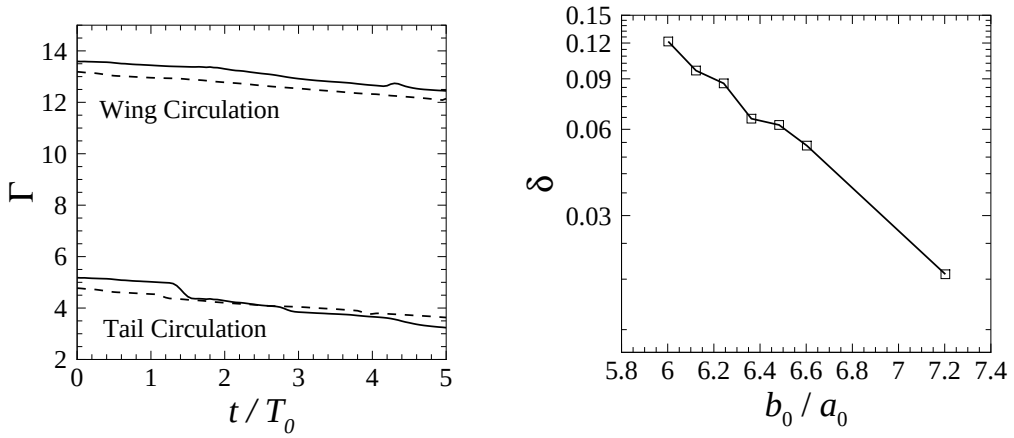

(a) (b)

FIGURE 4.5: (a) Time evolution of the circulation of the positive tail and wing vortex. The dashed lines show the circulation for the 'flat tail' cases and the solid lines show the 'high tail' cases. (b) Plot of the drop in tail vortex circulation to time $t/T_0 = 1.5$ for the 'high tail' case normalised by the initial tail vortex circulation, δ, as the weaker tail vortices pass between the stronger wing vortices against initial separation b_0/a_0. $Re = 20\,000$ for these simulations.

vertical mid-plane to enter the integration area used to calculate the circulation.

A number of two-dimensional simulations were run to examine the circulation drop present in figure 4.5(a) at $t/T_0 = 1.5$ for the 'high tail' case. The only variable that was changed was the vortex separation b_0/a_0, starting at $b_0/a_0 = 5.67$ used for the reference case, and increasing to $b_0/a_0 = 7.20$ where the circulation drop is almost negligible ($\delta = 0.018$). Figure 4.5(b) shows that the tail circulation drop present in figure 4.5(a) at $t/T_0 = 1.5$ for the 'high tail' case, is directly related to the initial horizontal spacing of the vortex system. When the vortices are placed closer together, more circulation is pulled off the tail vortex pair by the wing vortex pair as they are strained through the small space between the stronger wing vortex pair. It is this process that leads to the sudden circulation decrease seen for the 'high tail' tail vortex in figure 4.5(a).

4.2.3 Two-dimensional stability

This section examines the two-dimensional stability of the 'high tail' and 'flat tail' systems by examining the u-velocity component recorded at the position (0,0). Figure 4.6 shows a time history of the u-velocity component recorded at the position (0,0) for the 'flat tail' and 'high tail' cases described in the previous section. If the flow remains

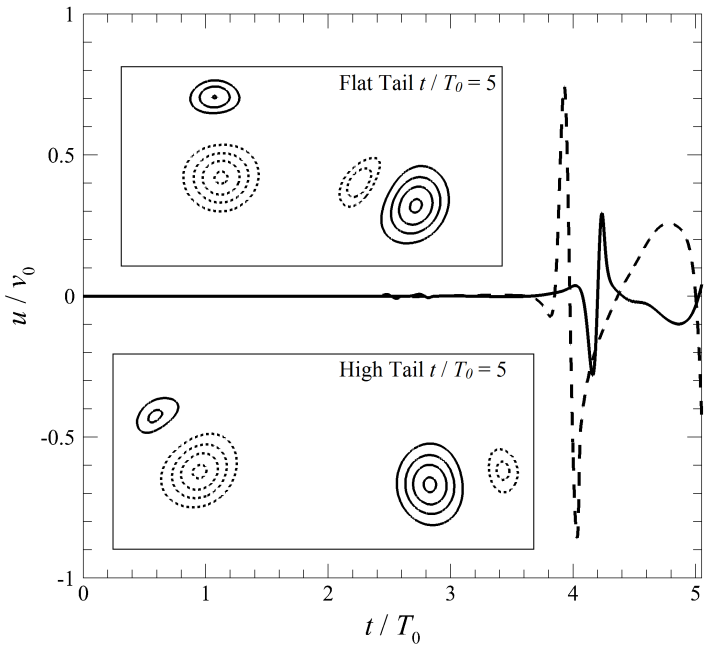

FIGURE 4.6: Plot of velocity in the x-direction against time for the position (0,0). The solid line represents the velocity for the 'high tail' case and the dashed line represents the flat tail case. The contour plots show the vorticity of the 'flat tail' and 'high tail' configurations as show at $t/T_0 = 5$. The minimum vorticity is -4 and the maximum is 4 in the right and left wing vortex respectively. Each contour line represents an unit increment of vorticity. Dashed and solid lines represent negative and positive vorticity respectively.

symmetrical about $x/b_1 = 0$, then the u-velocity at this point will remain zero. While any number of points would provide information about a break in symmetry about $x/b_1 = 0$, the location (0,0), between the wing vortices, lies in what is presumed to be the most sensitive position for asymmetry to be exhibited. As can be seen in the figure, the 'flat tail' case begins to show a slight disturbance in the velocity at $t/T_0 \approx 2.6$, as the tail vortex pair is squeezed between the wing vortex pair. This velocity disturbance increases in magnitude as a major symmetry-breaking instability develops in the flow. The inset vorticity contour plot shows that by $t/T_0 = 5$, the former reflective symmetry has been completely destroyed. This symmetry-breaking instability ultimately causes the system to become severely unbalanced. This symmetry breaking instability is covered in greater detail in § 4.2.5.

It can been seen in figure 4.6 that the 'high tail' case undergoes a similar symmetry-breaking instability, but while it is seen to develop at the same part of the tail orbit cycle, when the tail vortex pair passes between the wing vortex pair, its magnitude

is significantly smaller than that produced by the 'flat tail' arrangement at the corresponding point in the cycle. As a result of this, the 'high tail' case is not as unbalanced as the 'flat tail' case at $t/T_0 = 5$. The spikes in u-velocity are due to only one vortex being in the region between the wing vortex pair. The higher spike in u-velocity for the 'flat tail' case is due to this case being more asymmetric than the 'high tail' case around $t/T_0 \approx 4$.

These simulations were not explicitly perturbed, but instead the symmetry-breaking disturbance has developed from noise at the limit of machine precision. This demonstrates the extraordinary amplification of disturbances produced by these flows, and motivates the employment of transient growth analysis to investigate two- and three-dimensional perturbations throughout this thesis. The results in figure 4.6 imply that the 'flat tail' case is more susceptible to white-noise disturbances over a long time-frame in a two-dimensional plane. This is most likely due to the tail vortex pair in the 'flat tail' case beginning in a highly strained region between the stronger wing vortex pair. This also implies that the initial position of the tail vortex pair in relation to the wing vortex pair will have a significant effect on the onset of the symmetry breaking instability.

4.2.4 Strain rates at vortex centres

The strain rate (defined in § 1.2.2) was calculated at the centres of the vortices and their time histories are plotted in figure 4.7. The externally imposed strain on a vortex is the primary driving mechanism in the elliptic instability, as it causes the circular cross-section of the vortex to become elliptical (Moore & Saffman 1975; Tsai & Widnall 1976). As this is the primary driving mechanism for the elliptic instability, it is useful to understand how the strain varies through time.

It is interesting to note that the strain at the wing vortices is almost exactly the same for both the 'high tail' and 'flat tail' cases. In contrast, the strain at the tail vortices does differ a significant amount, with the strain at the tail vortex of the 'high tail' case being higher for $0 \leq t/T_0 \leq 0.5$. This significantly higher strain rate is due to the initial state of the tail vortices just entering the highly strained region between the wing vortex pair. Initially, the 'high tail' tail vortex experiences slightly less strain than the 'flat tail' tail vortex, as it is slightly further from the cores of the wing vortices. However, as it convects into the highly strained region, the tail vortices experience an

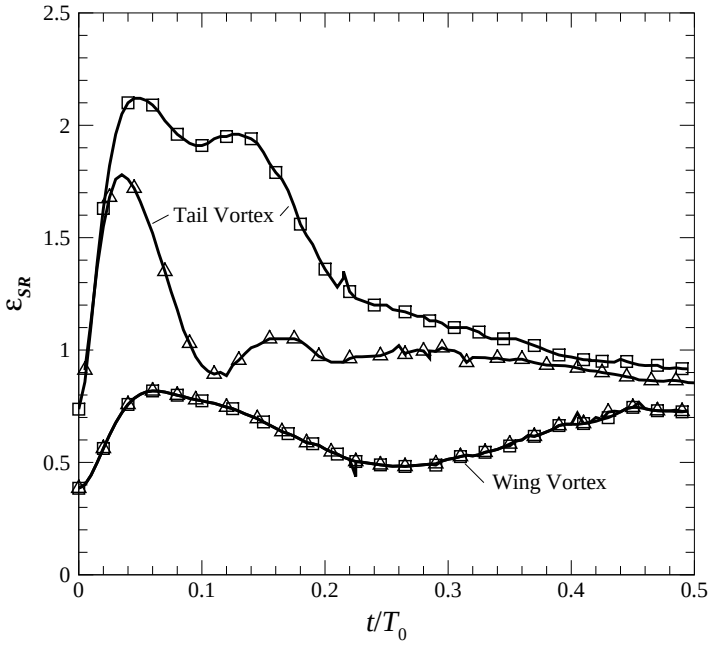

FIGURE 4.7: Plot of strainrate, ϵ_{SR}, against t/T_0 at the center of one of the wing and tail vortices for an axial wavenumber of $k\,a_1 = 0$ for the 'high tail' and 'flat tail' cases. $\triangle$ and $\square$ represent the 'flat tail' and 'high tail' case respectively.

externally imposed strain from both wing vortices as well as the other tail vortex. As the initial condition for the 'flat tail' case is half-way through the highly strained region between the wing vortex pair, the time it is within this region is significantly less and so drops off more quickly in the evolution time history shown in figure 4.7.

Figure 4.8(a) plots the same data as figure 4.7, but over a longer timeframe. It is of interest to note that the strainrate at the centres of the tail vortices peak to a similar value for both the 'high tail' and 'flat tail' case, with the 'high tail' case lagging slightly behind. This is because the tail vortices in the 'high tail' case enter the highly strained region between the wing vortex pair at a slightly later time to the 'flat tail' case. The observation of a similar trend between the cases, but with a time lag, implies that the four-vortex system can be modeled as a more general system, with the initial position of the tail vortex pair in the orbit path being the variable to be examined. This general case is investigated in § 4.4. The larger strain experienced by the tail vortex pair in both cases is likely to cause the elliptic instability to grow at a significantly higher rate than an instability in the wing vortex pair. The regions where the strain imposed on the tail vortex pair is at its highest is during the times where the tail vortex pair

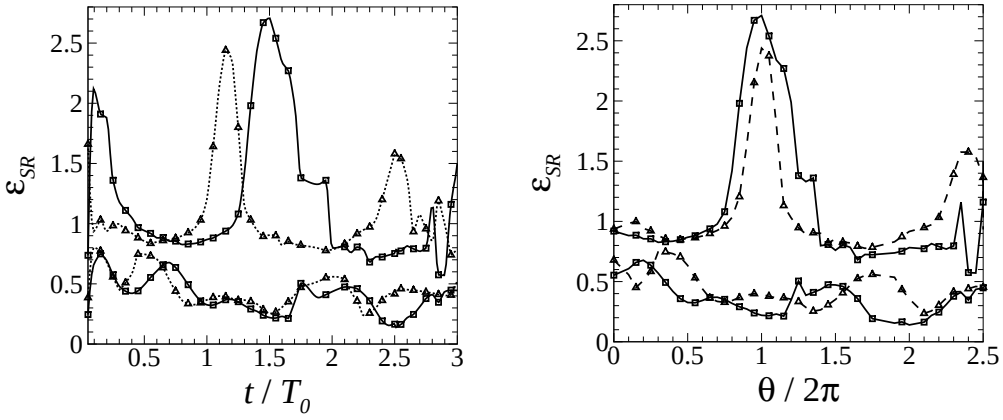

(a) (b)

FIGURE 4.8: Plot of strain rate, ϵ_{SR}, against (a) t/T_0 and (b) angle of the tail vortices in radians around the wing vortices (with the 'flat tail' case as zero angle) at the center of one of the wing and tail vortices for an axial wavenumber of $k\,a_1 = 0$ for the 'high tail' and 'flat tail' cases. △ and □ represents the 'flat tail' and 'high tail' case respectively. Note that the symbols shown are only every third data point.

are located within the region directly between the wing vortex pair. This can be used to predict that the instability growth during the times when the tail vortex pair are located in this highly strained region will be significantly higher than at other times. This hypothesis is investigated in section 4.3.

Figure 4.8(b) shows the change in strain in the wing and tail vortices as a function of the angle of the tail vortices from a (horizontal) orientation such as used ton initiate the 'flat tail' configuration. It demonstrates that the tail vortices experience the same very large peak in strain as they pass through the region directly between the wing vortices ($\theta = 2\pi$), with the tail vortices in the 'high tail' case experiencing slightly higher strain. It also demonstrates that the strain experienced by the tail vortices is significantly lower outside the highly strained region between the wing vortices.

Both cases begin with almost no strain, due to the numerical requirement for the vortices to relax from the imposed initial conditions to a state adapted to the presence of the other vortices and the strains that they impose. Due to the constantly changing motion of the vortices, the strain rate is also constantly changing, preventing a dedicated relaxation time. It is interesting to note that the strain rate is significantly higher than previous analytical studies (Leweke & Williamson 1998). This significantly higher strain may lead to the observation of other instability mode shapes.

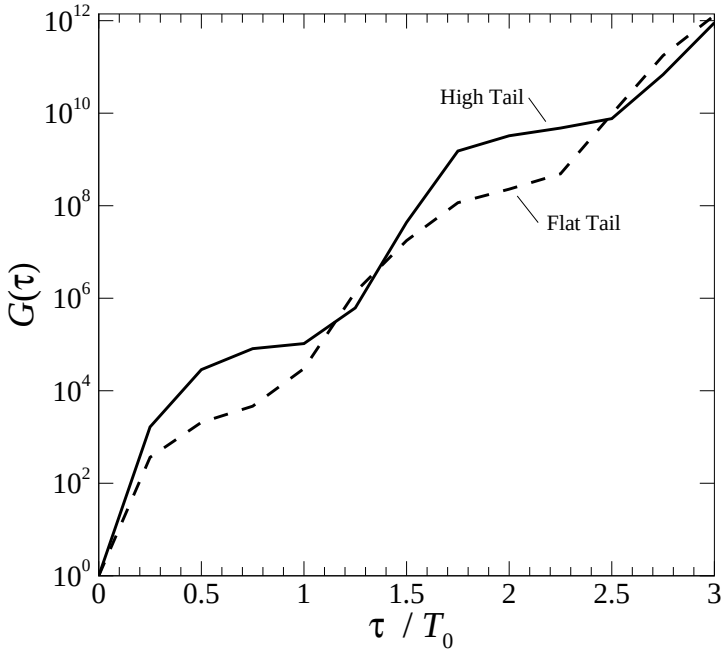

FIGURE 4.9: Plot of transient growth amplification factor, $G(\tau)$, against τ/T_0 for an axial wavenumber $k\,a_1 = 0$, and an initial time, $t_0/T_0 = 0$.

4.2.5 Transient growth

A transient growth analysis was computed for $0 \leq \tau/T_0 \leq 3$ for a two-dimensional disturbance with an axial wavenumber of $k\,a_1 = 0$, and the resulting amplification factor eigenvalues from this study are shown in figure 4.9. § 4.2.3 demonstrated that both the 'high tail' and 'flat tail' cases are naturally unstable in two-dimensional space. It can be seen in figure 4.9 that the 'high tail' case has consistently higher growth amplification factors for all values of τ below $\tau/T_0 = 2.5$. That the 'flat tail' case has higher $G(\tau)$ above $\tau/T_0 = 2.5$ fits with the previous data (figure 4.6), showing that over long timeframes, the 'flat tail' case will display symmetry breaking instability at an earlier time than the 'high tail' case. This is particularly visible in figure 4.6 at $t/T_0 = 4$, where the instability occurs at a similar time for both cases, but the magnitude is higher for the 'flat tail' case. The plateaus that can be seen in the 'high tail', and to a lesser extent the 'flat tail' case, at $0.5 \leq \tau/T_0 \leq 1$, correspond to times where the tail vortices are located on the outside of the vortex system, and are not subjected to the strong external strain field present between the stronger wing vortices. This plateau effect can also be seen around $2 \leq \tau/T_0 \leq 2.5$, which again is a region

where the tail vortices are outside the highly strained region between the wing vortex pair. This strongly implies that the primary mechanism for transient growth is directly related to the position of the tail vortices in relation to the wing vortices. Both the 'flat tail' and 'high tail' cases demonstrate extremely large growth amplification factors (in the order of 10^{12}) at $\tau/T_0 = 3$. These extremely large growth amplification factors strongly imply that, in a physical experiment, the flows would be dominated by localized transient disturbance growth rather than asymptotic instabilities (Barkley *et al.* 2008). Given the accuracy of double-precision arithmetic (accuracy of approximately 10^{-13}), errors at machine level can easily cause the two-dimensional flow to become unstable without the addition of additional disturbances (as shown in figure 4.6). Moreover, machine noise is many orders of magnitude smaller than what can be achieved in the laboratory, making it almost certain that these disturbances would be seen in practice.

The symmetry breaking instability described in figure 4.6 shows a very small ripple in the u-velocity (measured at the centre of the four-vortex system) at approximately $t/T_0 = 2.5$, which is consistent with the growth amplification factor shown in figure 4.9. At $t/T_0 = 2.5$ the growth amplification factor is $G(\tau) \approx 10^{10}$, and since the symmetry breaking instability (observed in figure 4.6) would be caused by errors at machine level arithmetic in the two-dimensional DNS (errors of an order of approximately 10^{-13}), the instability would have grown to a stage where it was becoming observable.

4.3 Three-dimensional flow

This section describes an investigation into the three-dimensional dynamics of the 'high tail' and 'flat tail' cases. First, the section covers a transient growth analysis to identify the peak axial wavenumbers where the growth amplification factor is a maximum. Next, it examines how the optimal perturbation fields found from the transient growth analysis at the peak axial wavenumber evolve in the linear domain. Then the section covers the overall dynamics of the 'high tail' and 'flat tail' cases through the use of three-dimensional DNS. Lastly, this section covers an investigation into the mechanisms that cause the 'flat tail' and 'high tail' cases to transition into non-linear growth.

4.3.1 Transient growth analysis

A transient growth analysis was conducted to examine the transient response of the 'high tail' and 'flat tail' cases in a three-dimensional domain. Figure 4.10(a) shows,

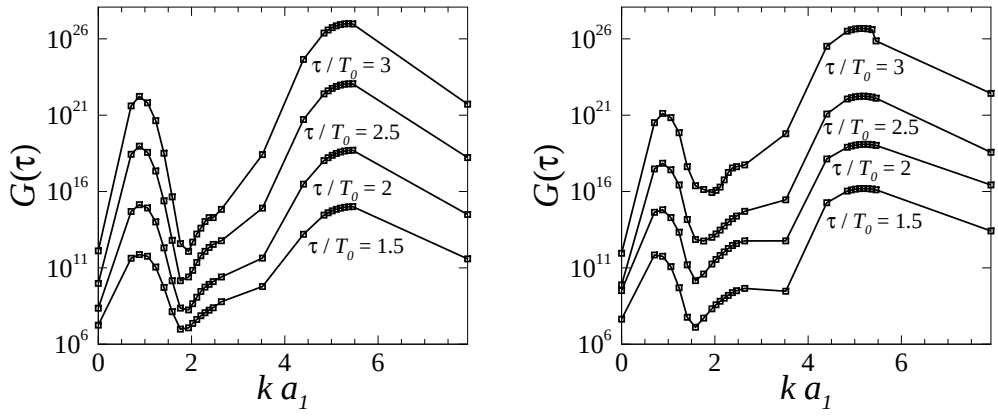

(a) (b)

FIGURE 4.10: Plot of (a) 'flat tail' and (b) 'high tail' transient growth amplification factor, $G(\tau)$, against non-dimensional axial wavenumber, $k\,a_1$, for an initial time of $t_0/T_0 = 0$. Each line represents a τ/T_0 value as shown.

for the 'flat tail' case, how the growth amplification factor, $G(\tau)$, changes with the non-dimensional axial wavenumber, $k\,a_1$, of the perturbation as well as the time that the perturbation is allowed to grow, τ/T_0. It is seen that as τ/T_0 increases, the general trend of the growth amplification factor against non-dimensional axial wavenumber remains similar. The peak growth for a given time interval occurs consistently for an axial wavenumber $k\,a_1 = 5.3$. This is interesting, as it shows, that regardless of the timeframe over which the perturbation is allowed to grow, the maximum growth amplification factor will occur at the same wavenumber (it is important to note that when normalised by the tail vortex, the normalised axial wavenumber is $k\,a_2 = 2.65$, which is more consistent with prior studies; Laporte & Corjon 2000). This means that a control system developed to incite the disturbance of this coherent vortex flow would only need to perturb the flow consistently at a frequency corresponding to this specific wavenumber in a trailing aircraft wake. The high value of $G(\tau)$ at the peak wavenumber indicates that it is likely that the perturbation is of sufficient size to cause large changes in the base flow, and that the flow is likely to be dominated by transient disturbance growth (Barkley *et al.* 2008).

Figure 4.10(b) shows, for the 'high tail' case, how $G(\tau)$ changes with $k\,a_1$ as well as the time that the perturbation is allowed to grow, τ/T_0. It shows qualitatively similar characteristics to the 'flat tail' case and peaks at a very similar axial wavenumber,

$k\,a_1 = 5.3$. Although not necessarily obvious on a logarithmic scale, it is interesting to note that the peak growth for the 'flat tail' case is higher, by approximately 200% at $\tau = 3$, than the 'high tail' case, indicating that it is more susceptible to transient growth. It is important to note that the peak growth amplification factor, $k\,a_1 = 5.3$, for both three-dimensional cases at $\tau/T_0 = 3$ is significantly higher ($G(\tau) \approx 10^{26}$) than the $k\,a_1 = 0$ case at $\tau/T_0 = 3$ shown in figure 4.9 ($G(\tau) \approx 10^{12}$). This indicates that the instabilities that affect this base flow field will be predominantly three-dimensional.

An interesting point that is shared by both the 'high tail' and 'flat tail' cases is a small peak at $k\,a_1 = 2.38$, displaying a growth amplification factor of $G(\tau) = 3.53 \times 10^{17}$ for the 'high tail' case and $G(\tau) = 1.96 \times 10^{14}$ for the 'flat tail' case. This peak corresponds to an axial wavenumber where the wing vortices are most susceptible to transient growth, and as the core size of the wing vortices is double the tail vortices, $a_2/a_1 = 0.5$, it is reasonable to expect the peak axial wavenumber for the wing vortices to be approximately half that of the tail vortices. Importantly, the prior assumption that the highest growth rate corresponds to an instability is correct, and is also shown in § 4.3.3.

Both cases also demonstrate a large long wavelength peak at $k\,a_1 = 0.88$ and 0.90 for the 'flat tail' and 'high tail' cases at $\tau/T_0 = 3$ respectively. It is interesting to note that both cases exhibit a small amount of drift with increasing value of τ. While the long wavelength peak is significantly smaller than the short wavelength peak, it still demonstrates significant growth amplification of $G(\tau) = 1.45 \times 10^{22}$ and 1.28×10^{21} for the 'flat tail' and 'high tail' cases at $\tau/T_0 = 3$ respectively. The larger value of $G(\tau)$ for the 'flat tail' case is of interest as it follows the same trend of the short wavelength instability.

The significantly smaller peak growth amplification factor for the wing vortices, compared to the overall peak, can be explained by the significant difference in strain that the vortices experience. Figure 4.8 clearly demonstrates that the externally imposed strain experienced by the wing vortices is significantly smaller than the strain experienced by the tail vortices.

As the growth amplification factor is significantly higher for the overall peak, where the tail vortices are expected to have a peak instability, than the smaller peak where the wing vortices are expected to exhibit peak instability growth (10^9 for the 'high tail' and 10^{12} for the 'flat tail'), the DNS examined in § 4.3.4 will focus on the axial wavenumber

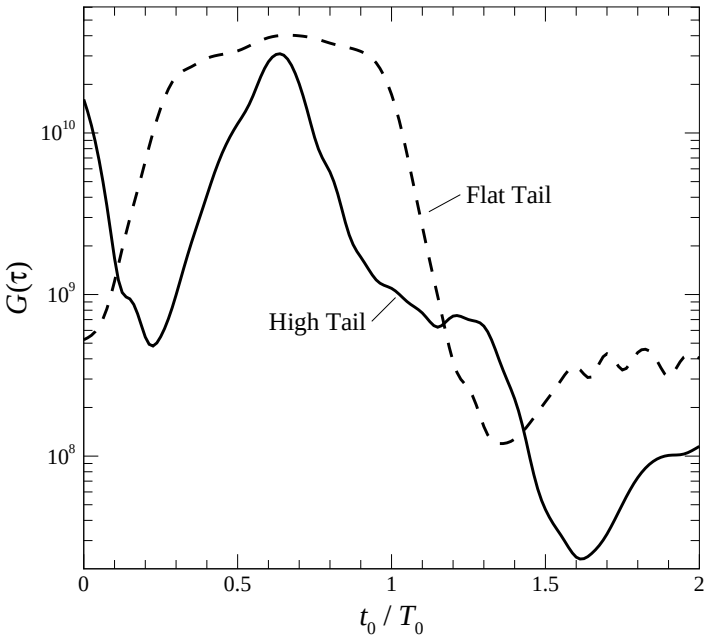

FIGURE 4.11: Plot of growth amplification factor, $G(\tau)$ against initial time, t_0/T_0. The wavenumber for both 'flat tail' and 'high tail' configurations are fixed at $ka_0 = 5.3$, and $\tau/T_0 = 1$.

of $k\,a_1 = 5.3$ (when normalised by the tail vortex pair it becomes $k\,a_2 = 2.65$). While the instability for the wing vortices should occur in reality, the timescale of the development of the instability would be significantly longer than the mode at $k\,a_1 = 5.3$, therefore the DNS examined in § 4.3.4 will accurately predict the initial non-linear development for the perturbations in the flow.

An important parameter in the transient growth analysis is the time at which the disturbance is added to the system, t_0. Figure 4.11 shows how a change in t_0 affects the growth amplification factor at the previously discovered peak axial wavenumber, $k\,a_1 = 5.3$. It can be seen in figure 4.11 that, for both vortex configurations, the stability of the flow varies with this initial time to a significant degree. As the tail vortex pair orbits the wing vortex pair, it experiences an increase, and then a decrease, in stability. Here the analysis was conducted using $\tau/T_0 = 1$, so the perturbations for the 'flat tail' case grow through the region in the strain (corresponding to $0.6 \leq t/T_0 \leq 1.6$ in figure 4.8 where the tail vortex pair in the 'flat tail' case reaches a very large peak). As the time horizon for the transient growth analysis overlaps less of this peak, the growth amplification factor drops off significantly. This is also demonstrated in the 'high tail'

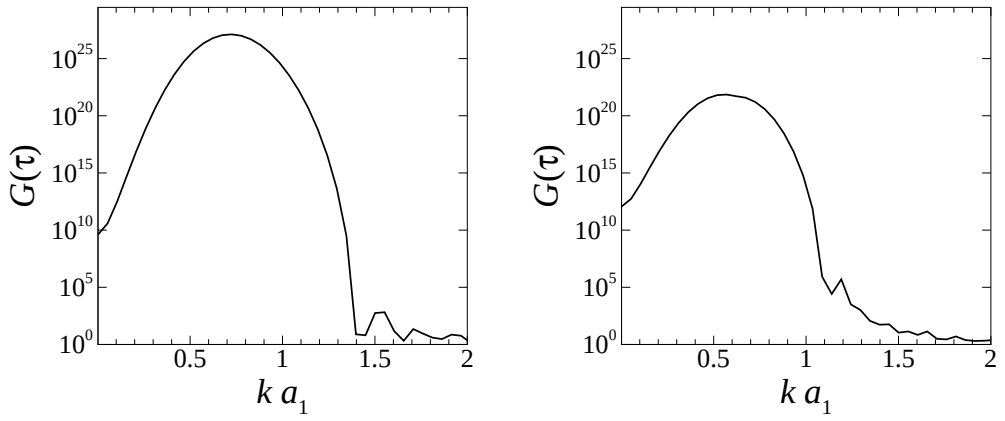

(a) (b)

FIGURE 4.12: Plot of (a) 'flat tail' and (b) 'high tail' transient growth amplification factor, $G(\tau)$, against non-dimensional axial wavenumber, $k\,a_1$, for an initial time of $t_0/T_0 = 0$. $\tau/T_0 = 3$ for these simulations. The solid line represents the vortex filament study conducted for the long wavelength Crow instability.

case, as the transient growth analysis with a start time of $t_0/T_0 = 0.25$ demonstrates a dip in the growth amplification factor (in figure 4.11) and this corresponds to the lower strain experienced by the tail vortex pair at $0.25 \leq t/T_0 \leq 1.25$ shown in figure 4.8.

It is interesting to note that, for $0.1 \leq t_0/T_0 \leq 1.2$, both cases produce the same general trend, with the high tail having a much narrower range in which it peaks. This suggests that the 'flat tail' case is initially susceptible to perturbations for a longer duration of its rotation. This also implies that the position of the tail vortex pair determines the characteristics of the transient growth of perturbations to the system for both cases during at least the first two orbits. It is also interesting to note that the growth amplification factor of the 'flat tail' case is higher than the 'high tail' case for all times except $1.2 \leq t_0/T_0 \leq 1.4$. This suggests that the 'flat tail' configuration is more susceptible to transient growth of perturbations than the 'high tail' configuration, for the majority of the first two tail orbits.

4.3.2 Vortex filament analysis

By utilising the method described in § 2.7, a theoretical prediction of the peak axial wavenumber expected for the Crow instability. This section demonstrates that the vortex filament method can provide a reasonable prediction for the four-vortex 'flat tail' and 'high tail' cases.

Figure 4.12(a) shows the results of a vortex filament analysis for the 'flat tail' case. The vortex filament method provides a good estimation of the peak axial wavenumber for the Crow instability, finding a peak with an axial wavenumber of $k\,a_1 = 0.75$. This corresponds very well with the peak found in the transient growth analysis, (figure 4.10(a)) $k\,a_1 = 0.87$. That the axial wavenumbers correspond very well indicates that the instability that the transient growth analysis found is definitely the Crow instability.

Figure 4.12(b) shows the results of a vortex filament analysis for the 'high tail' case. As with the 'flat tail' case, the vortex filament method provides a good estimation of the peak axial wavenumber for the Crow instability, finding a peak with an axial wavenumber of $k\,a_1 = 0.59$. This corresponds well with the peak for the transient growth analysis, $k\,a_1 = 0.87$.

As with the two-vortex case, the difference in $G(\tau)$ is due to the limitation of the vortex filament method assuming the shape of the instability mode, while the transient growth analysis finds the perturbation that leads to optimal energy growth and is limited only by available spatial resolution. The vortex filament method described here (and the method utilised by Crouch 1997) does provide a good approximation as to the expected peak axial wavenumbers, but is limited because of the need to specify a specific mode shape for the analysis and the lack of viscous interaction between the vortices.

4.3.3 Optimal perturbation fields

In this section the linearised evolution of the predicted optimal initial disturbances is considered for the three-dimensional asymmetric 'high tail' and 'flat tail' cases.

4.3.3.1 Evolution of short wavelength instability

Figure 4.13 shows the temporal evolution of the linearised perturbations, beginning with the initial optimal perturbation field, for the 'flat tail' case excited at the axial wavenumber ($k\,a_1 = 5.3$) that corresponds to the peak growth amplification factor found from the transient growth analysis. The initial perturbation field, seen in figure 4.13(a), shows that the majority of the perturbation is centered on the tail vortex pair, with tendrils of perturbation vorticity between and around the vortices. At $t/T_0 = 0.25$ (figure 4.13(b)), the perturbation vorticity has become concentrated in the tail vortex pair, with only a small magnitude circling around the wing vortex pair. From $t/T_0 = 0.5$

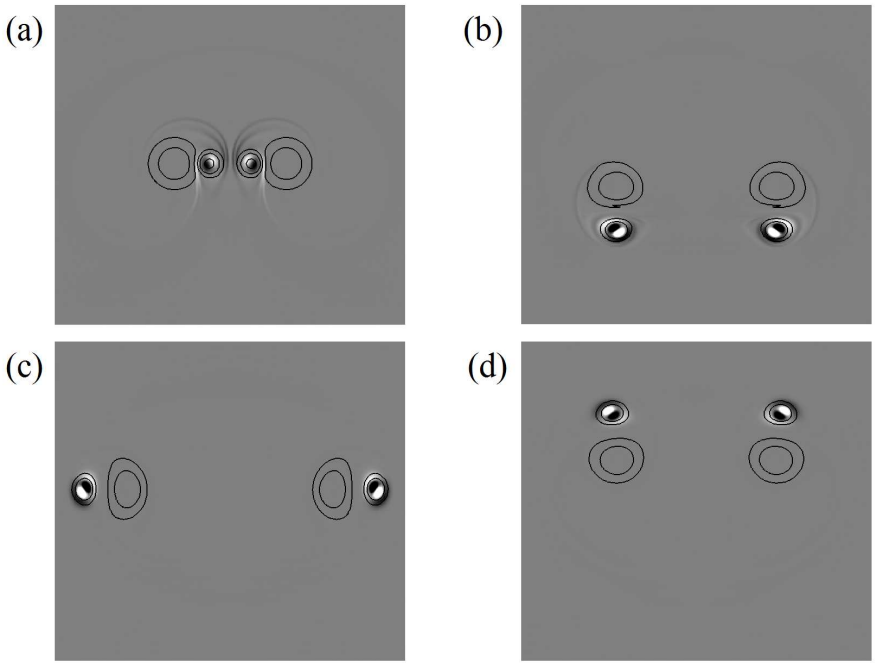

FIGURE 4.13: A time sequence of plots of spanwise vorticity in the linearised perturbation field (flooded contours) for the 'flat tail' case with an axial wavenumber of $k\,a_1 = 5.3$. Flooded contour levels are chosen arbitrarily to display the perturbation structure in each frame. The simulation was initialised with the optimal disturbance acquired with $\tau/T_0 = 3$. Solid contour lines show spanwise vorticity in the base flow at levels of vorticity of $\mid \omega_z \mid = 1, 3, 7$. (a)-(d) represent $t/T_0 = 0, 0.25, 0.5, 0.75$ respectively.

(figure 4.13(c)), the perturbation is only concentrated in the tail vortex pair, resembling a dipole similar to the elliptic instability with a mode of [-1,1,1]. It can be seen that this dipole rotates as the tail vortices are pulled around the stronger wing vortices, leading to the same vorticity sign of the dipole always facing the wing vortex. The dipole is arranged at an angle of 45° to a line between the wing and tail vortex centres. This is very similar to the elliptic instability with a mode of [-1,1,1] in a counter-rotating, equal strength vortex pair. This instability mechanism implies that the instabilities in these perturbations are due to the mutually imposed strain between the wing and tail vortices (Leweke & Williamson 1998; Le Dizès & Laporte 2002; So *et al.* 2011).

Figure 4.14 shows the temporal evolution of the linearised perturbations, beginning with the initial optimal perturbation field, for the 'high tail' case excited at the axial wavenumber ($k\,a_1 = 5.3$). This corresponds to the peak growth amplification factor found from the transient growth analysis. The initial perturbation field, figure 4.14(a), shows that the majority of the optimal disturbance structure is concentrated in a thin

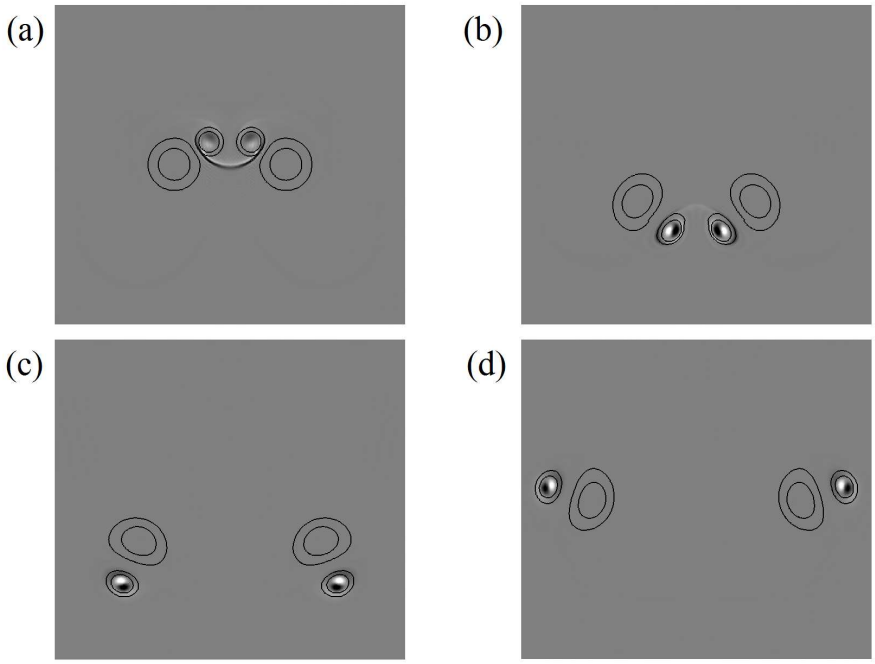

FIGURE 4.14: A time sequence of plots of spanwise vorticity in the linearised perturbation field (flooded contours) for the 'high tail' case, with an axial wavenumber of $k\,a_1 = 5.3$. Flooded contour levels are chosen arbitrarily to display the perturbation structure. The simulations was initialised with the optimal disturbance acquired with $\tau/T_0 = 3$. Solid contour lines show spanwise vorticity in the base flow at levels of vorticity of $\mid \omega_z \mid = 1, 3, 7$. (a)-(d) represent $t/T_0 = 0, 0.25, 0.5$ and 0.75 respectively.

band connecting the tail vortices. This thin band of vorticity is reminiscent of the optimal disturbance feeding the mode [-1,1,1] elliptic instability for the two-vortex case studied in chapter 3 and shown in figure 3.5. Like the evolution of the mode [-1,1,1] elliptic instability in the two-vortex case (figure 3.9), at $t/T_0 = 0.25$ for the 'high tail' case (figure 4.14(b)), the majority of the perturbation vorticity has become concentrated in the tail vortex pair, with only a small connection between them. From $t/T_0 = 0.5$ (figure 4.14(c)), the perturbation is only concentrated in the tail vortex pair, resembling a dipole similar to the elliptic instability with a mode of [-1,1,1], identifiable as it only contains a pair of lobes of opposite sign vorticity within the vortex cores. It can be seen that the dipole rotates as the tail vortices are pulled around the stronger wing vortices, leading to the same vorticity sign of the dipole always facing the wing vortex at an angle of 45° to the line between the wing and tail vortex centres. Similar to previous studies (Leweke & Williamson 1998; Laporte & Corjon 2000; So *et al.* 2011), an angle of 45° is anticipated as the majority of the interaction is between the wing and tail vortex pair.

The similarities between the 'flat tail' and 'high tail' cases, both forming dipole perturbations in the tail vortex pair at 45° to the line between the wing and tail vortex centres, demonstrate that the same instability mechanism is present here. This instability is very similar to an elliptic instability with a mode of [-1,1,1] in an equal strength, counter-rotating vortex pair, and so implies that the underlying mechanism is the mutually imposed strain between the stronger wing vortices and the weaker tail vortices. This result is very similar to the study conducted by So *et al.* (2011) for a circulation ratio of $\Gamma_1/\Gamma_2 = -0.3$, demonstrating a very strong perturbation of mode [-1,1,1] within the weaker vortex, but almost nothing within the stronger vortex. It is interesting to note that the theoretical peak axial wavenumber for an unequal vortex pair with circulation ratio of $\Gamma_1/\Gamma_2 = -0.4$ that So *et al.* (2011) found, was around $k\,a_1 \approx 2.9$. As So *et al.* (2011) used the same vortex core size for both vortices, it is not surprising that the peak axial wavenumber, $k\,a_1 = 5.3$, in the current case where the weaker tail vortices have a vortex core half the size of the wing vortices is approximately double (therefore when normalised by the tail vortex core size the axial wavenumber becomes $k\,a_2 = 2.65$), while still retaining the mode [-1,1,1] elliptic instability mode shape in the weaker vortex. That the peak axial wavenumber is not exactly double that of the isolated unequal vortex pair, will be due to the difference in rotation of the vortex system (Laporte & Corjon 2000), which in this study, is caused by the presence of the other two vortices.

4.3.3.2 Evolution of long wavelength instability

Figure 4.15 shows the temporal evolution of the linearised perturbations, beginning with the initial optimal perturbation field, for the 'flat tail' case excited at the axial wavenumber ($k\,a_1 = 0.881$) that corresponds to the growth amplification factor of the secondary, long wavelength peak found from the transient growth analysis. The optimal perturbation field begins with smears of opposing sign vorticity between the wing and tail vortices (figure 4.15(a)). As the perturbation evolves, a dipole of opposing sign vorticity forms within the tail vortices at an angle of approximately 45° to a line between the centre of the tail vortex and its corresponding wing vortex core (figure 4.15(b)). Unlike the short wavelength mode examined in § 4.3.3.1, the perturbation dipoles do not exhibit reflective symmetry about the mid-plane. This lack of reflective symmetry is typical of the Crow instability. It is also of interest that like the short wavelength mode,

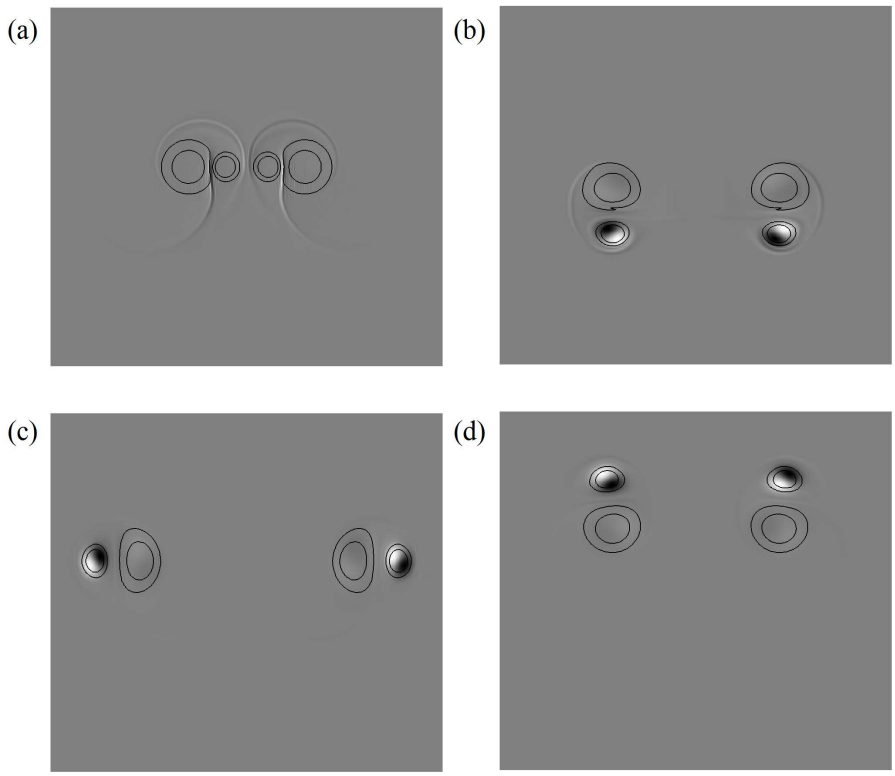

FIGURE 4.15: A time sequence of plots of spanwise vorticity in the linearised perturbation field (flooded contours) for the 'flat tail' case with an axial wavenumber of $k\,a_1 = 0.881$. Flooded contour levels are chosen arbitrarily to display the perturbation structure in each frame. The simulation was initialised with the optimal disturbance acquired with $\tau/T_0 = 3$. Solid contour lines show spanwise vorticity in the base flow at levels of vorticity of $\mid \omega_z \mid = 1, 3, 7$. (a)-(d) represent $t/T_0 = 0, 0.25, 0.5, 0.75$ respectively.

the perturbation is primarily contained within the tail vortex pair and any perturbation outside of this region is damped out (figure 4.15(c)). In addition, the perturbation rotates as the tail vortex orbits the corresponding wing vortex (figure 4.15(d)).

Figure 4.16 shows the temporal evolution of the linearised perturbations, beginning with the initial optimal perturbation field, for the 'high tail' case excited at the axial wavenumber ($k\,a_1 = 0.881$) that corresponds to the growth amplification factor of the secondary, long wavelength peak found from the transient growth analysis. The initial perturbation field, figure 4.16(a), shows that the majority of the optimal disturbance structure is concentrated in a thin band connecting the tail vortices. It is of interest to note that as the perturbation evolves, it forms into a dipole of perturbation within the tail vortex pair that maintains an angle of of approximately 45° to a line between the centre of the tail vortex and its corresponding wing vortex core (figure 4.16(b)). It is of

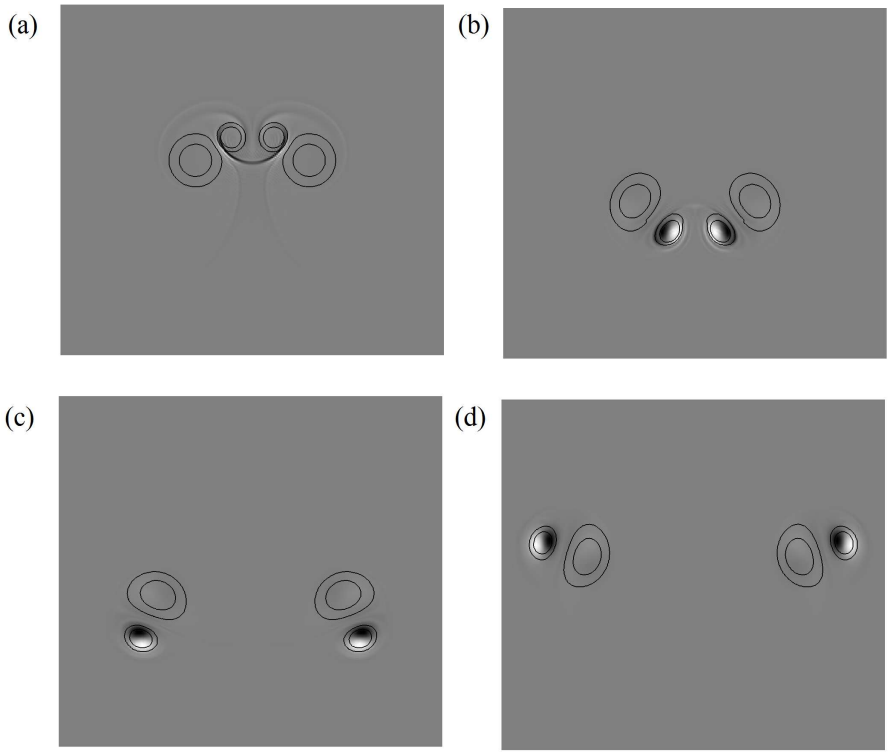

FIGURE 4.16: A time sequence of plots of spanwise vorticity in the linearised perturbation field (flooded contours) for the 'high tail' case with an axial wavenumber of $k\,a_1 = 0.881$. Flooded contour levels are chosen arbitrarily to display the perturbation structure. The simulations was initialised with the optimal disturbance acquired with $\tau/T_0 = 3$. Solid contour lines show spanwise vorticity in the base flow at levels of vorticity of $\mid \omega_z \mid = 1, 3, 7$. (a)-(d) represent $t/T_0 = 0, 0.25, 0.5, 0.75$ respectively.

interest to note that, unlike the long wavelength 'flat tail' case, the perturbation dipole present in the tail vortex of the 'high tail' case does exhibit reflective symmetry about the mid-plane as it rotates around the corresponding wing vortex (figure 4.16(c)). This indicates that the interaction between the tail vortex and the corresponding wing vortex is the driving factor behind the four-vortex instabilities, rather than any interaction across the mid-plane.

4.3.4 Direct numerical simulation

A DNS study of the symmetric four-vortex system was performed following the linear analysis. The energy in the perturbations of the linear simulations was compared to the energy in the non-zero Fourier modes of the DNS. The DNS was conducted by seeding the 'flat tail' and 'high tail' cases with either the optimal perturbation or white noise, to

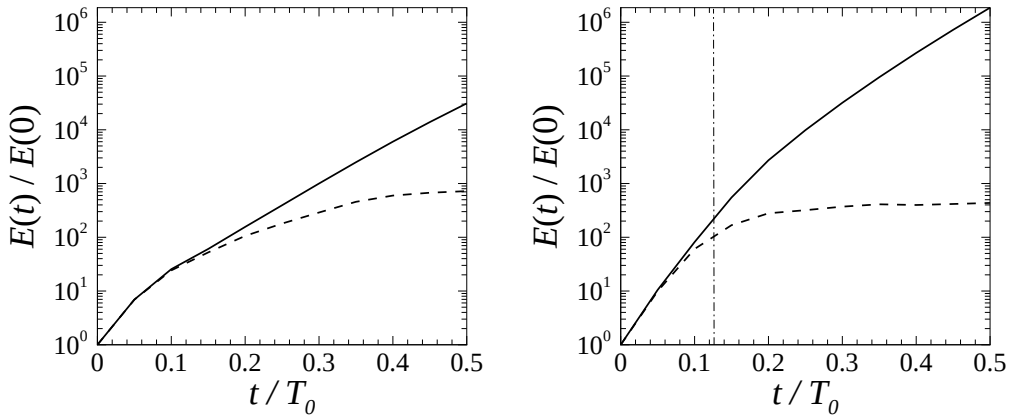

(a) (b)

FIGURE 4.17: Plot of (a) 'flat tail' and (b) 'high tail' perturbation energy normalised by initial energy. The solid line represents the solution of the linearised Navier–Stokes equation and the dashed line represents the energy in the non-zero Fourier modes of the DNS. The dash-dot line in (b) shows when the four-vortex cores are lined up horizontally. Simulations were initialised with the optimal disturbance captured with $k\,a_1 = 5.3$ and $\tau/T_0 = 3$

study the response of the system to the different perturbations. An axial wavenumber of $k\,a_1 = 5.3$ was chosen, as it corresponded to the peak in growth amplification factor found in the transient growth analysis. The axial domain was chosen to allow for one wavelength of the desired instability, and both the white noise and optimal cases were seeded in only the first Fourier mode (thus corresponding to exciting only a wavelength of $k\,a_1 = 5.3$). Sixteen Fourier modes were chosen for the simulations seeded with the optimal perturbation (as these exhibit greater instability growth rates and reach non-linear growth faster), and eight Fourier modes were chosen for the simulations seeded with white noise, to speed up the computation time as shown in the error analysis in § 2.6.3. The energy in the optimal perturbation used was 0.0033% of the initial energy in the base flow. The energy level of the white noise seeding used was 0.0040% of the base flow energy. The vortex core sizes and separations are as per § 2.1.

Figure 4.17 shows the energy in the perturbations evolved using the linearised Navier–Stokes equations, compared to the sum of energy across the non-zero Fourier modes of the DNS for the 'flat tail' and 'high tail' cases. These are normalised by the initial perturbation energy, $E(0)$, in the linearised Navier–Stokes equations and the non-zero Fourier modes of the DNS respectively. The perturbation fields become highly non-linear after only a short timeframe (signified by the departure of the pair

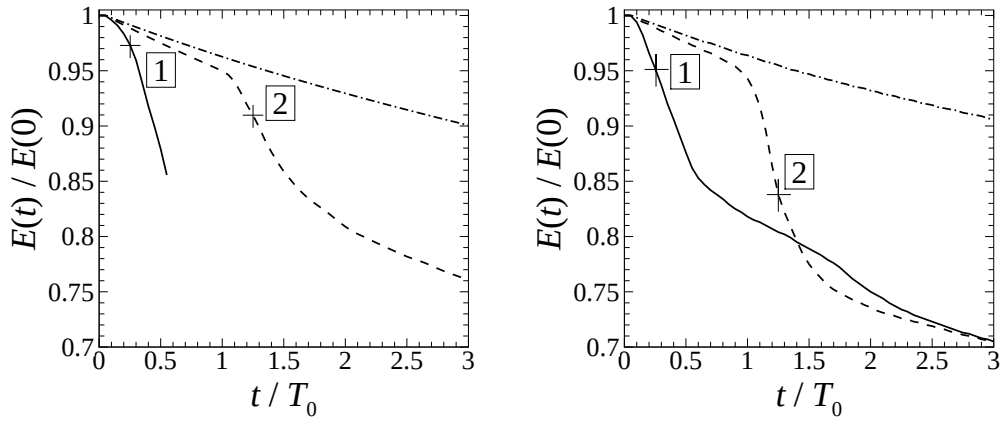

FIGURE 4.18: Time history of DNS zeroth mode energy for the (a) 'flat tail' and (b) 'high tail' case, normalised by initial energy in the zeroth Fourier mode. An axial wavenumber of $k\,a_1 = 5.3$ is prescribed for the perturbation field. Solid lines represent the cases seeded with an optimal perturbation with $\tau/T_0 = 3$, dashed lines represent the cases seeded with white noise and the dash-dot line represents a two-dimensional case. [1] and [2] show the times $t/T_0 = 0.25$ and 1.25 respectively.

of curves), with the 'flat tail' case having more energy once the non-linear disturbance saturates, leading to faster instability growth. The very short time frame that the DNS perturbation energy becomes non-linear implies that the primary effect of seeding with the optimal perturbations is to drive the flow into the non-linear regime extremely quickly.

Figure 4.18 shows a time history of the zeroth Fourier mode for the (a) 'flat tail' and (b) 'high tail' cases seeded with the optimal perturbation and white noise, as well as the two-dimensional reference case. It shows that the linear growth of the perturbations causes a large drop in the energy of the zeroth mode. This represents a large reduction in the coherency of the vortices. It is of interest to note that for the 'high tail' case, both the white noise and optimal seeding reach the same energy in the zeroth mode, $E(t)/E(0) = 0.705$, after a long period of time, $t/T_0 = 3$ (figure 4.18(a)). It also shows that the instabilities have the effect of significantly lowering the energy in the zeroth mode as compared to diffusion (as represented by the two-dimensional case). By $t/T_0 = 3$, the two-dimensional 'high tail' case has reached an energy level of $E(t)/E(0) = 0.906$ and the two-dimensional 'flat tail' case has reached an energy level of $E(t)/E(0) = 0.901$, both significantly higher than the three-dimensional cases. Another point of interest is that at $t/T_0 = 3$, the 'high tail' case reaches a lower energy level in

the zeroth mode, $E(t)/E(0) = 0.705$, than the 'flat tail' case, $E(t)/E(0) = 0.761$. This strongly implies that the 'high tail' case reaches a less coherent state by $t/T_0 = 3$ and so is more desirable in terms of wake reduction. This rapid drop in the zeroth Fourier mode can be related to the devolution of the tail vortex pair into small scale flow structures. Location [1] in figure 4.18(b) corresponds to the flow visualisation in figure 4.21(a ii) and shows that the large drop in zeroth Fourier mode energy is directly related to the devolution of the tail vortices. A comparison of location [1] in figure 4.18(a) with the related flow visualisation (figure 4.22(a ii)) demonstrates that the higher energy in the zeroth Fourier mode corresponds to a state where the tail vortices are larger coherent flow structures. A similar comparison can be made with the two cases seeded with white noise at location [2] in figure 4.18. Location [2] in figure 4.18(b) corresponds to the flow visualisation in figure 4.21(b vii). The drop in zeroth Fourier mode energy corresponds to the rapid devolution of the tail vortices into a region of small scale flow structures. The significantly higher zeroth Fourier mode energy at location [2] in figure 4.18(a) is demonstrated in the flow visualisation (figure 4.22(b vii)) where the tail vortices are still fairly coherent flow structures.

Figure 4.19 shows the time history of normalised perturbation energy calculated from DNS runs comparing the 'flat tail' and 'high tail' cases seeded with both the optimum perturbation found from the transient growth analysis and white noise. It can be seen that, for both the 'high tail' and 'flat tail' cases, the energy of the perturbation that leads to optimal energy growth from the transient growth analysis begins to grow immediately. This occurs before the flow subsequently forms into flow structures small enough for the energy to be dissipated by the viscosity in the fluid. In contrast, the energy in the white noise-perturbed flow begins to decay immediately as all of the decaying mode shapes are damped out before the unstable mode shapes grow sufficiently to dominate the perturbation field. The energy only begins to grow after approximately $t/T_0 = 0.5$ for the 'high tail' case and $t/T_0 = 0.75$ for the 'flat tail' case. This behaviour is the same observed in the two-vortex flow demonstrated in chapter 3, figure 3.14. A point of particular interest about the normalised energy growth of the perturbations is that for the cases seeded with the perturbation that leads to optimal energy growth, the 'flat tail' case peaks higher than the 'high tail' case. In contrast, in the cases seeded with white noise, the 'high tail' case peaks at a significantly higher level than the 'flat tail' case. This is opposite to the cases seeded with the perturbation that leads to optimal

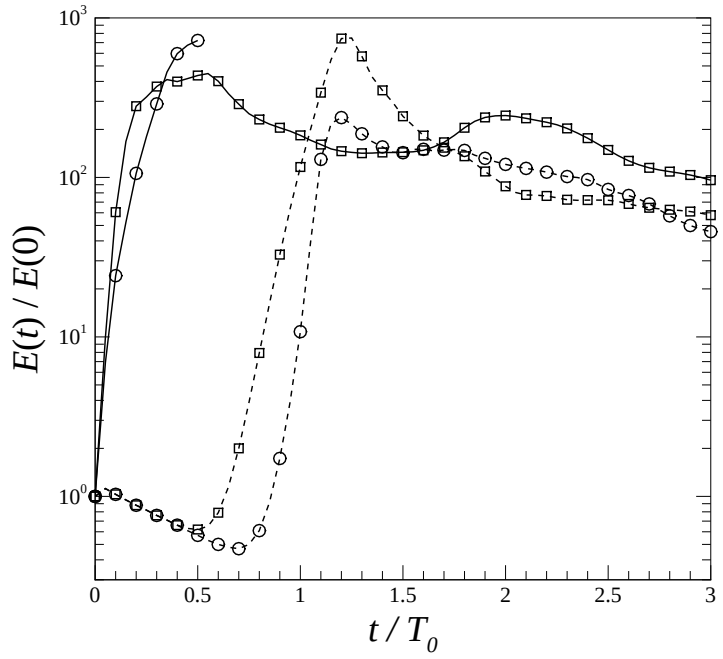

FIGURE 4.19: Time history of DNS perturbation energy, normalised by initial energy in the non-zero Fourier modes. An axial wavenumber of $k\,a_1 = 5.3$ is prescribed for the perturbation field. □ and ∘ represent the 'high tail' and 'flat tail' cases respectively. Solid lines represent the cases seeded with an optimal perturbation with $\tau/T_0 = 3$, and dashed lines represent the cases seeded with white noise.

energy growth. However, due to the random nature of the white noise seeding these cases, the overall peak height will be determined by the initial energy in the unstable mode shapes, not the initial overall energy of the white noise (which is very similar to the magnitude of the optimal perturbation seeding, $E(0)/E_{BF}(0) = 0.01522\%$ for the initial energy in the optimal perturbation field against $E(0)/E_{BF}(0) = 0.0189\%$ for the total energy in the white noise seeding).

Figure 4.20 shows a time history of the perturbation energy growth rate, σ_{GR}, for the 'high tail' and 'flat tail' cases seeded with the optimal perturbation and white noise. It is of interest to note that the peak growth rate the instability experiences, varies significantly depending on the seeding of the flow, and between the 'high tail' and 'flat tail' cases. The growth rate was calculated using a five-point stencil method to evaluate the derivative of the log of the perturbation energy. The 'high tail' case seeded with the optimal perturbation found from the transient growth analysis has the highest growth rate in the beginning of its evolution, $\sigma_{GR} = 0.755$. The 'flat tail' case also follows a similar trend, beginning with a high growth rate, $\sigma_{GR} = 0.6375$ that

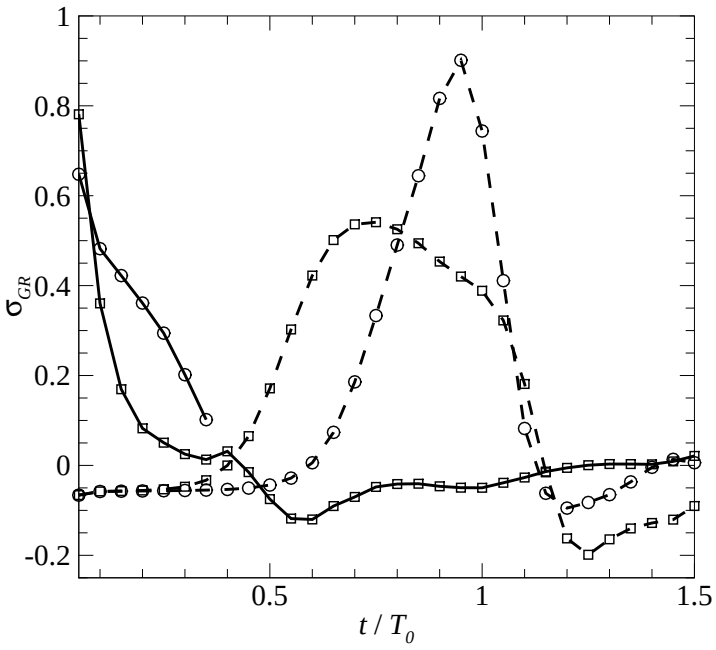

FIGURE 4.20: Time history of perturbation energy growth rate, σ_{GR}, for the 'high tail' and 'flat tail' cases seeded with the optimal perturbation and white noise. An axial wavenumber of $k\,a_1 = 5.3$ is prescribed for the perturbation field. □ and ○ represent the 'high tail' and 'flat tail' cases respectively. Solid lines represent the cases seeded with an optimal perturbation with $\tau/T_0 = 3$, and dashed lines represent the cases seeded with white noise.

then decays. It is of interest to note that the 'high tail' case seeded with white noise enters a linear phase of instability growth (where the growth rate reaches a plateau for a period of time) at a much lower growth rate of $\sigma_{GR} = 0.54$, which is lower than the 'high tail' case seeded with the optimal perturbation. It is also noted that the 'flat tail' case exhibits the opposite effect, with the peak growth rate of the 'flat tail' case seeded with white noise experiencing a higher growth rate, $\sigma_{GR} = 0.90$, than the 'flat tail' case seeded with the optimal perturbation.

It is interesting to note that, while the 'high tail' case seeded with white noise experiences a long period of almost constant growth, neither 'high tail' nor 'flat tail' cases seeded with the optimal perturbation experiences any constant growth regime. It is likely that the reason for this is that the seeding with the optimal perturbation is high enough in perturbation energy to drive the flow quickly into the non-linear regime (as shown by figure 4.17). The lack of a clearly defined, broad linear regime in the 'flat tail' case seeded with white noise is most likely due to the very high growth rate of the fastest-growing modes causing them to evolve large enough to exhibit non-linear

interaction with the base flow before other modes have time to decay to negligible levels.

4.3.4.1 Comparison of strain rate to growth rate

As in § 3.5.0.1, the strain rate imposed on the vortices can be related to the growth rate of the instability. As the four-vortex system is significantly more transient than the two-vortex system, a direct comparison between the strain rate and growth rate is more difficult. Even given this difficulty, the peak growth rate remains well below the theoretical maximum ratio of 9/16 (Waleffe 1990; Leweke & Williamson 1998) (becoming $\sigma_{GRpeak}/\epsilon_{peak} = 0.120$, based on velocity, for the 'high tail' case). This is not unexpected as σ_{GR} is the growth rate calculated from a global integration of the velocity field, rather than quantifying the growth of an isolated instability on a single vortex, and includes an extremely weak instability growth on the tail vortices. The rapid transition into the non-linear regime also contributes to the less than optimal nature of the growth rate. Determining the exact difference between the theoretical maximum and the local instability growth rate on a single vortex would be almost impossible. This is due to a number of factors present in the DNS, including the transient base flow, a vortex induced strain field rather than a uniform field, multiple vortices inducing strain on any given vortex in a time dependent fashion, and the simulations not being initialised with an exponentially growing mode (either white noise, or a superposition of many modes found from the transient growth analysis as the optimal initial perturbation field).

4.3.4.2 Visualisation of direct numerical simulation

Figure 4.21 shows a three-dimensional visualisation of the DNS evolution of the 'high tail' case when seeded with the perturbation found from the transient growth analysis and white noise. As the transient growth analysis predicted, the perturbation begins in the tail vortex pair, causing the cores to become unstable and distort significantly. The primary difference between the two cases is that the visible growth of the three-dimensional structures occurs much earlier in the evolution of the case seeded with the optimum perturbation than the case seeded with white noise. Once the tail vortex pair becomes highly disturbed, coinciding with the peak in perturbation energy seen in figure 4.21, the perturbation has a strong effect on the wing vortex pair (figure 4.21(a iii)). This effect causes the cores of the wing vortex pair to become highly distorted, which leads to destruction of the vortices. As the tail vortex pair enters the region between the wing vortex pair, it can be seen from the red shading of the flooded

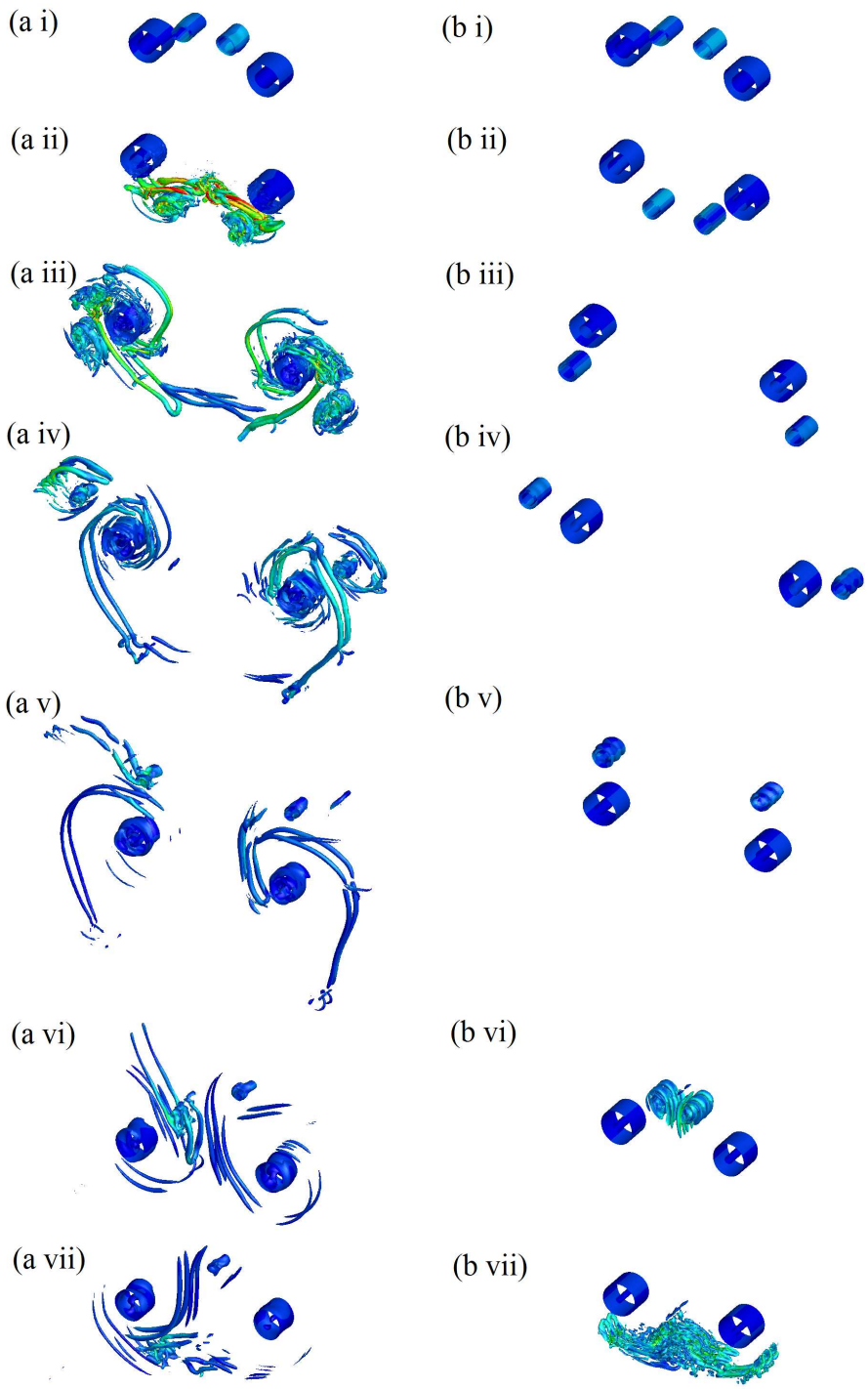

FIGURE 4.21: Time sequences of iso-surfaces of an arbitrarily small negative value of the λ_2 field (the criterion for identification of a vortex proposed by Jeong & Hussain 1995) plotted from a three-dimensional simulation of the 'high tail' case with an axial extent corresponding to a wavenumber of $k\,a_1 = 5.3$. The coloured shading shows levels of dominant strain, with blue corresponding to little or no strain and red corresponding to high values of dominant strain. (a i)-(a vii) displays the flow seeded with the perturbation that leads to optimum energy growth for $\tau/T_0 = 3$ at times $t/T_0 = 0, 0.25, 0.5, 0.75, 1, 1.25$ and 1.5 respectively. (b i)-(b vii) display the flow seeded with white noise at the same times.

contours that it is undergoing a very high level of strain (figure 4.21(a ii)). This dominant strain is influenced by both the destruction of the vortex and the proximity to the wing vortex pair. When the remnants of the tail vortex pair are close to the wing vortex pair (figure 4.21(a iii)), there is still a large amount of dominant strain in the flow structures close to the wing vortex pair (green shading). The primary interaction between the vortices is between the two tail vortices, referred from this point onwards as a T-T interaction (figure 4.21(a ii)). This interaction is characterised by flow of the tail vortices crossing the midplane of the domain and enhancing the destruction of the tail vortices. It is interesting to look at the similarities between the case seeded with the optimal perturbation at $t/T_0 = 0.25$ (figure 4.21(a ii)) and the case seeded with white noise at $t/T_0 = 1.5$ (figure 4.21(b vii)). Both cases are undergoing the T-T interaction and consist of a rapid devolution of the coherent tail vortices into significantly smaller flow structures. The case seeded with white noise has higher axial modes present, leading to less coherent and smaller flow structures. The smaller flow structures in the case with white noise seeding also leads to a lower strain, as the smaller flow structures cause less imposed strain than a smaller number of larger flow structures as present in the case seeded with the optimal perturbation.

The mechanism that causes destruction of the vortex system is very similar for both cases, except there is significant lag in the onset of the case seeded with white noise (figure 4.21(a ii) for the optimal seeding versus figure 4.21(b vii) for the white noise seeding). This is due to the white noise supplying energy to many sub-optimal mode shapes that are not conducive to growth and therefore decay. The increase in dominant strain in the tail vortex pair as it undergoes transition into small scale flow structures and also enters the highly strained region between the wing vortex pair can be seen in figure 4.21(b vi) as light blue and green flooding. The 'high tail' case seeded with white noise also undergoes the T-T interaction, causing a rapid destruction of the tail vortex pair (figure 4.21(b vii)).

Between the two 'high tail' cases, the case seeded with the optimal perturbation is preferable, from the perspective of vortex wake hazard reduction, as it begins to grow noticeably from seeding, and, by $t/T_0 = 1.5$, demonstrates significantly more distortion of the cores of the wing vortex pair. This distortion of the wing vortex pair demonstrates that an instability is already growing to disrupt the wing vortices. This situation is preferable, as the tail vortices in the case seeded with the optimal perturbation remain

as larger flow structures. The presence of a smaller number of larger, coherent flow structures (figure 4.21(a iii)) will cause a greater imposed strain for a longer period of time on the wing vortices, leading to faster instability growth in the wing vortices.

Figure 4.22 shows three-dimensional visualisation of the DNS evolution of the 'flat tail' case when seeded with the perturbation found from the transient growth analysis and when seeded with white noise. The initial perturbation energy in the seeding is the same as in the 'high tail' case stated at the beginning of this section. The method of destruction for these cases is very similar to the 'high tail' cases. The delay of the onset of the instability in the case seeded with white noise can be seen to occur in a similar manner to the two 'high tail' cases. In the 'flat tail' case seeded with the optimal perturbation, it can be seen that the flow does not cross the midplane. This results in an interaction between only the wing and tail vortex on each side, referred to as a T-W interaction from here on (figure 4.22(a ii)). As the tail vortices lose coherency in the axial direction due to the T-W interaction, the dominant strain increases significantly, as can be seen by the red shading in figure 4.22(a iii). The 'flat tail' case seeded with white noise also demonstrates the T-W interaction as flow from the tail vortices do not cross the mid-plane, while the tail vortices are within the highly strained region between the wing vortex pair (figure 4.22(b vi)).

Figure 4.23 shows a time history of the peak dominant strain, ε_{dom}, during the transition from the linear regime to the non-linear regime for an axial extent corresponding to a wavenumber of $k\,a_1 = 5.3$. It is of interest to note that the 'high tail' case (both cases seeded with the optimal perturbation and white noise) experiences a significantly higher peak dominant strain than both of the 'flat tail' cases. This is most likely due to the 'high tail' cases experiencing the T-T interaction, which leads to an enhancement of the instability destroying the tail vortices. In addition to this, the cases seeded with white noise experience a greater peak dominant strain. This is likely due to the cases with white noise retaining a small amount of energy in higher frequency modes, causing a slight damping in the primary mode that will lead to less distortion in the base flow. This reduced distortion of the base flow will lead to a delay of the onset of non-linear effects, producing the greater peak dominant strain. One thing that is of interest is that the peak dominant strain is greater where the flow is still mainly coherent ($t/T_0 = 0.1$ for the 'high tail' case seeded with the optimal perturbation shown in figure 4.21(a ii)) and drops off sharply when the flow devolves to random small scale flow structures

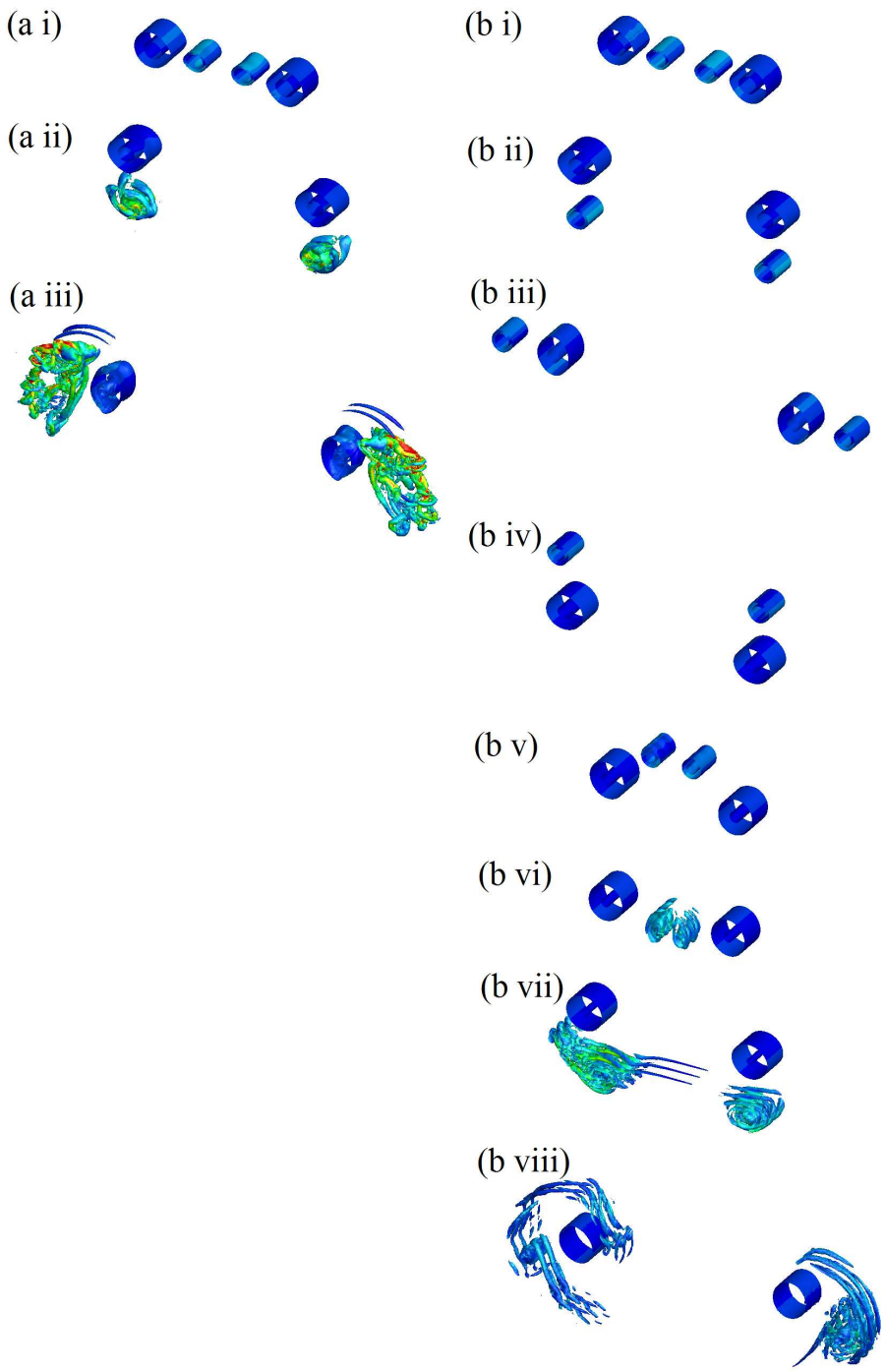

FIGURE 4.22: Time sequences of iso-surfaces of an arbitrarily small negative value of the λ_2 field plotted from a three-dimensional simulation of the 'flat tail' case with an axial extent corresponding to a wavenumber of $k\,a_1 = 5.3$. The coloured shading shows levels of dominant strain, with blue corresponding to little or no strain and red corresponding to high values of dominant strain. (a i)-(a iii) display the flow seeded with the perturbation that leads to optimum energy growth for $\tau/T_0 = 3$ at times $t/T_0 = 0, 0.25$ and 0.5 respectively. (b i)-(b viii) displays the flow seeded with white noise at $t/T_0 = 0, 0.25, 0.5, 0.75, 1, 1.25, 1.5$ and 1.75 respectively.

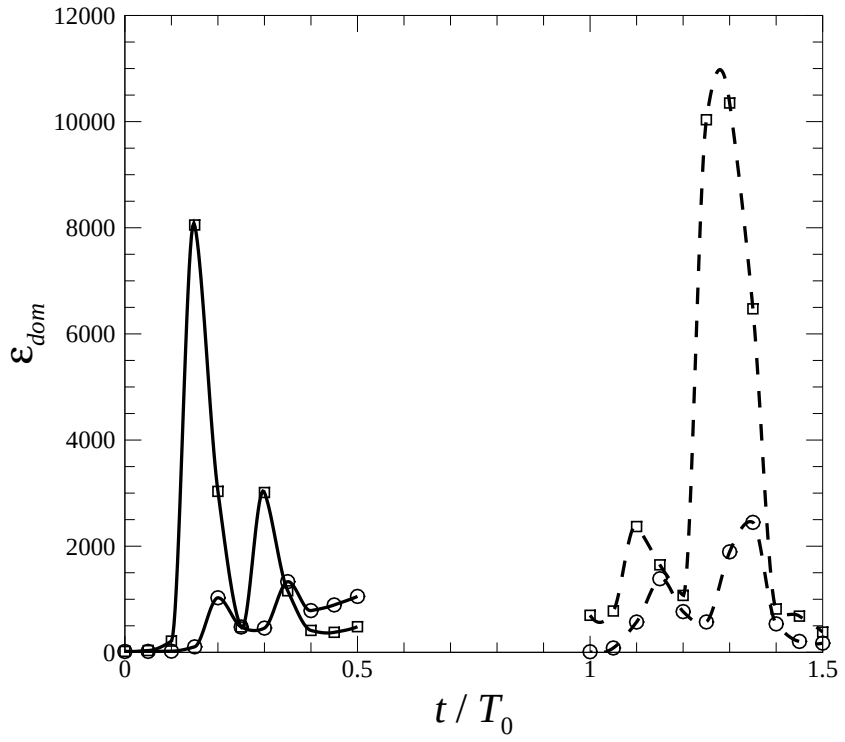

FIGURE 4.23: Time history of dominant strain, ε_{dom} (defined in § 2.2.1), during the transition into the non-linear regime for an axial extent corresponding to a wavenumber of $k\,a_1 = 5.3$. □ and ∘ represent the 'high tail' and 'flat tail' cases respectively. Solid lines represent the cases seeded with an optimal perturbation with $\tau/T_0 = 3$, and dashed lines represent the cases seeded with white noise.

($t/T_0 = 1.5$ for the 'high tail' case seeded with white noise shown in figure 4.21(b vii)). This is unsurprising, as a smaller number of larger, coherent flow structures will create stronger imposed strain than a large number of very weak, small scale flow structures.

Referring back to figure 4.19, it can now be seen that the switching of peak energy height between the 'high tail' and 'flat tail' cases seen in figure 4.19 is due to the instability interacting between the vortices. In the cases of the 'high tail' seeded with the perturbation that leads to optimal energy growth, the interaction is between the tail vortex pair as they are highly strained in the space between the wing vortex pair, causing a very large amount of flow across the mid-plane between the vortices (figure 4.21(a ii)). By contrast, the 'flat tail' case seeded with the perturbation that leads to optimal energy growth contains interactions causing the instability between the wing and tail vortices, with very little or no flow crossing across the mid-plane between the vortices (figure 4.22(a ii)). It is important to note that the nature of the white noise

means that the magnitude of the unstable modes is random as well. This can have the effect of changing the vortex interaction over two runs with the same initial conditions and magnitude of white noise from the T-W interaction to the T-T interaction and vice versa. These interactions can be seen clearly in figure 4.21 and 4.22. Figure 4.21(a ii) and (b vii) show a T-T interaction for both the case seeded with the optimal perturbation and the case seeded with white noise respectively. Figure 4.22(a ii) and (b vi) display a T-W interaction for both the case seeded with the optimal perturbation and white noise respectively. It is important to note that the instability can begin with a T-W interaction, and become a T-T interaction if the instability has reached sufficient magnitude in the tail vortex pair before it has reached the highly strained region between the wing vortex pair. A closer investigation into the physical mechanism behind the T-T and T-W interactions is covered in § 4.3.5.

It is important to note that the visualisations for the cases seeded with white noise in figures 4.21 and 4.22 are different simulation runs from the data shown in figure 4.19. This difference is due to the random nature of the white noise seeding producing a random magnitude of the unstable mode shapes. For figure 4.19, the 'high tail' case seeded with white noise is of the T-W interaction type while the 'flat tail' seeded with white noise is of the T-T interaction type.

Figure 4.24 shows a time sequence of flattened axial vorticity of the zeroth mode of the 'high tail' DNS case seeded with the optimal perturbation. By showing the flattened axial vorticity, the structure of the base flow as it devolves can be closely examined. Initially, both the tail and wing vortices are largely coherent with only the tail vortices demonstrating some deformation (figure 4.24(a)). Over a short time, the tail vortices become more distorted, becoming highly perturbed as the instability grows in them (figure 4.24(b)-(c)). These small scale structures begin to wrap around the wing vortices and the cores of the tail vortex pair become extremely distorted (figure 4.24(e)). The wing vortices interact with the tail vortices at their periphery and while the cores of the wing vortices remain fairly coherent, the strain imposed on them by the small scale flow structures surrounding them will vary significantly, potentially causing instability growth (figure 4.24(h)).

Figure 4.25 shows a time sequence of axial vorticity of the zeroth mode of the 'high tail' DNS case seeded with white noise. Before the tail vortex pair enters the highly strained region between the wing vortices, the tail vortices are contained in a relatively

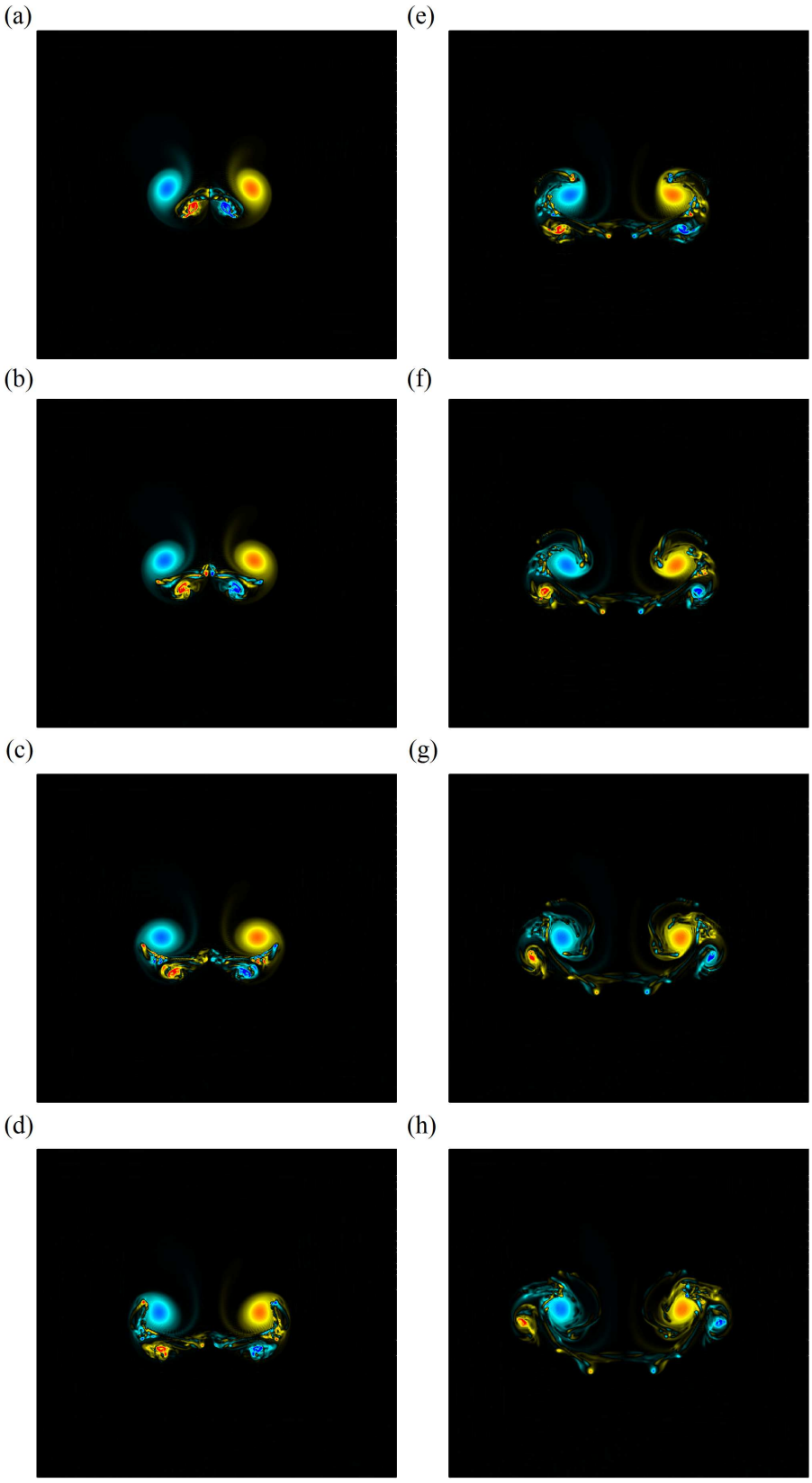

FIGURE 4.24: A time sequence of flattened vorticity across the axial domain showing the base flow of the 'high tail' DNS case seeded with the optimal perturbation. Red indicates positive vorticity and blue indicates negative vorticity. (a)-(h) displays times $t/T_0 = 0.15, 0.20, 0.25, 0.30, 0.35, 0.40, 0.45$ and 0.50 respectively.

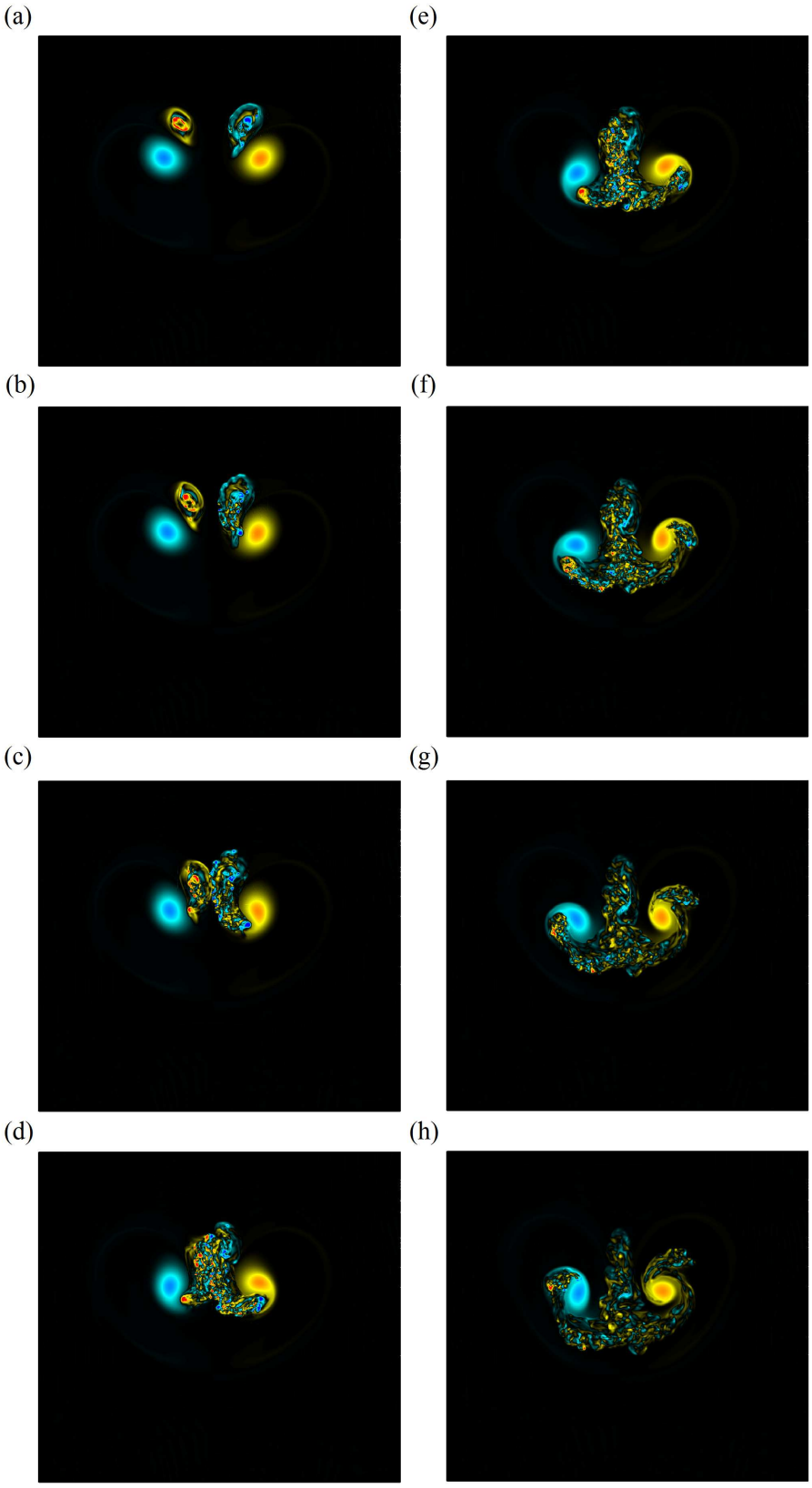

FIGURE 4.25: A time sequence of flattened vorticity across the axial domain showing the base flow of the 'high tail' DNS case seeded with white noise. Red indicates positive vorticity and blue indicates negative vorticity. (a)-(h) displays times $t/T_0 = 1.10, 1.15, 1.20, 1.25, 1.30, 1.35, 1.40, 1.45$ respectively.

small region. In addition to this the wing vortices are still very large, coherent structures with almost no distortion (figure 4.25(a)). The highly strained region between the wing vortex pair causes the tail vortices to become small scale flow structures. These small scale structures respond to externally imposed strain more severely and the region of these flow structures begins to surround the wing vortex pair as it is stretched and distorted (figure 4.25(c)). As the region of small scale flow structures extends and is pulled around the wing vortices, it begins to dominate the periphery of the wing vortices, reducing their size and deforming them (figure 4.25(d)). This is also demonstrated in the large reduction in the energy of the zeroth mode in figure 4.18(b). The wing vortex cores begin to form into a teardrop shape due to the strain imposed on them by the region of small scale flow structures, and rotate as they become surrounded by it (figure 4.25(f)). These small scale flow structures continue until they surround the wing vortices, reducing the area of the vortex cores (figure 4.25(h)).

Figure 4.26 shows a time sequence of axial vorticity of the base flow of the 'flat tail' DNS case seeded with the optimal perturbation. Initially, the four vortices are coherent flow structures with no obvious distortion of the vortex cores (figure 4.26(a)). The instability causes the core of the tail vortices to become a ring of strong vorticity (figure 4.26(c)) while the wing vortex pair is almost completely unaffected. This ring of strong vorticity that the tail vortex cores form into is the first stage of the degradation of these vortices towards small scale flow structures. The ring of strong vorticity that the tail vortex cores forms into breaks due to the instability, forming into two arcs while opposite-sign vorticity begins to form (figure 4.26(e)). The interaction between the wing vortex and tail vortex causes the tail vortices to slowly devolve into small scale flow structures, still leaving the wing vortices in a very coherent state with the devolved tail vortices occupying a relatively small region (figure 4.26(h)).

Figure 4.27 shows a time sequence of axial vorticity of the base flow of the 'flat tail' DNS case seeded with white noise. Initially, the flow exhibits similar characteristics to the case seeded with the optimal perturbation, that being the tail vortices forming into a ring of peak vorticity (as denoted by the strong red and blue colouring in figure 4.27(a)). As the tail vortices are forced through the highly strained region between the wing vortex pair, they are forced to interact with each other, causing rapid devolution into incoherent flow structures (figure 4.27(c)-(d)). This forcing of the tail vortices together allows the strain from the wing vortices to stretch the region of incoherent flow into

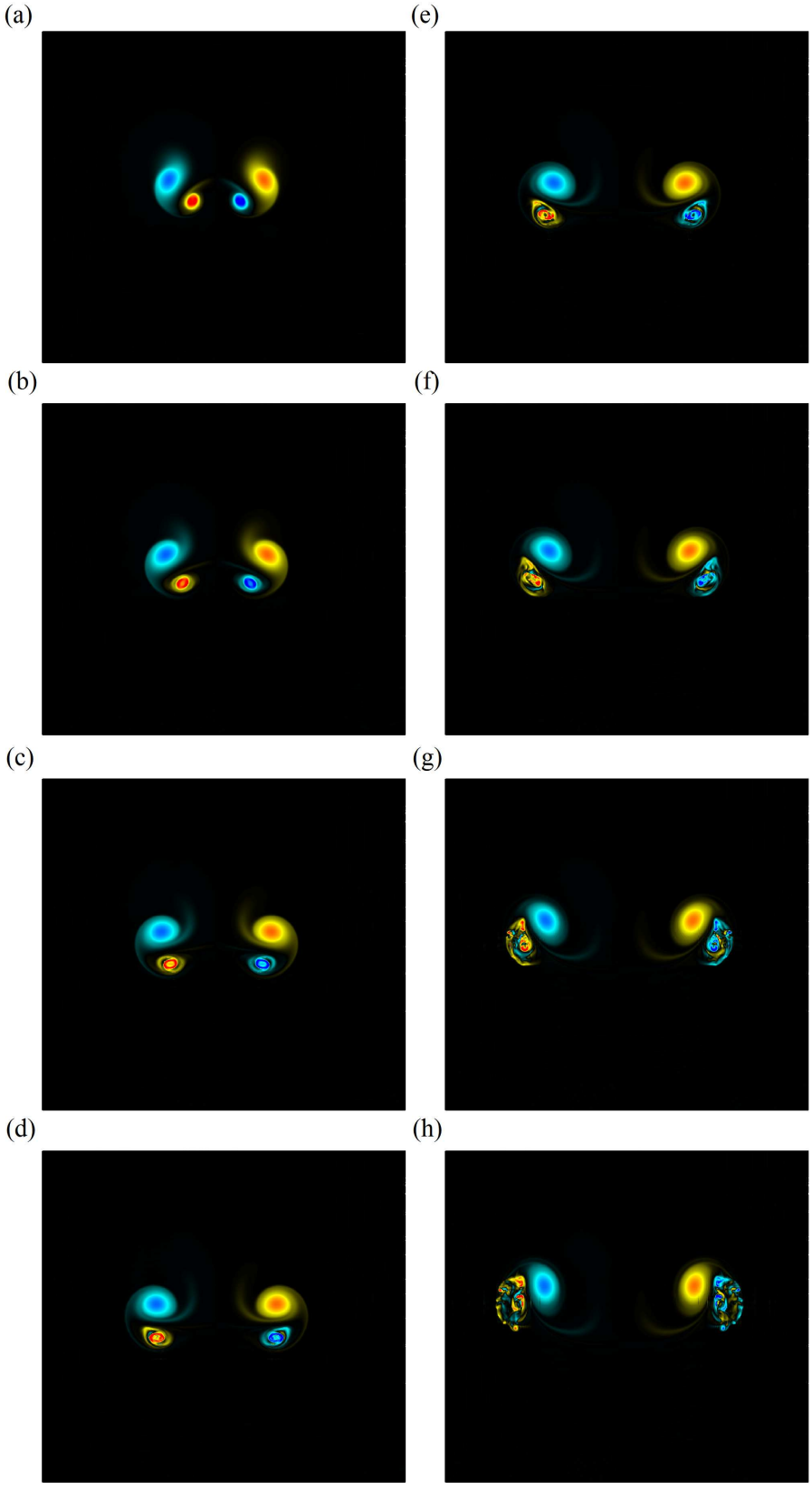

FIGURE 4.26: A time sequence of flattened vorticity across the axial domain showing the base flow of the 'flat tail' DNS case seeded with the optimal perturbation. Red indicates positive vorticity and blue indicates negative vorticity. (a)-(h) displays times $t/T_0 = 0.05, 0.10, 0.15, 0.20, 0.25, 0.30, 0.35, 0.40$ respectively.

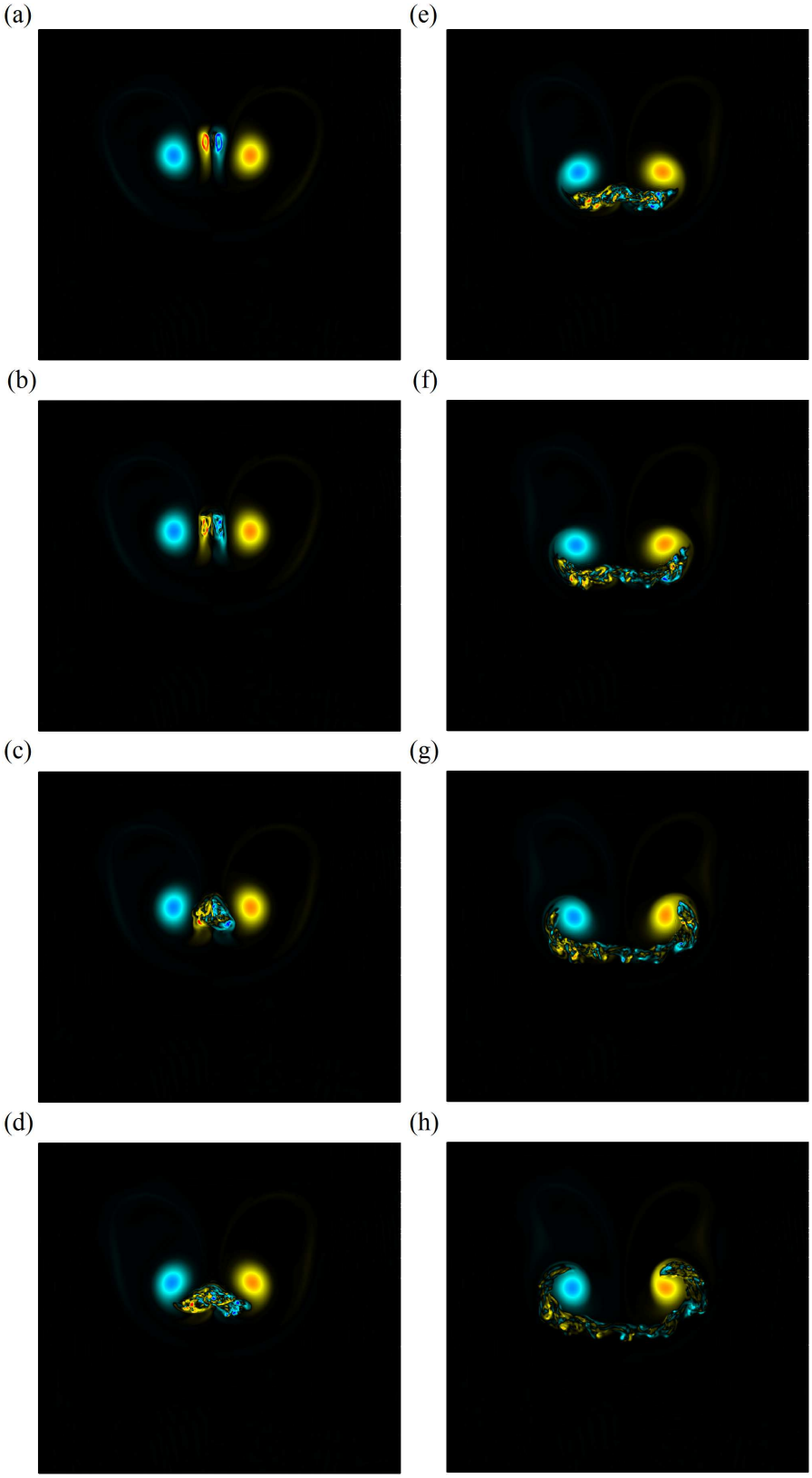

FIGURE 4.27: A time sequence of flattened vorticity across the axial domain showing the base flow of the 'flat tail' DNS case seeded with white noise. Red indicates positive vorticity and blue indicates negative vorticity. (a)-(h) displays times $t/T_0 = 1.10, 1.15, 1.20, 1.25, 1.30, 1.35, 1.40, 1.45$ respectively.

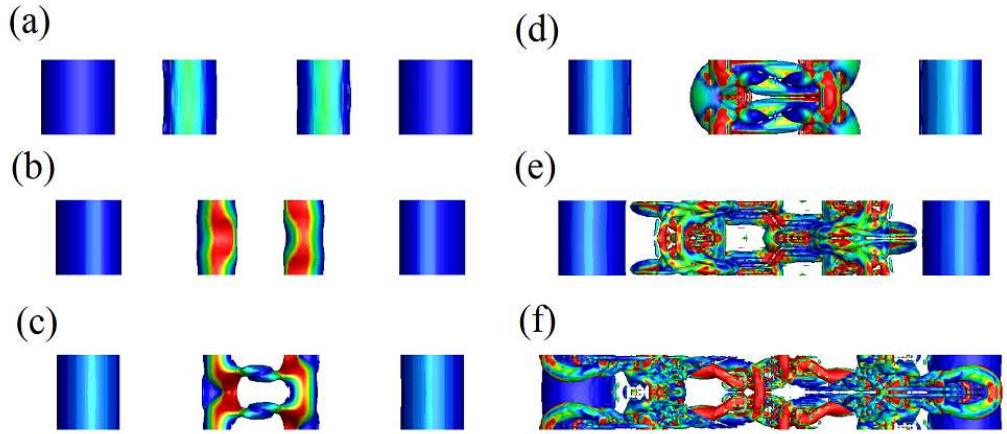

FIGURE 4.28: A time sequence of iso-surfaces of an arbitrarily small negative value of the λ_2 field plotted for the 'high tail' case, viewed from directly below, for an axial wavenumber of $k\,a_1 = 5.3$, seeded with the perturbation that leads to optimal energy growth for $\tau/T_0 = 3$. The iso-surfaces are coloured by dominant strain rate with blue and red corresponding to low and high levels respectively. (a)-(f) displays times $t/T_0 = 0, 0.05, 0.1, 0.15, 0.20$ and 0.25 respectively.

a long arc that starts to surround the wing vortices (figure 4.27(f)). The region of incoherent flow is pulled around, beginning to surround the wing vortices, and leaving the highly strained region between the wing vortices clear (figure 4.27(g)). While the tail vortices have devolved into incoherent flow, this had little effect on the coherence of the wing vortices (figure 4.27(h)). The main effect on the wing vortices is a slight deformation due to the imposed strain from the remnants of the wing vortices and a reduction in size around the periphery.

4.3.5 Transition into the non-linear phase

Throughout this section, the flow is visualised using three different definitions. The first is the λ_2 field, defined by Jeong & Hussain (1995) and shows the presence of a vortex as defined in their work. The second visualisation method utilises the vorticity magnitude field and is defined as $[\omega_z^2 + \omega_y^2 + \omega_x^2]^{0.5}$. The final visualisation method examines the non-axial vorticity field, defined as $[\omega_y^2 + \omega_x^2]^{0.5}$. Each of the visualisations in this section are examined in the order given here.

Figures 4.28-4.30 display the vortex systems of the iso-surfaces for the 'high tail' case seeded with the optimum mode shape. These show that, when the instability reaches a certain magnitude and is forced between the stronger vortex pair, it causes the tail vortices to interact with each other. This interaction causes the flow to become highly

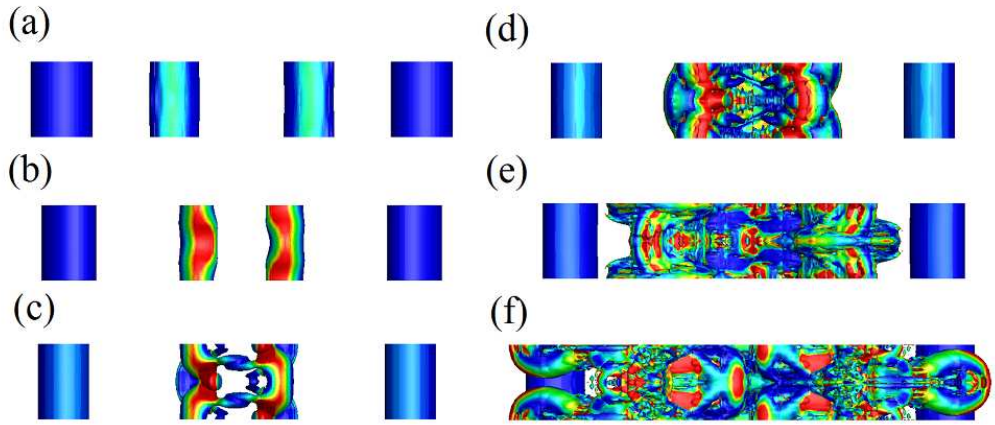

FIGURE 4.29: A time sequence of iso-surfaces of vorticity magnitude for the 'high tail' case, viewed from directly below, for an axial wavenumber of $k\,a_1 = 5.3$, seeded with the perturbation that leads to optimal energy growth for $\tau/T_0 = 3$. The colouring of the iso-surfaces and times are as per figure 4.28.

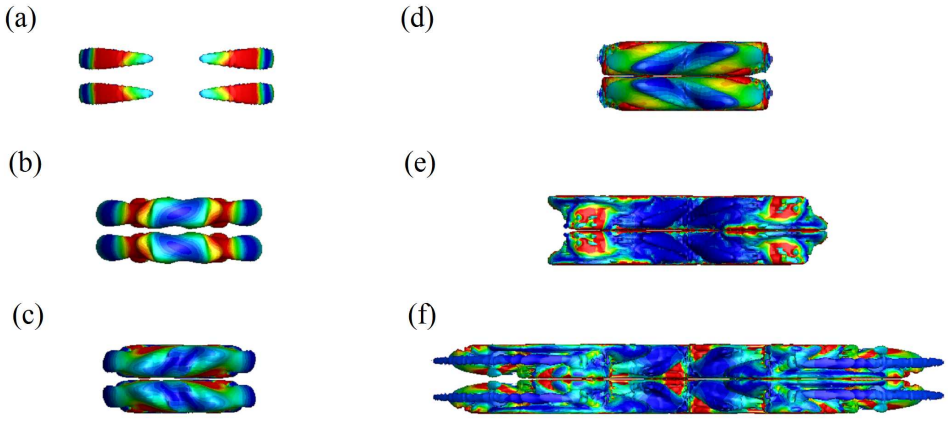

FIGURE 4.30: A time sequence of iso-surfaces of the $[\omega_y^2 + \omega_x^2]^{0.5}$ field with dominant strain flooding for the 'high tail' case, viewed from directly below, for an axial wavenumber of $k\,a_1 = 5.3$, seeded with the perturbation that leads to optimal energy growth for $\tau/T_0 = 3$. The colouring of the iso-surfaces and times are as per figure 4.28.

non-linear. As can be seen in figure 4.28(b), the instability begins in the tail vortex pair with a higher mode, leading to the tail vortices becoming highly distorted as they are forced close together between the stronger wing vortex pair. The crossing of vorticity over the centre (seen in figure 4.28(c)) demonstrates how the interaction is primarily between the tail vortices and not between the wing vortices (the aforementioned T-T interaction). The forcing of the tail vortex pair through the highly strained region between the wing vortices causes the tail vortex pair to interact strongly with each other. It can also be seen in figure 4.29(c) that lobes of vorticity magnitude are present

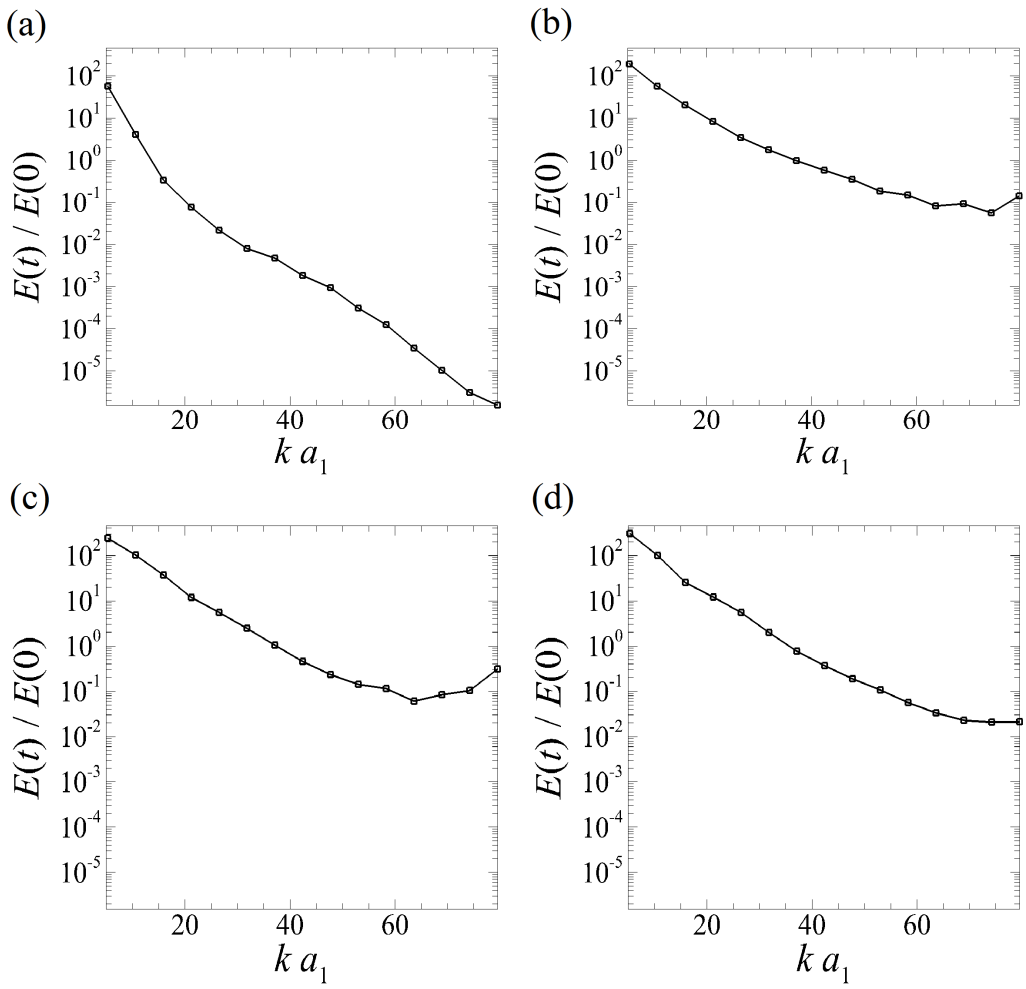

FIGURE 4.31: Plot of mode energy, $E(t)/E(0)$, against axial wavenumber, $k\,a_1$, for the 'high tail' case seeded with the optimal perturbation found from the transient growth analysis. (a)-(d) represent times, $t/T_0 = 0.1, 0.2, 0.4$ and 0.55 respectively.

in highly strained regions of the flow (red shading). This difference in iso-surfaces of vorticity magnitude (figure 4.29(c)) and λ_2 field (figure 4.28(c)) shows that the magnitude of the dominant strain is greater than the ω_z^2, therefore, the local fluid flow is dominated by the strain field and the λ_2 field will not identify a vortex core at this location (Jeong & Hussain 1995). Early in the transition, a comparison between figures 4.29(a)-(b) with figures 4.28(a)-(b) shows that the vorticity magnitude and λ_2 field correspond without the lobes of vorticity magnitude. This shows that early in the transition into the non-linear regime, there are no regions where the dominant strain is greater than ω_z^2 and so the flow is dominated by the axial vorticity.

Figure 4.30 shows that, early in the transition into the non-linear regime, there is a small amount of the $[\omega_y^2 + \omega_x^2]^{0.5}$ field present in the tail vortex pair, indicating that the

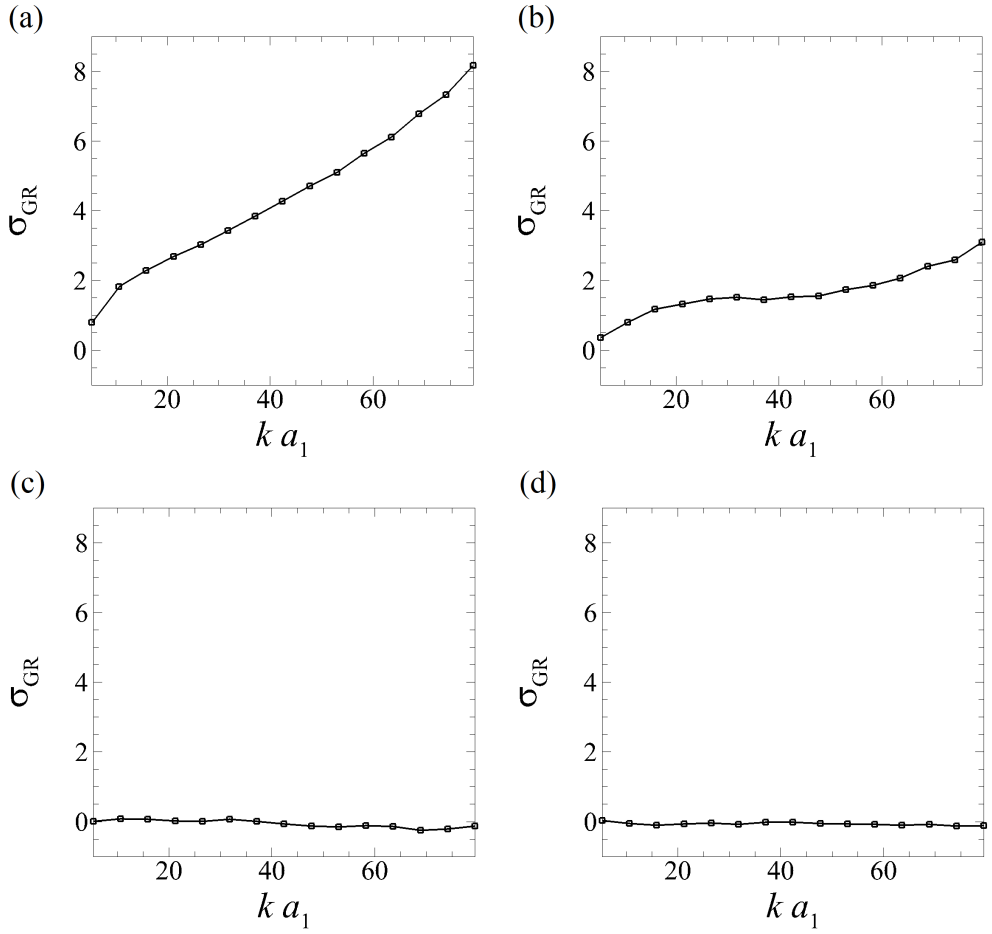

FIGURE 4.32: Plot of mode energy growth rate, σGR, against axial wavenumber, $k\,a_1$, for the 'high tail' case seeded with the optimal perturbation found from the transient growth analysis. (a)-(d) represent times, $t/T_0 = 0.15, 0.2, 0.4$ and 0.55 respectively.

flow is predominantly two-dimensional (figure 4.30(a)). As the flow evolves and the T-T interaction occurs, the $[\omega_y^2 + \omega_x^2]^{0.5}$ field joins across the centre, forming two horizonal bands where the tail vortices are interacting with each other (figure 4.30(b)). As the tail vortex pair evolves into small scale flow structures, the $[\omega_y^2 + \omega_x^2]^{0.5}$ field grows to encompass the whole axial direction in the vicinity of the tail vortex pair, indicating that the tail vortex pair has become highly three-dimensional (figure 4.30(e)).

Figure 4.31 displays the normalised energy in the individual Fourier modes for the 'high tail' case seeded with the optimal perturbation found from the transient growth analysis. Before the overall peak in the energy ($t/T_0 = 0.1$, figure 4.31(a)), there is still very little energy in the smaller axial wavenumbers. After this time, there is a very large growth in the energy of the smaller axial wavenumbers; for example, for an axial wavenumber of $k\,a_1 = 70$, the energy changes from $E(t)/E(0) \approx 10^{-5}$ at $t/T_0 = 0.1$ to

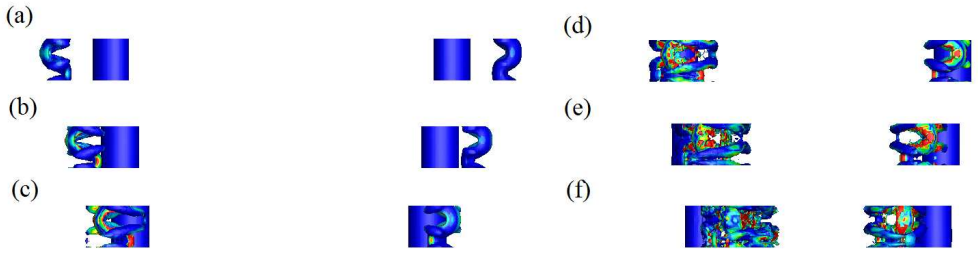

FIGURE 4.33: A time sequence of iso-surfaces of an arbitrarily small negative value of the λ_2 field plotted for the 'high tail' case, viewed from directly above, for an axial wavenumber of $k\,a_1 = 5.3$, seeded with white noise. The iso-surfaces are coloured by dominant strain rate with blue and red corresponding to low and high levels respectively. (a)-(f) displays times $t/T_0 = 0.85, 0.90, 0.95, 1.00, 1.05$ and 1.10 respectively.

$E(t)/E(0) \approx 10^{-1}$ at $t/T_0 = 0.2$ (figure 4.31(a)-(b)). This large increase implies that the higher harmonics of the axial wavenumber play a significant role in the transition of the flow into the non-linear regime. As the flow proceeds further into the non-linear regime, the higher axial wavenumbers begin to decay. This decay occurs because the size of possible flow structures is limited by the viscosity and therefore they become damped out once they reach this limitation (figure 4.31(d)).

Figure 4.32 displays the energy growth rate in the individual Fourier modes for the 'high tail' case seeded with the optimal perturbation found from the transient growth analysis. This shows that during the linear growth regime (figure 4.32(a)), the growth rate in the higher harmonics of the instability are significantly greater than the primary Fourier mode. These higher growth rates in the higher harmonics continue until around $t/T_0 = 0.4$ (figure 4.32(c)) where the growth rate remains slightly positive in the lower harmonics and becomes negative in the higher harmonics, reflecting the decrease in energy shown in the higher harmonics in figure 4.31(c). By $t/T_0 = 0.55$, the growth rate is slightly negative throughout the spectrum of the Fourier modes, which is not surprising since the non-linear regime is dominated by the tail vortices devolving into flow structures small enough to be damped out by the fluid viscosity.

Figures 4.33-4.35 show the iso-surfaces for the 'high tail' case seeded with white noise. The figures show that the instability is of a similar higher wavenumber to the case seeded with the perturbation that leads to optimal energy growth. The instability also begins in the tail vortex pair (figure 4.33(a)). However, in this case the instability grows due to the interaction between the wing and tail vortices (the aforementioned T-W interaction). This is the opposite of the case seeded with the optimal perturbation,

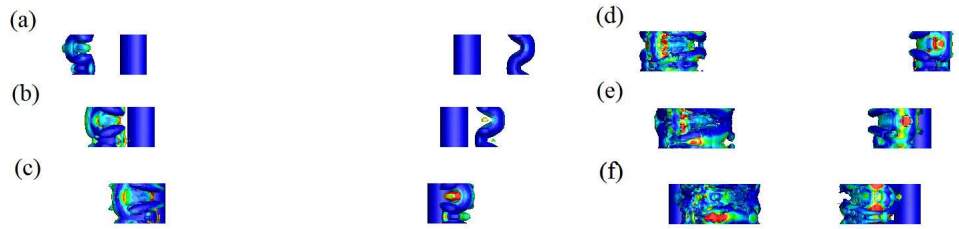

FIGURE 4.34: A time sequence of iso-surfaces of vorticity magnitude for the 'high tail' case, viewed from directly above, for an axial wavenumber of $k\,a_1 = 5.3$, seeded with white noise. The colouring of the iso-surfaces and times are as per figure 4.33.

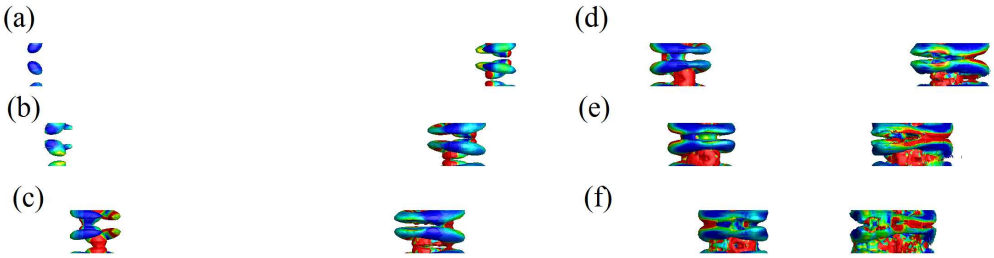

FIGURE 4.35: A time sequence of iso-surfaces of the $[\omega_y^2 + \omega_x^2]^{0.5}$ field with dominant strain flooding for the 'high tail' case, viewed from directly above, for an axial wavenumber of $k\,a_1 = 5.3$, seeded with white noise. The colouring of the iso-surfaces and times are as per figure 4.33.

where flow from the tail vortices crosses the mid-plane between the two wing vortices. This change in interaction occurs because the instability in the tail vortex pair requires a certain magnitude before it enters the highly strained region between the wing vortex pair. If the instability has grown to sufficient magnitude, the high strain and forcing of the tail vortices into close proximity will cause flow to occur across the mid-plane between the wing vortices (a T-T interaction). As in the 'high tail' case seeded with the optimal perturbation, early in the transition the λ_2 field (figure 4.33(a)) corresponds well with the vorticity magnitude at the same time (figure 4.34(a)). This shows that early in the transition into the non-linear regime, there are no regions where the dominant strain is greater than ω_z^2 and so the flow is dominated by the axial vorticity. Later in the evolution, lobes of vorticity in highly strained regions (red shading) appear in the vorticity magnitude (figure 4.34(b)) which are not present in the λ_2 field (figure 4.33(b)). This shows that in these regions of the flow the dominant strain is greater than ω_z^2, leading to the λ_2 field not identifying a vortex. Later in the evolution, the tail vortices have devolved into incoherent flow as shown in figures 4.33(f) and 4.34(f).

It is of interest to note that the right tail vortex displays a higher amount of $[\omega_y^2 +$

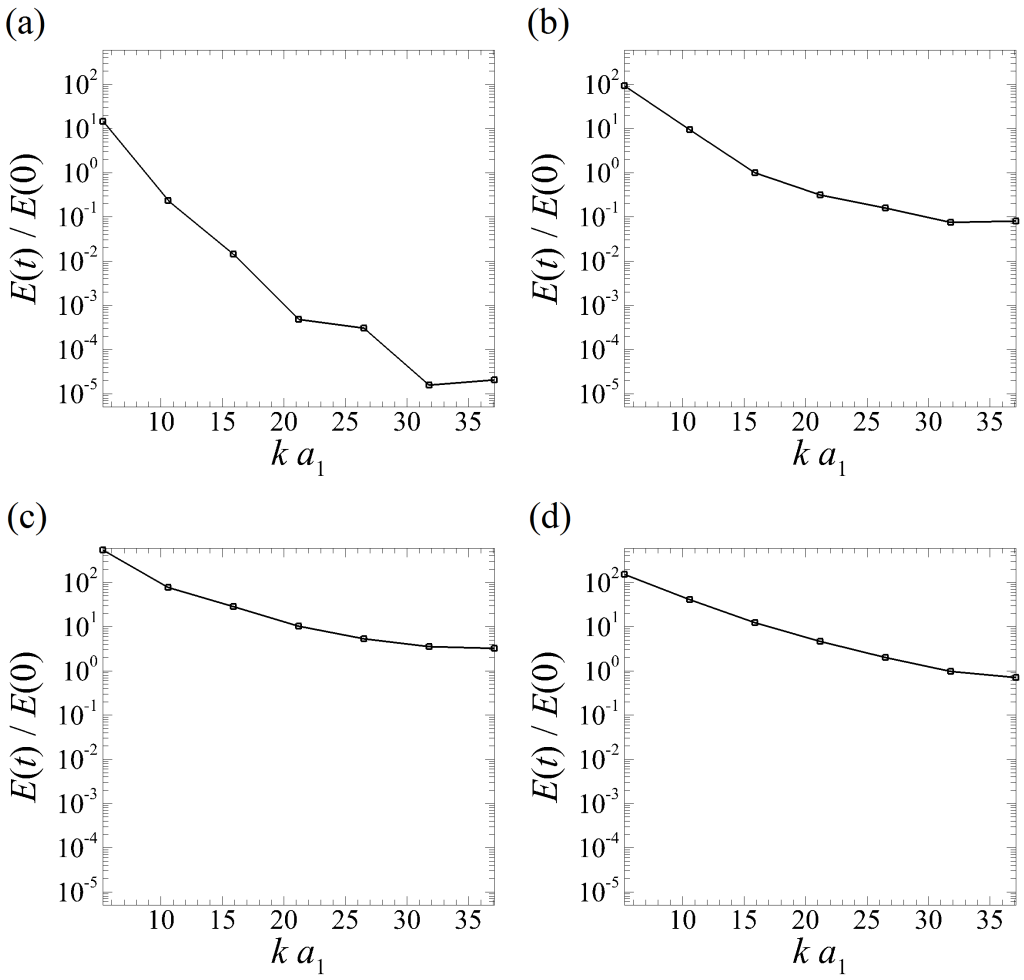

FIGURE 4.36: Plot of mode energy, $E(t)/E(0)$, against axial wavenumber, $k\,a_1$, for the 'high tail' case seeded with white noise. (a)-(d) represent times, $t/T_0 = 0.85, 1, 1.2$ and 1.5 respectively.

$\omega_x^2]^{0.5}$, indicating that it is transitioning into three-dimensional flow faster than the left tail vortex (figure 4.35(a)). The left tail vortex displays only a small amount of $[\omega_y^2 + \omega_x^2]^{0.5}$, indicating that it is still predominantly a two-dimensional flow. This effect is most likely due to the nature of the white noise that has been used to seed the flow. As the white noise is a combination of different magnitudes of different mode shapes, the modes that are conducive to instability growth may not be of the same energy magnitude in two localised regions of the flow. In this case, the ideal mode in the right tail vortex would have begun with more energy and so exhibits greater instability growth. The transition into non-linear and three-dimensional flow occurs in three bands, one on either end of the vortex and a band in the centre (figure 4.35(b)). As the flow evolves, tendrils of $[\omega_y^2 + \omega_x^2]^{0.5}$ curl around the vortex core, growing in size

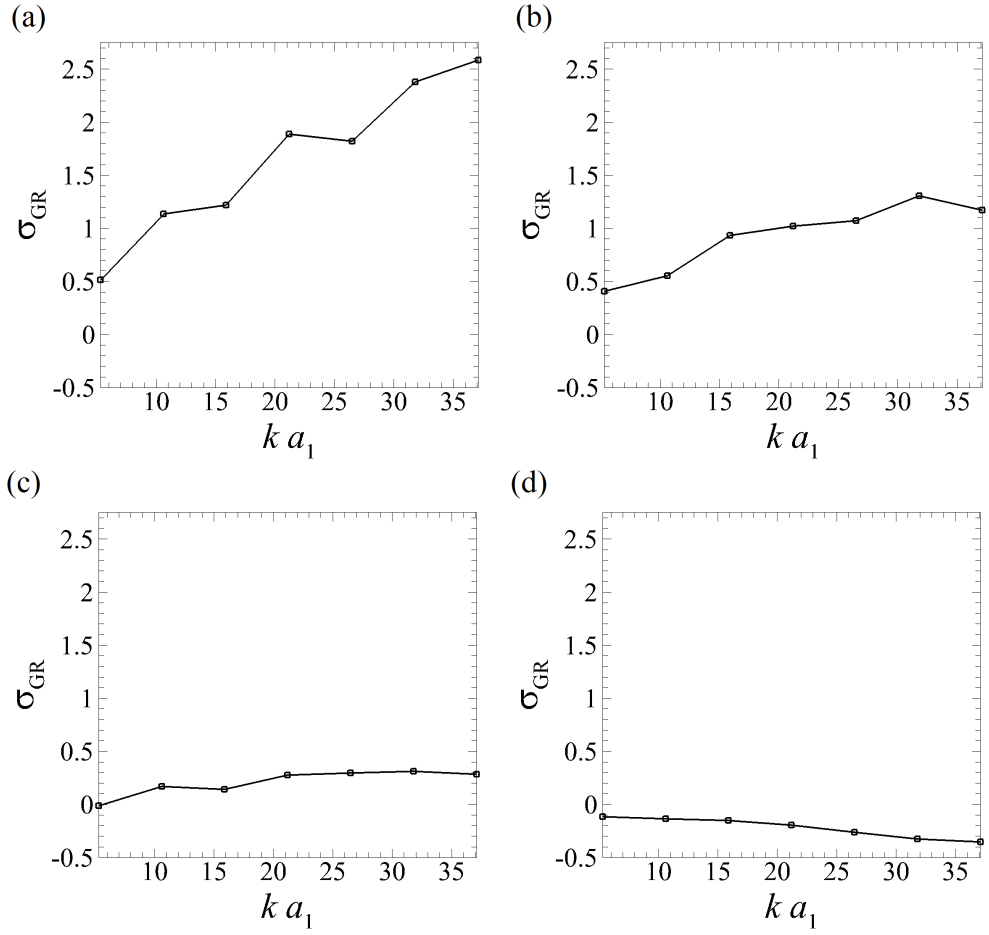

FIGURE 4.37: Plot of mode energy growth rate, σ_{GR}, against axial wavenumber, $k\,a_1$, for the 'high tail' case seeded with white noise. (a)-(d) represent times, $t/T_0 = 0.85, 1, 1.2$ and 1.5 respectively.

(figure 4.35(d)). It is of interest to note that the structure of the $[\omega_y^2 + \omega_x^2]^{0.5}$ flow is the same for both tail vortices, simply occurring at a later time for the left tail vortex and reflected about the centreline (figure 4.35(d) for the left tail vortex compared to figure 4.35(b) for the right tail vortex). As the instability grows, it begins to encompass the whole of the axial domain in the vicinity of the tail vortices, indicating they have become extremely three-dimensional (figure 4.35(f)).

Figure 4.36 displays the normalised energy in the individual Fourier modes for the 'high tail' case seeded with white noise. It shows that like the case seeded with the optimal perturbation, the energy in the higher harmonics increase significantly during the linear phase (figure 4.36(a)-(b)) and then begin to decay during the transition into the non-linear regime (figure 4.36(c)-(d)). The lower wavenumbers also follow a similar trend throughout the transition into the non-linear regime, but with a smaller increase

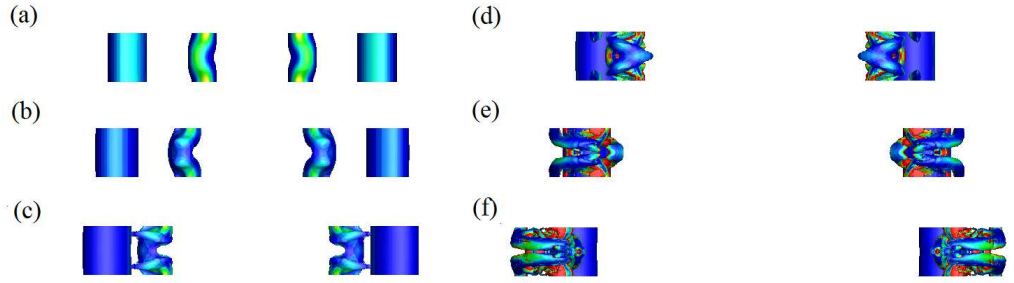

FIGURE 4.38: A time sequence of iso-surfaces of an arbitrarily small negative value of the λ_2 field plotted for the 'flat tail' case, viewed from directly below, for an axial wavenumber of $k\,a_1 = 5.3$, seeded with the perturbation that leads to optimal energy growth for $\tau/T_0 = 3$. The iso-surfaces are coloured by dominant strain rate with blue and red corresponding to low and high levels respectively. (a)-(f) displays times $t/T_0 = 0.05, 0.1, 0.15, 0.20, 0.25$ and 0.30 respectively.

and decrease in normalised energy. This rapid increase in energy in the higher axial wavenumbers indicates that the transition into the non-linear regime causes the vortices to break down into small scale (high axial wavenumber) flows that can be damped out by the fluid.

Figure 4.37 displays the energy growth rate in the individual Fourier modes for the 'high tail' case seeded with white noise. It shows that the higher wavenumbers have significantly larger growth rates during the linear regime and in the beginning of the transition into the non-linear regime (figure 4.37(a)-(b)). As the flow transitions further into the non-linear regime and the flow breaks down into smaller structures, the greater growth rate present in the higher axial wavenumbers decreases significantly (figure 4.37(c)). The energy in the higher axial wavenumbers indicate smaller flows and as such they can be damped out, resulting in the rapid decrease in the higher wavenumber modes until they have a larger negative growth rate (figure 4.37(d)). This behaviour implies that while the energy in the higher axial wavenumbers will grow at a faster rate, it will also reach a value that will lead to faster loss of energy as well.

Figures 4.38-4.40 show the iso-surfaces for the 'flat tail' case seeded with the perturbation that leads to optimal energy growth. These figures reveal that the instability growth and mechanisms are similar to the 'high tail' case seeded with white noise, in that the instability that arises due to the interaction between the stronger and weaker vortices, a W-T interaction, rather than between the tail vortex pair. This is emphasized by the lack of crossing of vorticity magnitude across the centreline. It can be seen in figure 4.39(c) that lobes of vorticity magnitude are present in regions of high

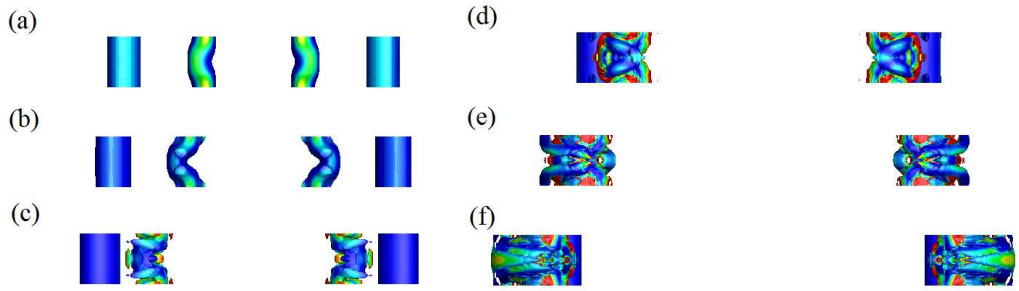

FIGURE 4.39: A time sequence of iso-surfaces of vorticity magnitude for the 'flat tail' case, viewed from directly below, for an axial wavenumber of $k\,a_1 = 5.3$, seeded with the perturbation that leads to optimal energy growth for $\tau/T_0 = 3$. The colouring of the iso-surfaces and times are as per figure 4.38.

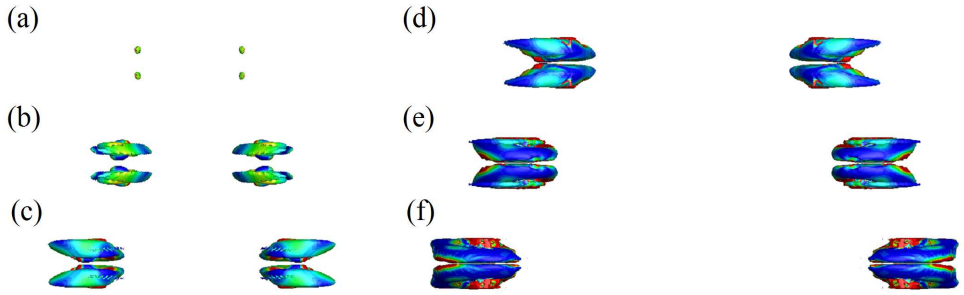

FIGURE 4.40: A time sequence of iso-surfaces of the $[\omega_y^2 + \omega_x^2]^{0.5}$ field with dominant strain flooding for the 'flat tail' case, viewed from directly below, for an axial wavenumber of $k\,a_1 = 5.3$, seeded with the perturbation that leads to optimal energy growth for $\tau/T_0 = 3$. The colouring of the iso-surfaces and times are as per figure 4.38.

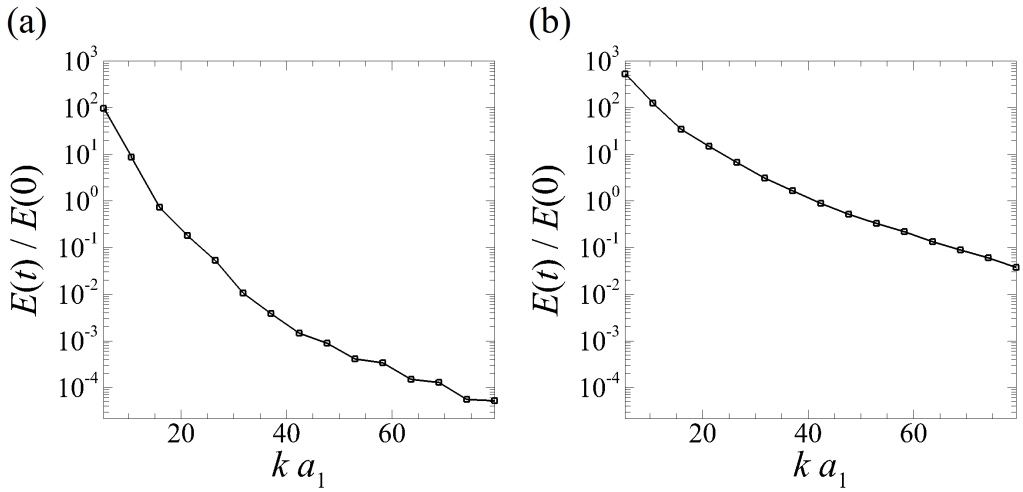

FIGURE 4.41: Plot of mode energy, $E(t)/E(0)$, against axial wavenumber, $k\,a_1$, for the 'flat tail' case seeded with the optimal perturbation found from the transient growth analysis. (a) and (b) represent times, $t/T_0 = 0.2$ and 0.5 respectively.

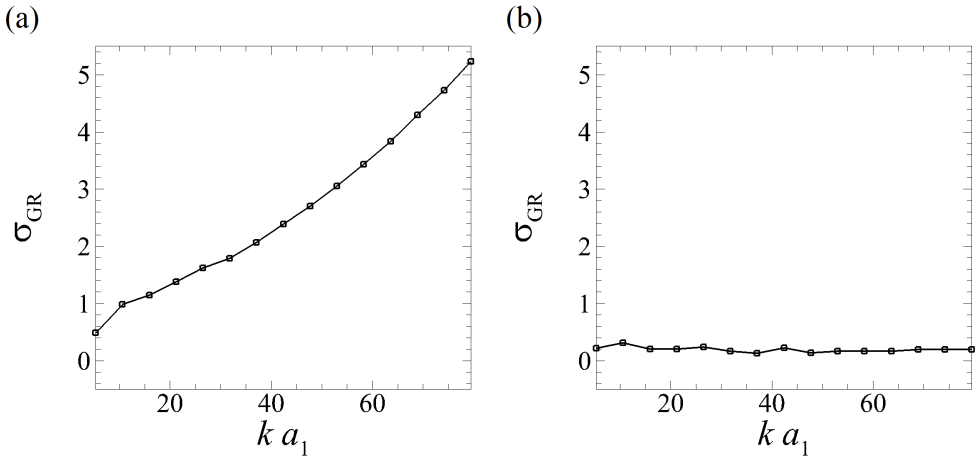

FIGURE 4.42: Plot of mode energy growth rate, σ_{GR}, against axial wavenumber, $k\,a_1$, for the 'flat tail' case seeded with the optimal perturbation found from the transient growth analysis. (a) and (b) represent times, $t/T_0 = 0.2$ and 0.4 respectively.

strain when compared to the λ_2 field (figure 4.38(c)) for the same reasons as described for the 'high tail' case seeded with the optimal perturbation. These lobes of vorticity magnitude are once again not present earlier in the flow evolution.

It can be seen that very early in the transition, there is almost no evidence of $[\omega_y^2 + \omega_x^2]^{0.5}$ (figure 4.40(a)). As the instability grows and the flow transitions into non-linear growth the $[\omega_y^2 + \omega_x^2]^{0.5}$ smears horizontally, forming into two bands that encircle the tail vortex cores (figure 4.40(b)). It is of interest to note that the transition into three-dimensional flow is symmetrical about the centerline dividing the vortices. As the flow evolves and transitions into the three-dimensional and non-linear regime, $[\omega_y^2 + \omega_x^2]^{0.5}$ forms into a pair of thick tendrils that encircle the tail vortex cores but do not cross the centreline (figure 4.40(e)).

Figure 4.41 displays the normalised energy in the individual Fourier modes for the 'flat tail' case seeded with the optimal perturbation found from the transient growth analysis. As with the previous cases shown, the higher Fourier modes experience a significant increase in normalised energy during the linear growth regime. While the leading Fourier mode experiences an increase in normalised energy of half an order of magnitude, the normalised energy in the higher Fourier modes increase by up to three orders of magnitude (figure 4.41(b)). This behaviour follows the same trend in the 'high tail' cases seeded with white noise and the optimal perturbation found from the transient growth analysis.

Figure 4.42 shows the energy growth rate in the individual Fourier modes for the 'flat tail' case seeded with the optimal perturbation found from the transient growth analysis. As in the previous cases examined, the higher Fourier modes experience a significantly higher growth rate than the leading Fourier modes during the linear growth phase (figure 4.42(a)). As with the 'high tail' cases, the growth rate of all of the modes reach a near constant growth rate in the non-linear regime (figure 4.42(b)).

Figures 4.43-4.45 show the iso-surfaces for the 'flat tail' case seeded with white noise. These figures reveal that the instability grows in a similar manner and with similar mechanisms to the 'high tail' case seeded with the perturbation that leads to optimal energy growth. As seen in the previous case, the instability mechanism has grown to a stage where the higher strain between the wing vortex pair forces vorticity across the centreline (figure 4.44(d)). This causes the tail vortices to primarily interact with each other, a T-T interaction, causing rapid destruction. As in the previous cases,

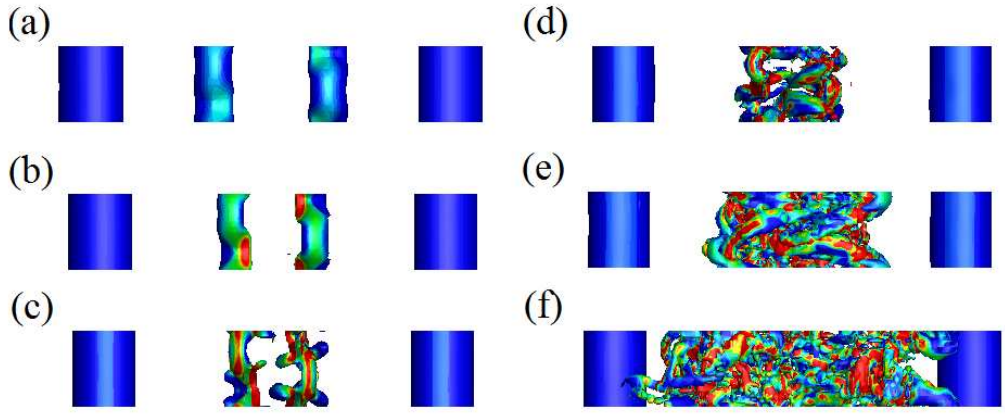

FIGURE 4.43: A time sequence of iso-surfaces of an arbitrarily small negative value of the λ_2 field plotted for the 'flat tail' case, viewed from directly below, for an axial wavenumber of $k\,a_1 = 5.3$, seeded with white noise. The iso-surfaces are coloured by dominant strain rate with blue and red corresponding to low and high levels respectively. (a)-(f) displays times $t/T_0 = 1.0, 1.05, 1.10, 1.15, 1.20$ and 1.25 respectively.

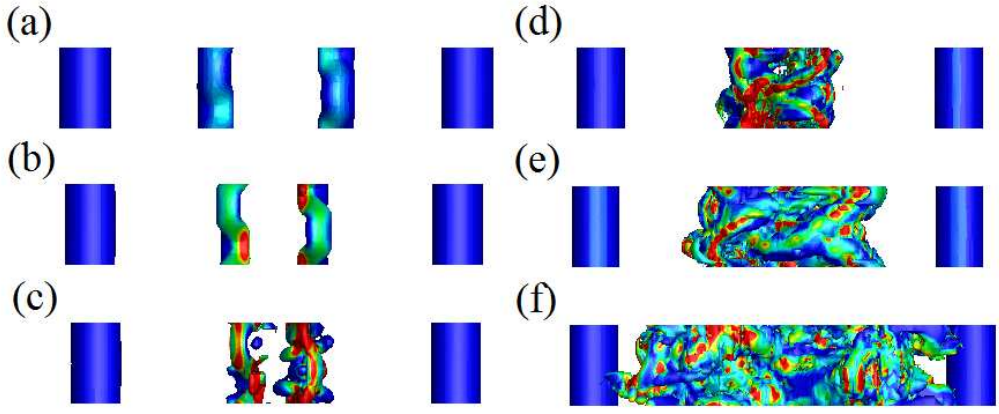

FIGURE 4.44: A time sequence of iso-surfaces of vorticity magnitude for the 'flat tail' case, viewed from directly below, for an axial wavenumber of $k\,a_1 = 5.3$, seeded with white noise. The colouring of the iso-surfaces and times are as per figure 4.43.

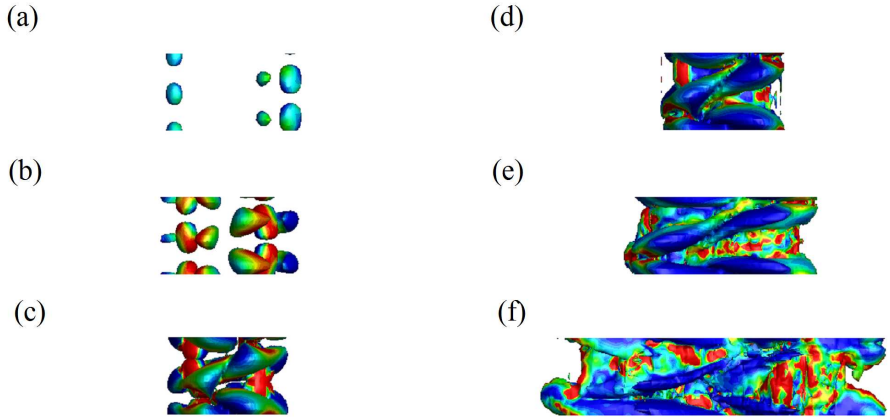

FIGURE 4.45: A time sequence of iso-surfaces of the $[\omega_y^2 + \omega_x^2]^{0.5}$ field with dominant strain flooding for the 'flat tail' case, viewed from directly below, for an axial wavenumber of $k\,a_1 = 5.3$, seeded with white noise. The colouring of the iso-surfaces and times are as per figure 4.43.

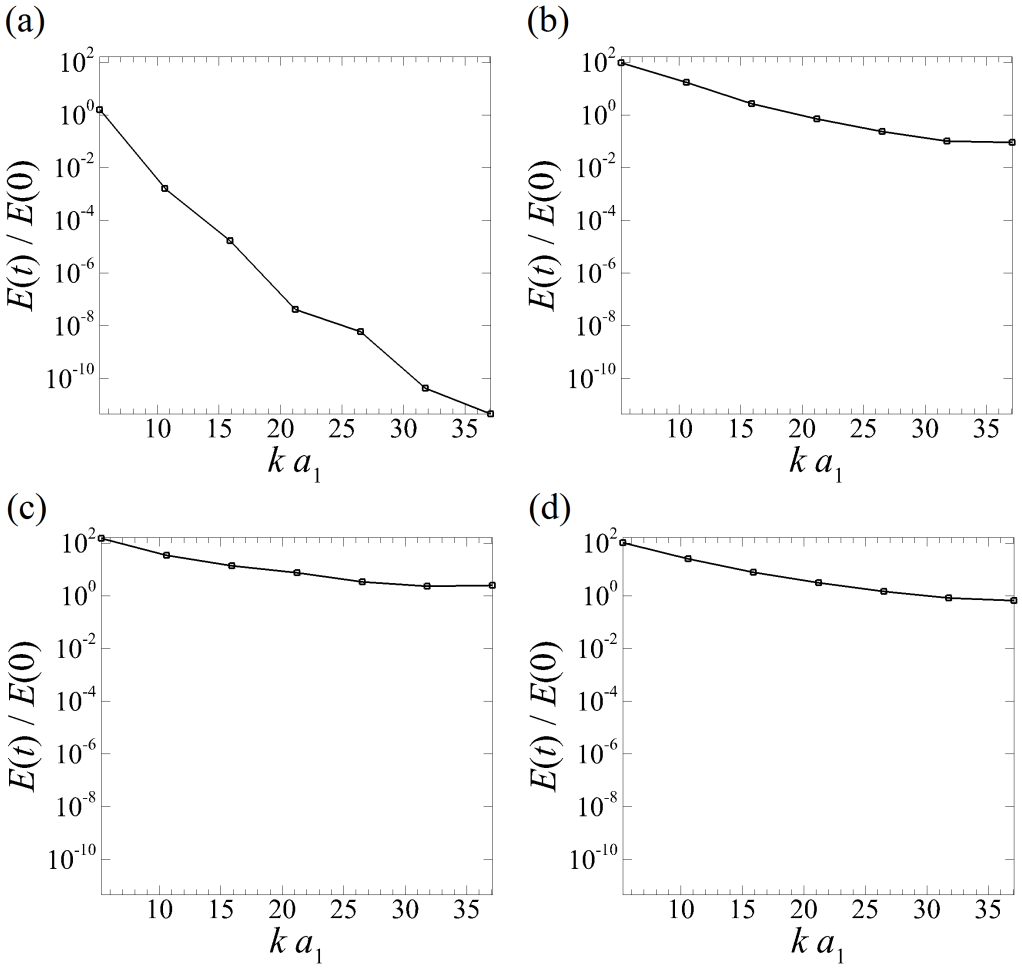

FIGURE 4.46: Plot of mode energy, $E(t)/E(0)$, against axial wavenumber, $k\,a_1$, for the 'flat tail' case seeded with white noise. (a)-(d) represent times, $t/T_0 = 0.9, 1.1, 1.2$ and 1.4 respectively.

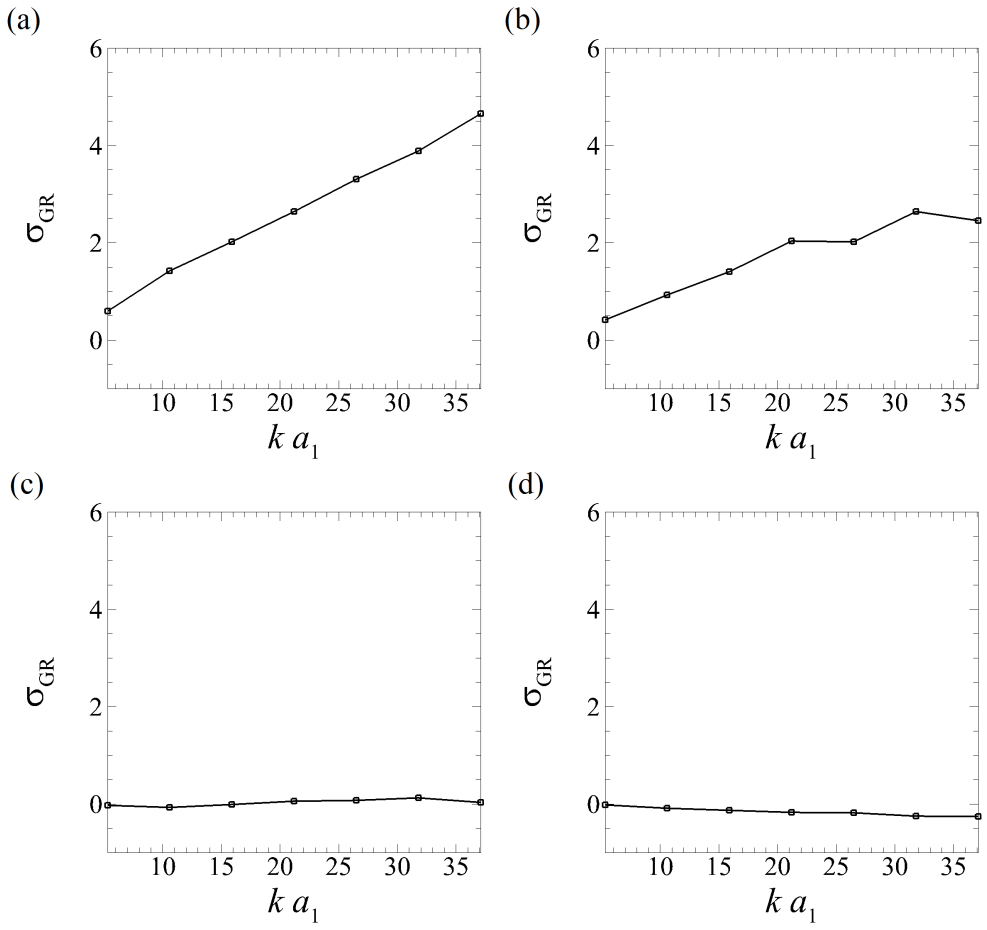

FIGURE 4.47: Plot of mode energy growth rate, σ_{GR}, against axial wavenumber, $k\,a_1$, for the 'flat tail' case seeded with white noise. (a)-(d) represent times, $t/T_0 = 0.9, 1.1, 1.2$ and 1.4 respectively.

early in the evolution the λ_2 field and vorticity magnitude correspond well with each other (figures 4.43(a)-(b) and 4.44(a)-(b)) due to the reasons described before. The lobes of vorticity magnitude that are not identified by the λ_2 field are first observed from $t/T_0 = 1.10$ (figures 4.44(c) and 4.43(c)). These lobes are most likely still present later in the evolution, but due to the transition of the tail vortices into a large region of small scale structures, are extremely difficult to identify (figures 4.44(f) and 4.43(f)).

As in the previous cases examined in relation to $[\omega_y^2 + \omega_x^2]^{0.5}$, the case of the 'flat tail' case seeded with white noise begins the transition into non-linear growth in a predominantly two-dimensional fashion (figure 4.45(a)). As the flow transitions into the non-linear regime, it becomes more three-dimensional, forming tendrils that begin to encircle the tail vortex pair, with the right tail vortex displaying a larger region of $[\omega_y^2 + \omega_x^2]^{0.5}$ (figure 4.45(b)). As in the 'high tail' case seeded with white noise, the disparity between the instability growth between the tail vortices is likely due to the initial white noise seeding having a slightly higher energy in the ideal mode shape present in one tail vortex than the other. Due to the T-T interaction, the tendrils of $[\omega_y^2 + \omega_x^2]^{0.5}$ join together to encircle both of the tail vortices (figure 4.45(c)). As the tail vortex pair becomes highly perturbed, the three-dimensional nature dominates the flow, encompassing the entire axial domain in the vicinity of the tail vortex pair with $[\omega_y^2 + \omega_x^2]^{0.5}$ (figure 4.45(f)).

Figure 4.46 displays the normalised energy in the individual Fourier modes for the 'flat tail' case seeded with white noise. As in the previous cases examined, the higher Fourier modes begin with very small normalised energy and rapidly increases during the linear phase (figure 4.46(a)-(b)). As the flow enters the non-linear regime, the higher Fourier modes begin to decay as the base flow breaks down into flows small enough to be damped out by the fluid. It is interesting to note that once the leading Fourier mode reaches a normalised energy of approximately $E(t)/E(0) = 10^2$, it remains at this level throughout the transition into the non-linear regime.

Figure 4.47 shows the growth rate in the individual Fourier modes for the 'flat tail' case seeded with white noise. As with the previous cases, the growth rate of the higher Fourier modes begins with a very large magnitude during the linear phase (figure 4.47(a)) and rapidly decreases as the flow transitions into the non-linear regime (figure 4.47(b)). Once the flow has entered the non-linear regime, the growth rate of the leading Fourier mode becomes almost zero and the higher Fourier modes be-

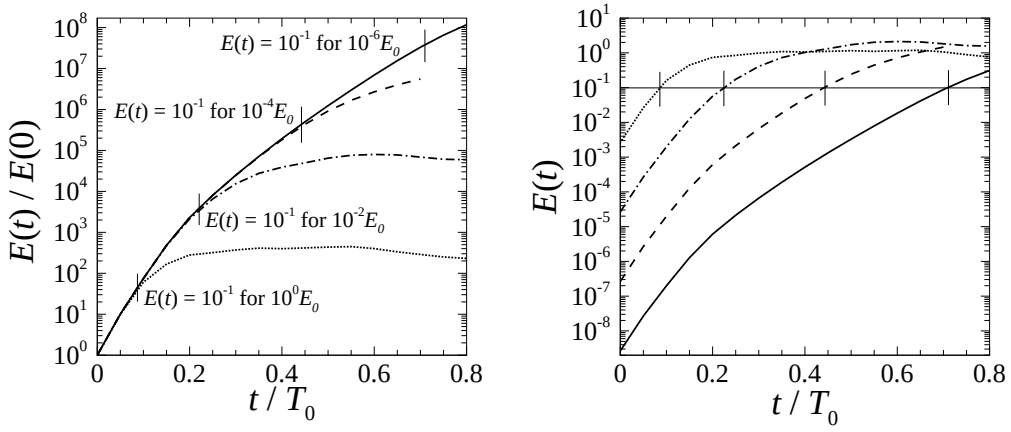

(a) (b)

FIGURE 4.48: Time histories of (a) normalised and (b) absolute perturbation energy of the 'high tail' case seeded with the optimal perturbation obtained for $\tau/T_0 = 3$ and an axial wavenumber of $k\,a_1 = 5.3$. Each case is seeded with an initial condition scaled to energy levels, E_0 (dotted line), $10^{-2}\,E_0$ (dashed-dot line), $10^{-4}\,E_0$ (dashed line), and $10^{-6}\,E_0$ (solid line). The short vertical lines represent the times when each plot enters the non-linear regime.

come negative, demonstrating that the small scale flows are becoming damped out (figure 4.47(d)).

The results shown in this section reveal that when the tail vortices are forced through the space between the wing vortices, this can initiate an interaction between the two tail vortices. This interaction is characterised by vorticity magnitude crossing the centreline of the flow. This T-T vortex interaction always leads to the vortices being destroyed at a much faster rate than the T-W interactions. The destruction of the tail vortices is what causes the instabilities in the wing vortex pair to form, leading to a faster destruction of the entire vortex flow in the T-T interaction.

4.3.6 Seeding with different initial magnitudes

This section shows the results of simulations seeding the 'high tail' case with different magnitudes of the optimal perturbation. The case used as a reference is the same 'high tail' case seeded with the optimal perturbation used in the previous sections with a perturbation energy of E_0 and is defined as having 0.01522% of the initial energy in the base flow. The values for the variables are as the 'high tail' case defined in table 2.1. This study was conducted to examine the effect of initial perturbation seeding energy on the types of vortex interaction, the T-T and T-W interaction shown in the previous section.

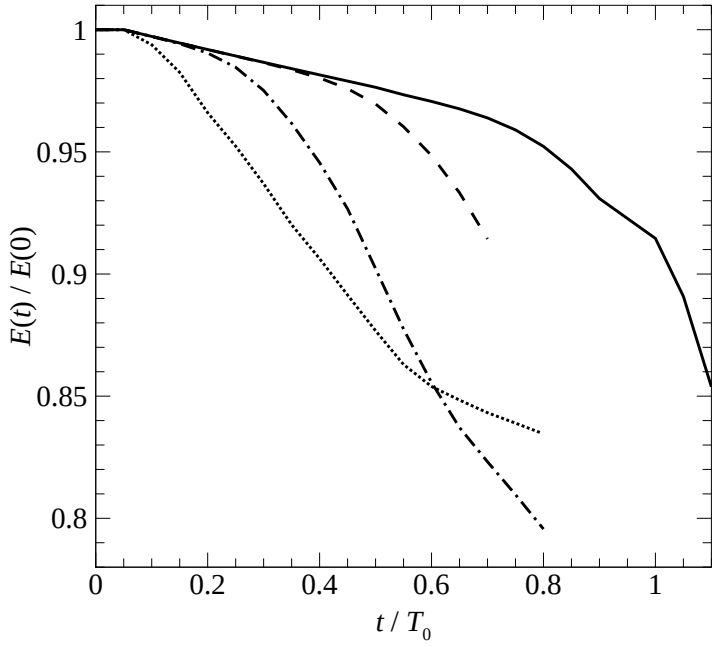

FIGURE 4.49: Time histories of the zeroth Fourier mode of the 'high tail' case seeded with the optimal perturbation obtained for $\tau/T_0 = 3$ and an axial wavenumber of $k\,a_1 = 5.3$. Each case is seeded with an initial condition scaled to energy levels, E_0 (dotted line), $10^{-2}\,E_0$ (dashed-dot line), $10^{-4}\,E_0$ (dashed line), and $10^{-6}\,E_0$ (solid line).

Figure 4.48 displays the (a) normalised and (b) absolute perturbation energy for the 'high tail' case seeded with the optimal perturbation obtained for $\tau/T_0 = 3$ and an axial wavenumber of $k\,a_1 = 5.3$ at a number of different seeding energy magnitudes. Figure 4.48(a) shows that by reducing the strength of the initial perturbation relative to the base flow, the onset of the non-linear phase is delayed, leading to a higher normalised energy peak. The deviation from the collapsed region in figure 4.48(a) signals the onset of non-linear effects in the growing disturbance. This is because it takes longer for the disturbance to grow to sufficient amplitude to modify the base flow. As the initial perturbation energy decreases, the onset of the non-linear regime is delayed even further.

Figure 4.48(b) shows that the delay of the non-linear regime has the overall effect of increasing the amount of energy that grows until it becomes saturated. This higher level of saturation indicates that the base flow will become more distorted and therefore lead to faster destruction. As each of the plots deviate from the linear evolution (figure 4.48(a)) they all have approximately the same level of absolute energy in the transition, $E(t) \approx O(0.1)$. This implies that once the absolute perturbation energy reaches this level, $E(t) \approx 10^{-1}$, it will always transition into the non-linear regime. As the absolute energy plateaus, all of the graphs reach a final energy of $E(t) \approx O(1)$.

Figure 4.49 displays the normalised energy in the zeroth Fourier mode for the 'high tail' case seeded with the optimal perturbation obtained for $\tau/T_0 = 3$ and an axial wavenumber of $k\,a_1 = 5.3$ at a number of different seeding energy magnitudes. It shows that the decrease in seeding magnitude has the effect of allowing the linear regime to decrease the energy in the base flow to a larger degree. The dashed-dot line, corresponding to a seeding magnitude of $10^{-2}\,E_0$ dips to a lower energy in the zeroth Fourier mode than the reference case. This indicates that while it may take a slightly longer time to reach the non-linear regime, it will dip to a lower energy in the zeroth Fourier mode.

This leads to the conclusion that there should be an optimal seeding energy that produces enough of a drop in the energy of the zeroth Fourier mode to reduce the coherence of the vortices (and therefore reduce the hazard to trailing aircraft), but does not take an extended period of time to reach this state.

Figure 4.50 illustrates the main difference between a flow that has become non-linear and one that is still in the linear growth regime. Before the tail vortex pair enters the

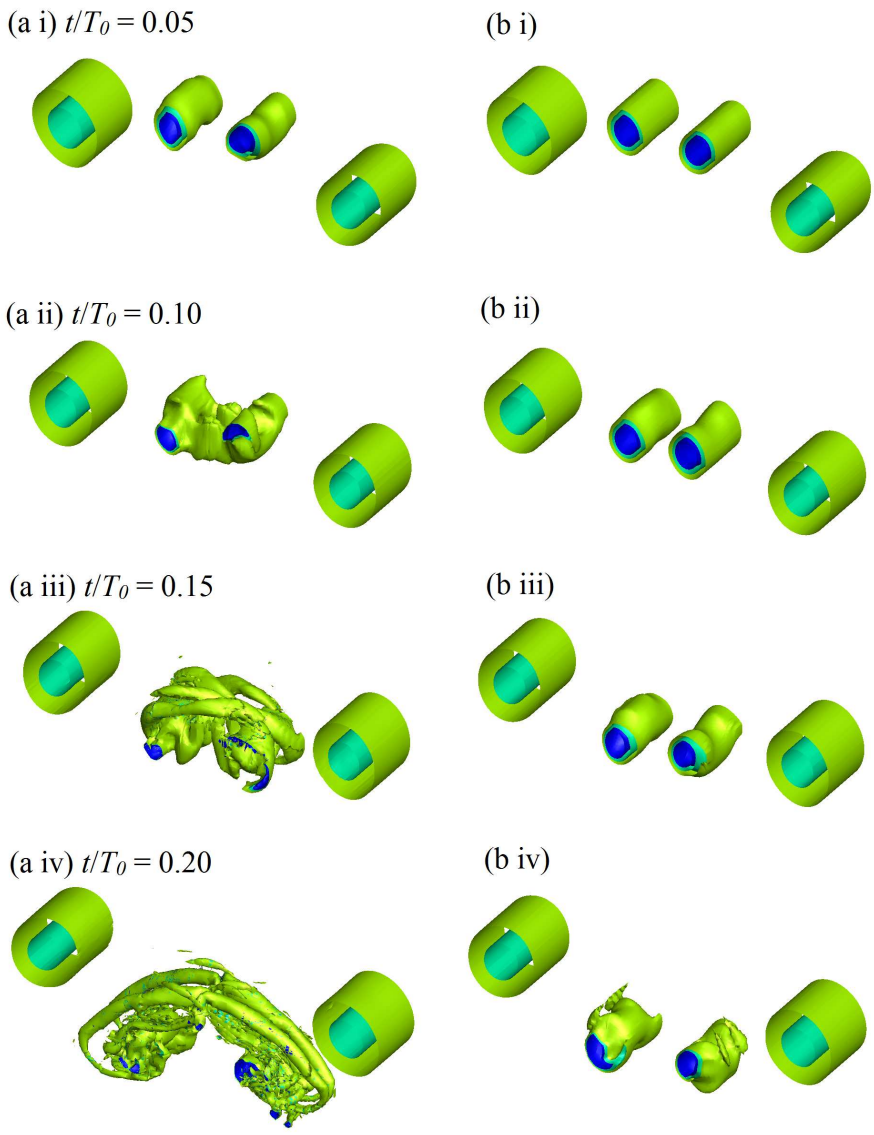

FIGURE 4.50: Plots of iso-surfaces of axial vorticity at times (i) - (iv) $t/T_0 = 0.05, 0.10, 0.15, 0.20$ for the 'high tail' case seeded with the optimal perturbation for $\tau/T_0 = 3$. The simulation has an axial extension of $k\,a_1 = 5.3$. The colours represent levels of the λ_2 field, with green representing small negative value to blue representing a high negative value. (a) and (b) show the cases seeded with disturbances of magnitudes E_0, and $10^{-2}\,E_0$ respectively.

highly strained region between the wing vortex pair, the tail vortices are still strong, coherent vortices (figure 4.50(a i) and (b i)). In the case of the disturbance seeded with a magnitude of E_0, a significant amount of flow from the tail vortices crosses the mid-plane at $t/T_0 = 0.10$, leading to a T-T interaction and causing the flow to become non-linear (figure 4.50(a ii)). At the same time, $t/T_0 = 0.1$, the flow seeded with a disturbance of magnitude $10^{-2}\,E_0$ is still in the linear growth regime, demonstrating a lack of perturbation energy required to cause a T-T interaction. This prevents any flow from the tail vortices crossing the mid-plane between the vortices and leading to a T-W interaction (figure 4.50(b ii)). The crossing of flow across the mid-plane between the wing vortices in the T-T interaction causes a rapid loss of coherence in the tail vortices, leading to a rapid destruction of the tail vortices (figure 4.50(a iv)) and a reduction in instability growth. In the case of the seeding of a magnitude $10^{-2}\,E_0$ perturbation, the tail vortices are still coherent vortices, and this allows the instability to continue growing (figure 4.50(b iv)). The delay of the interaction across the mid-plane allows for enhanced linear growth for an orbit until the tail vortices are next entering the highly strained region between the wing vortex pair.

4.4 Effect of seeding time during first tail vortex orbit

In this section the results of a study conducted to investigate the effect of seeding the flow with an optimum perturbation during the first orbit of the tail vortex pair around the wing vortex pair are discussed, beginning with the 'high tail' configuration. T_{st} is the seeding time and t_{VST} is taken as the time from seeding for this section, where $t_{VST} = t - T_{st}$. As T_{st} is normalised throughout by the orbit time of the tail vortex pair, then T_{st}/T_0 is the fraction of a complete orbit completed by the tail vortex pair. It is important to note that due to the requirement of the numerical method to initially relax from the imposed solution to a true solution of the Navier–Stokes equations over $0 \leq t/T_0 \leq 0.1$, the solutions for $T_{st}/T_0 = 1$ will not correspond to the solution for $T_{st}/T_0 = 0$. This has the effect of making the solutions not purely cyclic for the first orbit period, but due to the nature of the constantly changing position of the four-vortex system, obtaining a relaxed initial solution is almost impossible.

Figure 4.51 shows a schematic of the layout of the four-vortex system used for the position study. The tail orbit fraction, T_{st}/T_0, begins at $T_{st}/T_0 = 0$ when the tail vortices are in the position shown, and follows the path shown by the solid black arrow

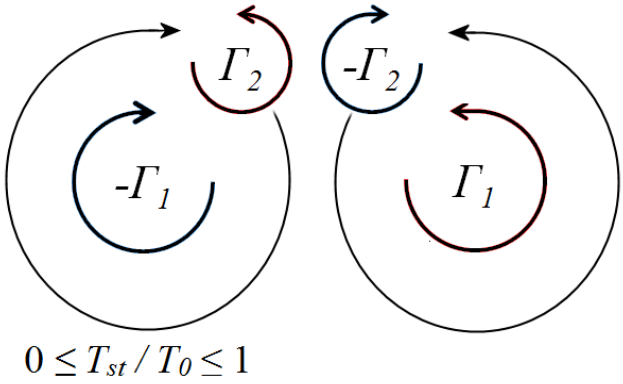

FIGURE 4.51: Diagram displaying the layout of the initial vortex set and defining the span variable for the 4 vortex system model for the position study.

until they return to that position after a complete orbit, $T_{st}/T_0 = 1$.

4.4.1 Transient growth analysis

Figure 4.52 shows a transient growth analysis of the 'high tail' case with growth amplification factor, $G(\tau)$ against the orbit fraction, T_{st}/T_0. It shows that the stability of a four-vortex system is directly related to the position of the tail vortex pair around the wing vortex pair. This gives the flow a stability of a cyclic nature based on the orbit of the tail vortex pair, with a maximum at $T_{st}/T_0 = 0.6$. This is interesting as it corresponds to an orbit fraction when the tail vortex pair is initially on the outside of the wing vortex pair. Given that $\tau/T_0 = 1$, this corresponds to a situation where the perturbation undergoes a majority of its transient growth while within the highly strained region between the wing vortex pair.

Figure 4.53 shows the initial optimal perturbation fields for orbit fractions of $T_{st}/T_0 = 0.15, 0.25, 0.35, 0.45, 0.55, 0.65, 0.75, 0.85, 0.95$. The initial optimal perturbation field is the perturbation field that leads to maximum energy growth for a given value of τ/T_0 and axial wavenumber, $k\,a_1$. An axial wavenumber of $k\,a_1 = 5.3$ was chosen as it corresponds to the peak in transient growth amplification factor found in § 4.3.1. It is interesting to note that the majority of the perturbation vorticity is contained in a mode [-1,1,1] within the cores of the tail vortex pair. This perturbation dipole rotates with the flow, maintaining an angle of approximately 45° to a line from the tail vortex core to the closest wing vortex core. This implies that the most effective way to destabilise the system is to add a perturbation to the tail vortex pair to maximise energy growth of the perturbation. It is also interesting to note that all of the cases exhibit

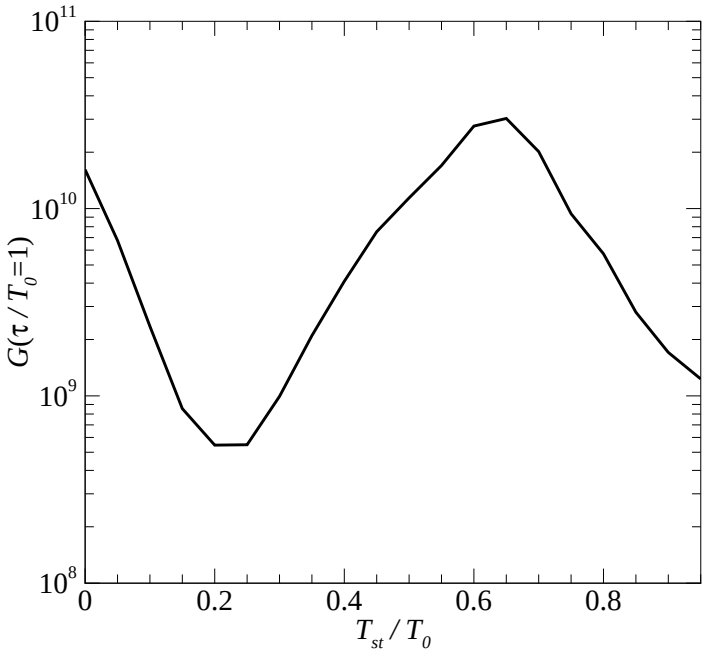

FIGURE 4.52: Plot of growth amplification factor, $G(\tau)$, against tail vortex orbit fraction, T_{st}/T_0 (where $T_{st}/T_0 = 0$ is equivalent to the 'high tail' case shown in previous sections). For this plot an optimal disturbance with $k\,a = 5.3$ and $\tau/T_0 = 1$ is used.

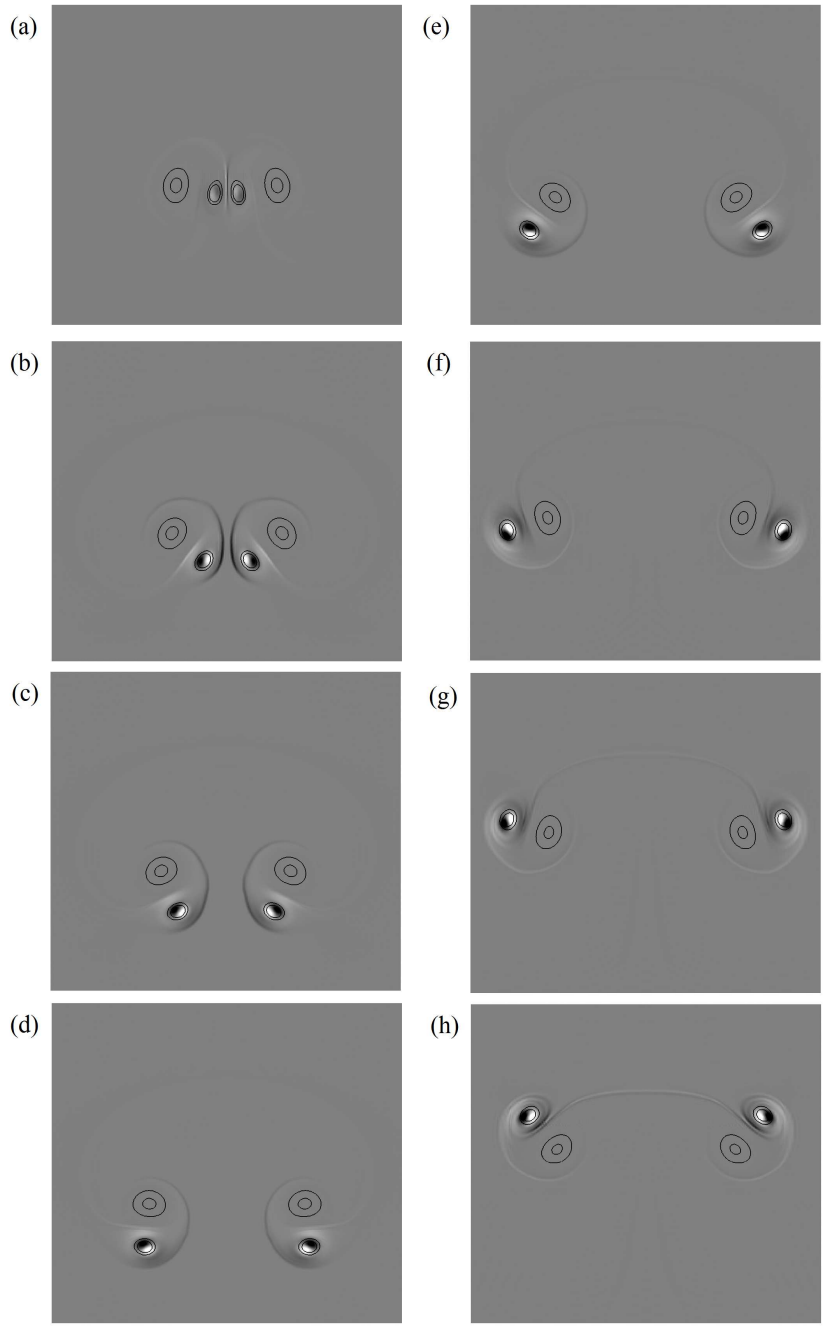

FIGURE 4.53: A sequence of spanwise vorticity in the initial optimal perturbation field (flooded contours) for the 'high tail' case for $\tau/T_0 = 3$. Flooded contour levels are chosen arbitrarily to display the perturbation structure. Solid contour lines show spanwise vorticity in the base flow at levels of vorticity of $\mid \omega_z \mid = 1, 3, 7$. An axial wavenumber of $k\,a_1 = 5.3$ to correspond to the peak found in the transient growth analysis in § 4.3.1. (a)-(h) are the initial optimal perturbations for $T_{st}/T_0 = 0.15, 0.25, 0.35, 0.45, 0.55, 0.65, 0.75, 0.85$ and 0.95 respectively.

symmetry about the mid-plane separating the vortices. When $T_{st}/T_0 = 0.15$, there is a thin smear of opposing perturbation vorticity directly between the vortices, which becomes a thin 'tail' of vorticity that wraps around the wing vortices for higher values of T_{st}/T_0. It is of interest to note that there is a thin band of perturbation vorticity that connects the perturbation present in the tail vortices when they are above the wing vortices (figure 4.53(g)-(h)). In these latter cases, the perturbation surrounding the vortex cores takes the form of a spiral of opposite sign perturbation vorticity. This is in contrast to the earlier cases, which exhibit a single region of perturbation with one sign of vorticity (figure 4.53(b)-(e)). This implies that the rotation of the tail vortex has the effect on the initial optimal perturbation field of drawing the spiral more tightly around the tail vortex pair.

4.4.2 Direct numerical simulation

A study comprising a number of direct numerical simulations was performed to observe the effect of seeding the flow with the optimal perturbations at different tail vortex orbit fractions, T_{st}/T_0, and the transition into non-linear flow. An axial wavenumber of $k\,a_1 = 5.3$ was chosen as it corresponded to the peak in growth amplification factor found in the transient growth analysis. The axial domain was chosen to allow for one wavelength of the desired instability and all the cases were seeded in only the first Fourier mode. Sixteen Fourier modes were chosen to give a good balance between computational time and error as shown in § 2.6.3. The energy levels of all the perturbations used to seed the different cases are the same and are of a magnitude of 0.01522% of the initial energy in the base flow. The vortex core sizes and separations are as per the 'high tail' case described in § 2.1.

The optimal perturbation fields found from the transient growth analysis by varying tail orbit fraction, T_{st}/T_0, were used to seed a number of direct numerical simulations. Figures 4.54-4.65 will be described in this section. Figures 4.54-4.57 show a time history of normalised perturbation energy for successive intervals of T_{st}/T_0 variation. The perturbation energy is the sum of all of the Fourier modes used for each simulation and is normalised by the initial perturbation energy, which is the same for all cases. The axial wavenumber is fixed at $k\,a_1 = 5.3$ to correspond with the peak axial wavenumber found in the transient growth analysis in § 4.3.1.

Figures 4.60-4.65 show temporal evolution and transition into the non-linear regime

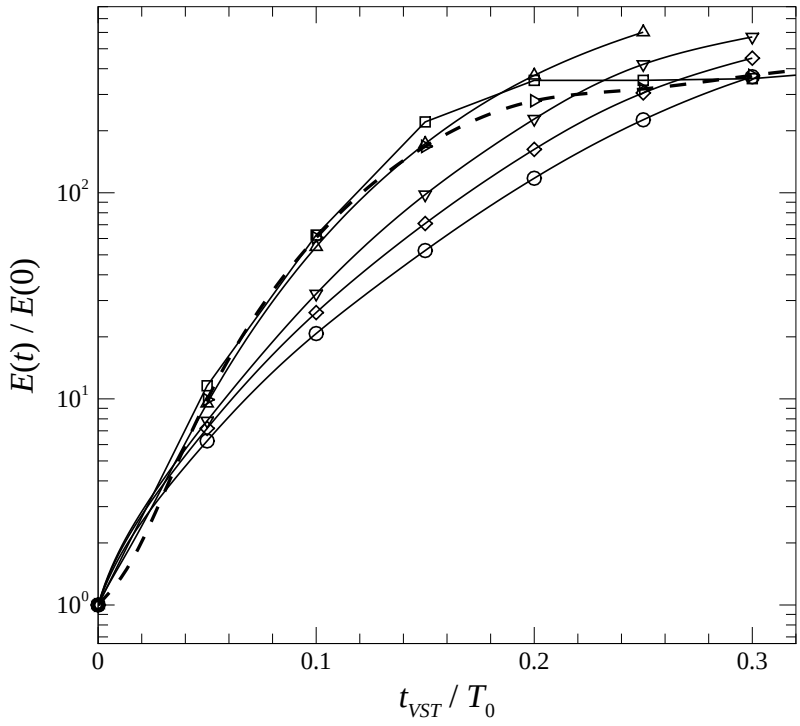

FIGURE 4.54: Time history of normalised perturbation energy with the flow seeded at different times during the first orbit of the tail vortex pair around the wing vortex pair. $\square, \triangle, \nabla, \diamondsuit$ and $\circ$ represent seeding at tail orbit fractions of $T_{st}/T_0 = 0.05, 0.10, 0.15, 0.20$ and 0.25 respectively. The reference seeding time of $T_{st} = 0$ is represented by $\triangleright$ and a dashed line. $t_{VST}/T_0 = 0$ is used to define initial time so that all curves originate at the vertical axis. An axial wavenumber of $k\,a_1 = 5.3$ was considered to correspond to the peak found in the transient growth analysis in § 4.3.1.

for successive intervals of T_{st}/T_0 variation. The iso-surfaces displayed in these plots are an arbitrarily small negative value of the λ_2 field with coloured shading representing levels of dominant strain, with blue and red corresponding to low and high values respectively.

Figure 4.54 shows a time history of normalised perturbation energy for a band of seeding for $T_{st}/T_0 = 0.05 - 0.25$. It can be seen that the growth rate of the instability is directly affected by the position of the tail vortex pair at seeding. When the tail vortex pair are seeded within the highly strained region between the wing vortex pair, the growth of the instability is greater and leads to a faster onset of non-linearity. As the tail vortex pair is seeded as it leaves the highly strained region between the wing vortex pair, the growth rate is lower, leading to a delay of the onset of non-linear growth. It is of interest to note that the perturbation energy of the cases where the onset of

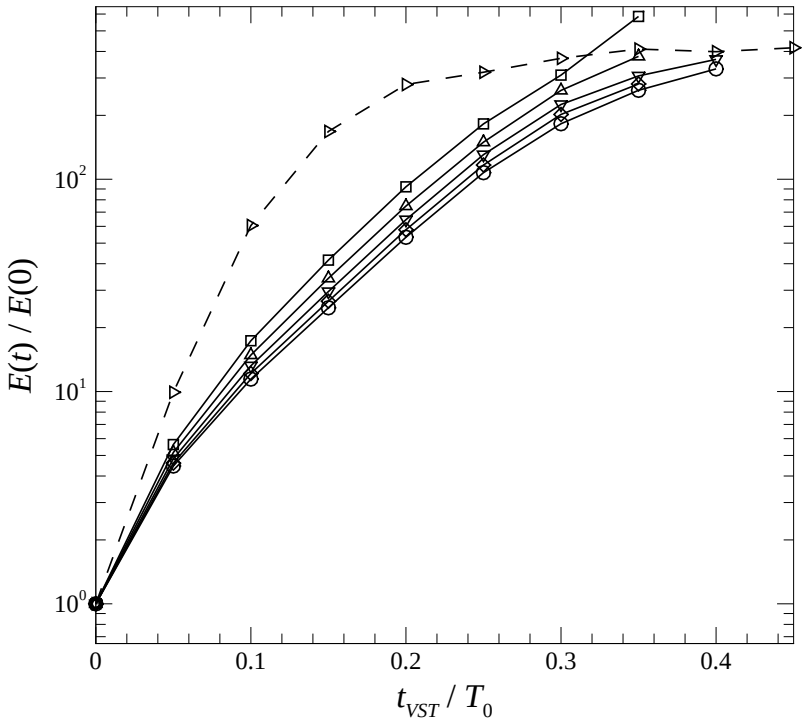

FIGURE 4.55: Time history of normalised perturbation energy with the flow seeded at different times during the first orbit of the tail vortex pair around the wing vortex pair. $\square, \triangle, \nabla, \diamondsuit$ and $\circ$ represent seeding at tail orbit fractions of $T_{st}/T_0 = 0.30, 0.35, 0.40, 0.45$ and 0.50 respectively. The reference seeding time of $T_{st} = 0$ is represented by $\triangleright$ and a dashed line. $t_{VST}/T_0 = 0$ is used to define initial time so that all curves originate at the vertical axis. An axial wavenumber of $k\,a_1 = 5.3$ was considered to correspond to the peak found in the transient growth analysis in § 4.3.1.

non-linear growth is delayed peaks at a higher level to the cases with earlier onset of non-linear growth.

Figure 4.55 shows a time history of normalised perturbation energy for a band of seeding for $T_{st}/T_0 = 0.30 - 0.50$. It can be seen that as the seeding of the flow occurs further away from the highly strained region between the wing vortex pair the growth rate of the instability decreases as well. The growth rate of the instability seeded at $T_{st}/T_0 = 0.50$ is lower than the growth rate of the instability seeded at $T_{st}/T_0 = 0.30$. It is of interest to note the case of $T_{st}/T_0 = 0.30$ as the lower growth rate of the instability allows it to grow to a higher energy before becoming non-linear.

Figure 4.56 shows a time history of normalised perturbation energy for a band of seeding for $T_{st}/T_0 = 0.55 - 0.75$. It can be seen that the growth rates of the seeding orbit fraction, $0.55 \leq T_{st} \leq 0.75$, are approximately the same, leading to all of the

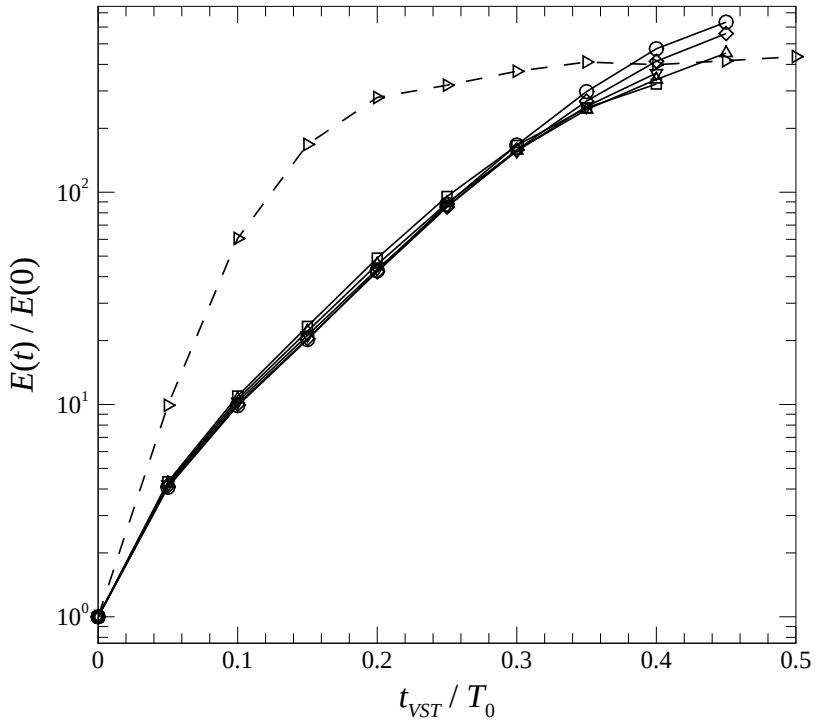

FIGURE 4.56: Time history of normalised perturbation energy with the flow seeded at different times during the first orbit of the tail vortex pair around the wing vortex pair. $\square, \triangle, \nabla, \diamondsuit$ and $\circ$ represent seeding at tail orbit fractions of $T_{st}/T_0 = 0.55, 0.60, 0.65, 0.70$ and 0.75 respectively. The reference seeding time of $T_{st} = 0$ is represented by $\triangleright$ and a dashed line. $t_{VST}/T_0 = 0$ is used to define initial time so that all curves originate at the vertical axis. An axial wavenumber of $k\,a_1 = 5.3$ was considered to correspond to the peak found in the transient growth analysis in § 4.3.1.

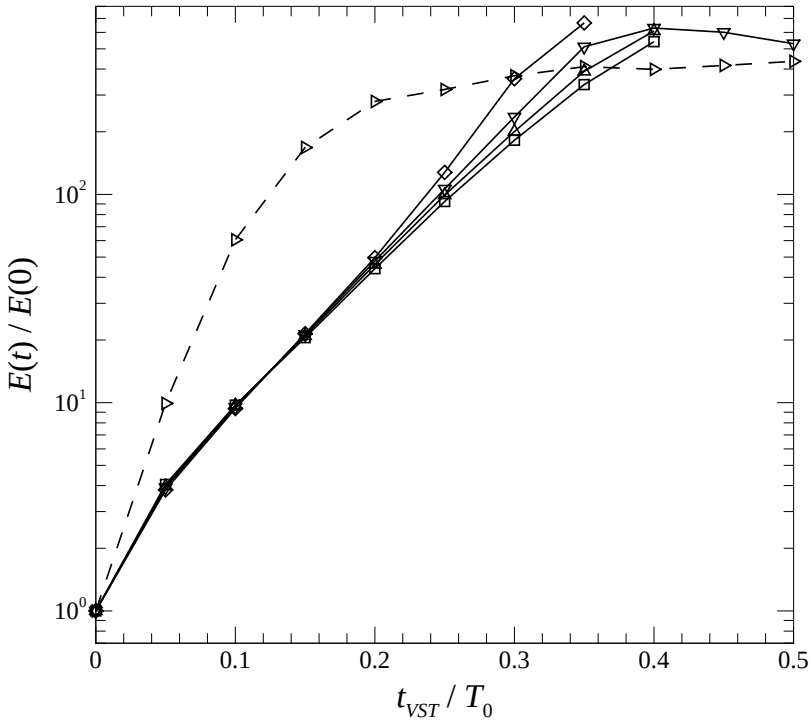

FIGURE 4.57: Time history of normalised perturbation energy with the flow seeded at different times during the first orbit of the tail vortex pair around the wing vortex pair. $\square, \triangle, \nabla$ and $\diamondsuit$ represent seeding at tail orbit fractions of $T_{st}/T_0 = 0.80, 0.85, 0.90$ and 0.95 respectively. The reference seeding time of $T_{st} = 0$ is represented by $\triangleright$ and a dashed line. $t_{VST}/T_0 = 0$ is used to define initial time so that all curves originate at the vertical axis. An axial wavenumber of $k\,a_1 = 5.3$ was considered to correspond to the peak found in the transient growth analysis in § 4.3.1.

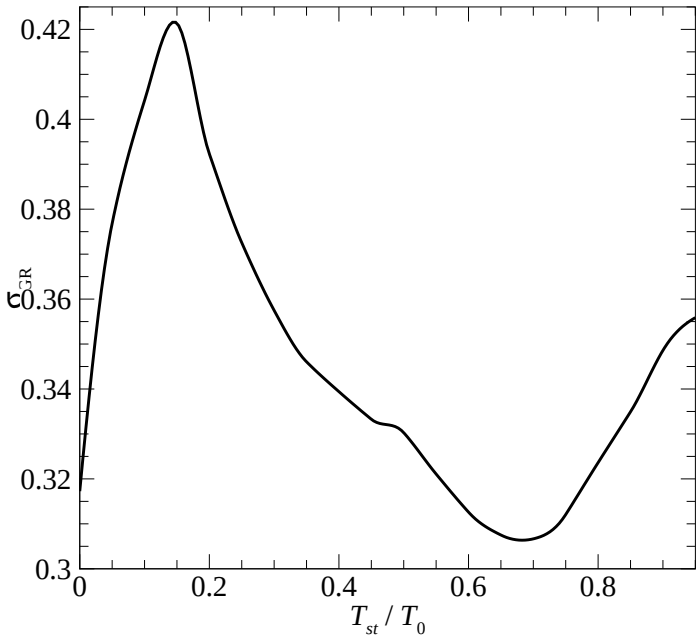

FIGURE 4.58: Perturbation energy growth rate, σ_{GR}, at $t_{VST}/T_0 = 0.15$ against the tail orbit fraction the flow is seeded at, T_{st}/T_0. An axial wavenumber of $k\,a_1 = 5.3$ is prescribed for the perturbation field.

perturbation energies collapsing into a similar trend. It is of interest to note that the perturbation energies for the latter seeding orbit fraction $T_{st}/T_0 = 0.75$ are higher at latter times due to a delay of the onset of the non-linear regime. The delay of onset of the non-linear regime for all of the cases means that the perturbation energy can reach a higher level than the reference case of $T_{st}/T_0 = 0$.

Figure 4.57 shows a time history of normalised perturbation energy for a band of seeding for $T_{st}/T_0 = 0.80 - 0.95$. It can be seen that early in the evolution the growth rates of the seeding orbit fraction, $0.80 \leq T_{st}/T_0 \leq 0.95$, are approximately the same for $0 \leq t/T_0 \leq 0.2$, leading to the perturbation energies collapsing into a similar trend. As the seeding orbit fraction increases, $T_{st}/T_0 = 0.95$, the growth rate later in the evolution, $t/T_0 \geq 0.2$, increases due to the proximity of the seeding close to the highly strained region between the wing vortex pair. In all of the cases the perturbation energy becomes greater than the reference case, $T_{st}/T_0 = 0$. This is because the lower growth rate delays the onset of the non-linear region and therefore the subcritical nature of the flows.

Figure 4.58 shows a time history of the perturbation energy growth rate, σ_{GR} for

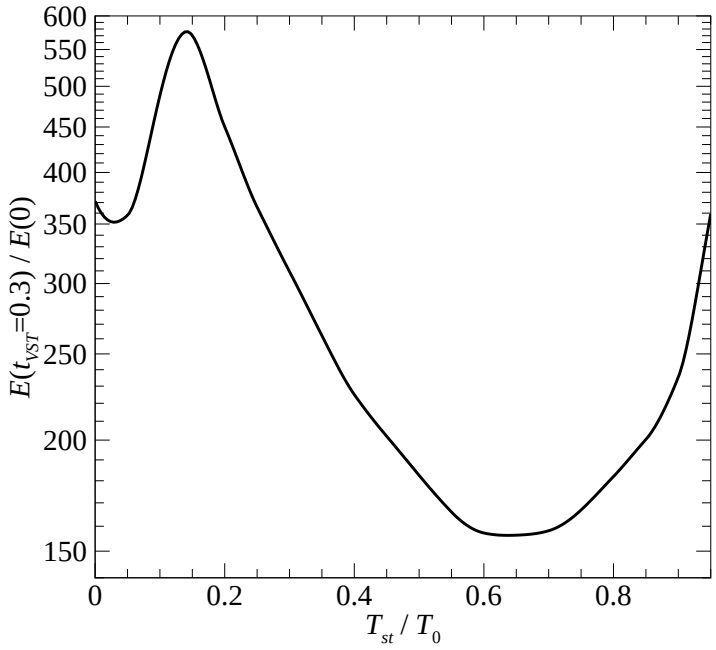

FIGURE 4.59: Perturbation energy at $t_{VST}/T_0 = 0.3$, normalised by initial perturbation energy, against tail orbit fraction, T_{st}/T_0, where the flow is seeded. An axial wavenumber of $k\,a_1 = 5.3$ is prescribed for the perturbation field.

the linear growth regime against the tail orbit fraction, T_{st}/T_0 the flow is seeded at. It demonstrates that the linear growth rate of the instability growth is directly related to the position of the tail vortices, given by the tail orbit fraction. When the flow is seeded just before or within the highly strained region between the wing vortices, $0 \leq T_{st}/T_0 \leq 0.3$ the growth rate is significantly higher than when the tail vortex pair is seeded after the tail vortex pair has passed the highly strained region between the wing vortex pair, $0.3 \leq T_{st}/T_0 \leq 0.9$. This shows that the growth rate of the instability is directly related to the proximity of the tail vortex pair to the highly strained region between the wing vortex pair.

Figure 4.59 shows the perturbation at $t_{VST}/T_0 = 0.3$, normalised by initial perturbation energy, against tail orbit fraction, T_{st}/T_0, where the flow is seeded. As the growth rate of the instability (as shown in figure 4.58) changes in a cyclic manner in relation to the tail vortex orbit fraction, T_{st}/T_0, it is unsurprising that the normalised perturbation energy at a specific time also follows a similar pattern with a maximum at $T_{st}/T_0 = 0.15$ and a minimum at $T_{st}/T_0 = 0.65$ (figure 4.59). As with the growth rate, the cases where the flow is seeded with the tail vortex pair just before or within the

highly strained region between the wing vortex pair, $0 \leq T_{st}/T_0 \leq 0.3$, the normalised perturbation energy is significantly higher than the cases where the flow is seeded when the tail vortex pair is outside of the highly strained region between the wing vortex pair, $0.3 \leq T_{st}/T_0 \leq 0.9$. Overall, figures 4.54-4.57 have a number of things in common. The growth rate of the linear region is directly related to the position of the tail vortex pair compared to the highly strained region between the wing vortex pair. When the flow is seeded just before the tail vortex pair enters the highly strained region between the wing vortex pair, $0 \leq T_{st}/T_0 \leq 0.10$, the growth rate is at its highest. When the tail vortex pair is seeded outside the highly strained region, $0.15 \leq T_{st}/T_0 \leq 0.75$, the growth rate is at its lowest and only begins to increase as the tail vortex pair approaches this region again, $T_{st}/T_0 \geq 0.80$.

Figure 4.60 shows the temporal evolution of the four-vortex DNS seeded at $T_{st}/T_0 = 0.05$ for the period $0.00 \leq t_{VST}/T_0 \leq 0.35$. It shows that the instability begins growing immediately from seeding. As the instability is growing while in the highly strained region between the wing vortex pair it leads to the tail vortices being forced to interact with each other in a T-T interaction (figure 4.60(b)). Loops of λ_2 from the tail vortices begin to cross the $x = 0$ plane, greatly enhancing the growth of the instability in the tail vortex pair (figure 4.60(d)). From this point, the tail vortices evolve into small scale flow structures as the stronger wing vortices pull them apart (figure 4.60(f)). As the tail vortex pair devolves into small scale structures, an instability begins to form in the wing vortex pair as an asymmetric bending at about $\pm 45^\circ$ to the line between the vortex cores (figure 4.60(h)).

Figure 4.61 shows the temporal evolution of the four-vortex DNS seeded at $T_{st}/T_0 = 0.2$ for the period $0.00 \leq t_{VST}/T_0 \leq 0.30$. It shows that the instability grows as the tail vortex pair is leaving the highly strained region between the wing vortex pair and presents as an asymmetric bending at about $\pm 45^\circ$ to the line between the vortex cores (figure 4.61(b)). As the tail vortices have left the highly strained region between the wing vortices before the instability has been seeded, the flow resolves into a T-W interaction (figure 4.61(c)). It of interest to note that the instability in the wing vortex pair becomes observable as early as $t_{VST}/T_0 = 0.25$ (figure 4.61(f)), unlike the earlier seeding case where it is is not as evident until $t_{VST}/T_0 = 0.35$ (figure 4.60(h)). The instability beginning to form in the wing vortex pair is an asymmetric bending at about $\pm 45^\circ$ to the line between the vortex cores, which is similar to the previous case.

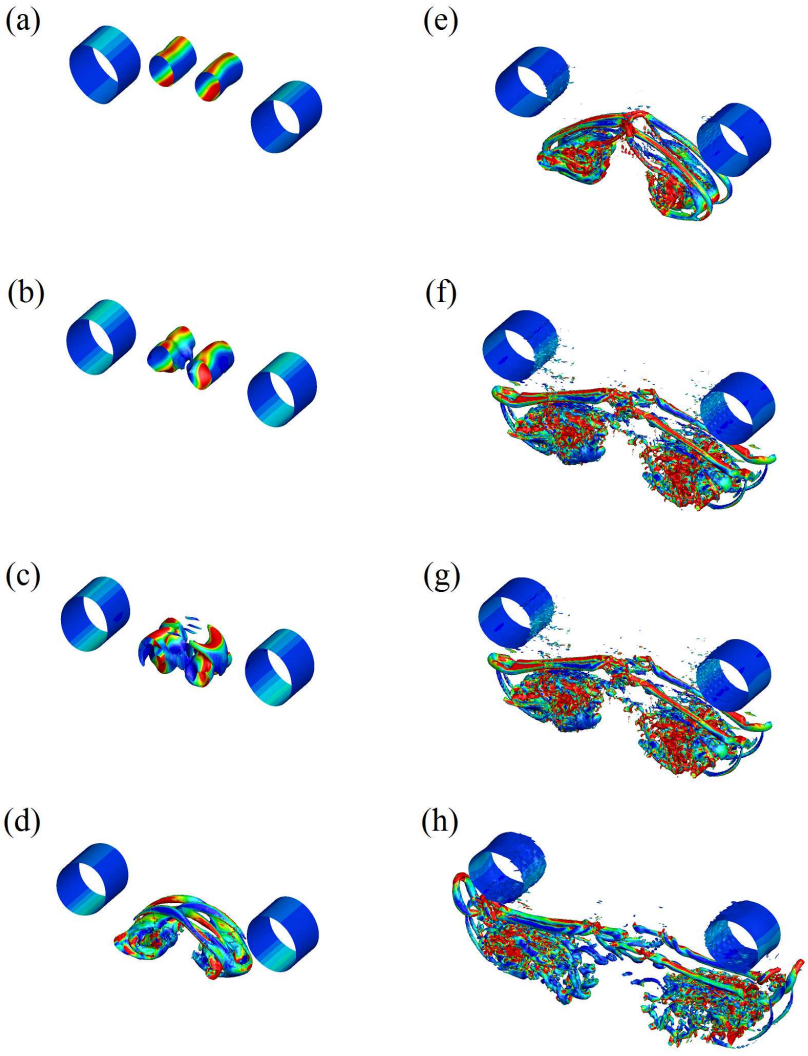

FIGURE 4.60: Time sequences of iso-surfaces at an arbitrarily small negative value of the λ_2 field plotted from a three-dimensional simulation of the $T_{st}/T_0 = 0.05$ case with an axial extent corresponding to a wavenumber of $k\,a_1 = 5.3$. The flow is seeded initially with the optimal perturbation for $\tau/T_0 = 1$. The coloured shading shows levels of dominant strain, with blue and red corresponding to low and high values respectively. (a)-(h) displays the evolution of the instability for times $t_{VST}/T_0 = 0.00, 0.05, 0.10, 0.15, 0.20, 0.25, 0.30$ and 0.35 where $t_{VST}/T_0 = 0$ is taken as seeding time.

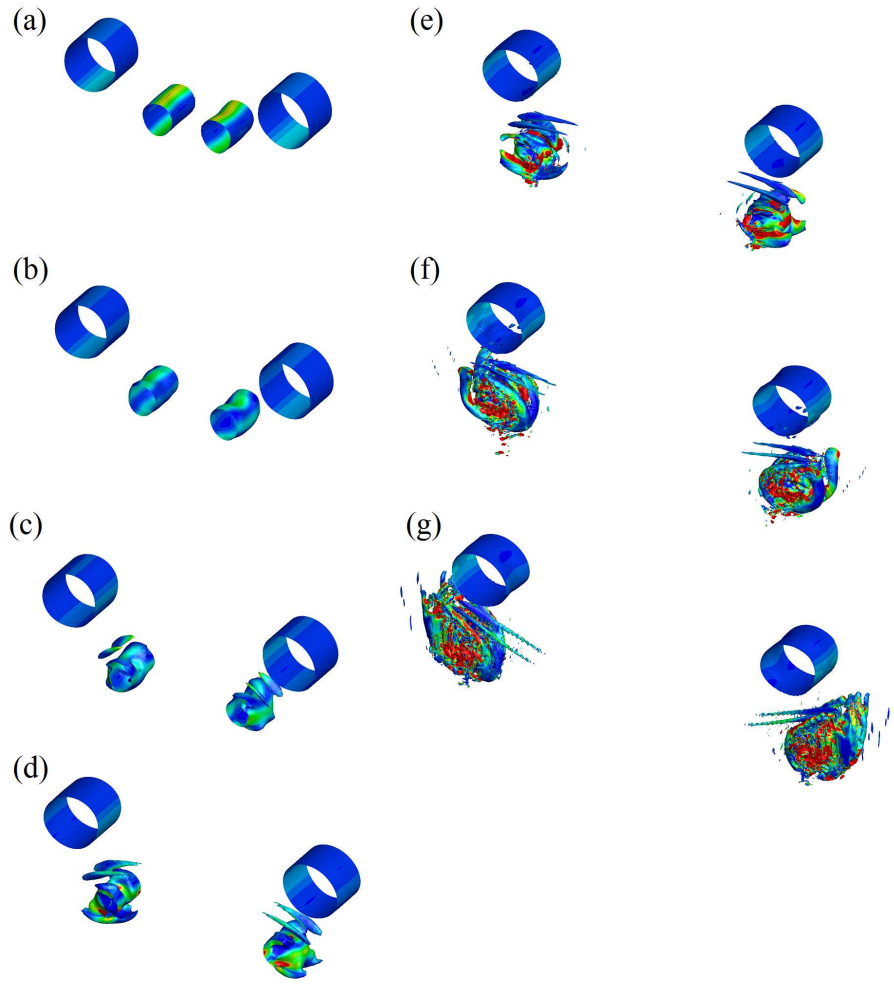

FIGURE 4.61: Time sequences of iso-surfaces at an arbitrarily small negative value of the λ_2 field plotted from a three-dimensional simulation of the $T_{st}/T_0 = 0.2$ case with an axial extent corresponding to a wavenumber of $k\,a_1 = 5.3$. The flow is seeded initially with the optimal perturbation for $\tau/T_0 = 1$. The coloured shading shows levels of dominant strain, with blue and red corresponding to low and high values respectively. (a)-(g) displays the evolution of the instability for $t_{VST}/T_0 = 0.00, 0.05, 0.10, 0.15, 0.20, 0.25$ and 0.30 where $t_{VST}/T_0 = 0$ is taken as seeding time.

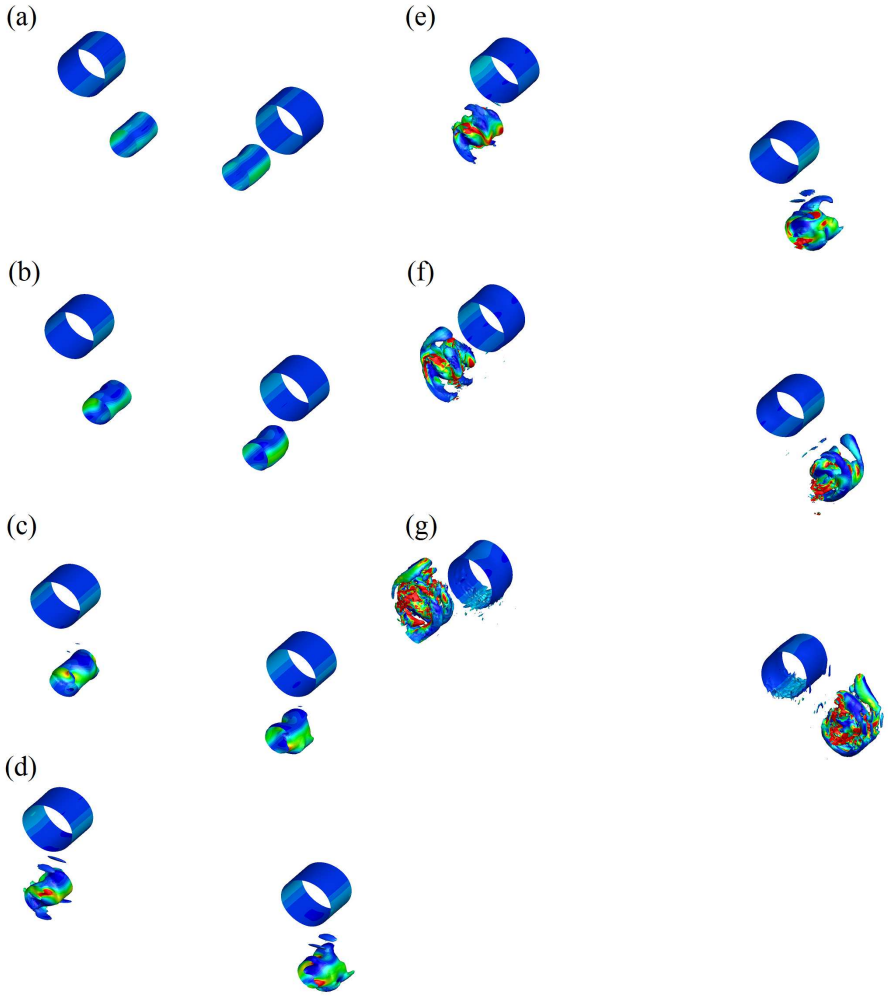

FIGURE 4.62: Time sequences of iso-surfaces at an arbitrarily small negative value of the λ_2 field plotted from a three-dimensional simulation of the $T_{st}/T_0 = 0.3$ case with an axial extent corresponding to a wavenumber of $k\,a_1 = 5.3$. The flow is seeded initially with the optimal perturbation for $\tau/T_0 = 1$. The coloured shading shows levels of dominant strain, with blue and red corresponding to low and high values respectively. (a)-(g) displays the evolution of the instability for $t_{VST}/T_0 = 0.00, 0.05, 0.10, 0.15, 0.20, 0.25$ and 0.30 where $t_{VST}/T_0 = 0$ is taken as seeding time.

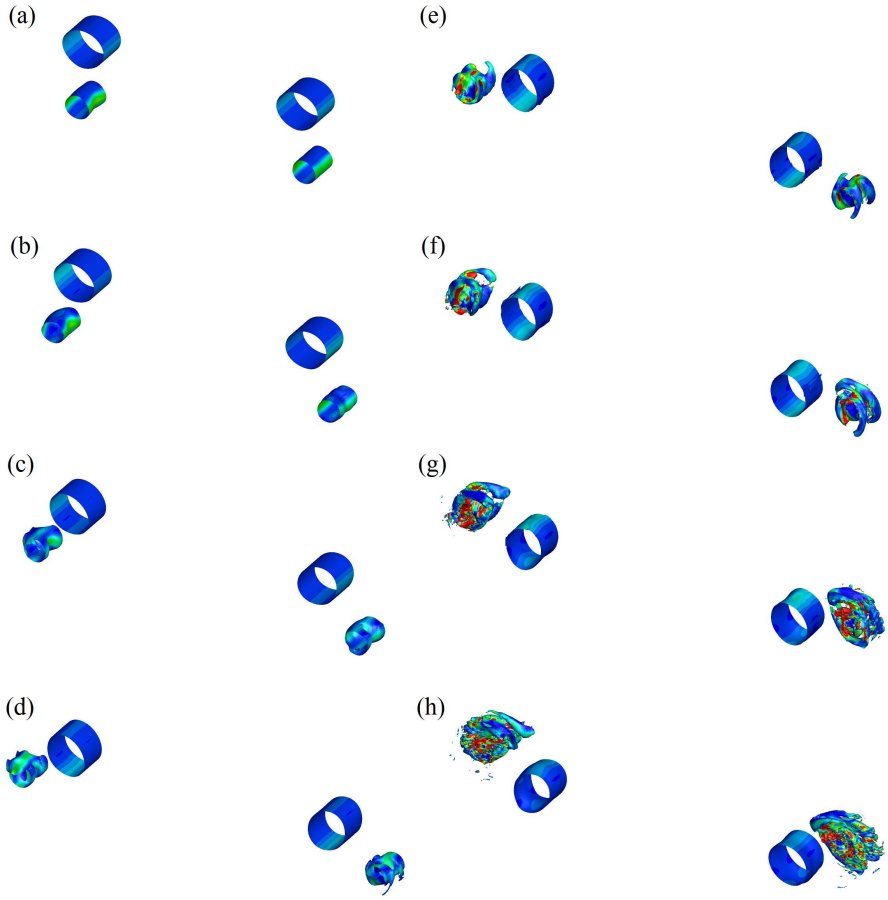

FIGURE 4.63: Time sequences of iso-surfaces at an arbitrarily small negative value of the λ_2 field plotted from a three-dimensional simulation of the $T_{st}/T_0 = 0.45$ case with an axial extent corresponding to a wavenumber of $k\,a_1 = 5.3$. The flow is seeded initially with the optimal perturbation for $\tau/T_0 = 1$. The coloured shading shows levels of dominant strain, with blue and red corresponding to low and high values respectively. (a)-(h) displays the evolution of the instability for $t_{VST}/T_0 = 0.00, 0.05, 0.10, 0.15, 0.20, 0.25, 0.30$ and 0.35 where $t_{VST}/T_0 = 0$ is taken as seeding time.

Figure 4.62 shows the temporal evolution of the four-vortex DNS seeded at $T_{st}/T_0 = 0.3$ for the period $0.00 \leq t_{VST}/T_0 \leq 0.30$. It shows that the instability in the tail vortex pair evolves in a similar manner to the $T_{st}/T_0 = 0.2$ case, leading to a T-W interaction. As the tail vortices were seeded with the instability when they were outside the highly strained region between the vortex pair, the tail vortices maintain coherence for longer before evolving into small scale flow structures (figure 4.62(e)). This extension of the coherence of the tail vortex pair appears to lead to an enhanced instability growth in the wing vortex pair, leading to it becoming first evident at $t_{VST}/T_0 = 0.2$ (figure 4.61(e)).

Figure 4.63 shows the temporal evolution of the four-vortex DNS seeded at $T_{st}/T_0 = 0.45$ for the period $0.00 \leq t_{VST}/T_0 \leq 0.35$. The instability mechanisms are similar to the $T_{st}/T_0 = 0.3$ case with the instability in the tail vortex evolving away from the highly strained region between the wing vortex pair, leading to a T-W type interaction. The tail vortices maintain coherence for a longer period of time before evolving into small scale flow structures, leading to an earlier deformation of the wing vortex pair, $t_{VST}/T_0 = 0.15$ (figure 4.63(d)). By the time the tail vortices have become highly perturbed (figure 4.63(h)) the instability in the wing vortex pair has grown to be significant and exhibits the asymmetric bending at about $\pm 45^\circ$ to the line between the vortex cores.

Figure 4.64 shows the temporal evolution of the four-vortex DNS seeded at $T_{st}/T_0 = 0.6$ for the period $0.00 \leq t_{VST}/T_0 \leq 0.35$. The instability that forms is very similar to the $T_{st}/T_0 = 0.45$ case with the instability in the tail vortex pair evolving away from the highly strained region between the wing vortex pair, leading to a T-W interaction. Similar to the previous case, the evolution of the instability away from the highly strained region between the wing vortex pair leads to a slower growth of the instability in the tail vortex pair, which in turn leads to a longer imposed strain from the tail vortex to the wing vortex. By the time the tail vortices have become highly perturbed (figure 4.64(h)) the instability in the wing vortex pair has grown to be significant and exhibits the asymmetric bending at about $\pm 90^\circ$ to the line between the vortex cores.

Figure 4.65 shows the temporal evolution of the four-vortex DNS seeded at $T_{st}/T_0 = 0.9$ for the period $0.00 \leq t_{VST}/T_0 \leq 0.35$. It shows that this seeding case exhibits properties of both previous cases. As it is seeded when the tail vortex pair is outside the highly strained region between the wing vortex pair (figure 4.65(a)) the instability

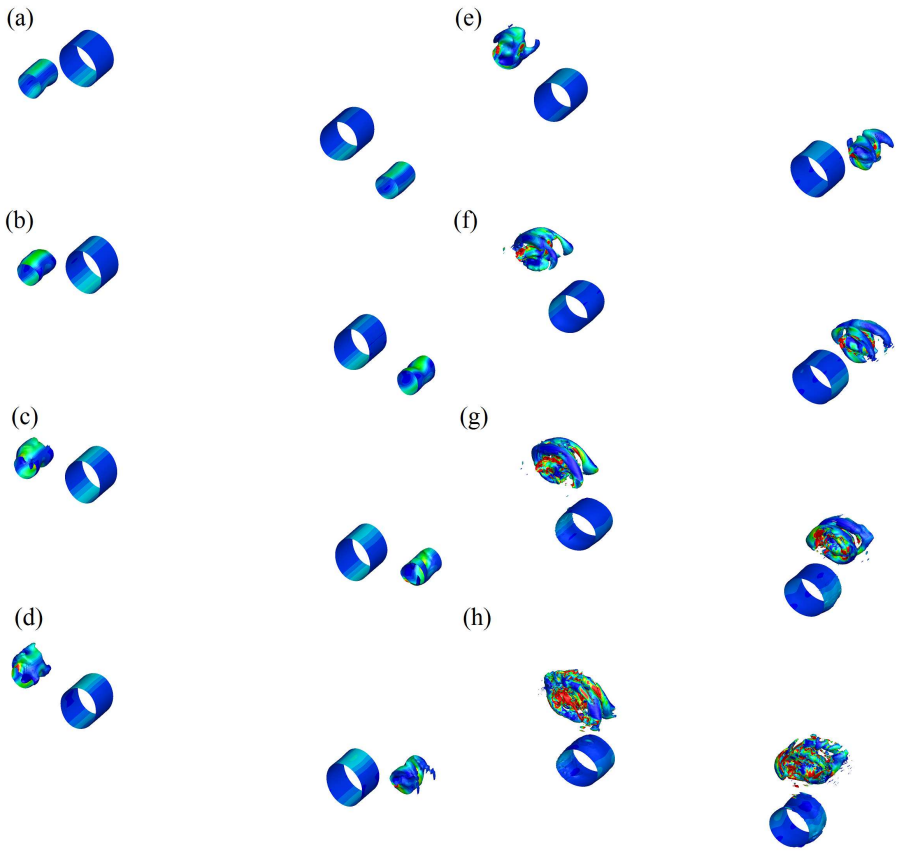

FIGURE 4.64: Time sequences of iso-surfaces at an arbitrarily small negative value of the λ_2 field plotted from a three-dimensional simulation of the $T_{st}/T_0 = 0.6$ case with an axial extent corresponding to a wavenumber of $k\,a_1 = 5.3$. The flow is seeded initially with the optimal perturbation for $\tau/T_0 = 1$. The coloured shading shows levels of dominant strain, with blue and red corresponding to low and high values respectively. (a)-(h) displays the evolution of the instability for $t_{VST}/T_0 = 0.00, 0.05, 0.10, 0.15, 0.20, 0.25, 0.30$ and 0.35 where $t_{VST}/T_0 = 0$ is taken as seeding time.

in the tail vortex pair grows as a T-W interaction (figure 4.65(a)-(f)). This leads to an earlier growth of instability in the wing vortex pair as the imposed strain from the tail vortex remains for longer. The interaction changes to a T-T interaction as the highly perturbed tail vortices are pulled through the highly strained region between the wing vortex pairs (figure 4.65(h)). As the type of interaction changes and speeds the destruction of the tail vortex pair, the wing vortex pair has a smaller level of evident instability growth than either the $T_{st}/T_0 = 0.45$ or $T_{st}/T_0 = 0.6$ cases.

Figures 4.60-4.65 show a number of points of interest. One is that the time of seeding before the tail vortex pair enters the highly strained region between the wing vortex pair will determine if a T-W or T-T interaction occurs. When the flows are seeded with the tail vortex pair outside the highly strained region between the wing

vortex pair, $0.2 \leq T_{st}/T_0 \leq 0.9$ then the first type of interaction that occurs is a T-T interaction. This can change as the instability grows in the tail vortex pair and is then highly strained as can be seen later in the evolution of the $T_{st}/T_0 = 0.9$ case. If the flow is seeded while the tail vortex pair is within the highly strained region, the $T_{st}/T_0 = 0.05$ case, then the first interaction is a T-T interaction that leads to a very rapid evolution of the tail vortex pair into small scale flow structures. The second point is that the T-W interaction, while leading to a slower destruction of the tail vortex pair, allows the tail vortices to impose a strain on the wing vortices for a longer period of time. This is shown in the $0.2 \leq T_{st}/T_0 \leq 0.6$ cases where the instability in the wing vortices becomes more evident earlier in the evolution.

Figure 4.66 shows the energy in the zeroth Fourier mode at $t_{VST}/T_0 = 0.3$, normalised by the initial energy in the zeroth mode, against tail orbit fraction, T_{st}/T_0, where the flow is seeded. The energy in the zeroth mode is a good indicator of how coherent the vortices are in the flow. Figure 4.66 shows that to obtain rapid breakdown of the vortices, the ideal place to seed the flow is when the tail vortices are within the highly strained region between the wing vortices, $0.05 \leq T_{st}/T_0 \leq 0.2$. It also shows that when the flow is seeded when the tail vortices are outside of this region, $0.25 \leq T_{st}/T_0 \leq 0.9$, the reduction in zeroth mode energy is less and so the vortices are more coherent.

4.5 Summary

This chapter has reported on the results of a study into the dynamics of a symmetric four-vortex flow as a model of an aircraft wake entrained behind its wings and tail. The study started with a two-dimensional transient growth and DNS study. This study found that at long timeframes, the four-vortex system underwent a two-dimensional instability that leads to a breaking of the symmetry of the system along the $x = 0$ plane. The transient growth analysis found that over the timeframe of three orbits of the tail vortex pair ($\tau/T_0 = 3$), massive transient growth of perturbations was possible (in the order of 10^{12}) implying that any tiny perturbation (even to the level of machine code error) would cause a two-dimensional instability to grow.

The study proceeded to investigate three-dimensional transient growth of instabilities in the four-vortex system. The transient growth analysis demonstrated that both the 'high tail' and 'flat tail' cases demonstrated even more massive transient growth

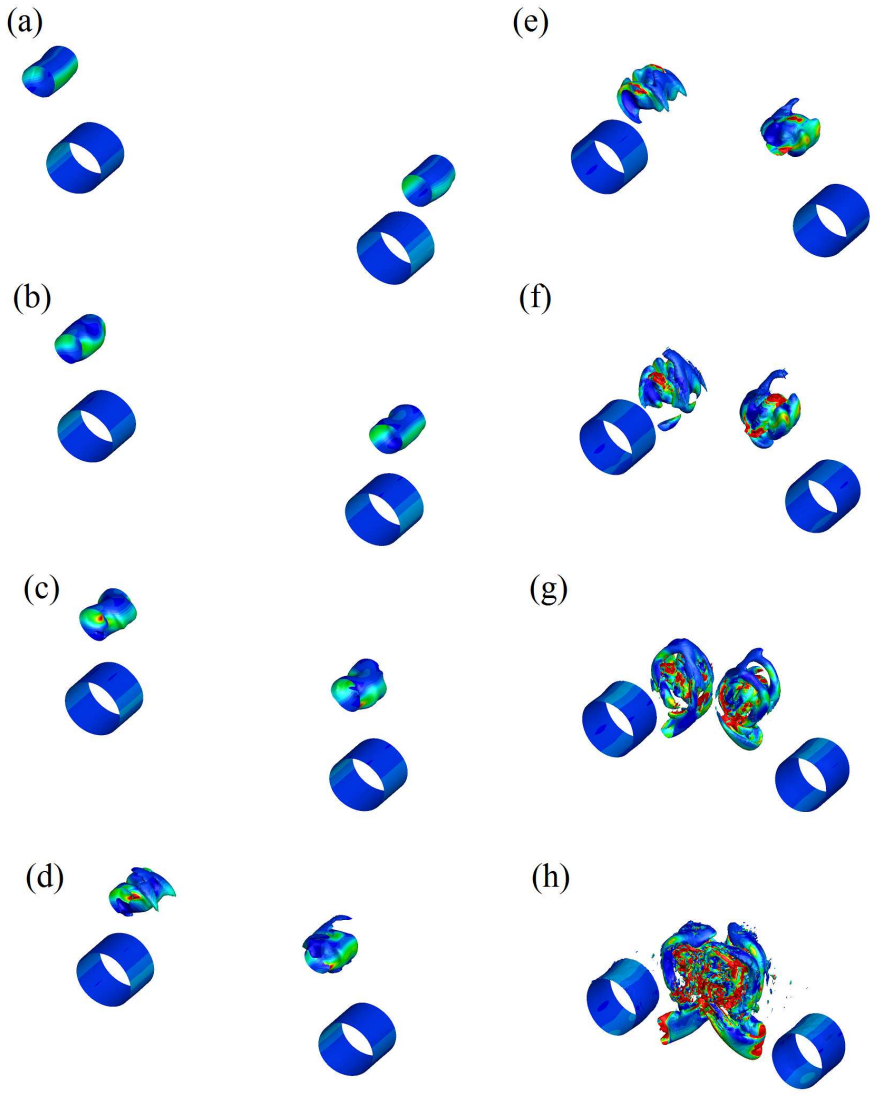

FIGURE 4.65: Time sequences of iso-surfaces at an arbitrarily small negative value of the λ_2 field plotted from a three-dimensional simulation of the $T_{st}/T_0 = 0.9$ case with an axial extent corresponding to a wavenumber of $k\,a_1 = 5.3$. The flow is seeded initially with the optimal perturbation for $\tau/T_0 = 1$. The coloured shading shows levels of dominant strain, with blue and red corresponding to low and high values respectively. (a)-(h) displays the evolution of the instability for $t_{VST}/T_0 = 0.00, 0.05, 0.10, 0.15, 0.20, 0.25, 0.30$ and 0.35 where $t_{VST}/T_0 = 0$ is taken as seeding time.

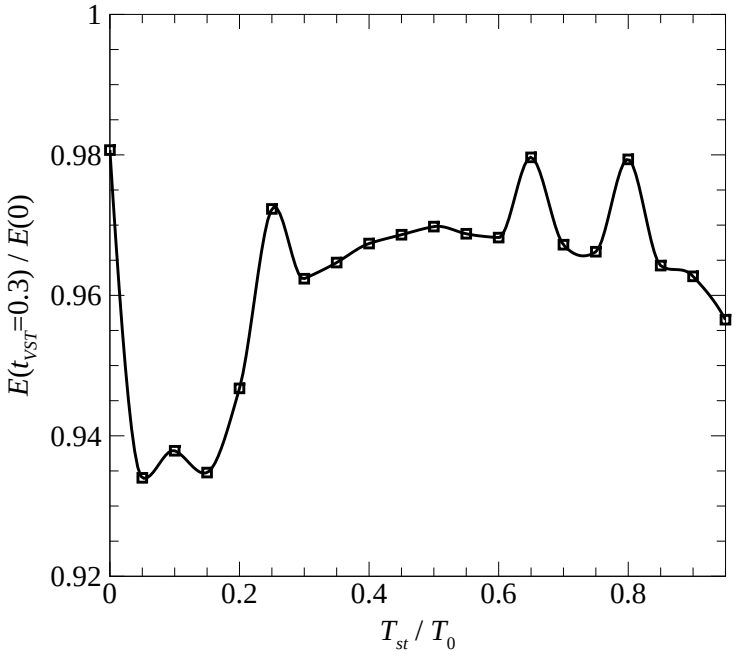

FIGURE 4.66: Zeroth Fourier mode energy at $t_{VST}/T_0 = 0.3$, normalised by initial energy in the zeroth mode, against tail orbit fraction, T_{st}/T_0, where the flow is seeded. An axial wavenumber of $k\,a_1 = 5.3$ is prescribed for the perturbation field.

of perturbations (order of 10^{26} for $\tau/T_0 = 3$) with a peak corresponding to an axial wavenumber of $k\,a = 5.3$. The transient growth analysis also discovered that, for both the 'high tail' and 'flat tail' cases, the perturbations that leads to optimal energy growth appear as a dipole angled at approximately 45° from a line between the centre of the tail vortex to the wing vortex, similar to a [-1,1,1] mode elliptic instability in a counter-rotating vortex pair. This constant angle of perturbation between the tail and wing vortex demonstrates that during the linear regime, the primary interaction driving the instability is the interaction between the wing and tail vortex.

By using three-dimensional DNS, a comparison was made between the 'high tail' and 'flat tail' cases seeded with both white noise and the optimal perturbations. The study found that by seeding with the optimal perturbations, immediate growth of the instabilities occurred. In contrast, the cases seeded with white noise entered a region of decaying perturbation energy as the modes not conducive to growth were damped out before the optimal modes dominated the instability. The three-dimensional DNS also discovered that four-vortex interactions were possible. The first is where the tail vortices are forced to interact with each other as they pass through the highly strained region between the wing vortices (referred to as a T-T interaction). The second type of interaction is where the primary interaction is between the wing and tail vortices without any crossing of flow across the mid-plane between the vortices (referred to as a T-W interaction). This demonstrates that while the primary interaction during the linear phase is the T-W interaction, the non-linear regime (which the DNS quickly enters) can change this interaction to one between the tail vortices.

A study into varying the energy magnitude of the optimal perturbation and the seeding position discovered that the triggering of the T-T interaction is directly related to the magnitude of the instability before the tail vortex pair enters the highly strained region between the wing vortices. If the tail vortices have become sufficiently perturbed, they can be forced to interact with each other as they pass through the highly strained region between the wing vortex pair.

Lastly, a more generalised study into the effect of seeding position in the first orbit of the tail vortex pair around the wing vortex pair was examined. A transient growth analysis was conducted at intervals through the first orbit of the tail vortex pair around the wing vortex pair. The transient growth analysis found that the magnitude of the growth amplification factor was directly related to the proximity of the tail vortex pair

to the highly strained region between the wing vortex pair. When the perturbation was allowed to grow predominantly within the highly strained region between the wing vortex pair, the growth amplification factor was significantly higher (approximately two orders of magnitude). Using the initial optimal perturbations found from the transient growth analysis to seed DNS, the non-linear response of the effect of seeding position was studied. The DNS study found that the growth rate of the instability was directly related to the position of the tail vortex pair. When the tail vortex pair was seeded within or just before entry into the highly strained region between the wing vortex pair, the growth rate of the instability was significantly higher, resulting in a more rapid transition into the non-linear regime and a faster reduction in the energy in the zeroth Fourier mode. This result implies that seeding just before or within the highly strained region between the wing vortex pair will lead to a more rapid destruction of the wake hazard for trailing aircraft.

Chapter 5

Results: Kinematics and stability of an unequal-strength four-vortex system

This chapter covers the study of a four-vortex, counter-rotating aircraft wake model with an asymmetric vortex strength about the vertical mid-plane. Applications of this model include banking aircraft. As in the previous chapter, this chapter also investigates the effect of the vertical displacement of the tail vortex pair.

5.1 Problem outline

The asymmetric model used in this chapter is similar to the symmetric 'high tail' and 'flat tail' cases considered in the previous chapter. To model the change in vortex circulation representative of a banking aircraft, the circulation of the left wing vortex was increased by 15% to model the change in lift across the wings with the circulation of the right tail vortex increased by 15% to model the necessary change in tail lift required to maintain an aircraft banking manoeuvre (McCormick 1995). This configuration intrinsically breaks the reflective symmetry of the 'high tail' and 'flat tail' configurations investigated in the previous chapters.

The change in circulation strength of 15% was chosen as a mild difference, in order to investigate the magnitude of the effect of such an imbalance in the system. A preliminary study showed that even a small difference produced significant differences in the two-dimensional kinematics of the system and as such the change in circulation strength of 15% was chosen as a representative case. As the results in this chapter show, a mild imbalance in circulation strength can have a severe effect on the overall dynamics and instability of the system.

To maintain consistency, all times in this chapter are normalised by the same value of T_0 used in the previous chapter.

5.2 Two-dimensional flow

In this section, first the two-dimensional kinematics of the asymmetric four-vortex aircraft wake model are considered. Then the long-term stability of the system is considered, and last the two-dimensional transient growth model of the system is considered to elucidate the observations from the DNS.

5.2.1 Two-dimensional kinematics

The two-dimensional kinematics of the asymmetric four-vortex wake model were examined to determine the trajectories of the vortices over a short timeframe.

Figure 5.1 shows the trajectory over $0 \leq t/T_0 \leq 0.5$ for the asymmetrical 'flat tail' case. It can be seen that while the system is highly unbalanced, the average vertical displacement of the wing vortex pair is very similar to the symmetrical case shown in chapter 4. The imbalance between vortex circulation strengths of the initial system leads to a rotation of the vortex system, through a similar process to that which invokes the tail vortex orbit around each wing vortex. It is of interest to note that the main wing vortices are drawn apart as the flow evolves. The negative-vorticity wing vortex (the stronger of the wing vortices) does not translate a significant distance from the initial position. This is a result of the larger circulation of this vortex increasing the rotation of the positive-vorticity tail vortex around the wing vortex. This increase in rotation rate means that the velocity induced on the negative-vorticity wing vortex will be rotating faster (shown by it completing approximately 3/4 of an orbit by $t/T_0 = 0.5$), leading to a shorter time in which the wing vortex is being drawn in any specific direction and therefore creating a significantly smaller circular path. This effect is compounded by the weaker vorticity in the positive (left) tail vortex. By contrast, the positive (right) wing vortex has a lower level of vorticity, slowing the rotation of the negative (right) tail vortex around that wing vortex (closer to 1/2 an orbit by $t/T_0 = 0.5$). Combined with the larger circulation strength of the negative-vorticity tail vortex, the positive tail vortex is drawn significantly further away from its initial position by the higher induced velocity from the tail vortex and the longer time that this induced velocity is acting in one direction. An additional effect that the stronger negative-vorticity tail

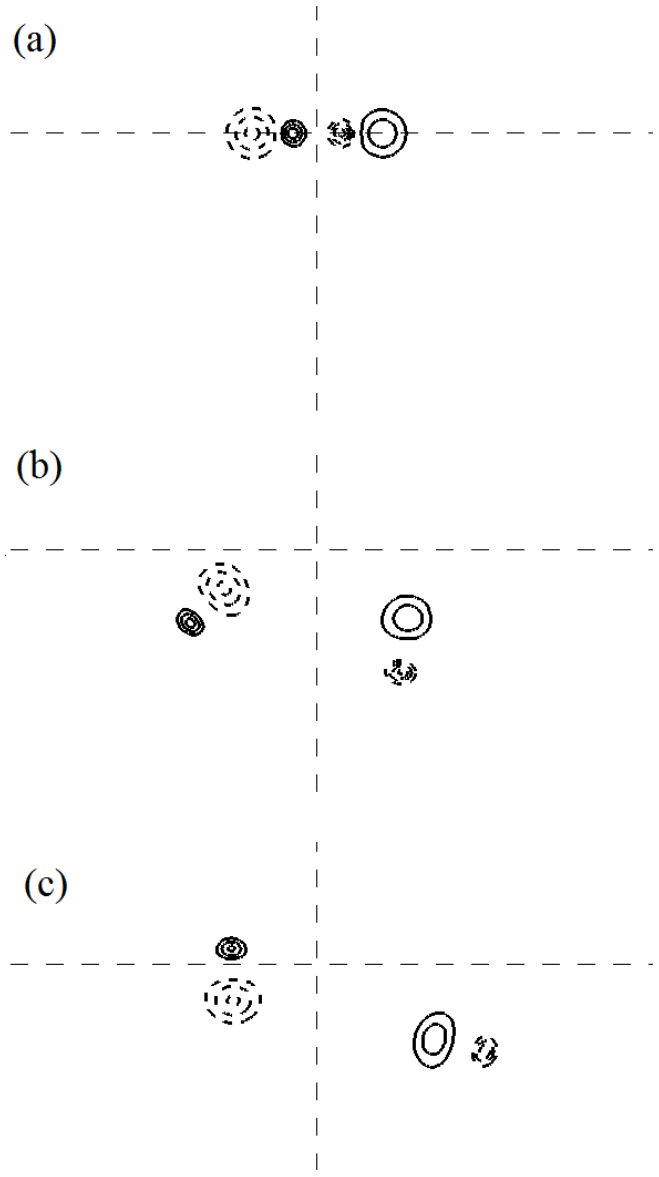

FIGURE 5.1: A time sequence of contour plots of vorticity for the 'flat tail' case at (a) $t/T_0 = 0$, (b) 0.25 and (c) 0.5. Contour lines are at vorticity increments of 2. The minimum vorticity is -8 and the maximum is 6 in the right and left tail vortex respectively. Dashed and solid lines represent negative and positive vorticity respectively. The vertical thin dashed line shows $x = 0$. The horizontal thin dashed line shows $y = 0$.

vortex has is a small deformation of the positive-vorticity wing vortex into an elliptic profile.

This drawing apart of the vortices will have three main effects on the flow. The first effect is that the induced strain between the wing vortices will be reduced, slowing the growth of any instabilities that are caused by this region of higher induced strain. The second effect is that the overall average downward propagation of the system will be reduced due to the greater distance between the wing vortices created by the effects

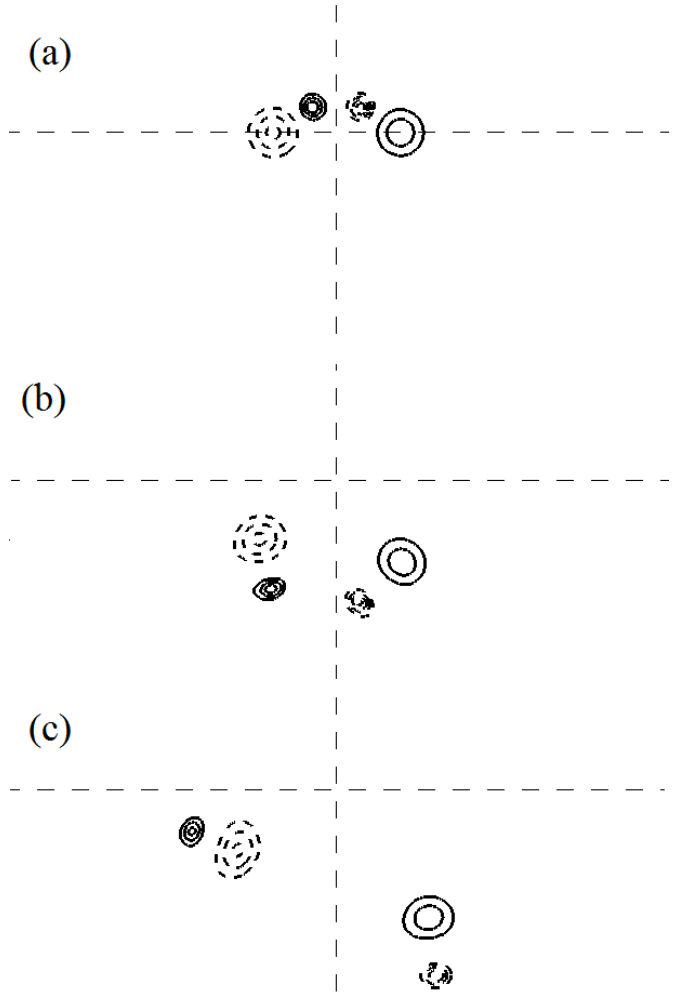

FIGURE 5.2: A time sequence of contour plots of vorticity for the 'high tail' case at (a) $t/T_0 = 0$, (b) 0.25 and (c) 0.5. Contour levels and lines are as per figure 5.1.

described previously. The third effect is due to the difference in downward propagation of the wing vortices. This will lead to a change in the direction of the velocities induced on each wing vortex by the other, causing the overall rotation of the system.

Figure 5.2 shows the trajectory over $0 \leq t/t_0 \leq 0.5$ for the asymmetrical 'high tail' case. The left wing/tail vortex pair tends to remain close to the level of the initial system with little observable vertical displacement (note that similar behaviour is observed in figure 5.1). In contrast, the right wing/tail vortex pair tends to translate downwards significantly more. As in the 'flat tail' case shown previously, the change in relative strengths of the wing and tail vortices have a significant effect on the trajectories of the individual vortices. One of the primary differences is that the vertical displacement of the tail vortices in the 'high tail' case causes the tail vortices to linger within the region between the wing vortices. The lingering of the tail vortices between the wing

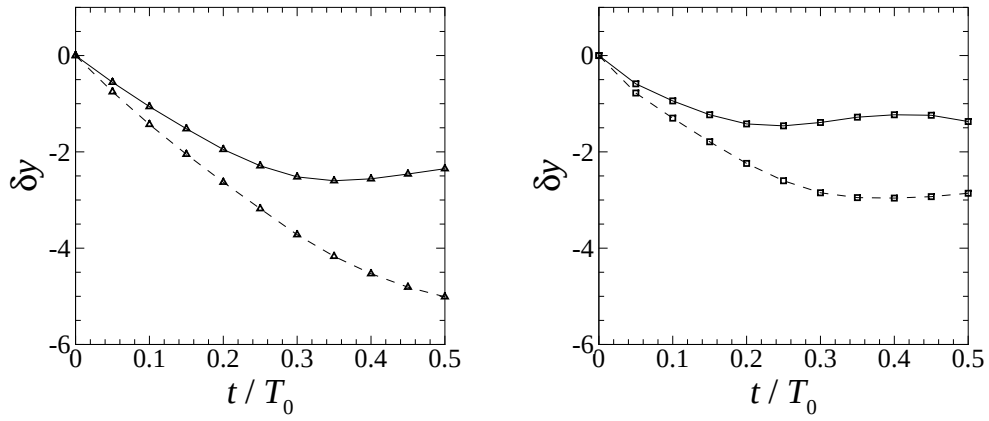

FIGURE 5.3: A plot of vertical displacement, δy, against normalised time, t/T_0, of the centre of the wing vortex core, for the asymmetric (a) 'high tail' and (b) 'flat tail' cases. The dashed line represents the position of the right wing vortex and the solid line represents the position of the left wing vortex.

vortices slows down the orbit of the tail vortices as the induced velocity from one side of the system to the other is reduced by the close proximity of the tail vortices to each other (the positive-vorticity tail vortex travels approximately 2/3 of an orbit by $t/T_0 = 0.5$, while the negative-vorticity tail vortex travels approximately 1/3 of an orbit by $t/T_0 = 0.5$). This lag of the tail vortices have the effect of keeping the wing vortices together for a longer period of time, allowing for an increased time that the wing vortices can induce a velocity on each other and propagate downward. After the tail vortices have left the region between the wing vortices, they begin to induce velocities that draw the wing vortices apart. As the negative-vorticity (right) tail vortex is rotating at a slower rate and has a higher circulation, it has a greater effect on the positive-vorticity (right) wing vortex, leading to a significantly higher downward propagation than the negative (left) wing vortex.

As in the 'flat tail' case, the separation of the wing vortices will reduce the induced strain within the region between the wing vortices as well as reducing the induced velocity between the wing vortices. The difference in downward propagation of the two wing vortices also changes the direction of the induced velocities, causing the system to rotate in a similar manner to the 'flat tail' case.

The respective changes in the vertical displacement of the wing vortices are considered in figure 5.3. The asymmetric 'high tail' case shown in figure 5.3(a) demonstrates

that the stronger left wing vortex is less influenced by its corresponding tail vortex and undergoes a smaller drop in vertical displacement, while the weaker right wing vortex is more influenced by its corresponding tail vortex and so drops a greater amount. The asymmetric 'flat tail' case undergoes a similar pattern to the drop of the left and right wing vortices (figure 5.3(b)), with the stronger left vortex undergoing a smaller drop due to the reasons described earlier. It is of interest to note that each of the wing vortices in the asymmetric 'flat tail' case undergoes less drop than the corresponding wing vortex in the asymmetric 'high tail' case. This is unsurprising as this behaviour, a larger drop in the 'high tail' case compared to the 'flat tail case, was seen for the symmetric four-vortex system in the previous chapter.

5.2.2 Two-dimensional stability

This section describes the long term two-dimensional stability of the asymmetric four-vortex system by examining the long term evolution of the flow through a two-dimensional DNS. It is important to note that unlike the symmetric four-vortex system described in the previous chapter, the asymmetric case begins the temporal evolution without reflective symmetry about $x = 0$.

Figure 5.4 shows a long-term temporal evolution of vorticity of the asymmetrical 'high tail' case that was depicted in figure 5.2(a). The asymmetry of the flow can be seen in figure 5.4(b) where the tail vortices have already reached a state where they are orbiting the wing vortices at different rates, leading to severe asymmetry about the horizontal mid-plane. At longer time frames, this asymmetry allows the tail vortices to closely approach the wing vortex with the same sign of vorticity (figure 5.4(e)). This allows vortex merger to occur, stripping vorticity off the weaker tail vortex and feeding the larger wing vortex (Meunier *et al.* 2002; So *et al.* 2007). The contour levels in figure 5.4 do not clearly display the stripping and merging process; these are elucidated in more detail shortly. The stripping of vorticity off a vortex occurs when vorticity diffuses into the hyperbolic points in the streamlines relative to the pair of vortices and is rapidly convected away (Meunier *et al.* 2002; So *et al.* 2007). It is important to note that this was not observed in any of the symmetric four-vortex cases. After a long period of time, this can be seen in figure 5.4(f). By the time the tail vortices have merged with the wing vortices, the line between the wing vortices is almost perpendicular to the x-axis, implying the wing vortices will translate primarily in the horizontal plane.

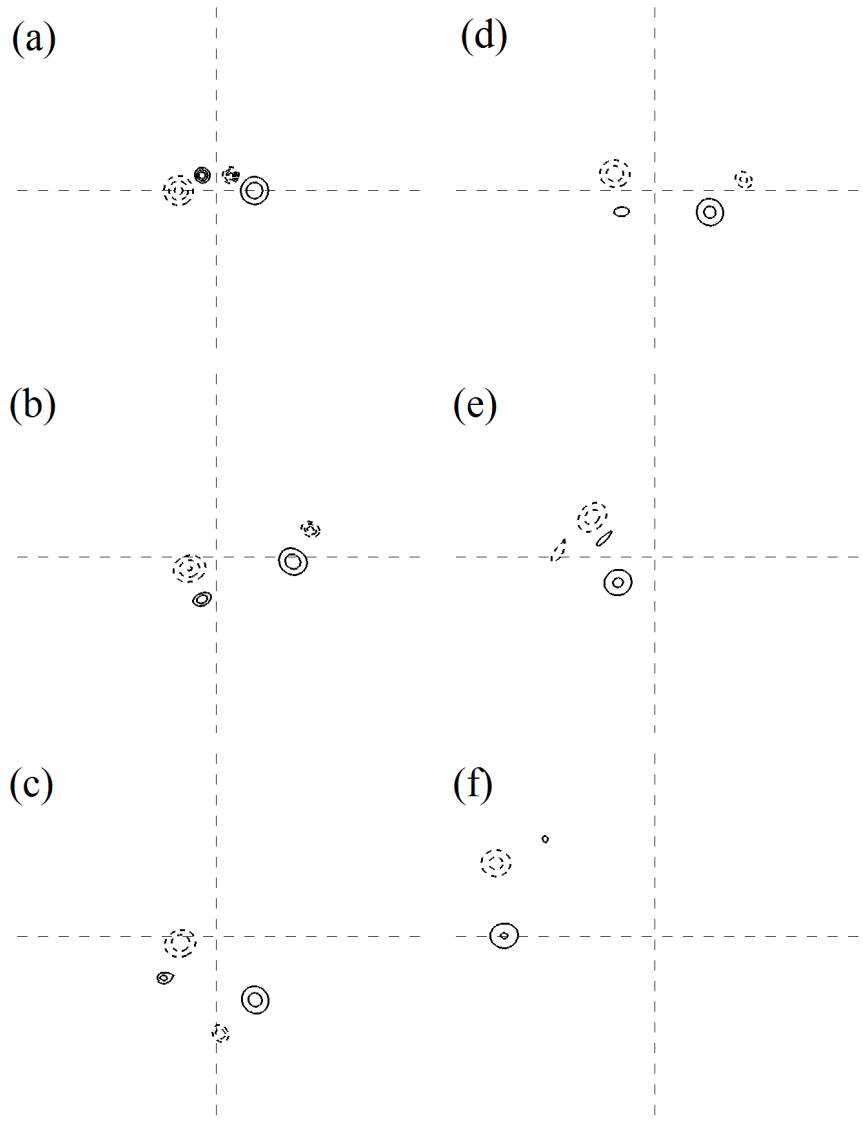

FIGURE 5.4: A time sequence of contour plots of vorticity for the unequal 'high tail' case at (a) $t/T_0 = 0$, (b) 1, (c) 2,(d) 3, (e) 4 and (f) 5. Contour scale and lines are as per figure 5.1.

There is likely to still be a small rotation present as the positive tail vortex is still just visible, and the wing vortices have become very similar, but not quite equal, in vorticity levels (under 15%).

Figure 5.5 shows a long-term temporal evolution of vorticity of the asymmetrical 'flat tail' case that was depicted in figure 5.1(a). In a similar manner to the 'high tail' case, the tail vortices in the asymmetric 'flat tail' case quickly break symmetry due to the differences in strength of the wing vortices (figure 5.5(b)). While the asymmetry of the system does allow the tail vortices to approach the wing vortices of the same sign, there is not as large a stripping of vorticity off the tail vortex pair (figure 5.5(e))

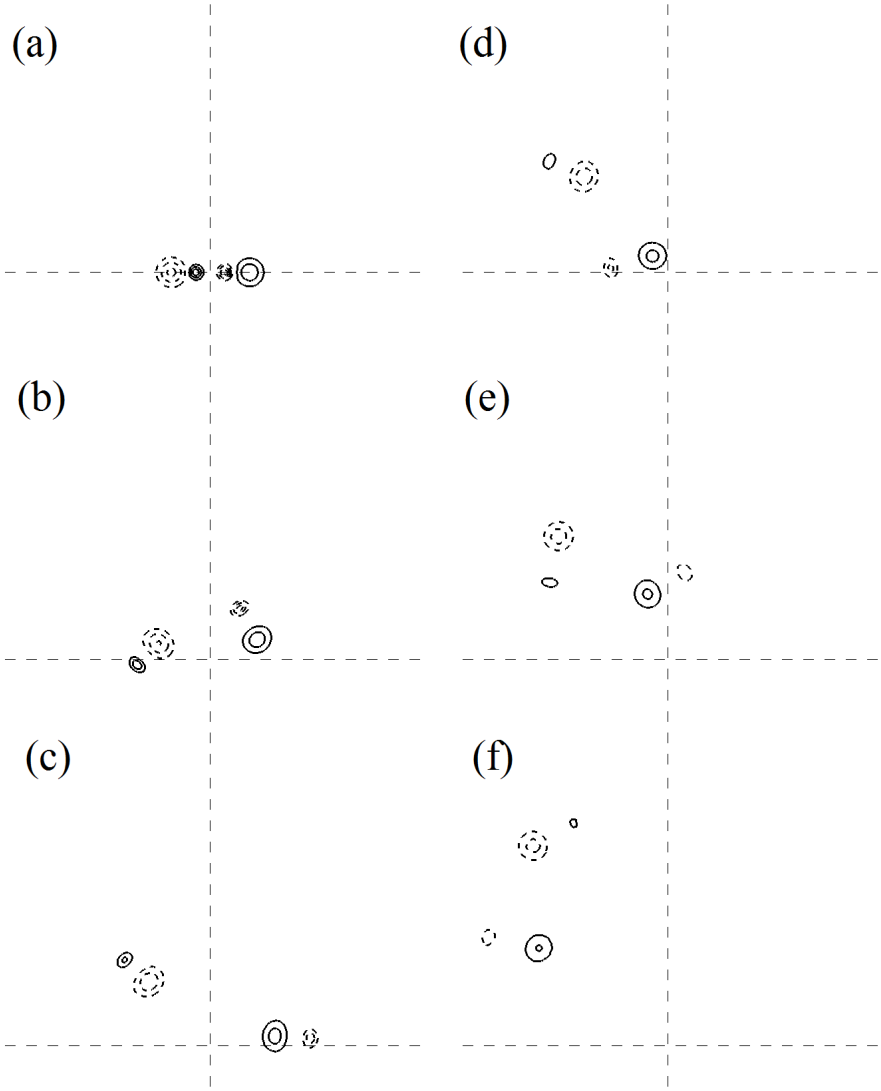

FIGURE 5.5: A time sequence of contour plots of vorticity for the unequal 'flat tail' case at $t/T_0 = (a)0$, (b) 1, (c) 2,(d) 3, (e) 4 and (f) 5. Contour levels and lines are as per figure 5.1.

as was found for the asymmetric 'high tail' case (figure 5.4(e)). This leads to the tail vortices lingering for a longer period of time and still being present at the end of the long timeframe evolution (figure 5.5(f)).

In order to elucidate the effect of vortex stripping described earlier, figure 5.6 shows a time sequence of flooded contour plots of vorticity for the asymmetric 'high tail' case at times in the vicinity of frame (e) from figure 5.4. At $t/T_0 = 3.65$, all four vortices show little evidence of deformation, with only a slight deformation in the weaker tail vortices. As the tail vortex with negative vorticity is pulled through the highly strained region between the two wing vortices, it becomes distorted and stretched due to the close proximity of the wing vortices (figure 5.6(b)). The distorted and stretched negative-

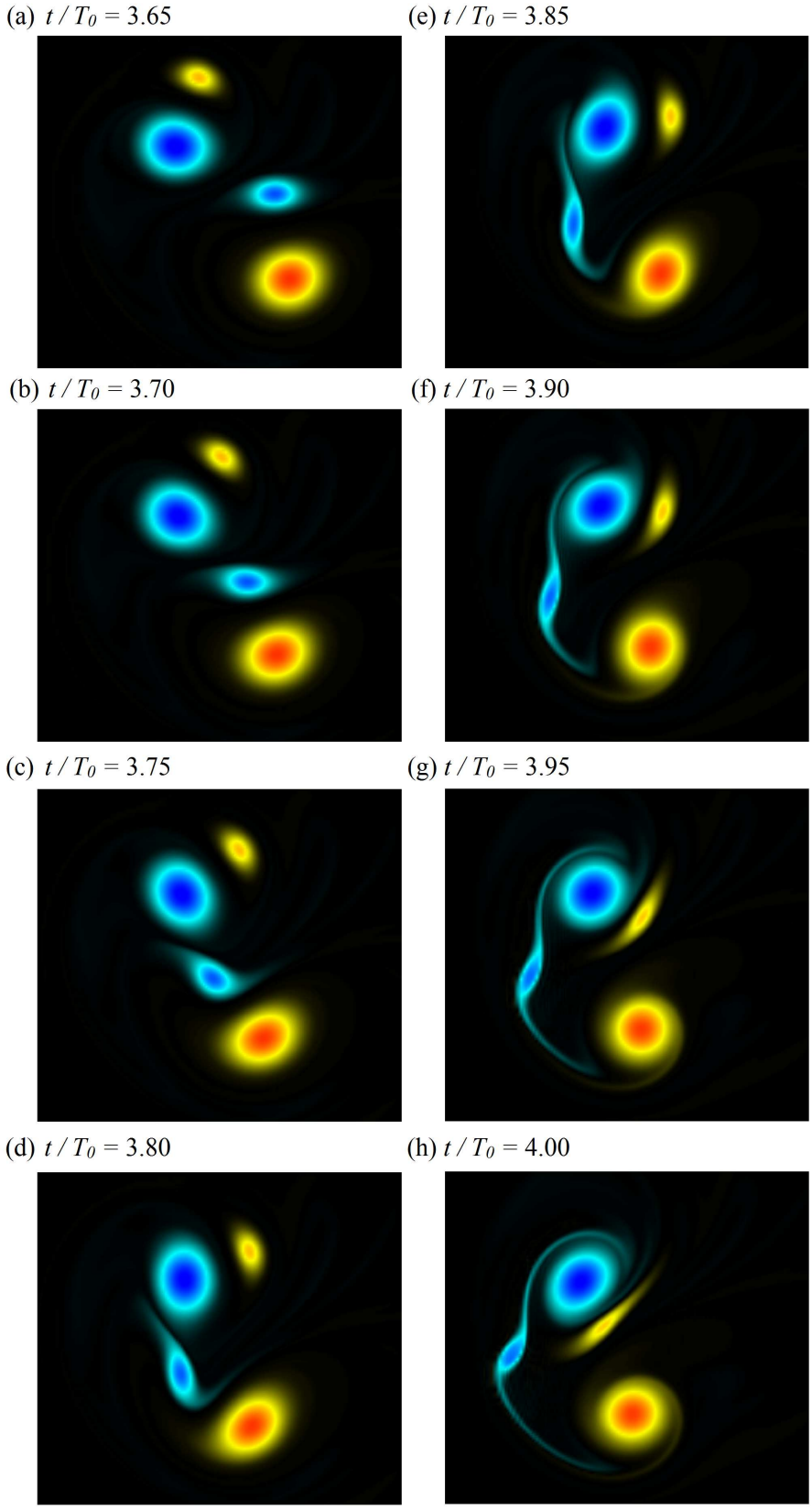

FIGURE 5.6: A time sequence of flooded contour plots of vorticity for the unequal 'high tail' case. Blue flooding represents negative vorticity and red and yellow shading represents positive vorticity. (a)-(h) represent times $t/T_0 = 3.65, 3.70, 3.75, 3.80, 3.85, 3.90, 3.95$ and 4.00 respectively.

vorticity tail vortex rotates as it travels through the highly strained region between the wing vortex pair, setting up a condition on the far side of the highly strained region where the strained vortex is approximately an equal distance between the two vortices, with tendrils of vorticity entraining from the tail vortex being equally convected around each of the wing vortices (figure 5.6(d)). This is due to the vorticity in the tail vortex entering a hyperbolic point in the relative streamlines and being rapidly convected away.

The tendrils of vorticity from the negative-vorticity tail vortex are stretched and pulled around the two wing vortices, but predominantly around the negative-vorticity wing vortex. This prevents the negative-vorticity tail vortex from continuing in its original orbit around the positive wing vortex (figure 5.6(e)). At the same time, the positive-vorticity tail vortex is just beginning to approach the highly strained region, becoming stretched and distorted as the strain from the wing vortex pair becomes more severe (figure 5.6(f)). As the flow evolves, the negative-vorticity tail vortex is held at an equal distance between the wing vortices in the horizontal direction by the relatively large proximity to the two wing vortices compared to the velocity the wing vortices are inducing on the negative-vorticity tail vortex. It does exhibit a small drift away from the wing vortices due to the combined velocities acting together in that direction. These two velocities acting in opposite directions causes two thin tendrils of vorticity to be pulled off the periphery of the negative-vorticity tail vortex, while the core remains in place (figure 5.6(g)). As the negative-vorticity tail vortex is maintaining its position due to the competing velocities induced on it, the positive-vorticity tail vortex is being rapidly transported through the highly strained region between the wing vortices. This has the effect of elongating the positive-vorticity tail vortex significantly, and also placing it into a position where it can prevent the negative-vorticity tail vortex from returning to its original orbit around the positive-vorticity wing vortex thus leading to the negative-vorticity tail vortex being transported from one wing vortex to the other. It is important to note that this is not seen at all in the symmetric four-vortex cases shown in the previous chapter. This excision of the negative-vorticity tail vortex from its original orbit around the positive-vorticity wing vortex and subsequent capture by the negative-vorticity wing vortex sets up the eventual merger of the negative-vorticity tail vortex with the negative-vorticity wing vortex. This is of interest as it leads to the elimination of the stronger tail vortex from the system, while also strengthening the

negative-vorticity wing vortex, and so is counterproductive to the desired destruction of the wing vortices.

To elucidate the effect of vortex stripping in the 'flat tail' case described earlier, figure 5.7 shows a time sequence of flooded contour plots of vorticity for several times in the vicinity of frame (e) from figure 5.5. As in the asymmetric 'high tail' case, the vorticies at the beginning of the sequence are still predominantly circular, with little evidence of stretching or distortion (figure 5.7(a)). One interesting thing to note is that the wing vortices are significantly further apart than the asymmetric 'high tail' case. This indicates that the tail vortices will not experience as much strain as they are pulled through this region. This is shown in figure 5.7(b)-(d) where the positive-vorticity tail vortex travels through the strained region between the wing vortices with little appreciable change in shape. It is interesting to note that as the positive-vorticity tail vortex leaves the strained region between the wing vortices (around $t/T_0 = 3.85$), it begins to deform into an elongated ellipse. This is interesting as it shows that the positive tail vortex is more susceptible to strain when the imposed strain from each of the wing vortices are perpendicular to each other (figure 5.7(f)). This effect of two strain fields being imposed at right angles on the positive-vorticity tail vortex has the effect of drawing the positive tail vortex into an elongated, spiral shape (figure 5.7(g)). As the negative-vorticity tail vortex is on the opposite side of the positive-vorticity wing vortex, it is largely unaffected by the strain from the negative-vorticity wing vortex.

Both the asymmetric 'high tail' and 'flat tail' two-dimensional cases demonstrate that the presence of only one of the tail vortices within the strained region between the wing vortices has the effect of causing the tail vortex to become highly elongated and distorted as it exits the highly strained region. This straining on exiting the highly strained region can lead to one of two effects, depending on where the other tail vortex is located. If the other tail vortex is closely following, as in the asymmetric 'high tail' case (e.g. figure 5.6), it can force the tail vortex to become separated from the wing vortex it was originally orbiting. This leads to the tail vortex orbiting the wing vortex of the same vorticity sign and eventual merger of the two. The other effect is shown by the 'flat tail' case, where the tail vortex becomes highly elongated and distorted into a spiral shape due to the imposed strain fields at right angles from the wing vortices when leaving the strained region between the wing vortices. However, as the other tail vortex is not following closely, the highly strained and distorted tail vortex continues

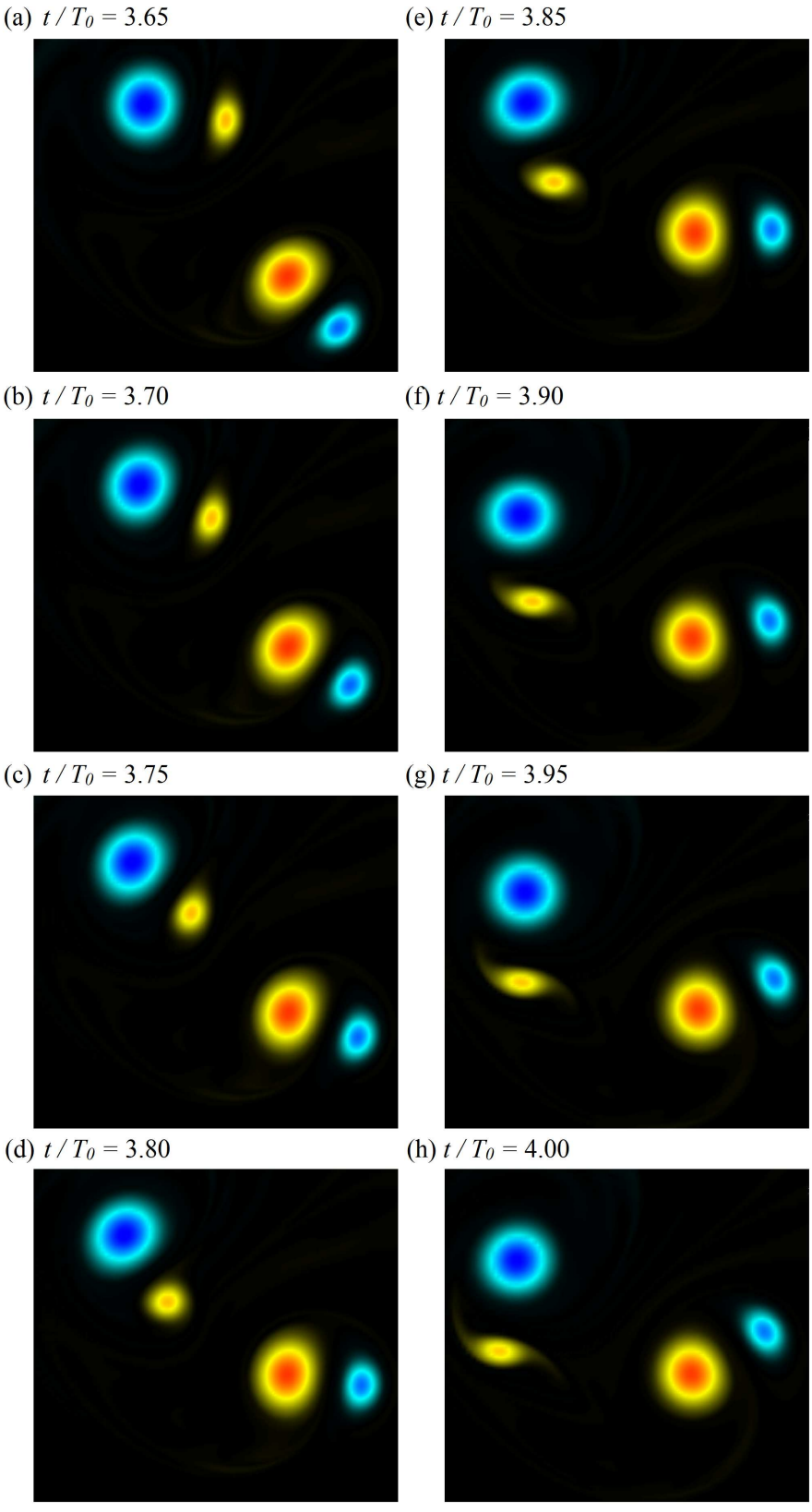

FIGURE 5.7: A time sequence of flooded contour plots of vorticity for the unequal 'high tail' case. Blue flooding represents negative vorticity and red and yellow shading represents positive vorticity. (a)-(h) represent times $t/T_0 = 3.65, 3.70, 3.75, 3.80, 3.85, 3.90, 3.95$ and 4.00 respectively.

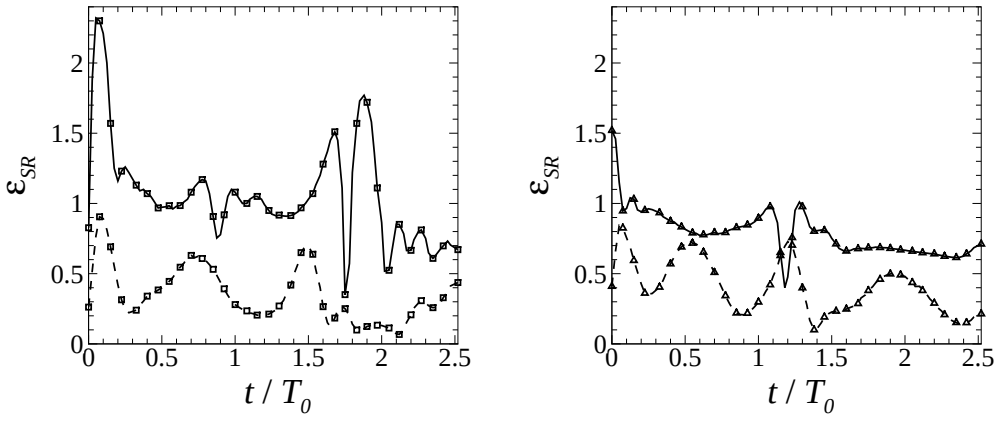

(a) (b)

FIGURE 5.8: Plot of strain rate, ϵ_{SR}, against t/T_0 at the center of the positive vorticity wing and tail vortices for an axial wavenumber of $k\,a_1 = 0$ for the asymmetric (a) 'high tail' and (b) 'flat tail' cases. $\triangle$ and $\square$ represent the 'flat tail' and 'high tail' case respectively. The solid line represents the strain rate at the centre of the positive vorticity tail vortex and the dashed line represents the strain rate at the centre of the positive vorticity wing vortex. For clarity only every third data point is plotted.

to move around the wing vortex it was originally orbiting.

5.2.3 Strain rate at vortex centres

This section investigates the change in the strain rate experienced by the positive vorticity wing and tail vortices for both the asymmetric 'high tail' and 'flat tail' cases as the strain rate is one of the driving mechanisms for the elliptic instability examined later.

Figure 5.8 shows the strain rate at the centre of the positive vorticity wing and tail vortex for the (a) 'high tail' and (b) 'flat tail' cases. As in the symmetric four-vortex case (shown in § 4.2.4), the tail vortices in the asymmetric case experience a higher strain rate due to the proximity and difference in vortex strength between the wing and tail vortices. It is interesting to note that due to the asymmetry of the system the tail vortices do not experience the large peak in strain rate that the symmetric four-vortex case does. This is because, aside from the initial time, the tail vortices do not enter the highly strained region between the wing vortices at the same time. The wing vortex examined in both the 'flat tail' and 'high tail' cases experiences a very similar strain rate, but slightly offset due to the difference in position of the tail vortices. It is interesting to note that the tail vortex in the asymmetric 'high tail' case experiences

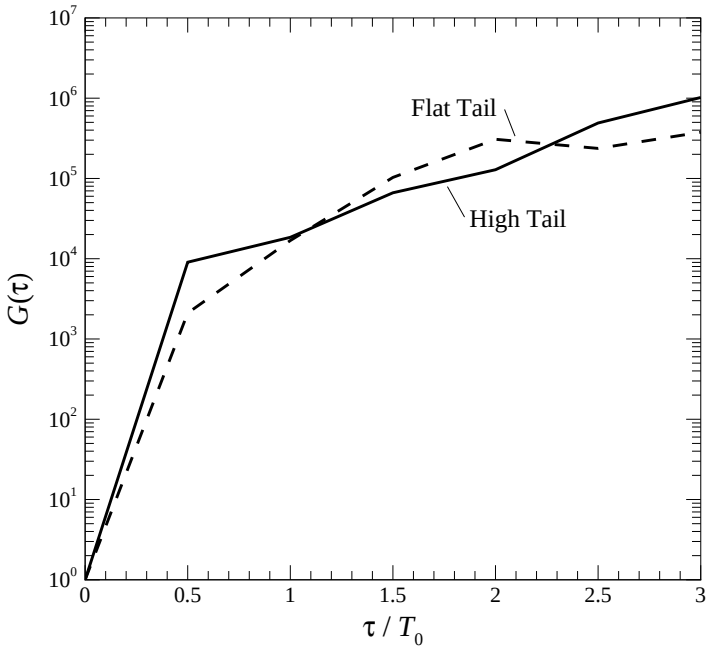

FIGURE 5.9: Plot of transient growth amplification factor, $G(\tau)$, against τ for an axial wavenumber $k\,a_1 = 0$, and an initial time, $t_0/T_0 = 0$.

a significantly more varying strain rate, while the positive vorticity tail vortex in the asymmetric 'flat tail' case experiences an almost constant strain rate.

5.2.4 Transient growth

It can be seen from § 5.2.2 that two very different effects can occur during the two-dimensional evolution of the asymmetric four-vortex system. It is of interest to know whether either of these effects causes the flow to be more susceptible to the transient growth of perturbations.

Figure 5.9 displays the growth amplification factor, $G(\tau)$, against τ for an axial wavenumber of $k\,a_1 = 0$ (a two-dimensional perturbation). As τ/T_0 increases, the 'flat tail' and 'high tail' cases alternatively reach higher peak values of growth amplification factor. For $\tau/T_0 < 1$, the 'high tail' case exhibits a greater growth amplification factor. For the region $1 \leq \tau/T_0 \leq 2.25$, the 'flat tail' case exhibits a larger growth amplification factor and as $\tau/T_0 \geq 2.25$ the 'high tail' once again exhibits a larger growth amplification factor. The trend for the high tail case to exhibit a greater growth amplification factor at higher values of τ implies that the merging of the tail vortices with the wing vortices makes the flow more susceptible to transient growth of perturbations. One

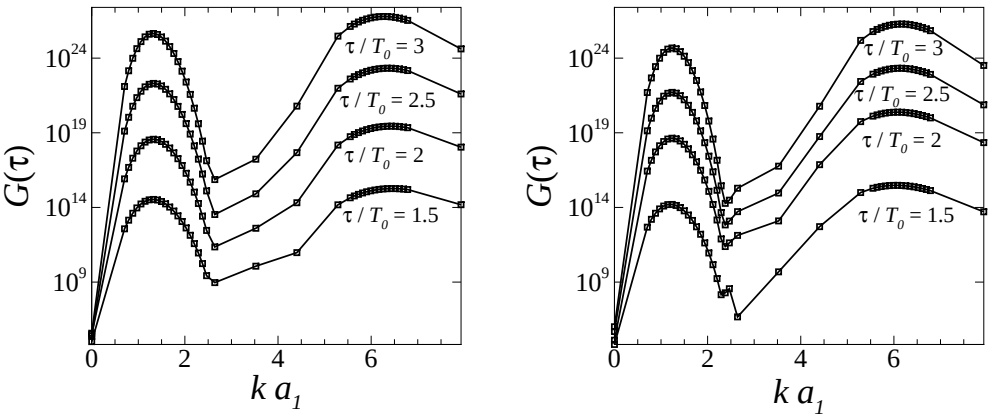

FIGURE 5.10: Plot of asymmetric (a) 'flat tail' and (b) 'high tail' transient growth amplification factor, $G(\tau)$, against non-dimensional axial wavenumber, $k\,a_1$, for an initial time of $t_0 = 0$. Each line represents a τ value as shown.

thing that is interesting to note is that the growth amplifications in the asymmetrical case are significantly smaller ($G(\tau = 3) \approx 10^6$) than the symmetrical case examined in the previous chapter ($G(\tau = 3) \approx 10^{12}$). This implies that in two-dimensional space, the asymmetric cases are significantly more stable to the transient growth of perturbations than the symmetric four-vortex cases.

5.3 Three-dimensional flow

Consideration is now given to the transient response of the asymmetric four-vortex system to three-dimensional disturbances. First, a transient growth analysis is performed on the asymmetric four-vortex aircraft wake model with a range of axial wavenumber. The optimal perturbation fields obtained through the transient growth analysis are also shown. Then the results of DNS of both the 'high tail' and 'flat tail' cases are compared seeding with the optimal perturbations. Last, a study of the transition of the flow into the non-linear domain is conducted.

5.3.1 Transient growth analysis

A transient growth analysis was conducted to examine the transient response of the asymmetric 'high tail' and 'flat tail' cases in a three-dimensional domain.

Figure 5.10 displays the growth amplification factor against τ for the asymmetric (a) 'flat tail' and (b) 'high tail' cases. Both cases demonstrate a similar behaviour to

the respective symmetrical cases. The 'flat tail' case does demonstrate a small drift in peak axial wavenumber for larger values of τ, while the 'high tail' case displays almost no change with τ. This implies that there is only a weak connection between peak axial wavenumber and τ. This change in peak wavenumber for the 'flat tail' case is likely due to the greater spacing of the vortices and longer time the tail vortices linger outside the highly strained region between the wing vortices. The asymmetry of the flow changes the axial wavenumber where the peak growth amplification factor occurs compared to the symmetric case. This is likely due to the instability occurring on only the weak tail vortex, leading to a change in the global rotation rate for that vortex when compared to the symmetric case, leading to the change in $k\,a_1$ (Bristol *et al.* 2004). For $\tau/T_0 = 3$, the 'flat tail' case peaks at an axial wavenumber of $k\,a_1 = 6.25$, and $k\,a_1 = 6.12$ for the 'high tail' case with the same value of τ. Also for $\tau/T_0 = 3$, the 'flat tail' case demonstrates a larger peak growth amplification factor, $G(\tau) = 6.14 \times 10^{26}$, than the 'high tail' case, $G(\tau) = 1.89 \times 10^{26}$. Because of the disparity between the strength of the tail vortices, the peak response of the system produces a broader range of axial wavenumbers with a growth amplification factor in the order of $G(\tau) \approx 10^{26}$. This is likely due to this region actually being a superposition of two different peaks with slightly different peak axial wavenumbers corresponding to each tail vortex.

It is of interest that the long wavelength peak for the asymmetric cases are significantly larger than the symmetric cases and occur at a shorter wavelength ($k\,a_1 = 1.233$ and 1.32 for the asymmetric 'high tail' and 'flat tail' cases respectively). The amplitudes of the long wavelength modes are significant, reaching $G(\tau) = 4.17 \times 10^{24}$ and 4.47×10^{24} for the asymmetric 'high tail' and 'flat tail' cases. A direct comparison of the growth amplification regime between the symmetric and asymmetric cases is examined below.

Figure 5.11 shows a direct comparison between the symmetric four-vortex transient growth analysis (shown in § 4.3.1) and the asymmetric four-vortex transient growth analysis shown above. It shows that for both the symmetric 'flat tail' and 'high tail' cases, the growth amplification factor for the short wavelength elliptic instability that forms in the tail vortices peaks to a higher value and has a slightly longer wavelength ($k\,a_1 = 5.3$ for both of the symmetric cases against $k\,a_1 \approx 6.2$ for the asymmetric cases). This is likely due to the presence of both tail vortices within the highly strained region acting to increase the strain on the tail vortices and therefore the instability growing

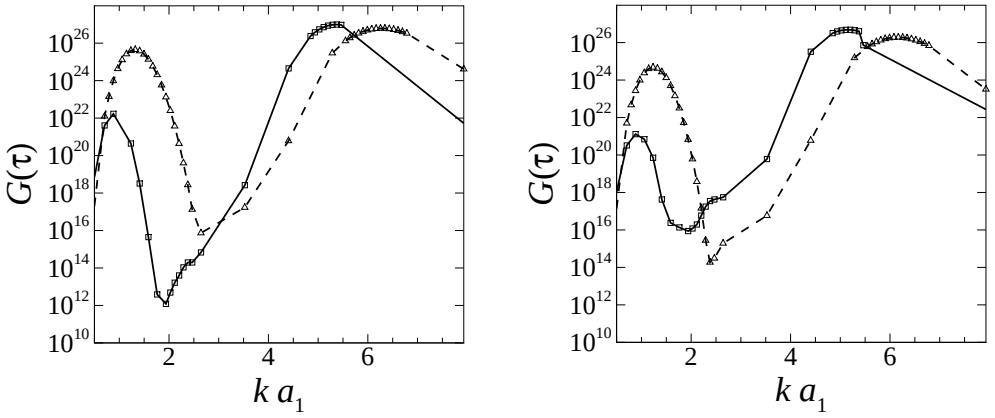

(a) (b)

FIGURE 5.11: Plot of asymmetric and symmetric (a) 'flat tail' and (b) 'high tail' transient growth amplification factor, $G(\tau)$, against non-dimensional axial wavenumber, $k\,a_1$, for an initial time of $t_0 = 0$. $\tau/T_0 = 3$ for the cases shown here. The solid line (and $\square$) represents the growth amplification factors for the four-vortex symmetric case and the dashed line (and $\triangle$) represents the growth amplification factors for the four-vortex asymmetric cases.

on both the tail vortices (in the symmetric case) as opposed to the asymmetric cases where the instability only grows in the weaker tail vortex.

It is of interest that both of the asymmetric cases exhibit a significantly larger growth amplification factor for the long wavelength mode (approximately three orders of magnitude larger for the asymmetric cases), but that the wavelength that it occurs at is shorter ($k\,a_1 \approx 1.25$ for the asymmetric cases compared to $k\,a_1 \approx 0.89$ for the symmetric cases). It is theorised that the reason for the asymmetric case having such a significantly larger growth amplification factor for the long wavelength mode is due to the presence of only one vortex in the highly strained region between the wing vortices at any given time. The presence of the other tail vortex in the highly strained region between the wing vortices has the effect of minimising the local rotation rate of the tail vortices and therefore damping the possible growth of the long wavelength instability. As the asymmetric case only has one vortex in the region between the wing vortices, the local rotation rate experienced by the vortex is significantly increased, leading to a larger growth of the long wavelength instability, even though it only occurs on the weaker tail vortex.

As with the symmetrical four-vortex systems, the size of the growth amplification factor at the peak axial wavenumber indicates that it is likely that the perturbation is

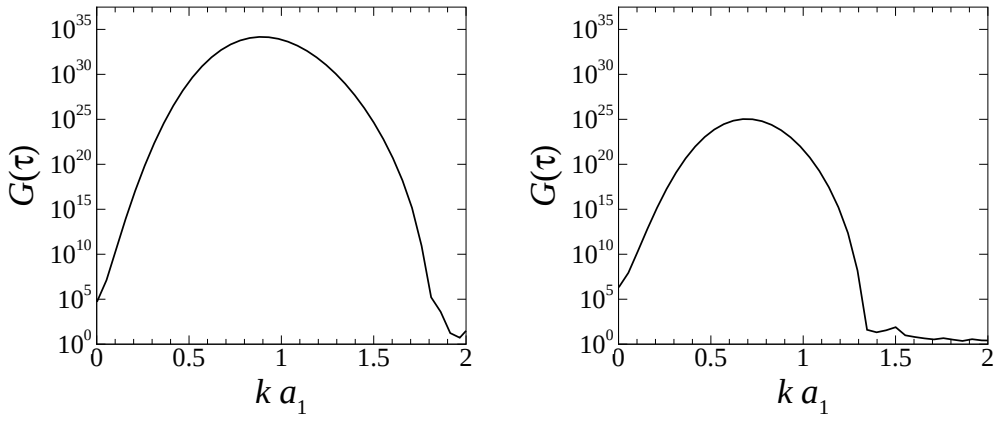

(a) (b)

FIGURE 5.12: Plot of asymmetric (a) 'flat tail' and (b) 'high tail' transient growth amplification factor, $G(\tau)$, against non-dimensional axial wavenumber, $k\,a_1$, for an initial time of $t_0/T_0 = 0$. $\tau/T_0 = 3$ for these simulations. The solid line represents the vortex filament study conducted for the long wavelength Crow instability.

of sufficient size to cause large changes in the base flow and that the flow is likely to be dominated by transient disturbance growth (Barkley *et al.* 2008). In addition, the significantly larger values for the growth amplification factors found in the three-dimensional transient growth analysis when compared to the two-dimensional transient growth analysis indicate that the predominant instability will be three-dimensional in nature.

5.3.2 Vortex filament analysis

By utilising the method described in § 2.7, a theoretical prediction of the peak axial wavenumber expected for the Crow instability can be determined. This section demonstrates that the vortex filament method can provide a reasonable prediction for the four-vortex, asymmetric, 'flat tail' and 'high tail' cases.

Figure 5.12(a) shows the results of a vortex filament analysis for the asymmetric 'flat tail' case. As with the symmetric case, the vortex filament method provides a reasonable prediction for the peak axial wavenumber for the Crow instability, finding a peak at $k\,a_1 = 0.91$ as compared to the peak found in figure 5.10(a), $k\,a_1 = 1.31$.

Figure 5.12(b) shows the results of a vortex filament analysis for the asymmetric 'high tail' case. The vortex filament method provides a reasonable estimate for the peak axial wavenumber of the Crow instability, $k\,a_1 = 0.70$, but is still under-estimating

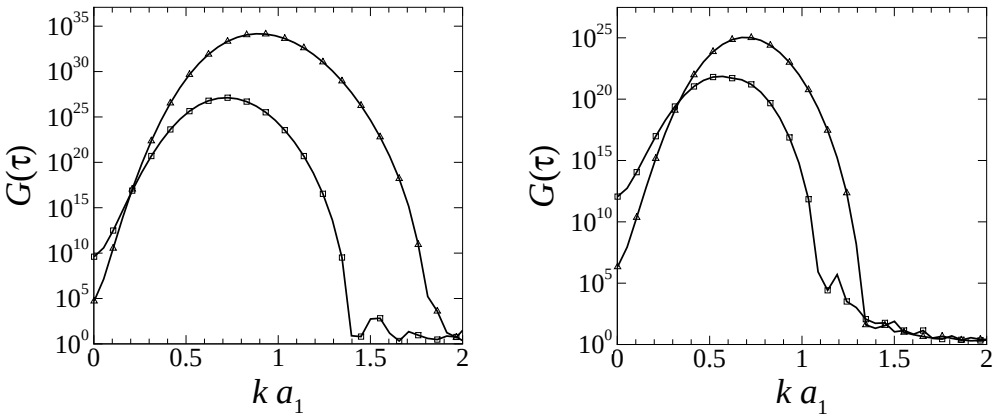

(a) (b)

FIGURE 5.13: Plot of a comparison between asymmetric and symmetric (a) 'flat tail' and (b) 'high tail' transient growth amplification factor, $G(\tau)$, against non-dimensional axial wavenumber, $k\,a_1$, for an initial time of $t_0/T_0 = 0$. $\tau/T_0 = 3$ for these simulations. The solid line represents the vortex filament study conducted for the long wavelength Crow instability. $\triangle$ and $\square$ represent the asymmetric and symmetric cases respectively.

the peak axial wavenumber predicted by the transient growth analysis, $k\,a_1 = 1.24$ (figure 5.10(b)).

As with the symmetric four-vortex case, the difference in $G(\tau)$ between the vortex filament method and transient growth analysis is due to the limitation of the vortex filament method assuming the shape of the instability mode, while the transient growth analysis finds the perturbation that leads to optimal energy growth and is limited only by available spatial resolution. The vortex filament method described here (and the method utilised by Crouch 1997) does provide a good approximation as to the expected peak axial wavenumbers, but is limited because of the need to specify a specific mode shape for the analysis and the lack of viscous interaction between the vortices.

Figure 5.13(a) shows the comparison of the results of the vortex filament analysis for the symmetric 'flat tail' case contrasted to the asymmetric 'flat tail' case. The vortex filament analysis predicts a similar increase in $G(\tau)$ for the Crow instability from the symmetric case to the asymmetric case.

Figure 5.13(b) shows the comparison of the results of the vortex filament analysis for the symmetric 'high tail' case contrasted to the asymmetric 'high tail' case. The comparison for the 'high tail' cases with the vortex filament analysis produces the same agreement with the transient growth analysis as the 'flat tail' cases (agreeing with an

increase $G(\tau)$ in the Crow instability for the asymmetric case).

While the vortex filament method (both the general method utilised in this thesis and such as those utilised by Crow 1970; Jiménez *et al.* 1996; Crouch 1997; Fabre & Jacquin 2000; Fabre *et al.* 2002) does have limitations (primarily the requirement of a pre-defined instability mode shape and a lack of viscous interaction), the vast reduction in computational power required for the vortex filament analysis does provide a useful tool to determine the best regions of axial wavenumber to concentrate a study utilising the transient growth analysis method.

5.3.3 Optimal perturbation fields

In this section the linearised evolution of the predicted optimal initial disturbances is considered for the three-dimensional asymmetric 'high tail' and 'flat tail' cases.

5.3.3.1 Evolution of short wavelength instability

The optimal perturbations evolved for the asymmetric 'high tail' and 'flat tail' cases for the short wavelength instability are at $k\,a_1 = 6.12$ and 6.25 respectively, for $\tau/T_0 = 3$ to correspond to the peak response of the systems found from the transient growth analysis.

Figure 5.14 displays a temporal evolution of the linearised perturbation field for the asymmetric 'flat tail' case, beginning with the perturbation field that leads to optimal energy growth. The initial optimal perturbation field (figure 5.14(a)) shows that the perturbation begins in the weaker, left tail vortex and manifests as a [-1,1,1] mode dipole at about 45° to the line from the centre of the tail vortex to the closest wing vortex. A small smear of perturbation vorticity in a spiral pattern also appears on the outside of the left tail vortex. As the perturbation evolves, it remains in the same vortex, rotating with it, and maintaining the same angle with respect to the line between the tail vortex and the closest wing vortex. In addition, the small spiral smear present in the initial field forms into a weaker dipole of opposite sign surrounding the main [-1,1,1] dipole present in the left tail vortex. It is of interest to note that throughout the evolution, the perturbation grows in magnitude, but remains confined to the one tail vortex (figure 5.14(h)). This is similar to the symmetric 'high tail' case except that in the symmetric case, the perturbation is present in both tail vortices (figure 4.14). This isolation of the perturbation to the weaker tail vortex is likely due to the increased strain experienced by the weaker tail vortex being in close proximity to the stronger

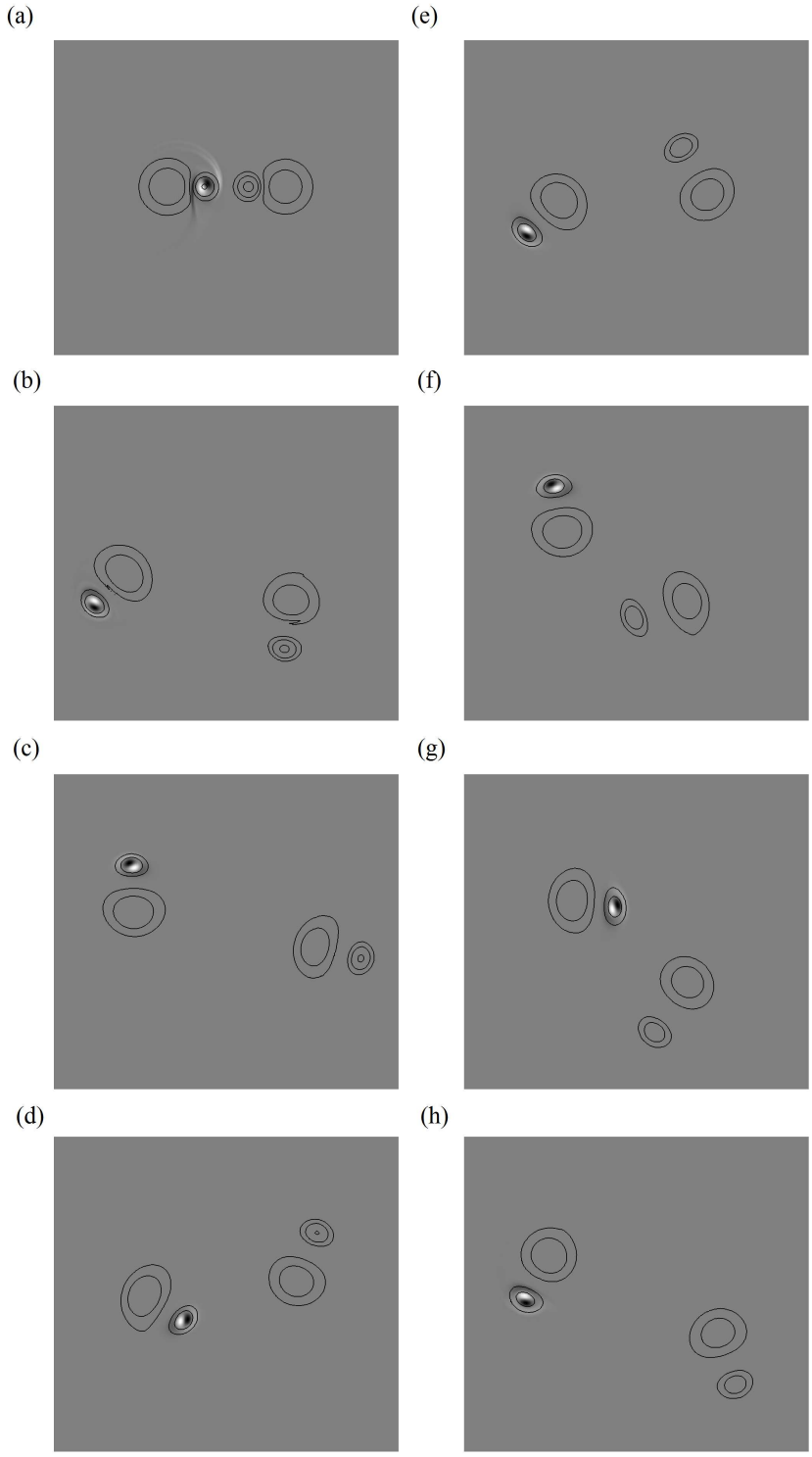

FIGURE 5.14: A time sequence of plots of spanwise vorticity in the linearised perturbation field (flooded contours) for the asymmetric 'flat tail' case with an axial wavenumber of $k\,a_1 = 6.25$. Flooded contour levels are chosen arbitrarily to display the perturbation structure. The simulation were initialised with the optimal disturbance acquired with $\tau/T_0 = 3$. Solid contour lines show spanwise vorticity in the base flow at levels of vorticity of $\mid \omega_z \mid = 1, 3, 7$. (a)-(h) represent $t/T_0 = 0, 0.25, 0.5, 0.75, 1.00, 1.25, 1.50$ and 1.75 respectively.

wing vortex.

Figure 5.15 displays a temporal evolution of the linearised perturbation field for the asymmetric 'high tail' case, beginning with the perturbation field that leads to optimal energy growth. The initial optimal perturbation field (figure 5.15(a)) consists of a strong [-1,1,1] mode dipole located within the weaker left vortex with a smear of vorticity that begins with significant magnitude at the bottom left of the weaker, left tail vortex and weakens in a semicircle under the tail vortices to end at the bottom right of the stronger, right vortex. As the flow evolves, the majority of the extra vorticity present outside the weaker, left vortex, in the perturbation field has decayed away, leaving a small visible halo of vorticity around the primary dipole in the weaker left vortex (figure 5.15(b)). In addition, the perturbation dipole rotates as the tail vortex orbits the wing vortex, maintaining an angle of approximately 45° from the centre of the left wing vortex to the left tail vortex. Even after a significant evolution, the perturbation is still confined to the weaker of the two tail vortices (figure 5.15(h)). The perturbation being confined to the weaker tail vortex can be explained through the increased strain that the weaker tail vortex experiences due to its proximity to the stronger wing vortex, and the lack of initial perturbation around the stronger tail vortex.

5.3.3.2 Evolution of long wavelength instability

The optimal perturbations evolved for the asymmetric 'high tail' and 'flat tail' cases for the long wavelength instability are at $k\,a_1 = 1.23$ and 1.32 respectively, for $\tau/T_0 = 3$ to correspond to the secondary peak response of the systems found from the transient growth analysis.

Figure 5.16 displays a temporal evolution of the linearised perturbation field for the asymmetric 'flat tail' case, beginning with the perturbation field that leads to optimal energy growth for an axial wavenumber of $k\,a_1 = 1.32$. It is interesting to note that although the instability is at a considerably different wavenumber to the short wavelength case ($k\,a = 6.25$, figure 5.14) it exhibits almost exactly the same mode shape, that of a mode [-1,1,1] elliptic instability in the weaker tail vortex (figure 5.16(b)). As in the short wavelength case, the perturbation dipole in the long wavelength case also forms at an angle of approximately 45° to a line between the centre of the tail and the respective wing vortex (figure 5.16(c)). The dipole perturbation rotates, retaining the angle of approximately 45° to a line between the centre of the tail and the respective

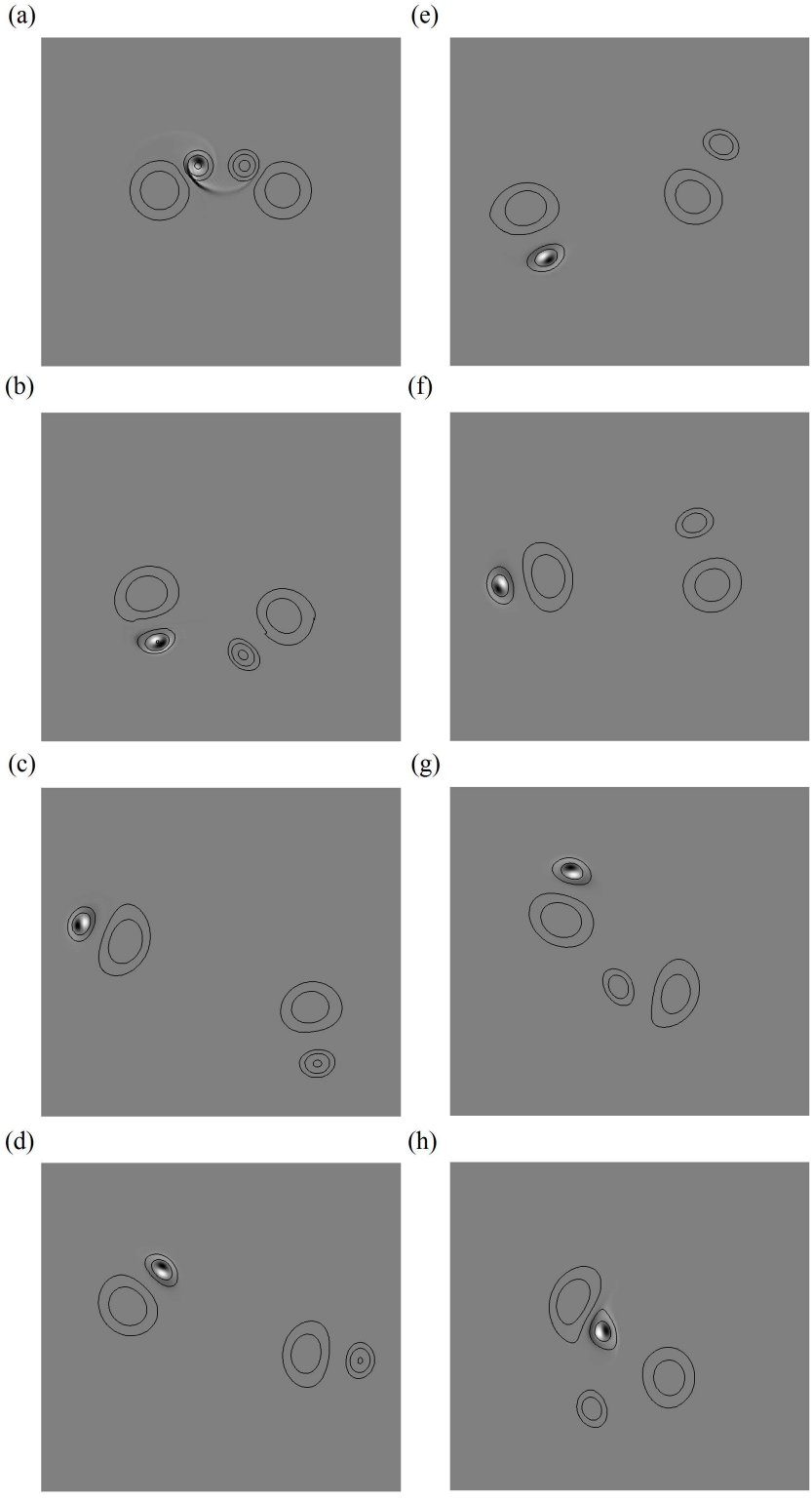

FIGURE 5.15: A time sequence of plots of spanwise vorticity in the linearised perturbation field (flooded contours) for the asymmetric 'high tail' case with an axial wavenumber of $k\,a_1 = 6.12$. Flooded contour levels are chosen arbitrarily to display the perturbation structure. The simulation were initialised with the optimal disturbance acquired with $\tau/T_0 = 3$. Solid contour lines show spanwise vorticity in the base flow at levels of vorticity of $\mid \omega_z \mid = 1, 3, 7$. (a)-(h) represent $t/T_0 = 0, 0.25, 0.5, 0.75, 1.00, 1.25, 1.50$ and 1.75 respectively.

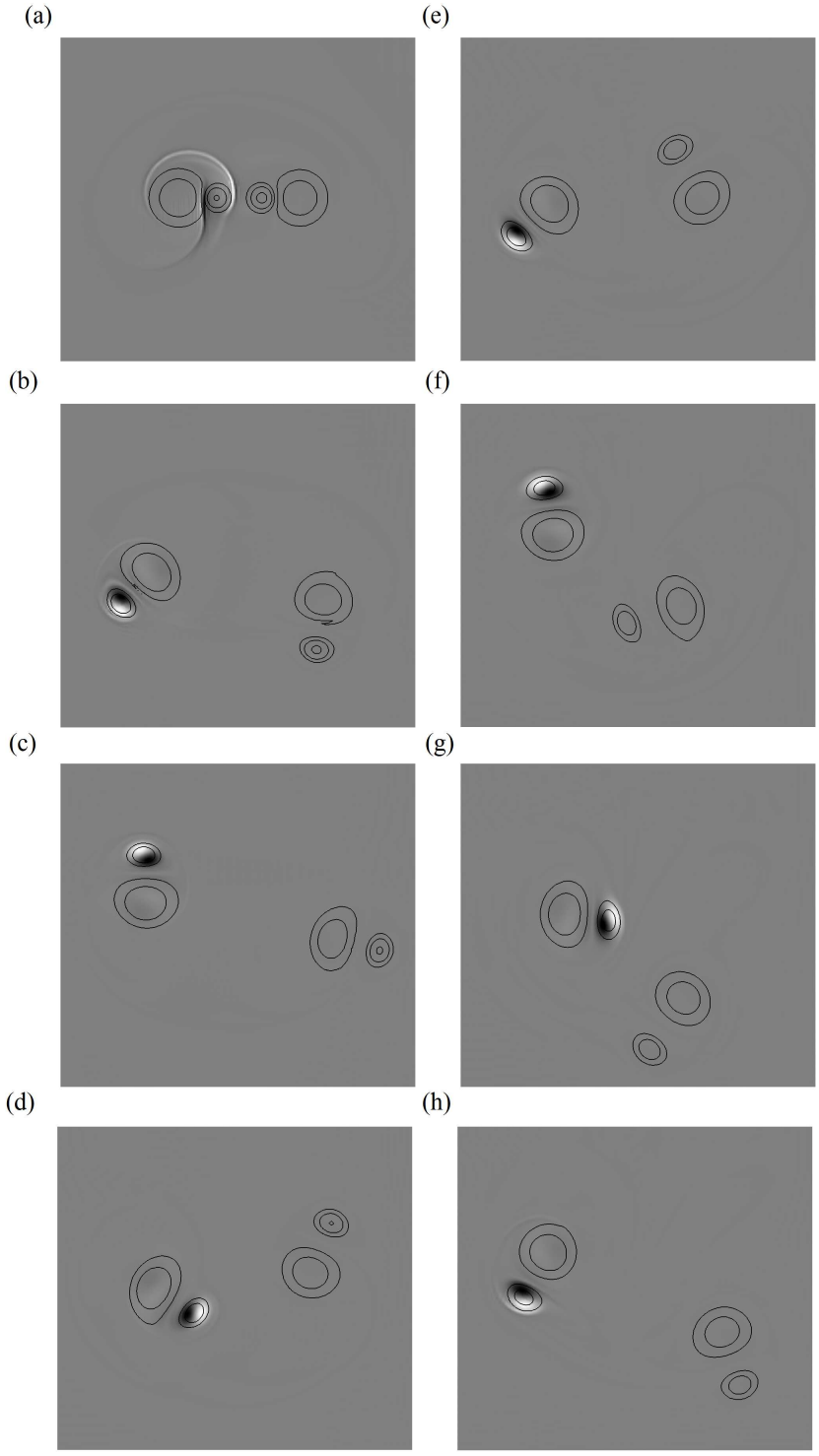

FIGURE 5.16: A time sequence of plots of spanwise vorticity in the linearised perturbation field (flooded contours) for the asymmetric 'flat tail' case with an axial wavenumber of $k\,a_1 = 1.32$. Flooded contour levels are chosen arbitrarily to display the perturbation structure. The simulation were initialised with the optimal disturbance acquired with $\tau/T_0 = 3$. Solid contour lines show spanwise vorticity in the base flow at levels of vorticity of $\mid \omega_z \mid = 1, 3, 7$. (a)-(h) represent $t/T_0 = 0, 0.25, 0.5, 0.75, 1.00, 1.25, 1.50$ and 1.75 respectively.

wing vortex as the tail vortex orbits the respective wing vortex. This dominance of instability in the weaker tail vortex is likely due to the increased strain and rotation rate experienced by the weaker tail vortex being in close proximity to the stronger wing vortex.

Figure 5.17 displays a temporal evolution of the linearised perturbation field for the asymmetric 'high tail' case, beginning with the perturbation field that leads to optimal energy growth for an axial wavenumber of $k\,a_1 = 1.23$. As with the long wavelength mode of the asymmetric 'flat tail' case, the asymmetric 'high tail' case excited at the long wavelength mode exhibits a very similar mode shape (that of the Crow instability in the weaker tail vortex) to the long wavelength instability for the asymmetric 'flat tail' case. As with the previous cases, the dipole forms at an angle of approximately 45° to a line between the centre of the tail and the respective wing vortex (figure 5.17(c)). In addition, the perturbation rotates as the tail vortex orbits the corresponding wing vortex, maintaining the approximately 45° angle to the line between the centre of tail and the respective wing vortex (figure 5.17(d)). As in the long wavelength asymmetric 'flat tail' case, the dominance of the instability in the weaker tail vortex in the long wavelength 'high tail' case is most likely due to the increased strain and rotation rate experienced by the weaker tail vortex being in close proximity to the stronger wing vortex.

5.3.4 Direct numerical simulation

A DNS study of the asymmetric system was performed following the linear analysis. The energy in the perturbations of the linear simulations was compared to the energy in the non-zero Fourier modes of the DNS. To study the response of the system to the optimal perturbation, the DNS was conducted by seeding the 'flat tail' and 'high tail' cases with the optimal perturbation. Axial wavenumbers $k\,a_1 = 6.25$ and 6.12 were chosen for the asymmetric 'flat tail' and 'high tail' cases respectively. These axial wavenumbers were chosen to correspond to the peak axial wavenumbers predicted by the transient growth analysis. The axial domain was chosen to allow for one wavelength of the desired instability with both the 'flat tail' and 'high tail' cases being seeded in only the first Fourier mode (thus corresponding to exciting only a wavelength of $k\,a_1 = 6.25$ and 6.12 for the 'flat tail' and 'high tail' cases respectively). Sixteen Fourier modes were employed for these simulations as per § 2.6.3. The energy in the optimal initial

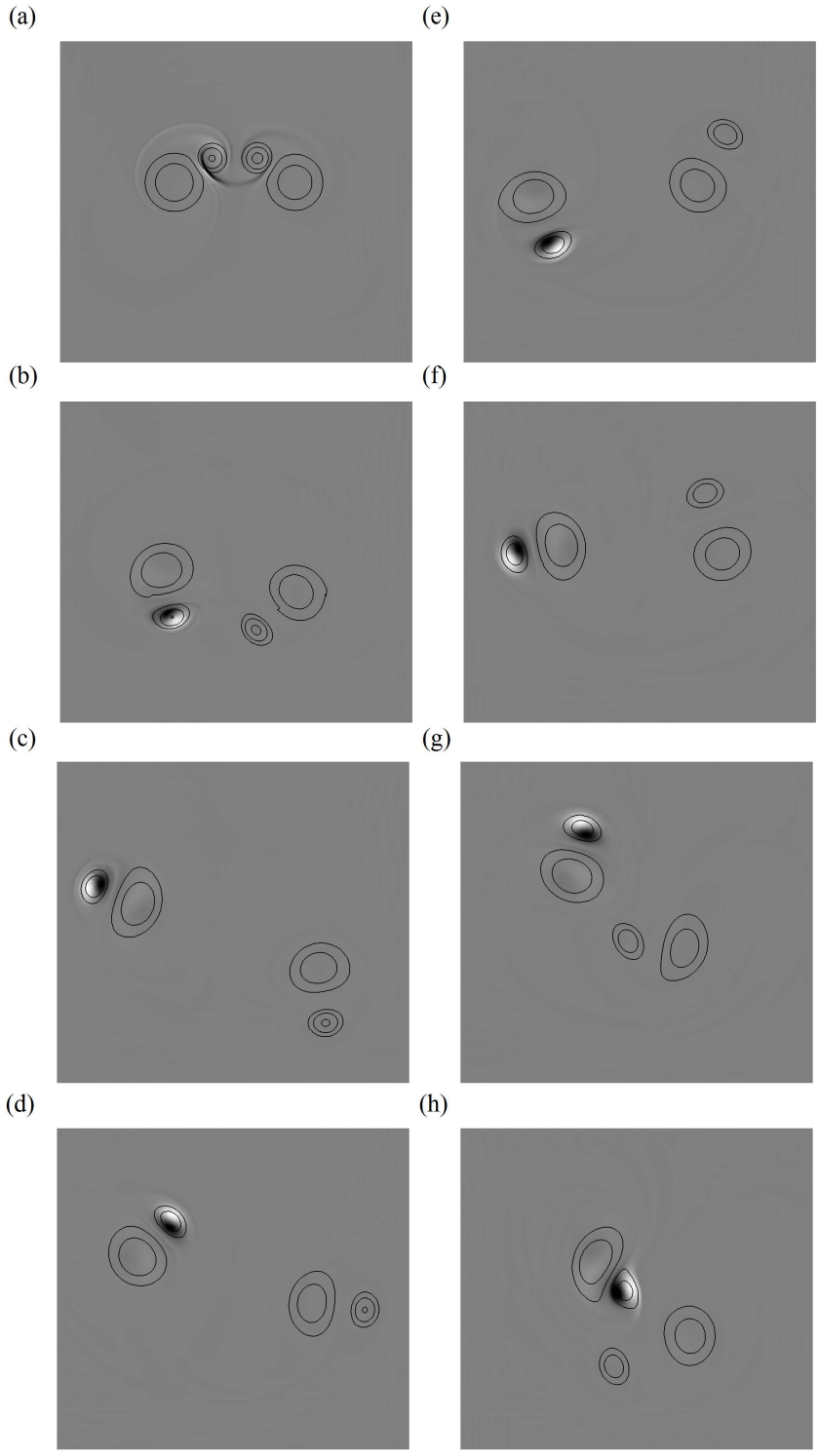

FIGURE 5.17: A time sequence of plots of spanwise vorticity in the linearised perturbation field (flooded contours) for the asymmetric 'high tail' case with an axial wavenumber of $k\,a_1 = 1.23$. Flooded contour levels are chosen arbitrarily to display the perturbation structure. The simulation were initialised with the optimal disturbance acquired with $\tau/T_0 = 3$. Solid contour lines show spanwise vorticity in the base flow at levels of vorticity of $\mid \omega_z \mid = 1, 3, 7$. (a)-(h) represent $t/T_0 = 0, 0.25, 0.5, 0.75, 1.00, 1.25, 1.50$ and 1.75 respectively.

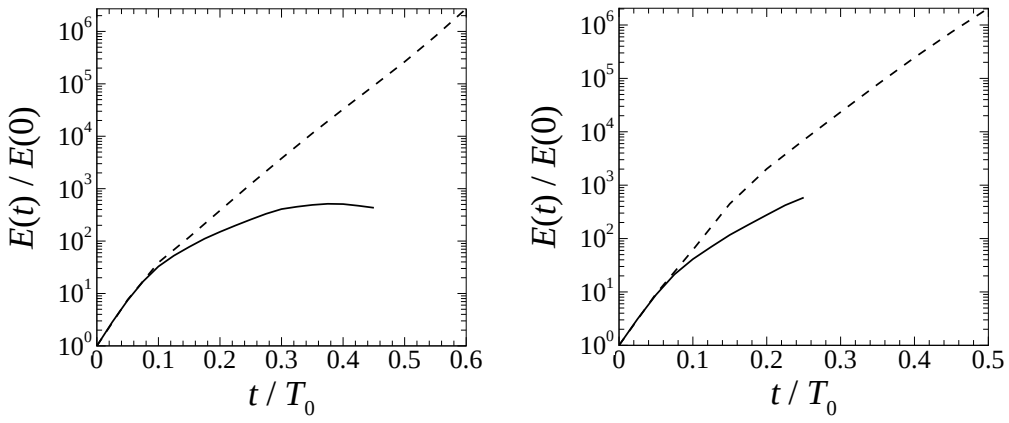

(a) (b)

FIGURE 5.18: Plot of asymmetric (a) 'flat tail' and (b) 'high tail' perturbation energy normalised by initial energy. The dashed line represents the solution of the linearised Navier–Stokes equation and the solid line represents the energy in the non-zero Fourier modes of the DNS. Simulations were initiated with the optimal disturbance computed with $k\,a_1 = 6.25$ and 6.12 for the 'flat tail' and 'high tail' cases respectively, with $\tau/T_0 = 3$.

perturbation was 0.00248% of the initial energy in the base flow. The vortex core sizes and separations are as per § 2.1.

Figure 5.18 shows the normalised energy in the perturbations evolved using the linearised Navier–Stokes equations compared to the energy in the Fourier modes of the non-linear simulation for the 'flat tail' and 'high tail' cases. The perturbation fields become highly non-linear after only a short timeframe (signified by the departure of the pair of curves), with the 'high tail' case exhibiting more disturbance energy than the 'flat tail' case once the non-linear disturbance saturates, leading to faster instability growth.

Figure 5.19 shows the time history of normalised perturbation energy in the DNS comparing the asymmetric 'flat tail' and 'high tail' cases seeded with the optimum perturbation found from the transient growth analysis. It can be seen that for both the asymmetric 'high tail' and 'flat tail' cases seeded with the optimal perturbations, the instability begins to grow immediately as the flow is evolved in time. The 'high tail' case seeded with the optimal perturbation reaches a significantly higher perturbation energy in a similar period of time to the 'flat tail' case, implying that the flow is becoming significantly more perturbed in a shorter timeframe.

Table 5.1 shows the peak grow rate, and the time that the peak occurs, of the asym-

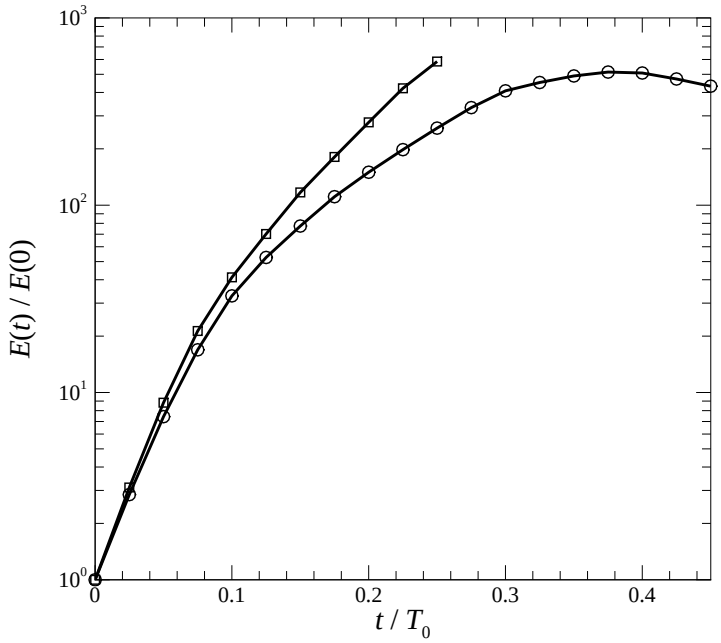

FIGURE 5.19: Time history of perturbation energy, normalised by initial energy. □ and ∘ represent the 'high tail' and 'flat tail' cases respectively. Simulations were initiated with the optimal disturbance computed with $k\,a_1 = 6.25$ and 6.12 for the 'flat tail' and 'high tail' cases respectively, with $\tau/T_0 = 3$.

TABLE 5.1: Table of peak energy growth rate, σ_{GR}, for the asymmetric four-vortex cases.

'High tail' - Optimal Seeding	'Flat tail' - Optimal Seeding
$\sigma_{GR}(t/T_0 = 0.1)$	$\sigma_{GR}(t/T_0 = 0.1)$
0.506	0.466

metric cases seeded with the optimal perturbation. The growth rate was calculated using a five-point stencil method to evaluate the derivative of the log of the perturbation energy. It shows that the asymmetric 'high tail' case seeded with the optimal perturbation reaches a higher growth rate than the asymmetric 'flat tail' case seeded with the optimal perturbation. This higher growth rate indicates that the asymmetric 'high tail' case is more unstable than the 'flat tail' case and should saturate faster. It is interesting to note that both the asymmetric 'high tail' and 'flat tail' cases exhibit a smaller instability growth rate than the symmetric 'high tail' and 'flat tail' cases (shown in § 4.3.4). This is of interest as it shows that the symmetric cases are more unstable than the asymmetric cases when seeded with the perturbation that leads to optimal energy growth.

As with the relationship between the strain rate and the instability growth rate cov-

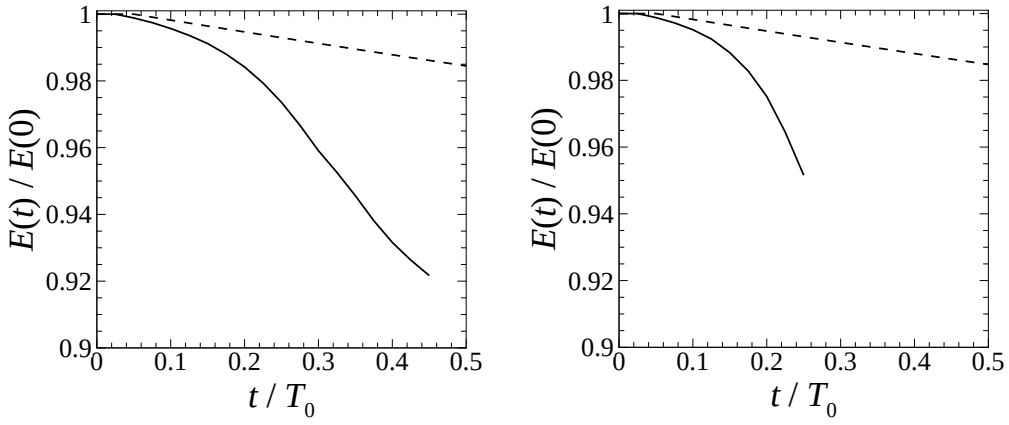

FIGURE 5.20: Time history of DNS zeroth mode energy for the asymmetric (a) 'flat tail' and (b) 'high tail' case, normalised by initial energy in the zeroth Fourier mode. Simulations were initiated with the optimal disturbance computed with $k\,a_1 = 6.25$ and 6.12 for the 'flat tail' and 'high tail' cases respectively. Solid lines represent the cases seeded with an optimal perturbation with $\tau/T_0 = 3$ and the dashed line represents a two-dimensional case.

ered in the previous chapters (§ 3.5.0.1 and 4.3.4.1), the four-vortex asymmetric system also exhibits a ratio of growth rate to strain rate of less than the theoretical maximum the literature describes for the elliptic instability of 9/16 (Leweke & Williamson 1998; Kerswell 2002).

Figure 5.20 shows a normalised-energy time history for the zeroth Fourier mode for the asymmetric (a) 'flat tail' and (b) 'high tail' cases seeded with the optimal perturbation and the two-dimensional reference case. It shows that the linear growth of the perturbations causes a large drop in the energy of the zeroth mode, which represents a large reduction in the coherency of the vortices. As in the symmetrical case, the energy in the zeroth Fourier mode begins to drop significantly earlier in the case seeded with the optimal perturbation as the linear regime begins almost immediately after the flow is seeded when compared to diffusion present in the two-dimensional case. This demonstrates that the three-dimensional instability development does accelerate the destruction of the coherency of the two-dimensional vortices. The asymmetric 'high tail' case seeded with the optimal perturbation reaches a smaller base flow energy in a shorter period of time than the asymmetric 'flat tail' case seeded with the optimal perturbation, indicating that the base flow is becoming less coherent.

Figure 5.21 shows a three-dimensional visualisation of the DNS evolution of the

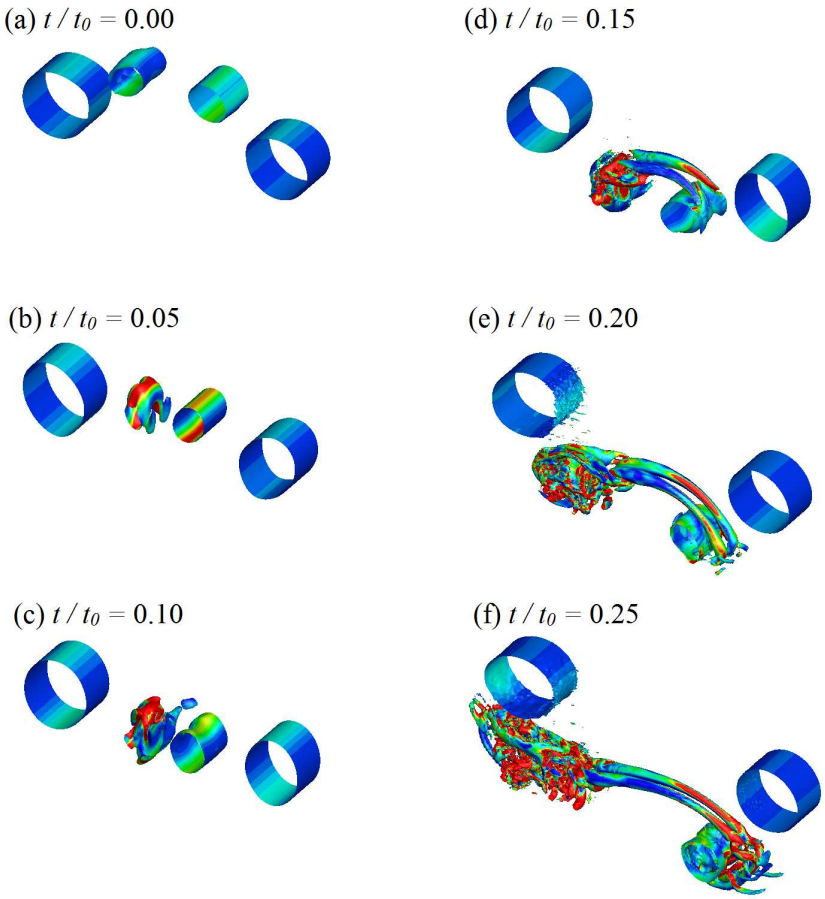

FIGURE 5.21: Time sequences of iso-surfaces of an arbitrary small negative value of the λ_2 field plotted from a three-dimensional simulation of the asymmetric 'high tail' case with an axial extent corresponding to a wavenumber of $k\,a_1 = 6.12$. The coloured shading shows levels of dominant strain, with blue and red corresponding to low and high values respectively. (a)-(f) display the flow seeded with the perturbation that leads to optimum energy growth for $\tau/T_0 = 3$ at $t/T_0 = 0, 0.05, 0.10, 0.15, 0.20, 0.25$ respectively.

asymmetric 'high tail' case seeded with the perturbation that leads to optimal energy growth. The seeding of the optimal perturbation can be seen initially as a slight deformation of the left tail vortex (figure 5.21(a)). As the flow evolves, the tail vortex pair enters the highly strained region between the wing vortex pair, leading to the already deformed vortex becoming highly deformed (figure 5.21(c)). This extreme deformation of one of the tail vortices leads to tendrils visible in the λ_2 field crossing the vertical mid-plane and wrapping around the the other, less deformed, tail vortex (figure 5.21(d)). The wrapping of these tendrils causes a greater strain in the right tail vortex, increasing its deformation, while the left tail vortex disintegrates into extremely

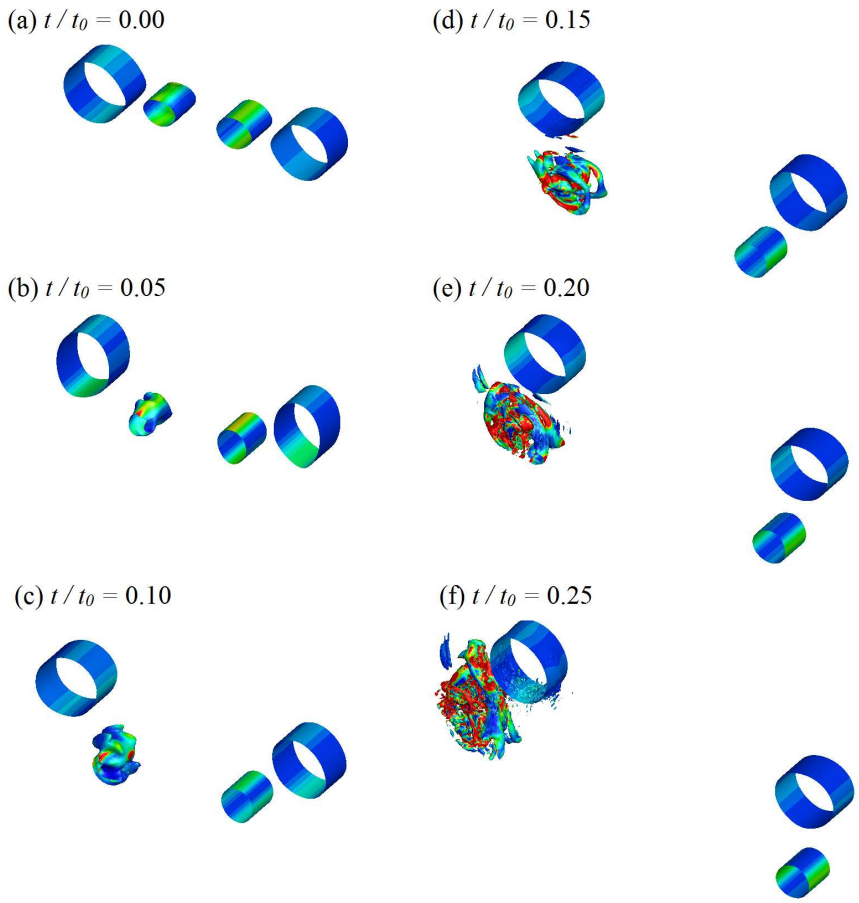

FIGURE 5.22: Time sequences of iso-surfaces of an arbitrary small negative value of the λ_2 field plotted from a three-dimensional simulation of the asymmetric 'flat tail' case with an axial extent corresponding to a wavenumber of $k\,a_1 = 6.25$. The coloured shading shows levels of dominant strain, with blue and red corresponding to low and high values respectively. (a)-(f) display the flow seeded with the perturbation that leads to optimum energy growth for $\tau/T_0 = 3$ at $t/T_0 = 0, 0.05, 0.10, 0.15, 0.20, 0.25$ respectively.

small scale flow structures (figure 5.21(e)). The left tail vortex continues its transition into small scale flow structures, with the tendrils greatly speeding up the transition of the right vortex into a similar state of small scale flow structures (figure 5.21(f)). This type of interaction is analogous to the T-T interaction demonstrated in chapter 4.

Figure 5.22 shows a three-dimensional visualisation of the DNS evolution of the asymmetric 'flat tail' case seeded with the perturbation that leads to optimal energy growth. As with the 'high tail' case seeded with white noise, a small deformation of the left tail vortex can be seen due to the seeding of the optimal perturbation (figure 5.22(a)). This deformation begins to grow as the flow evolves in time and the tail vortex pair leaves the highly strained region between the wing vortex pair, but only

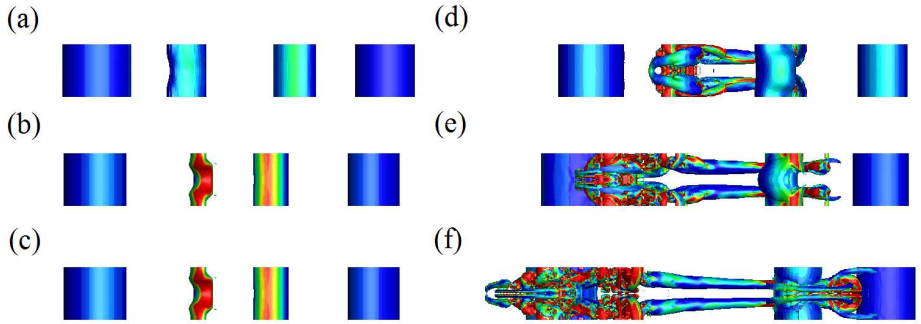

FIGURE 5.23: A time sequence of iso-surfaces an arbitrarily small negative value of the λ_2 field plotted for the asymmetric 'high tail' case, viewed from directly below, for an axial wavenumber of $k\,a_1 = 6.12$, seeded with the perturbation that leads to optimal energy growth for $\tau/T_0 = 3$. The iso-surfaces are coloured by dominant strain rate with blue and red corresponding to low and high levels respectively. (a)-(f) display the times $t/T_0 = 0, 0.05, 0.1, 0.15, 0.20$ and 0.25 respectively.

in the left tail vortex (figure 5.22(b)-(c)). As the instability in the left tail vortex has not grown to sufficient magnitude before leaving the highly strained region between the wing vortex pair, the instability growth is predominantly due to the imposed strain between the wing and tail vortex pair, which is analogous to the T-W interaction shown in chapter 4. This is more likely to remain a T-W interaction without any interaction between the tail vortices as the asymmetry of the system means that after the initial condition the tail vortices are never in the highly strained region between the wing vortex pair at the same time.

5.3.5 Transition into the non-linear regime

Throughout this section, the flow is visualised using three different definitions to examine the transition of the flow from the linear regime to the non-linear regime. The first is the λ_2 field, defined by Jeong & Hussain (1995) and shows the presence of a vortex as defined in their work. The second visualisation method utilises the vorticity magnitude field and is defined as $[\omega_z^2 + \omega_y^2 + \omega_x^2]^{0.5}$. The final visualisation method examines the non-axial vorticity field, defined as $[\omega_y^2 + \omega_x^2]^{0.5}$. Each visualisation in this section is examined in the order given here.

Figures 5.23-5.25 display the iso-surfaces for the asymmetric 'high tail' case seeded with the optimal perturbation. As the instability grows in the left tail vortex (weaker tail vortex) in the form of a sinusoidal axial deformation (figure 5.23(b)) it forms two tendrils visible in the λ_2 field which begin to extend towards the right tail vortex

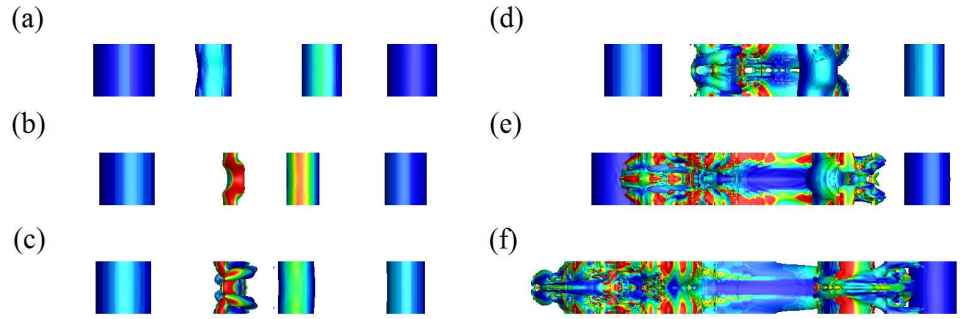

FIGURE 5.24: A time sequence of iso-surfaces of vorticity magnitude for the asymmetric 'high tail' case, viewed from directly below, for an axial wavenumber of $k\,a_1 = 6.12$, seeded with the perturbation that leads to optimal energy growth for $\tau/T_0 = 3$. The iso-surfaces are coloured by dominant strain rate with blue and red corresponding to low and high levels respectively. (a)-(f) displays the times $t/T_0 = 0, 0.05, 0.1, 0.15, 0.20$ and 0.25 respectively.

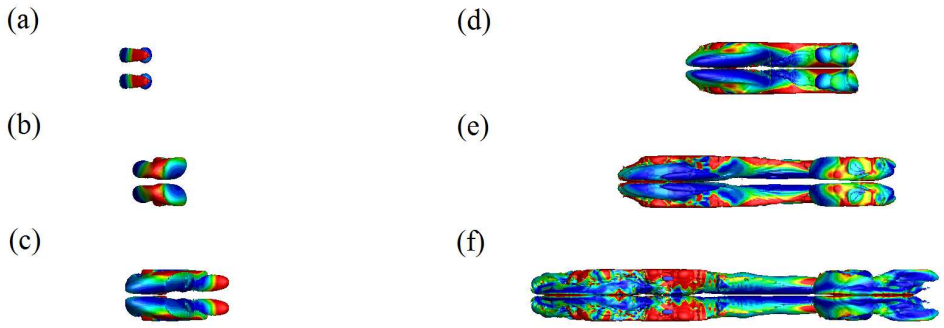

FIGURE 5.25: A time sequence of iso-surfaces of the $[\omega_y^2 + \omega_x^2]^{0.5}$ field with dominant strain flooding for the asymmetric 'high tail' case, viewed from directly below, for an axial wavenumber of $k\,a_1 = 6.12$, seeded with the perturbation that leads to optimal energy growth for $\tau/T_0 = 3$. The iso-surfaces are coloured by dominant strain rate with blue and red corresponding to low and high levels respectively. (a)-(f) displays the times $t/T_0 = 0, 0.05, 0.1, 0.15, 0.20$ and 0.25 respectively.

(figure 5.23(c)). These tendrils form a loop that begins to wrap around the right vortex, causing it to sinusoidally deform in the axial direction (figure 5.23(d)). The combination of the linking of the two vortices through these tendrils and the highly strained region between the wing vortex pair causes a T-T type interaction, which, in turn, causes a rapid devolution into small scale flow structures in the tail vortex pair (figure 5.23(f)).

Figure 5.24 displays similar characteristics to figure 5.23. As with the symmetrical cases, the λ_2 and vorticity magnitude fields correspond well in early in the evolution due to the dominant strain being weaker than ω_{xy}^2 and so the flow is dominated by the

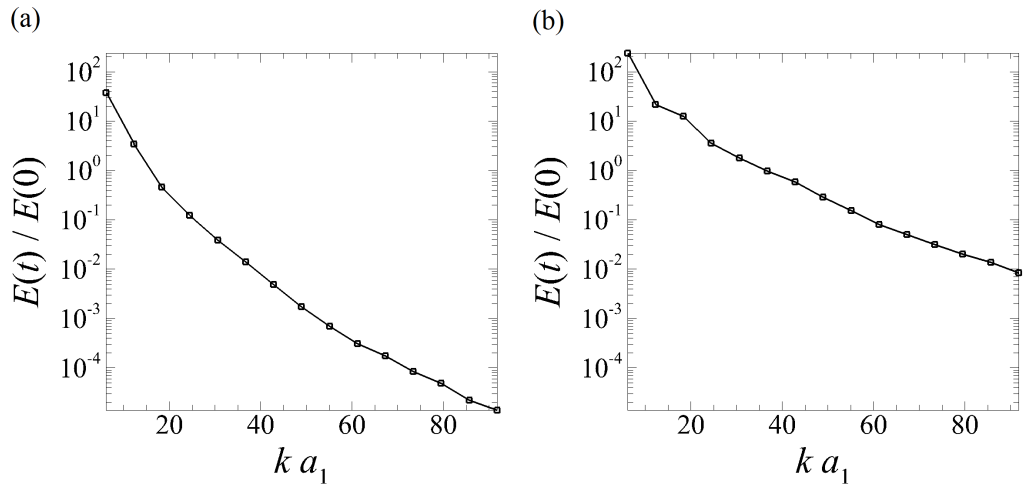

FIGURE 5.26: Plot of mode energy, $E(t)/E(0)$, against axial wavenumber, $k\,a_1$, for the asymmetric 'high tail' case seeded with the optimal perturbation found from the transient growth analysis. (a)-(b) represent times, $t/T_0 = 0.1$ and 0.2 respectively.

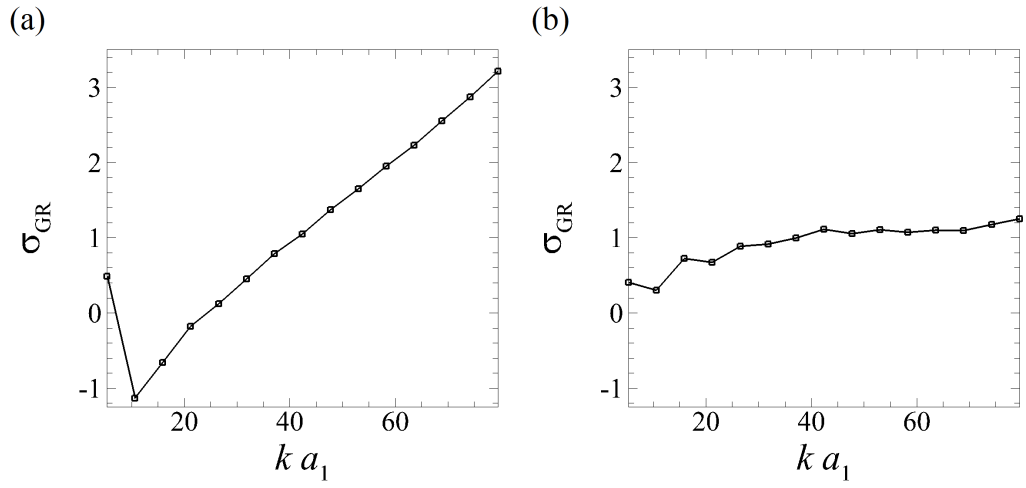

FIGURE 5.27: Plot of mode energy growth rate, σGR, against axial wavenumber, $k\,a_1$, for the asymmetric 'high tail' case seeded with the optimal perturbation found from the transient growth analysis. (a)-(b) represent times, $t/T_0 = 0.05$ and 0.15 respectively.

axial vorticity (figure 5.24(a)-(c)). As the flow evolves into the non-linear regime, the dominant strain becomes greater than ω_z^2 and so regions of the vorticity magnitude are visible that are not identified in the λ_2 field (Figure 5.24(d)-(f)).

Figure 5.25 shows that the majority of the system is two-dimensional with only a small amount of three-dimensional flow in the left tail vortex. This three-dimensional flow begins as a pair of distortions in line with the vortex core (figure 5.25(a)) with a highly strained region (red shading) beginning to surround the core. This non-axial flow spreads across the domain, eventually interacting with the right tail vortex and

causing it to become three-dimensional (figure 5.25(d)). As the instability grows, the tail vortices become highly three-dimensional, dominating the domain close to the tail vortices (figure 5.25(f)).

Figure 5.26 displays the normalised energy in the individual Fourier modes for the asymmetric 'high tail' case seeded with the optimal perturbation found from the transient growth analysis. It shows that at $t/T_0 = 0.1$ (figure 5.26(a)), the energy is primarily concentrated in the smaller Fourier modes. This is to be expected as the flow is initially seeded in only the leading Fourier mode. Figure 5.26(b) demonstrates that during the linear regime the flow is still dominated by the leading Fourier mode, but the higher Fourier modes undergo significant energy growth ($E(t)/E(0) = 1.4 \times 10^{-5}$ at $t/T_0 = 0.1$ to $E(t)/E(0) = 8.8 \times 10^{-3}$ at $t/T_0 = 0.2$). This result shows that the higher Fourier modes play a significant role in the devolution of the flow into small scale flow structures.

Figure 5.27 displays the energy growth rate in the individual Fourier modes for the asymmetric 'high tail' case seeded with the optimal perturbation found from the transient growth analysis. The growth rates were calculated using a five-point stencil method utilising the energy in the individual Fourier modes. Early in the disturbance evolution ($t/T_0 = 0.05$, figure 5.27(a)), there is significant growth in the leading Fourier mode and larger growth in the Fourier modes with an axial wavenumber of $k\,a_1 \geq 40$. This reflects the rapid development of small scale flow structures noted earlier in figure 5.21. By $t/T_0 = 0.15$, the growth rate of all of the Fourier modes have levelled out, with the leading Fourier modes having slightly less energy growth rate (figure 5.27(b)). This reduction in growth rate indicates that the non-linear growth of the instability is not as conducive to growth as the base flow devolves into small scale flow structures. That the energy growth in the Fourier modes is still non-zero indicates that the disturbance has not completely saturated at this time.

Figures 5.28-5.30 display the iso-surfaces for the asymmetric 'flat tail' case seeded with the optimal perturbation. It can be seen in figure 5.28(a) that the instability begins in the weaker tail vortex (left tail vortex as seen from the bottom). As in the previous cases, the instability begins as a sinusoidal deformation in the one tail vortex (figure 5.28(b)). The unstable tail vortex forms a 'bow' of fluid that has regions of high dominant strain (red shading in figure 5.28(c)) before disintegrating (figure 5.28(e)). By the time the weaker tail vortex has disintegrated, a slight distortion has grown along

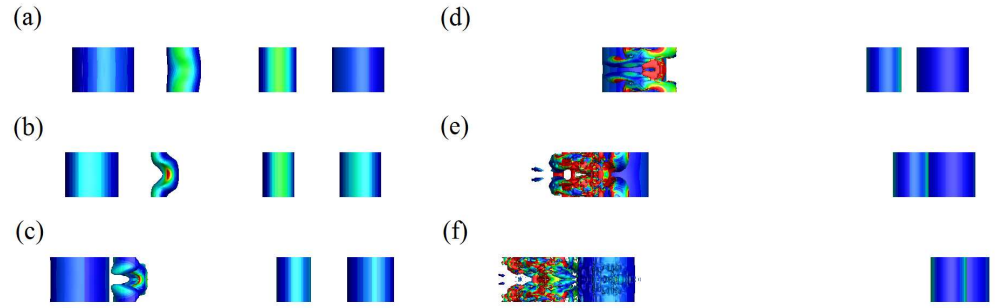

FIGURE 5.28: A time sequence of iso-surfaces of an arbitrarily small negative value of the λ_2 field plotted for the asymmetric 'flat tail' case, viewed from directly below, for an axial wavenumber of $k\,a_1 = 6.25$, seeded with the perturbation that leads to optimal energy growth for $\tau/T_0 = 3$. The iso-surfaces are coloured by dominant strain rate with blue and red corresponding to low and high levels respectively. (a)-(f) displays the times $t/T_0 = 0, 0.05, 0.1, 0.15, 0.20$ and 0.25 respectively.

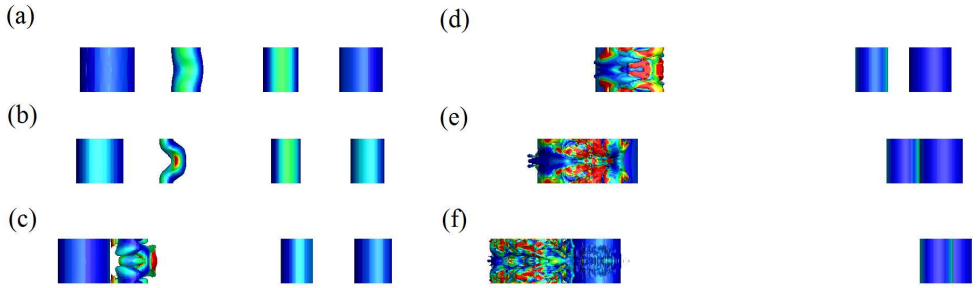

FIGURE 5.29: A time sequence of iso-surfaces of vorticity magnitude for the asymmetric 'flat tail' case, viewed from directly below, for an axial wavenumber of $k\,a_1 = 6.25$, seeded with the perturbation that leads to optimal energy growth for $\tau/T_0 = 3$. The iso-surfaces are coloured by dominant strain rate with blue and red corresponding to low and high levels respectively. (a)-(f) displays the times $t/T_0 = 0, 0.05, 0.1, 0.15, 0.20$ and 0.25 respectively.

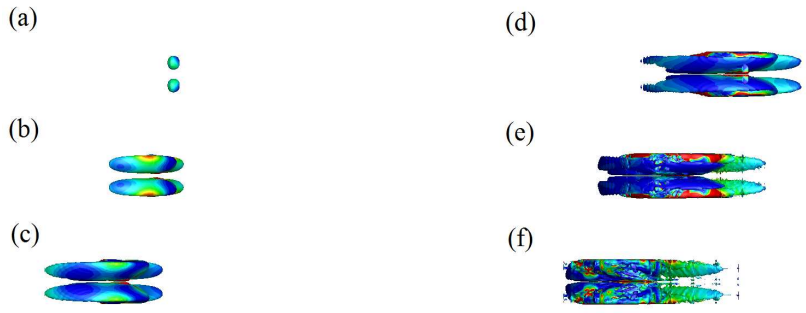

FIGURE 5.30: A time sequence of iso-surfaces of the $[\omega_y^2 + \omega_x^2]^{0.5}$ field with dominant strain flooding for the asymmetric 'flat tail' case, viewed from directly below, for an axial wavenumber of $k\,a_1 = 6.25$, seeded with the perturbation that leads to optimal energy growth for $\tau/T_0 = 3$. The iso-surfaces are coloured by dominant strain rate with blue and red corresponding to low and high levels respectively. (a)-(f) displays the times $t/T_0 = 0.05, 0.1, 0.15, 0.20$ and 0.25 respectively.

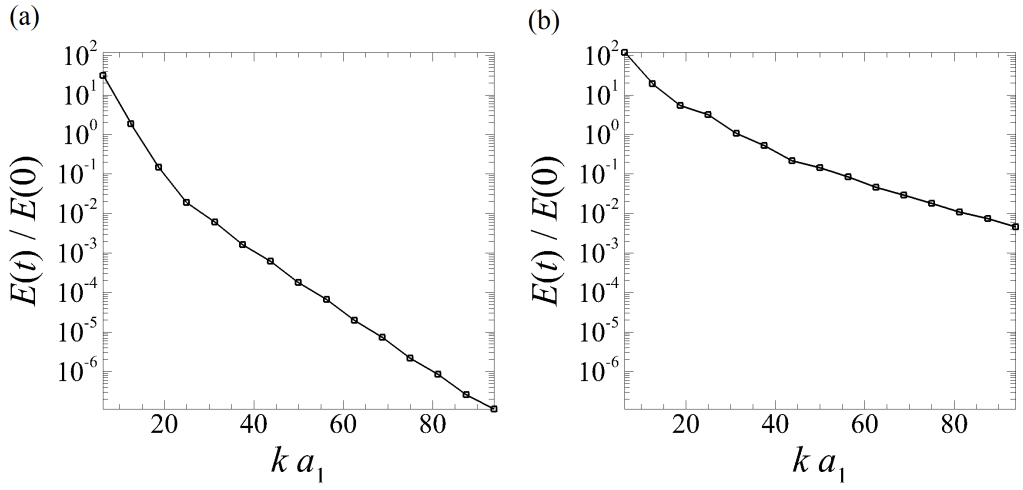

FIGURE 5.31: Plot of mode energy, $E(t)/E(0)$, against axial wavenumber, $k\,a_1$, for the asymmetric 'flat tail' case seeded with the optimal perturbation found from the transient growth analysis. (a) and (b) represent times, $t/T_0 = 0.1$ and 0.2 respectively.

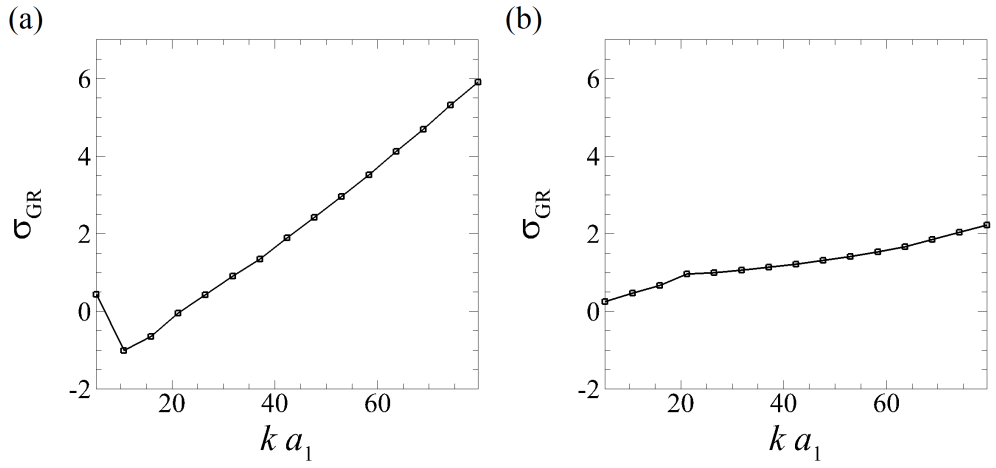

FIGURE 5.32: Plot of mode energy growth rate, σ_{GR}, against axial wavenumber, $k\,a_1$, for the asymmetric 'flat tail' case seeded with the optimal perturbation found from the transient growth analysis. (a) and (b) represent times, $t/T_0 = 0.10$ and 0.15 respectively.

the axis of the left wing vortex (figure 5.28(f)). Throughout the devolution of the left tail vortex into small scale flow structures, the right side of the system remains free of any type of noticeable instability. This type of vortex interaction is analogous to the T-W interaction described in the previous chapter (chapter 4).

As in the previous cases, early in the transition into the non-linear regime, the vorticity magnitude corresponds well to the λ_2 field (figures 5.29(a)-(b) and 5.28(a)-(b)). As the flow transitions into the non-linear regime, the vorticity magnitude begins to diverge from the λ_2 field for the reasons described previously (figures 5.29(c)-(d) and

5.28(c)-(d)).

Figure 5.30(a) shows that the majority of the flow is two-dimensional, with only a small region of three-dimensional flow present in the weaker tail vortex. As the flow transitions into the non-linear regime, the deformation in the weaker tail vortex becomes stronger, forming two regions around the vortex core, which also show high dominant strain (red shading in figure 5.30(c)-(d)). As the tail vortex devolves into very small scale flow structures, it also becomes highly three-dimensional, covering the entire axial domain around the left tail vortex (figure 5.30(f)-(g)).

Figure 5.31 displays the normalised energy in the individual Fourier modes for the asymmetric 'flat tail' case seeded with the optimal perturbation found from the transient growth analysis. This case is very similar to the 'high tail' case seeded with the optimal perturbation where the higher Fourier modes begin with very little energy and proceed to grow at an extremely high rate, while the leading Fourier mode only undergoes a relatively small growth in perturbation energy. The energy in the highest Fourier mode at $t/T_0 = 0.1$ begins at $E(t)/E(0) = 1.14 \times 10^{-7}$ (figure 5.31(a)) and transitions to $E(t)/E(0) = 4.69 \times 10^{-3}$ at a time of $t/T_0 = 0.2$ (figure 5.31(b)). This extremely large increase in the energy of the highest Fourier mode indicates that the flow is rapidly devolving into very small scale flow structures in a very short period of time.

Figure 5.32 shows the energy growth rate in the individual Fourier modes for the asymmetric 'flat tail' case seeded with the optimal perturbation found from the transient growth analysis. Early in the linear regime, $t/T_0 = 0.1$, the highest Fourier modes experience a high energy growth rate (figure 5.32(a)), which is consistent with the asymmetric 'high tail' cases examined previously. This indicates that the flow is rapidly degrading into very small scale flow structures. As the flow transitions into the non-linear regime, around $t/T_0 = 0.15$, the growth in the highest Fourier modes begins to decrease, indicating that the flow is reaching a scale limited by the fluid viscosity (figure 5.32(b)). It is of interest that, while the leading Fourier mode begins with a smaller energy growth rate, it also undergoes a smaller reduction in growth rate into the non-linear regime. This indicates that it is less affected by the transition into the non-linear regime.

5.4 Summary

This chapter reported on the results of a study into the dynamics of an asymmetric four-vortex flow as a model of an aircraft wake shed off an aircrafts wings and tail. The study started with a two-dimensional transient growth and DNS study. It was found that the short term two-dimensional kinematics of the system are extremely unbalanced, but exhibit a similar downward translation to the symmetrical case. In both the 'high tail' and 'flat tail' cases, the left wing/tail pair exhibited less drop than the right side, with the 'flat tail' case showing less drop overall. For the zero-wavenumber (two-dimensional) transient growth analysis, there is a band of τ where the 'flat tail' case exhibits larger growth ($1 \leq \tau/T_0 \leq 2.25$), but for the majority of the time, the 'high tail' case demonstrates a larger growth amplification factor.

The study continued with a three-dimensional transient growth analysis of both the asymmetrical 'flat tail' and 'high tail' cases. It was found that the asymmetry of the system has the effect of shifting the peak axial wavenumber at which the system is most susceptible to the transient growth of perturbations ($k\,a_1 = 6.12$ and 6.25 for the 'high tail' and 'flat tail' cases respectively). The system does have a broad wave band over which significant growth amplification factors of $G(\tau) \approx O(10^{26})$ are maintained. This magnitude of the growth amplification factor is in the same order as the symmetrical case.

The evolution of the optimal perturbation fields in the linear regime was considered, and it was found that the optimal seeding for this flow is to introduce a [-1,1,1] Kelvin mode into the weaker tail vortex only. In the linear regime, the instability is confined to the weaker tail vortex.

A three-dimensional DNS study was conducted, seeding both the 'high tail' and 'flat tail' cases with the optimal perturbation at axial wavenumbers $k\,a_1 = 6.25$ and 6.12 for the asymmetric 'flat tail' and 'high tail' cases respectively. The DNS demonstrated that similar vortex interactions are present in the asymmetrical case to the symmetrical case, namely the T-T and T-W interactions. The T-T interaction is significantly rarer as it requires both tail vortices to reach a level of instability and be present within the highly strained region between the wing vortex pair, and was only observed to occur in the 'high tail' case seeded with the optimal perturbation. The requirement of both tail vortices being present between the highly strained region between the wing vortex pair is uncommon in these cases. This is because the orbit period of the tail vortices are

different due to the different strength ratios between the wing and tail vortices on each side of the domain. In the two cases, the weaker tail vortex is the one that undergoes destruction first, with the stronger tail vortex following and then the wing vortices.

The implication of this study is that a minor instability in this flow can cause the wake to be destroyed in a very different manner. The destruction of the vortices begins in the weaker tail vortex and then spreads throughout the remaining vortices. The asymmetry of the flow means that the T-T interaction is significantly rarer, as the tail vortices are rarely within the highly strained region between the wing vortices at the same time. Therefore, aside from the 'high tail' case seeded with the optimal perturbation, the destruction of the wake will take a longer period of time when compared to the 'flat tail' case.

Chapter 6

Conclusions

This thesis has described a numerical study into the stability of two systems of parallel vortices and their application to wingtip vortices produced in fixed-wing aviation. The first system comprises a counter-rotating pair of parallel vortices, and the second system comprises a strong counter-rotating vortex pair, representing the wing vortex pair, in conjunction with a pair of weaker opposite-sign vortices, representing tail vortices. The investigation of the second system was split into two different studies: one comprising a system where the wing and tail vortices had symmetric strength (but opposing sign) across the mid-plane, and a second study where the circulation strengths were asymmetric across the mid-plane. The major conclusions arising from this study are highlighted in the sections to follow.

6.1 Equal strength two-vortex system

The equal strength two-vortex study found that the first two Kelvin modes, [-1,1,1] and [-1,1,2], require a certain amount of time before they become apparent in the transient growth analysis. The [-1,1,1] mode only becomes apparent at $\tau = 2.67$ with an axial wavenumber of $k\,a_1 = 2.12$. The second mode, [-1,1,2], appears at $\tau = 3.56$ with an axial wavenumber of $k\,a_1 = 3.7$. It interesting that for the values of τ that were investigated, the Crow instability becomes apparent at $\tau = 1.78$ with an axial wavenumber of $k\,a_1 = 0.155$. This is of interest as the literature had identified the global mode of the Crow instability with an axial wavenumber of $k\,a = 0.18$ (Brion *et al.* 2007).

The transient growth analysis provides the perturbation that will lead to optimal energy growth, and an analysis of these fields for the Crow and elliptic instability was conducted. In addition, the fields were evolved and investigated using the linearised

Navier–Stokes equations. It was found that the elliptic instability formed into the asymptotic solution of a pair of dipoles similar to that found in the literature. While the initial optimal perturbation field for the Crow instability at an axial wavenumber of $k\,a_1 = 0.155$ looks very different to the global mode, it does evolve into the global mode after a short period of time.

Next, a DNS study was conducted on both the elliptic and Crow instability, investigating the effect of seeding the flow with the optimal perturbations against white noise of similar energy magnitude. Literature in this area indicated that this type of study has not been conducted before. This study found that the instability in the DNS, seeded with the optimal perturbation quickly grew to a stage where it became non-linear and caused the base flow to deform significantly. By contrast, the perturbation that consisted of white noise began to decay almost immediately before growing after a very long period of time. This decaying of the white noise perturbation is because only a small number of instability mode shapes are conducive to growth. This means that all of the mode shapes that are not conducive to growth have to decay away before the mode shapes that are conducive to growth can dominate the flow.

6.2 Equal strength four-vortex system

The 'high tail' configuration has the kinematic effect of initially driving the wing vortex pair vertically downward to almost double the distance of the 'flat tail' case. While the 'flat tail' case displays slightly less circulation in both the wing and tail vortices, the decay rate is very similar between the two. This implies that both cases will take a similar time to decay via viscous diffusion alone. There is a drop in the circulation in the tail vortex of the 'high tail' case, which is due to the stripping of circulation as the tail vortex is forced through the highly strained region between the wing vortex pair. This drop in circulation is directly related to the initial horizontal spacing of the wing vortex pair, where smaller initial separation results in higher circulation drop. The slow decay time of the tail circulation will cause greater vibration in the wing vortex pair, potentially leading to greater three dimensional instabilities in the wing vortex pair, thus causing the system to reach destruction faster. The two-dimensional, symmetry breaking instability present after a long timeframe were found to occur around $t/T_0 \approx 4$ for both cases. However, the 'flat tail' case did display a significantly higher magnitude of instability. This symmetry breaking instability causes the system to become highly

unbalanced, potentially causing three-dimensional instabilities to form faster. This work highlights just how significant a small change in vertical displacement of the tail vortex pair can be in the dynamics of the entire wake system.

This is also significant as some of the previous work, which utilised a stationary vortex filament analysis method, would not have found this. This symmetry breaking instability leads to a non-symmetrical vibration in the wing vortex pair. Therefore, the non-symmetrical vibration is likely to lead to a faster onset of three-dimensional instability.

When a transient growth analysis is applied to a zero wavenumber (two dimensional) case, it accurately predicts the slightly faster onset of a two-dimensional symmetry breaking instability in the 'flat tail' case when compared to the 'high tail' case.

The transient growth analysis of the three-dimensional perturbations shows that both the 'high tail' and 'flat tail' cases respond optimally to a perturbation of an axial wavenumber of $k\,a_0 = 5.3$. This is confirmed by the three-dimensional DNS and shows that in very short times, both configurations seeded with the perturbation that leads to optimal growth, cause the flow to become highly perturbed and non-linear. After this peak energy occurs, the instabilities in the vortex cores of the wing vortices are destroyed, leaving only a weak level of vorticity. This is in contrast to the simulations seeded with white noise, where the perturbations decay away as the decaying modes damp out until the unstable modes grow to dominate the flow, taking significantly longer to cause destruction. The interesting result to note is that the 'high tail' case seems more susceptible to white noise perturbations than the 'flat tail' case. This is the opposite to the cases seeded with the perturbations that lead to optimal energy growth found from the transient growth analysis. Given the nature of white noise, this can change from simulation to simulation, as the magnitude of the transient modes conducive to growth can vary in magnitude.

Regardless, in both cases, the seeding of the flow by the perturbation that leads to optimal energy growth reduces significantly the time the flow takes to be destroyed from simple seeding with white noise. The instability takes the form of two types of vortex interaction. If the instability in the tail vortex pair has grown to sufficient magnitude as it enters the highly strained region between the wing vortex pair, the tail vortices are forced to interact with each other with flow crossing the mid-plane (T-T interaction), causing a rapid devolution into small scale flow structures. The other interaction that

can occur is between the wing and tail vortices with no flow crossing the mid-plane (T-W interaction). The interaction between only the wing and tail vortices causes the instability to grow at a smaller rate, therefore extending the time it takes for the tail vortices to devolve into small scale flow structures.

The magnitude study found that the magnitude of the instability as the tail vortices enter the highly strained region between the wing vortices directly affects the type of vortex interaction. If the instability is of insufficient magnitude, no flow occurs across the mid-plane of the domain, leading to the T-W interaction. If the instability has grown to sufficient magnitude as the tail vortices enter the highly strained region between the wing vortex pair, the tail vortices interact with each other, causing flow across the mid plane, leading to the T-T interaction.

The position that the vortices are seeded in the first orbit also has an effect on the type of interaction that occurs. This is directly related to the energy present in the instability in the tail vortex pair as they enter the highly strained region between the wing vortex pair. When the tail vortices are seeded just before they enter the highly strained region, the instability has enough time to grow to allow the flow to cross the mid-plane and cause the T-T interaction. If the flow is seeded when the tail vortex pair is leaving, or outside, the highly strained region, then the interaction is of the T-W type, as the instability grows due to the mutually induced strain between the wing and tail vortex, with little effect from the other side of the midplane. The DNS study found that the growth rate of the instability was directly related to the position of the tail vortex pair. When the tail vortex pair was seeded within, or just before, entry into the highly strained region between the wing vortex pair, the growth rate of the instability was significantly higher, resulting in a more rapid transition into the non-linear regime and a faster reduction in the energy in the zeroth Fourier mode. This result implies that seeding with a certain magnitude of instability, so that the transition of the flow into non-linear regime occurs in a favourable position, will lead to a more rapid destruction of the wake hazard for trailing aircraft.

6.3 Unequal strength four-vortex system

The study investigating the unequal strength four-vortex system found that the short term two-dimensional kinematics of the system are extremely unbalanced, but exhibit a similar drop to the symmetrical case. In both the ‘high tail’ and ‘flat tail’ cases, the left

wing/tail pair exhibited less drop than the right side, with the 'flat tail' case showing less drop overall. For the zero-wavenumber (two-dimensional) transient growth analysis, there is a band of τ where the flat tail exhibits larger growth ($1 \leq \tau/T_0 \leq 2.25$), but for the majority of the time, the 'high tail' demonstrates a larger growth amplification factor.

The study continued with a three-dimensional transient growth analysis of both the asymmetrical 'flat tail' and 'high tail' cases. It was found that the asymmetry of the system has the effect of shifting the peak axial wavenumber where the system is most susceptible to transient growth of perturbations ($k\,a_1 \approx 6.1$). However, the system does have a fairly broad band of wavenumbers that it will respond to however and still maintain growth amplification factors of $G(\tau) \approx O(10^{26})$. This magnitude of growth amplification factor is in the same order as the symmetrical case.

The evolution of the optimal perturbation fields in the linear regime was considered next. It showed that the optimal way to seed this flow with an instability is to introduce a [-1,1,1] Kelvin mode into the weaker tail vortex only. In the linear regime, the instability is confined to the weaker tail vortex.

A three-dimensional DNS study was conducted, seeding both the 'high tail' and 'flat tail' cases with the optimal perturbation. An axial wavenumber of $k\,a_1 = 6.25$ and 6.12 were chosen for the asymmetric 'flat tail' and 'high tail' cases respectively. The DNS demonstrated that similar vortex interactions are present in the asymmetrical case to the symmetrical case, the T-T and T-W cases. The T-T case is significantly rarer, as it requires both tail vortices to reach a level of instability, and both be present within the highly strained region between the wing vortex pair. It was only observed to occur in the 'high tail' case seeded with the optimal perturbation. The requirement of both tail vortices being present between the highly strained region between the wing vortex pair is uncommon in these cases, as the orbit period of the tail vortices are different, due to the different strength ratios between the wing and tail vortices on each side of the domain. In the two cases, the weaker tail vortex is the one that undergoes destruction first, with the stronger tail vortex following and then the wing vortices in the same order.

The implications of the asymmetric study is that a minor instability in this flow can cause the wake flow to be destroyed in a very different manner. The destruction of the vortices begins in the weaker tail vortex and then spreads throughout the rest of

the vortices. The asymmetry of the flow means that the T-T interaction is significantly rarer, as the tail vortices are rarely within the highly strained region between the wing vortices at the same time, and so, aside from the 'high tail' cases seeded with the optimal perturbation, the destruction of the wake will take a longer period of time.

Bibliography

Abid, M. 2008 Nonlinear mode selection in a model of trailing line vortices. *J. Fluid Mech.* **605**, 19–45.

Akima, H. 1970 A new method of interpolation and smooth curve fitting based on local procedures. *J. Assoc. Comput. Mach.* **17**, 589–602.

Allen, A. & Breitsamter, C. 2008a Landing gear influence on the wake of a large transport aircraft. *J. Aircraft* **45** (4), 1367–1372.

Allen, A. & Breitsamter, C. 2008b Transport aircraft wake influenced by a large winglet and winglet flaps. *J. Aircraft* **45** (2), 686–699.

Allen, A. & Breitsamter, C. 2009a Experimental investigation of counter-rotating four-vortex aircraft wake. *Aerosp. Sci. Technol.* **13** (2-3), 114–129.

Allen, A. & Breitsamter, C. 2009b Transport aircraft wake influenced by oscillating winglet flaps. *J. Aircraft* **46** (1), 175–188.

Antkowiak, A. & Brancher, P. 2004 Transient energy growth for the Lamb-Oseen vortex. *Phys. Fluids* **16** (1), L1–L4.

Babie, B. & Nelson, R. 2010 An experimental investigation of bending wave instability modes in a generic four-vortex wake. *Phys. Fluids* **22** (7), 077101.

Baker, G., Barker, S., Bofah, K. & Saffman, P. 1974 Laser anemometer measurements of trailing vortices in water. *J. Fluid Mech.* **65** (Part 2), 325–336.

Barker, S. & Crow, S. 1975 Core instabilities of a vortex pair. *B. Am. Phys. Soc.* **20**, 1428–1428.

Barkley, D., Blackburn, H. & Sherwin, S. 2008 Direct optimal growth analysis for timesteppers. *Int. J. Numer. Meth. Fluids* **57**, 1435–1458.

Batchelor, G. 1964 Axial flow in trailing line vortices. *J. Fluid Mech* **20** (part 4), 645–658.

Bayly, B. 1986 Three-dimensional instability of elliptical flow. *Phys. Rev. Letters* **57** (17).

Bearman, P., Heyes, A., Lear, C. & Smith, D. 2007 Evolution of a forced counter-rotating vortex pair for two selected forcing frequencies. *Exp. Fluids* **43**, 501–507.

Blackburn, H., Barkley, D. & Sherwin, S. 2008a Convective instability and transient growth in flow over a backward facing step. *J. Fluid Mech.* **603**, 271–304.

Blackburn, H. & Sheard, G. 2010 On quasi-periodic and subharmonic Floquet wake instabilities. *Phys. Fluids* **22** (3), 031701.

Blackburn, H., Sherwin, S. & Barkley, D. 2008b Convective instability and transient growth in steady and pulsatile stenotic flows. *J. Fluid Mech.* **607**, 267–277.

Boustead, N., Ryan, K. & Sheard, G. 2010 Short-wave instability growth in closely spaced vortex pairs. *Prog. Comput. Fluid Dy.* **10** (5-6), 276–283.

Brandt, S. & Iverson, J. 1977 Merging of aircraft trailing vortices. *J. Aircraft* **14** (12), 1212–1220.

Brion, V., Sipp, D. & Jacquin, L. 2007 Optimal amplification of the Crow instability. *Phys. Fluids* **19** (11), 111703.

Bristol, R., Ortega, J., Marcus, P. & Savaş, O. 2004 On co-operative instabilities of parallel vortex pairs. *J. Fluid Mech.* **517**, 331–358.

Burnham, D. & Hallock, J. 1982 Chicago monostatic acoustic vortex sensor system. *Tech. Rep.* DOT-TSC-FAA-79-103.IV. FAA.

Constant, G., Foord, R., Forrester, P. & Vaughan, J. 1994 Coherant laser radar and the problem of aircraft wake vortices. *J. Modern Opt.* **41**, 2153–2173.

Courant, R., Friedrichs, K. & Lewy, H. 1928 Partial differential equations of mathematical physics. *MATH. ANN.* **100**, 32–74.

Crouch, J. 1997 Instability and transient growth for two trailing-vortex pairs. *J. Fluid Mech.* **350**, 311–330.

Crouch, J., Miller, G. & Spalart, P. 2001 Active-control system for breakup of airplane trailing vortices. *AIAA J.* **39** (12), 2374–2381.

Crow, S. 1970 Stability theory for a pair of trailing vortices. *AIAA J.* **8**, 2172–2179.

Crow, S. 1974 Motion of a vortex pair in a stably stratified fluid. *Poseidon Research, Rept. 1, Los Angeles* .

Donnadieu, C., Ortiz, S., Chomaz, J.-M. & Billiant, P. 2009 Three-dimensional instabilities and transient growth of a counter-rotating vortex pair. *Phys. Fluids* **21** (9), 094102.

Eloy, C. & Le Dizès, S. 1999 Three-dimensional instability of Burgers and Lamb-Oseen vortices in a strain field. *J. Fluid Mech.* **378**, 145–166.

Fabre, D. & Jacquin, L. 2000 Stability of a four-vortex aircraft wake model. *Phys. Fluids* **12** (10), 2438–2443.

Fabre, D., Jacquin, L. & Loof, A. 2002 Optimal perturbations in a four-vortex aircraft wake in counter-rotating configuration. *J. Fluid Mech.* **451**, 391–328.

Fontane, J., Brancher, P. & Fabre, D. 2008 Stochastic forcing of the Lamb-Oseen vortex. *J. Fluid Mech.* **613**, 233–254.

Garten, J., Arendt, S., Fritts, D. & Werne, J. 1998 Dynamics of counter-rotating vortex pairs in stratified and sheared environments. *J. Fluid Mech.* **361**, 189–236.

Gerz, T., Holzäpfel, F. & Darracq, D. 2002 Commercial aircraft wake vortices. *Prog. Aerosp. Sci.* **38**, 181–208.

Gunston, B. 1995 *The Encyclopedia of Modern Warplanes*, 1st edn. MetroBooks (NY).

Haverkamp, S., Neuwerth, G. & Jacob, D. 2005 Active and passive vortex wake mitigation using control surfaces. *Aerosp. Sci. Technol.* **9**, 5–18.

Heaton, C. & Peake, N. 2007 Transient growth in vortices with axial flow. *J. Fluid Mech.* **587**, 271–301.

Henderson, R. 1999 *High-Order Methods for Computational Physics*. Springer.

Hill, D. & Saffman, P. 2002 Counter-rotating vortex patches in shear: a model of the effect of wind shear on aircraft trailing vortices. *Proc. R. Soc. Lond. A* **458** (2023), 1527–1553.

Holzapfel, F. & Gerz, T. 1999 Two-dimensional wake vortex physics in the stably stratified environment. *Aerosp. Sci. Technol.* **3** (5), 261–270.

Holzapfel, F., Gerz, T. & Baumann, R. 2001 The turbulent decay of trailing vortex pairs in stably stratified environments. *Aerosp. Sci. Technol.* **5**, 95–108.

Hubbard, S. & Marquis, A. 2005 Inviscid effects of thin shear layers on a four-vortex system. *J. Aircraft* **42** (2), 391–401.

Jacquin, L., Fabre, D., Geffroy, P. & Coustols, E. 2001 The properties of a transport aircraft wake in the extended near field: an experimental study. AIAA Conference proceedings, (2001-1038).

Jeong, J. & Hussain, F. 1995 On the identification of a vortex. *J. Fluid Mech.* **285**, 69–94.

Jiménez, J., Moffatt, H. & Vasco, C. 1996 The structure of the vortices in freely decaying two-dimensional turbulence. *J. Fluid Mech.* **313**, 209–222.

Karniadakis, G. 1990 Spectral element–Fourier methods for incompressible turbulent flows. *Meth. Appl. Mech. Eng.* **80**, 367–380.

Karniadakis, G., Israeli, M. & Orszag, S. 1991 High-order splitting methods for the incompressible Navier–Stokes equations. *J. Comp. Phys.* **97**, 414–443.

Karniadakis, G. & Sherwin, S. 1999 *Spectral/hp Element Methods for CFD*. Oxford University Press.

Kauertz, S. & Neuwerth, G. 2007 Excitation of instabilities in the wake of a wing with winglets. *AIAA J.* **45** (3), 577–592.

Kerswell, R. 2002 Elliptical instability. *Annu. Rev. Fluid Mech.* **34**, 83–113.

Khorrami, M. 1991 On the viscous modes of instability of a trailing line vortex. *J. Fluid Mech.* **225**, 197–212.

Lacaze, L., Ryan, K. & Le Dizès, S. 2007 Elliptic instability in a strained Batchelor vortex. *J. Fluid Mech.* **577**, 341–361.

Lamb, H. 1923 *Hydrodynamics*, 6th edn. New York: Dover.

Landman, M. J. & Saffman, P. G. 1987 The three-dimensional instability of strained vortices in a viscous fluid. *Phys. Fluids* **30** (8), 2339–2342.

Laporte, F. & Corjon, A. 2000 Direct numerical simulations of the elliptic instability of a vortex pair. *Phys. Fluids* **12** (5), 1016–1031.

Laporte, F. & Leweke, T. 2002 Elliptic instability of counter-rotating vortices: Experimental and direct numerical simulation. *AIAA J.* **40** (12), 2483–2494.

Le Dizès, S. & Laporte, F. 2002 Theoretical predictions for the elliptic instability in a two-vortex flow. *J. Fluid Mech.* **471**, 169–201.

Le Dizès, S. & Verga, A. 2002 Viscous interactions of two co-rotating vortices before merging. *J. Fluid Mech.* **467**, 389–410.

Lele, S. 2001 Vortex-wake pollution: A problem in fluid mechanics. *Lecture Notes in Physics -New York then Berlin-* pp. 163–182.

Leweke, T., Thompson, M. & Hourigan, K. 2004 Vortex dynamics associated with the collision of a sphere with a wall. *Phys. Fluids* **16**, L74.

Leweke, T. & Williamson, C. 1998 Cooperative elliptic instability of a vortex pair. *J. Fluid Mech.* **360**, 85–119.

Leweke, T. & Williamson, C. 2010 Experiments on long-wavelength instability and reconnection of a vortex pair. *Phys. Fluids* **23** (024101).

Lezius, D. 1973 Study of the far wake vortex field generated by a rectangular airfoil in a water tank. *AIAA Paper* **73-682**.

Liu, H.-T. 2006 Laboratory investigation of detrainment in vortex wakes. *AIAA J.* **44** (8), 1872–1882.

Marquet, O., Sipp, D. & Jacquin, L. 2006 Global optimal perturbations in a separated flow over a backward-rounded-step. pp. 2006–2897. 36th AIAA Fluid Dyn. Conf. and Exhibit. San Francisco.

Mason, H. & Marchman, J. 1972 The farfield structure of aircraft wake turbulence. *AIAA J.* **72-40**.

Matalanis, C. & Eaton, J. 2007 Wake vortex control using static segmented gurney flaps. *AIAA J.* **45** (8), 1874–1884.

Mayer, E. & Powell, K. 1992 Viscous and inviscid instabilities of a trailing vortex. *J. Fluid Mech.* **245**, 91–114.

McCormick, B. 1995 *Aerodynamics, Aeronautics and Flight Mechanics*, 2nd edn. John Wiley & sons, Inc.

Meunier, P., Ehrenstein, U., Leweke, T. & Rossi, M. 2002 A merging criterion for two-dimensional co-rotating vortices. *Phys. Fluids* **14** (8), 2757–2766.

Meunier, P. & Leweke, T. 2001 Three-dimensional instability during vortex merging. *Phys. Fluids* **13** (10), 2747–2750.

Meunier, P. & Leweke, T. 2005 Elliptic instability of a co-rotating vortex pair. *J. Fluid Mech.* **533**, 125–159.

Miller, E. & Brown, C. 1971 An experimental study of trailing vortex wakes using a large towing tank. *Hydronautics Tech. Rep.* **7105-1**.

Moore, D. & Saffman, P. 1972 Motion of a vortex filament with axial-flow. *Philos. Tr. R. SOC. S.-A* **272**, 403.

Moore, D. & Saffman, P. 1975 The instability of a straight vortex filament in a strain field. *Proc. R. Soc. Lond. A* **259**, 241–264.

Nomura, K., Tsutsui, H., Mahoney, D. & Rottman, J. 2006 Short wavelength instability and decay of a vortex pair in a stratified fluid. *J. Fluid Mech.* **553**, 283–322.

Olendraru, C. & Sellier, A. 2002 Viscous effects in the absolute-convective instability of the Batchelor vortex. *J. Fluid Mech.* **459**, 371–396.

Orlandi, P. 2007 Two-dimensional and three-dimensional direct numerical simulation of co-rotating vortices. *Phys. Fluids* **19** (013101).

Ortega, J. & Savaş, O. 2000 Rapidly growing instability mode in trailing multiple-vortex wakes. *AIAA J.* **39** (4), 750–754.

Pierrehumbert, R. 1980 A family of steady, translating vortex pairs with distributed vorticity. *J. Fluid Mech.* **99**, 129–144.

Pierrehumbert, R. 1986 Universal shortwave instability of two-dimensional eddies in an invisid fluid. *Phys. Rev. Letters* **57** (17).

Proctor, F. 1998 The NASA-Langley wake vortex modelling effort in support of an operational aircraft spacing system. AIAA Conference proceedings, (1998-0589).

Raab, H. 2011 Crow instability in contrails - earth science picture of the day. http://epod.usra.edu/blog/2011/08/crow-instability-in-contrails.html, accessed: 06 Oct 2011.

Rennich, S. & Lele, S. 1999 A method for accelerating the destruction of aircraft wake vortices. *J. Aircraft* **36**, 398–404.

Roy, C., Schaeffer, N., Le Dizès, S. & Thompson, M. 2008 Stability of a pair of co-rotating vortices with axial flow. *Phys. Fluids* **20** (094101).

Ryan, K., Butler, C. & Sheard, G. 2011 Stability characteristics of a counter-rotating unequal strength Batchelor vortex pair. *J. Fluid Mech.* **696**, 374–401.

Saffman, P. 1979 The approach of a vortex pair to a plane surface in an inviscid fluid. *J. Fluid Mech.* **92**, 497–503.

Saffman, P. 1992 *Vortex Dynamics*. Cambridge University Press.

Saffman, P. & Szeto, R. 1980 Equilibrium shapes of a pair of equal uniform vortices. *Phys. Fluids* **23**, 2339–2342.

Sarpkaya, T. 1983 Trailing vortices in homogeneous and density stratified media. *J. Fluid Mech.* **136**, 85–109.

Schaeffer, N. & Le Dizès, S. 2010 Nonlinear dynamics of the elliptic instability. *J. Fluid Mech.* **646**, 471–480.

Sheard, G. 2011 Wake stability features behind a square cylinder: Focus on small incidence angles. *J. Fluids Struct.* **35** (5-6), 734–742.

Sheard, G., Fitzgerald, M. & Ryan, K. 2009 Cylinders with square cross section: Wake instabilities with incidence angle variation. *J. Fluid Mech.* **630**, 43–69.

Sheard, G., Leweke, T., Thompson, M. & Hourigan, K. 2007 Flow around an impulsively arrested circular cylinder. *Phys. Fluids* **19** (8), 083601.

Sipp, D., Jacquin, L. & Cosssu, C. 2000 Self-adaption and viscous selection in concentrated two-dimensional vortex dipoles. *Phys. Fluids* **12** (2), 245–248.

So, J., Ryan, K. & Sheard, G. 2007 Interaction of an unequal-strength vortex pair. pp. 1457–1462. 16th Australian Fluid Mechanics Conference.

So, J., Ryan, K. & Sheard, G. 2008 Linear stability analysis of a counter-rotating vortex pair of unequal strength. *ANZIAM J.* **50**, C137–C151.

So, J., Ryan, K. & Sheard, G. 2011 Short-wave instabilities on a vortex pair of unequal strength circulation ratio. *App. Math. Model.* **35**, 1581–1590.

de Sousa, P. & Pereira, J. 2009 Laminar co-rotating Batchelor vortex merging. *Theor. Comp. Fluid Dyn.* **21** (1), 1–14.

Stumpf, E. 2005 Study of four-vortex aircraft wakes and layout of corresponding aircraft configurations. *J. Aircraft* **32** (3), 722–730.

Thomas, P. & Auerbach, D. 1994 The observation of the simultaneous development of a long- and short-wave instability mode on a vortex pair. *J. Fluid Mech.* **265**, 289–302.

Thomson, W. 1880 Vibrations of a columnar vortex. *Philos. Mag. Series 5* **10** (61), 155–168.

Tsai, C.-Y. & Widnall, S. 1976 The stability of short waves on a straight vortex filament in a weak externally imposed strain field. *J. Fluid Mech.* **73**, 721–733.

Waleffe, F. 1990 On the three dimensional instability of strained vortices. *Phys. Fluids* **2** (1).

Widnall, S., Bliss, D. & Tsai, C.-Y. 1974 The instability of short waves on a vortex ring. *J. Fluid Mech.* **66**, 35–47.

Winkelmans, G., Thirifay, F. & Ploumhans, P. 2000 Effect of non-uniform wind shear onto vortex wakes: parametric models for operational systems and comparison with CFD studies. Handouts of the Fourth WakeNet Workshop on "Wake Vortex Encounter", Amsterdam, The Netherlands.